Theory and Numerical Modelling of Parity-Time Symmetric Structures for Photonics

Sendy Phang, BEng (Hons.) MSc

Thesis submitted to The University of Nottingham
for the degree of Doctor of Philosophy, January 2016

Abstract

This thesis presents the study of a relatively new class of photonic structures invoking Parity-Time ($\mathcal{PT}$)-symmetry. $\mathcal{PT}$-symmetric structures in photonics, as a realisation of $\mathcal{PT}$-symmetric Quantum Mechanics problems, are constructed by a judicious design of refractive index modulation which requires the real part of the refractive index to be an even function and the imaginary part of the refractive index to be an odd function in space. $\mathcal{PT}$-symmetric structures in the form of Bragg gratings, coupled resonators and chain resonators are the main configurations studied in this thesis. These $\mathcal{PT}$-symmetric structures feature a spontaneous symmetry breaking at which interesting wave behaviour such as an asymmetric response depending on the direction of the incident wave, unidirectional invisibility, simultaneous coherent-perfect-absorber lasing and localised termination modes are observed; these behaviours are presented in this thesis. Theoretical and numerical studies of these $\mathcal{PT}$-symmetric structures are undertaken which assume realistic material parameters, including material dispersion and material non-linearity. Moreover, in this thesis, potential applications of these $\mathcal{PT}$-symmetric stuctures are explored.

The first part of the thesis considers $\mathcal{PT}$-symmetric Bragg grating structures which are formed by introducing a $\mathcal{PT}$-symmetric refractive index modulation into a Bragg grating structure. If gain/loss dispersion is considered, it is shown that dispersion limits the $\mathcal{PT}$-symmetric operation to just a single frequency. As such spontaneous symmetry breaking can only be achieved by varying the gain/loss parameter. Nevertheless, it is shown that by switching the gain/loss in the system, a switching operation can be achieved by using the $\mathcal{PT}$-Bragg grating at a single frequency. Subsequently, a non-linear $\mathcal{PT}$-Bragg grating is investigated by using a time-domain numerical method, namely the Transmission-Line modelling (TLM) method. For

the present work a TLM code is developed from scratch in order to ensure full-flexibility when modelling a dispersive and non-linear material. Using the TLM solver, it is demonstrated that gain/loss saturation is an important material property which should be considered as it may impact the practical applications of a $\mathcal{PT}$-symmetry-based device. In the context of a non-linear $\mathcal{PT}$-Bragg grating (NPTBG), the gain/loss saturation affects the interplay between the $\mathcal{PT}$-symmetric opearation and the Kerr non-linear effect. It is further shown that gain/loss saturation plays a crucial role in securing a stable operation of non-linear $\mathcal{PT}$-based devices. For practical applications, it is demonstrated that a non-linear $\mathcal{PT}$-symmetric Bragg grating offers an additional degree of freedom in their operation, by modulating the gain/loss and the intensity of the input signal, compared to a passive structure which can only be manipulated by the input signal intensity. Two applications based on the interplay of $\mathcal{PT}$-symmetric behaviour and Kerr non-linearity are demonstrated, namely a memory device and a logic-gate device.

The second part of the thesis studies $\mathcal{PT}$-symmetric resonator structures as a coupled system and as a periodic chain system. For these studies, a semi-analytical method based on the Boundary Integral Equation (BIE) method is developed and used together with a two-dimensional TLM method. The impact of realistic material parameter on the spectral properties of the structure is again investigated. It is shown that the $\mathcal{PT}$-symmetric behaviour can be observed at a single frequency. Moreover, it is shown that $\mathcal{PT}$-symmetry-like behaviour is observed but with complex eigenfrequencies due to the radiation losses; this is a deviation of the strict definition of a $\mathcal{PT}$-symmetric structure with balanced gain and loss. Lowering lasing threshold by increasing loss in the system is demonstrated; this occurs due to induced early symmetry breaking. The final part of the thesis studies the spectral properties of an infinite and finite chain of $\mathcal{PT}$-symmetric resonators. It is shown that the type of modulation along the $\mathcal{PT}$-chain affects the position of the breaking point of the $\mathcal{PT}$-structure. For a finite $\mathcal{PT}$-chain structure, and for a particular

type of refractive index modulation, early $\mathcal{PT}$-symmetry breaking is observed and shown to cause the presence of termination states which are localised at the edge of the finite-chain resulting in localised lasing and dissipative modes at each end of the chain.

* * *

Acknowledgements

Although my name is the only one that appears in the cover of this book, the work presented in this thesis cannot be achieved by myself alone. I would like, first of all, to expressed my deepest gratitude to my supervisor Dr Ana Vukovic, not only for her excellent academic guidance but also for her warmth and friendship during my time in the GGIEMR[‡]. I also would like to thank Ana for her help in securing the funding for the project; without her effort this project would not have been established. I hope that one day I would become an understanding supervisor to my students as Ana has been to me.

I would like to acknowledge Dr Hadi Susanto for introducing me to the subject of parity-time symmetry photonics and for, without any hesitation, helping to secure the funding for me to undertake the project.

I am grateful to Professor Trevor M. Benson, not only for his excellent supervising and inspiration, but especially for his endless support to accommodate my never-ending personal ambition. Trevor has inspired me and supported me to be an independent researcher; I find no words to quantify all the opportunities he has given to me to build my academic career. I also would like to thank Trevor for his patience on my clumsiness in writing and for carefully reading and commenting on countless revisions on all my publications and my thesis.

It has been a great fortune for me to meet Dr Stephen Creagh and having him as my supervisor. Working with Stephen has been a brilliant experience, I have learnt so many things in which especially his tireless patience to explain to me over-over-

[‡]George Green Institute for Electromagnetics Research, University of Nottingham

over-over-and-over until I fully understand.

I would like to thank Dr Gabriele Gradoni for the fruitful discussion and collaborations. Talking with Gabriele has been thought-provoking and has inspired me in my scientific journey.

I would also to acknowledge the support of Professor Phillip D. Sewell for his input and ideas during the project. Furthermore, I would like to thank Phil without whose generous support, I would not be able to attend any of the conference meetings during my PhD.

Finally I would like to thank all the members of the GGIMER: Dr Xuesong Meng for the fruitful collaboration and for letting me disturb your work everytime to discuss some technical issues; Ahmed Elkash, Dan Simmons and Hayan Nasser for the friendliness and interesting discussions on all kind of subjects; Dr Hiroki Wakatsuchi, Dr Harshana Gihan Dantarayana and Dr Brian Teo for the valuable input during my first year of PhD, friendliness and academic inspirations; Zhewen Zhang, Alphonso and Latifah Abdul Aziz for allowing me to bother you during the final year of my PhD.

Last but not the least, none of this would have been possible without the love and patience of my family. My family to whom this dissertation is dedicated to, has been a constant source of love, concern, support and strength all these years.

Nottingham,

January 2016

S.P.

Publications related to this thesis

Book chapters:

S. Phang, A. Vukovic, H. Susanto, S. C. Creagh, P. Sewell, G. Gradoni, and T. M. Benson, "Theory and Numerical Modelling of Parity-Time Symmetric Structures in Photonics: Part I Introduction and Grating Structures in One Dimension," in *Recent Trends in Computational Photonics*, (ed.) Arti Agrawal, Trevor M. Benson, Richard DeLaRue, and Gregory Wurtz (*in editorial*) Springer (2016).

S. Phang, A. Vukovic, S. C. Creagh, P. Sewell, G. Gradoni, and T. M. Benson, "Theory and Numerical Modelling of Parity-Time Symmetric Structures in Photonics: Part II Boundary Integral Equation for Coupled Microresonator Structure," in *Recent Trends in Computational Photonics*, (ed.) Arti Agrawal, Trevor M. Benson, Richard DeLaRue, and Gregory Wurtz (*in editorial*) Springer (2016).

Peer reviewed journal articles:

[J1] **S. Phang**, A. Vukovic, H. Susanto, T. M. Benson, and P. Sewell, "Ultrafast optical switching using paritytime symmetric Bragg gratings," J. Opt. Soc. Am. B 30, 29842991 (2013).

[J2] **S. Phang**, A. Vukovic, H. Susanto, T. M. Benson, and P. Sewell, "Impact of dispersive and saturable gain/loss on bistability of nonlinear parity-time Bragg gratings," Optics Letters 39, 26036 (2014).

[J3] **S. Phang**, A. Vukovic, T. M. Benson, H. Susanto, and P. Sewell, "A versatile all-optical parity-time signal processing device using a Bragg grating

induced using positive and negative Kerr-nonlinearity," Optical and Quantum Electronics 47 (1), 37-47 (2014).

[J4] **S. Phang**, A. Vukovic, T. M. Benson, S. C. Creagh, P. Sewell, and G. Gradoni, "Parity-time symmetric coupled microresonators with a dispersive gain/loss," Optics Express 23(9), 11493-11507 (2015).

[J5] **S. Phang**, A. Vukovic, S. C. Creagh, P. Sewell, G. Gradoni, and T. M. Benson "Localized single frequency lasing states in a finite parity-time symmetric resonator chain," Scientific Reports 6 (20499), 1-11 (2016).

Publications in conference proceeding:

[C1] **S. Phang**, A. Vukovic, H. Susanto, T. Benson, and P. Sewell, "Time Domain Modeling of All-Optical Switch based on PT-Symmetric Bragg Grating," in 29th Annual Review of Progress in Applied Computational Electromagnetics (Applied Computational Electromagnetics Society, 2013), Monterey, USA pp. 693698.

[C2] **S. Phang**, A. Vukovic, H. Susanto, T. M. Benson, and P. Sewell, "Practical limitation on operation of nonlinear parity-time Bragg gratings," in META 2014 Conference (2014), Singapura, Singapore pp. 270275. (Invited)

[C3] **S. Phang**, A. Vukovic, H. Susanto, T. M. Benson, and P. Sewell, "Modelling of Dispersive PT-Symmetric Bragg Grating," in 9th IET International Conference on Computation in Electromagnetics (CEM 2014) (Institution of Engineering and Technology, 2014), London, UK pp. 5.045.04.

[C4] **S. Phang**, A. Vukovic, T. M. Benson, S. C. Creagh, P. Sewell, and G. Gradoni, "Saturable and dispersive parity-time symmetric directional coupler: A transmission-line modelling study," in 2014 16th International Conference on Transparent Optical Networks (ICTON) (IEEE, 2014), Graz, Austria, pp.

16. (Invited)

[C5] **S. Phang**, A. Vukovic, T. M. Benson, S. C. Creagh, P. Sewell, and G. Gradoni, "Coupled Parity-Time Symmetric Cavities: Results from the Transmission Line Modelling Simulations," in 2015 17th International Conference on Transparent Optical Networks (ICTON) (IEEE, 2015), Budapest, Hungary. (Invited)

Conferences with abstract:

[A1] **S. Phang**, A. Vukovic, H. Susanto, T. M. Benson, and P. Sewell "Nonlinear and dispersive Parity Time (PT)-symmetric Bragg grating for information photonics" in Information Photonics Conference (2013), Warsaw, Poland.

[A2] **S. Phang**, A. Vukovic, H. Susanto, T. M. Benson, and P. Sewell "Nonlinear Parity-Time Bragg Grating: Applications" in Photonic North 2014, (SPIE 2014), Montreal, Quebec. (Invited)

[A3] **S. Phang**, A. Vukovic, T. M. Benson, S. C. Creagh, P. Sewell, and G. Gradoni "Threshold Preservation of PT-Resonant Structures in Realistic-Dispersive Medium" in Optical wave and waveguide theory and numerical modelling workshop (2015), London, UK

[A4] **S. Phang**, A. Vukovic, T. M. Benson, S. C. Creagh, P. Sewell, and G. Gradoni "Parity-Time coupled microresonators: Kramers-Kronig limitation" in CLEO Europe 2015, Munich, Germany

[A5] **S. Phang**, A. Vukovic, T. M. Benson, S. C. Creagh, P. Sewell, and G. Gradoni "Parity-Time Chain of Whispering-Gallery Mode Resonators" in Metamaterial and Photonic Crystal conference (2015), New York, USA.

[A6] **S. Phang**, A. Vukovic, T. M. Benson, S. C. Creagh, P. Sewell, and G. Gradoni

"Threshold Manipulation in Parity-Time Symmetric Microresonator Chain" in Meta 2015 congress, Oxford, UK

[A7] **S. Phang**, A. Vukovic, S. C. Creagh, P. Sewell, G. Gradoni, and T. M. Benson "Parity-Time Symmetric Chain Resonators," in Metamaterial and Photonic Crystal conference (2016), Malaga, Spain.

[A8] **S. Phang**, A. Vukovic, S. C. Creagh, P. Sewell, G. Gradoni, and T. M. Benson "Time-Modulated Gain and Loss Parity-Time Symmetric Resonators," Optical wave and waveguide theory and numerical modelling workshop (2016), Warsaw, Poland.

Contents

List of Symbols

This list registers symbols that are consistently used throughout in the thesis. Local symbols which are used in a specific section are not listed here to avoid ambiguity.

Symbol	Description	Unit	First used
$\boldsymbol{E}$	Electric field vector (TD[‡])	V/m	(2.1)
$\boldsymbol{D}$	Electric flux density vector (TD)	C/m^2	(2.1)
$\boldsymbol{P_e}$	Dielectric polarisation vector (TD)	C/m^2	(2.1)
$\boldsymbol{H}$	Magnetic field vector (TD)	A/m	(2.1)
$\boldsymbol{B}$	Magnetic flux density vector (TD)	Wb/m^2	(2.1)
$\boldsymbol{J_e}$	Electric current density vector (TD)	A/m^2	(2.1)
$\boldsymbol{M}$	Magnetic current density vector (TD)	V/m^2	(2.1)
ε	Electric permittivity	F/m	(2.3)
ε_0	Free-space permittivity	F/m	(2.3)
$\bar{\varepsilon}$	Relative permittivity	–	(2.3)
χ_e	Dielectric susceptibility	–	(2.3)
σ	Electrical conductivity	S/m	(2.2)
μ	Magnetic permeability	H/m	(2.4)
μ_0	Free-space permeability	H/m	(2.4)
$\boldsymbol{S}$	Poynting vector	W/m^2	(2.7)
$\boldsymbol{\mathcal{E}}$	Electric field vector (FD[*])	V/m	(2.14)
$\boldsymbol{\mathcal{D}}$	Electric flux density vector (FD)	C/m^2	(2.14)

[‡]Time-Domain
[*]Frequency-Domain

$\boldsymbol{\mathcal{P}_e}$	Dielectric polarisation vector (FD)	$\mathrm{C/m^2}$	(2.14)
$\boldsymbol{\mathcal{H}}$	Magnetic field vector (FD)	A/m	(2.14)
$\boldsymbol{\mathcal{B}}$	Magnetic flux density vector (FD)	$\mathrm{Wb/m^2}$	(2.14)
$\boldsymbol{\mathcal{J}_e}$	Electric current density vector (FD)	$\mathrm{A/m^2}$	(2.14)
$\boldsymbol{\mathcal{M}}$	Magnetic current density vector (FD)	$\mathrm{V/m^2}$	(2.14)
$\mathcal{F}\{.\}$	Fourier transform operator	–	(2.16)
ω	Angular frequency	rad/s	(2.14)
j	Imaginary number $\sqrt{-1}$	–	(2.14)
γ	Complex propagation constant	rad/m	(2.21)
α	Attenuation (+) or amplification (−)	$\mathrm{m^{-1}}$	(2.21)
β	Real part of propagation constant	rad/m	(2.21)
$\boldsymbol{\mathcal{S}}$	Poynting vector (FD)	$\mathrm{W/m^2}$	(2.24)
$\mathbf{S}$	Scattering matrix	–	(2.29)
s_n	Eigenvalue of scattering matrix	–	(3.27)
$\boldsymbol{a}$	Normalised incoming wave amplitude	–	(2.28)
$\boldsymbol{b}$	Normalised outgoing wave amplitude	–	(2.28)
S_{nm}	Scattering matrix element index (n, m)	–	(2.30)
$\hat{H}$	Hamiltonian of a system	–	(3.1)
n	Refractive index	–	(3.12)
t	Transmission coefficient	–	(3.16)
r	Reflection coefficient	–	(3.16)
$\mathbf{M}$	Transfer matrix	–	(3.18)
T	Transmittance, i.e. $T = \lvert t^2 \rvert$	–	(3.25)
R	Reflectance, i.e. $R = \lvert r^2 \rvert$	–	(3.25)
$\mathbb{R}$	Set of real number	–	(3.22)
Λ	Physical length of a unit cell of grating	m	(4.1)
τ	Atomic relaxation time	s	(5.1)
ω_σ	Atomic transitional frequency	Hz	(5.1)
$\mathbb{S}$	Saturation coefficient	–	(5.1)

V	Voltage	Volt	(5.10)
I	Current	Ampere	(5.10)
G	Conductivity	S	(5.10)
C	Capacitance	Farad	(5.10)
L	Inductance	Henry	(5.11)
Z	Impedance	Ohm	(5.17)
$\mathcal{Z}$	Bilinear $\mathcal{Z}$-transform	–	(5.27)
z^{-1}	Delay operator	–	(5.27)
J_m	Bessel function of the 1$^{\text{st}}$ kind order m	–	(9.11)
Y_m	Bessel function of the 2$^{\text{nd}}$ kind order m	–	(9.11)
$H_m^{(1)}$	Hankel function of the 1$^{\text{st}}$ kind order m	–	(9.11)
$H_m^{(2)}$	Hankel function of the 2$^{\text{nd}}$ kind order m	–	(9.11)
Q	Quality factor	–	(9.18)
G_0	Free-space Green's function	–	(9.24)

List of Abbreviation

$\mathcal{PT}$	Parity-Time
NBG	Non-linear Bragg grating
PTBG	Parity-time Bragg grating
NPTBG	Non-linear Parity-time Bragg grating
K-NPTBG	Kerr Non-linearity induced Parity-time Bragg grating
CPAL	Coherent-Perfect-Absorber and Lasing
TLM	Transmission Line Modelling
BIE	Boundary Integral Equation
QM	Quantum mechanics
T-matrix	Transfer matrix
S-matrix	Scattering matrix
FWHM	Full-Width Half-Magnitude
CW	Continuous wave
FDTD	Finite-Difference Time-Domain
WGM	Whispering-Gallery Modes
Q-factor	Quality factor
μR	micro-resonator
p.v.	Principal value of an indefinite integration

1

Introduction

This chapter provides the background of the work presented in this thesis, i.e. parity-time symmetric photonic systems. An interpretation of parity-time symmetry in the simplest form, as a source-drain problem, is conceptually introduced. This chapter also shows the development of research in the area of $\mathcal{PT}$-symmetry systems and further shows the development of research, especially in $\mathcal{PT}$-symmetric photonics systems. Finally this chapter outlines the contents of the thesis.

* * *

1.1 Background to the Thesis

In 1998, Bender and Boetcher published a seminal paper [1.1] in which they studied the spectra of a new class of complex quantum mechanical systems[‡]. In the paper, it is established that a complex quantum mechanical system which satisfies Parity and Time ($\mathcal{PT}$) symmetry *may* have a completely real spectrum, i.e. it is a stable[*] system.

This concept of a $\mathcal{PT}$-symmetric system is elaborated further in [1.2] where Bender, *et al.* provided an example of a simple $\mathcal{PT}$-symmetric system as [1.2,1.3],

$$H = \begin{bmatrix} -j\alpha & \kappa \\ \kappa & j\alpha \end{bmatrix}. \tag{1.1}$$

Interestingly, the system given in (1.1) is similar to the eigenvalue problem matrix of a source and drain, in which α represents source $(+)$ and drain $(-)$ that are coupled by a coupling mechanism represented by κ. As such, in the simplest form, the concept of $\mathcal{PT}$-symmetry can be depicted as a source-drain system which is schematically illustrated in Fig. 1.1. It can be seen from Fig. 1.1(a) that a system with a source is unstable, in the same way as for a system with a drain, portrayed in Fig. 1.1(b); the system with a source has a growing (unbounded) state while the system with a drain has a decaying state. It is, however, by coupling these systems together that a system with growing energy can be *tamed* by a dissipating system which yields to a stable system, as illustrated in Fig. 1.1(c).

Since the publications of [1.1–1.6], $\mathcal{PT}$-symmetric systems have been the subject of intense investigation in the last couple of years. Figure 1.2 shows the number of publications associated with $\mathcal{PT}$-symmetry (blue bar) from its conceptualisation in 1998

[‡]Within this context the quantum mechanical system refers to the Hamiltonian of the Schrödinger equation. The formal definition of a Hamiltonian is presented in Section 3.1.

[*]A stable system here refers to a system which yields neither a non-decaying nor amplifying output.

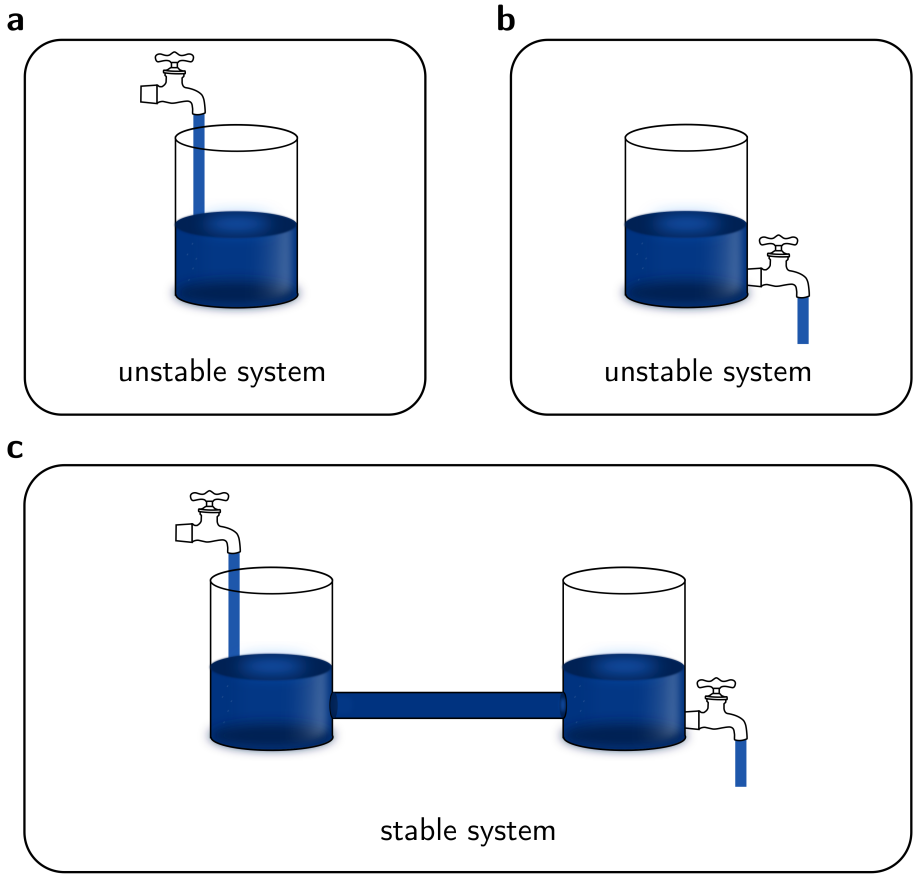

Figure 1.1 | Illustration of source-drain system. An isolated system with (**a**) source, (**b**) drain and (**c**) the coupled source-drain system.

up to 2014. Note that in 2014 on average almost one publication associated with $\mathcal{PT}$-symmetry was published daily. Despite the extensive theoretical developments of the $\mathcal{PT}$-symmetric system [1.1–1.10], experimental observation of $\mathcal{PT}$-symmetry within its original context of a quantum mechanical system is found to be elusive and very challenging [1.11–1.13]. Meanwhile, $\mathcal{PT}$-symmetry has also been reported in a variety of physical systems such as gravity theory [1.14], cold atom systems [1.15–1.17], electronics [1.18–1.20], mechanical oscillators [1.21], acoustics [1.22,1.23], microwave electromagnetics [1.24,1.25] and optics-photonics [1.11,1.12,1.26–1.63].

In particular, it is noted that an enormous amount of research on $\mathcal{PT}$-symmetry has been done within the optical framework; from 2011 more than half of the publications in the field are associated with $\mathcal{PT}$-symmetric optical structures, which in-

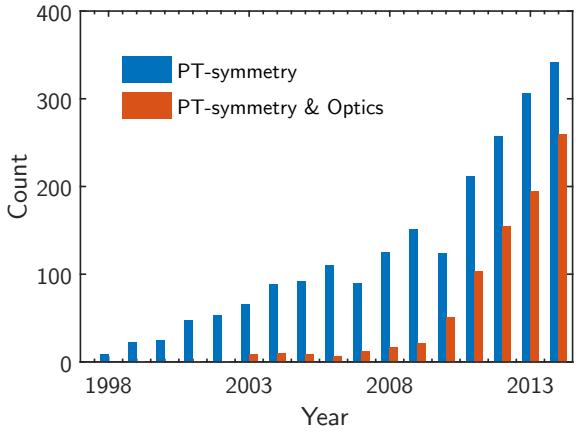

Figure 1.2 | Number of publications on $\mathcal{PT}$-symmetry from 1998 to 2014. Data from publication query service Scopus accessed in October 2015.

clude gratings [1.26–1.28,1.30,1.37,1.42,1.44,1.47,1.51,1.64,1.65], lattices [1.26,1.31, 1.41,1.66,1.67], waveguides [1.13,1.29,1.38,1.39,1.43,1.48,1.54,1.68–1.70], plasmonics [1.32,1.55,1.60] and resonant cavities [1.11,1.53,1.56,1.61,1.62,1.71]. Motivated by the source-drain $\mathcal{PT}$-symmetry concept, simple $\mathcal{PT}$-waveguide couplers have been demonstrated on a $LiNbO_3$ platform where one waveguide was providing gain and the other an equal amount of loss [1.34], marking the first experimental observation of $\mathcal{PT}$-symmetric photonics. Since [1.34], more experimental work on $\mathcal{PT}$-symmetric photonics has emerged such as $\mathcal{PT}$-symmetric Bragg gratings [1.72] in which the authors demonstrate the unidirectional transparency previously theoretically predicted by [1.26,1.30], $\mathcal{PT}$-symmetric ring gratings for the demonstration of single-frequency laser application [1.58,1.73], $\mathcal{PT}$-symmetric lattices and $\mathcal{PT}$-symmetric microresonators. These structures are summarised in Fig. 1.3.

Within the optical context, the main feature of $\mathcal{PT}$-symmetric photonic structures is that they may have purely real spectra, i.e. zero net-power amplification or dissipation, despite having both gain and loss in the system [1.13,1.34,1.75]. However, there exists a threshold defined for a certain amount of gain/loss for which the $\mathcal{PT}$-system undergoes a spontaneous $\mathcal{PT}$-symmetry breaking, and above which the power grows exponentially [1.13,1.34,1.38,1.57,1.75] within the structure. Interesting properties of $\mathcal{PT}$-photonic structures at this threshold point have been

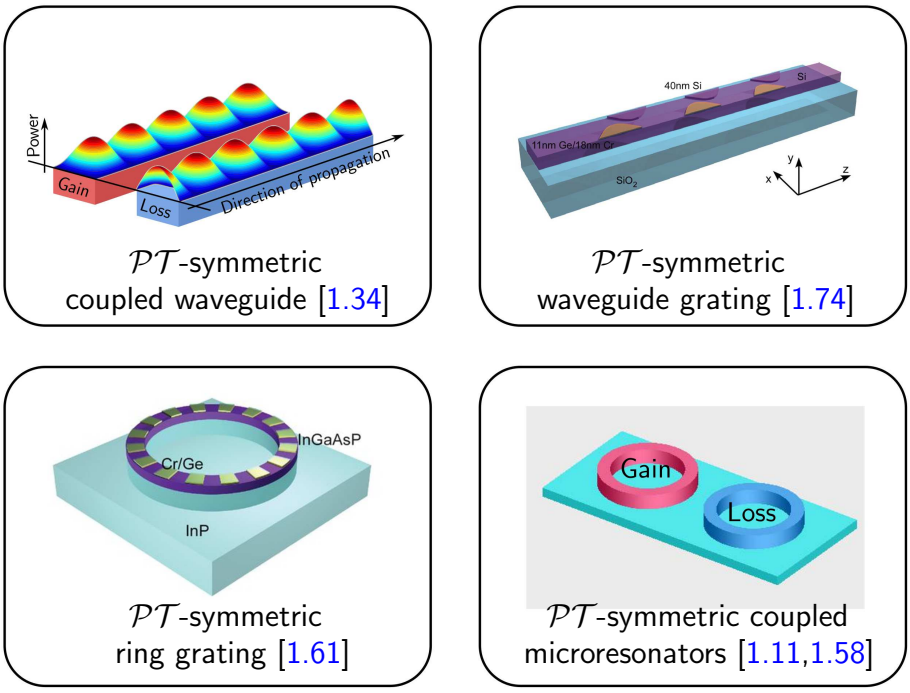

Figure 1.3 | Examples of experimentally demonstrated $\mathcal{PT}$-symmetric photonic structure.

observed which include loss-induced invisibility [1.12,1.26,1.30,1.72], simultaneous lasing and coherent perfect absorption [1.57,1.75], anomalous Bloch-mode power oscillation [1.12,1.76], asymmetric beam scattering [1.69,1.72] and lasing in a loss-dominated system [1.56,1.71].

$\mathcal{PT}$-symmetric structures in optics come in a vast range of configurations, for that very reason this thesis will focus mainly on the study of $\mathcal{PT}$-symmetric Bragg grating and $\mathcal{PT}$-symmetric resonant microcavities structures. In particular the work presented in this thesis addresses some fundamental challenges in the modelling and practical consideration of $\mathcal{PT}$-symmetric photonic structures.

From the aspect of model analysis, it came to my attention during the course of this work that most of the published works on $\mathcal{PT}$-symmetric photonic structures have neglected the dispersive behaviour of material which naturally occurs in all realistic implementation with gain or loss [1.47,1.50,1.69,1.71,1.77–1.79]. As a result it has raised questions regarding the influence this may have on the practical application

of $\mathcal{PT}$-symmetry-based devices. For that reason a significant part of this thesis has been devoted to modelling $\mathcal{PT}$-symmetric photonic structures under a realistic dispersive material scenario. It will present the impact of realistic dispersive gain/loss media on the performance of $\mathcal{PT}$-symmetric structures, and in particular on how realistic dispersion puts a fundamental limitation on the practical application of $\mathcal{PT}$-symmetric based devices. Despite this limitation, the work described in this thesis will demonstrate the potential applications which *can* be exploited from the unique properties $\mathcal{PT}$-symmetric structures.

As for the method of study, a time-domain Transmission-Line Modelling (TLM) code is developed from scratch to provide a greater flexibility to model $\mathcal{PT}$-symmetric structures, incorporating dispersive gain and loss material, within a time-domain framework. Moreover, an accurate analytical method based on the Boundary Integral Equation (BIE) method has been developed to aid the modelling of microcavity structures. The aim of using both frequency and time-domain methods of analysis is to provide complete temporal and spectral pictures of $\mathcal{PT}$-symmetric photonic structures, which has been missing from most of the previously reported results.

1.2 Overview of the Thesis

Chapter 2 presents the fundamental theories of electromagnetism which form the foundation of the work described in this thesis. The chapter starts with a description of the time-varying and time-harmonic electromagnetic fields and introduces the concept of the time causality properties of matter. This chapter also defines the scattering matrix formalism which describes a multi-port optical network system. The concept of reciprocity is described and found to place a symmetry condition on the scattering matrix. Finally, the concept of causal material properties is elaborated and gives the Kramers-Kronig conditions which relate the real and imaginary parts

of the dielectric permittivity.

It is followed by chapter 3 which describes the concept of $\mathcal{PT}$-symmetric photonics as a translation of the $\mathcal{PT}$-symmetric Hamiltonian problem in quantum mechanics. The chapter also studies the spectral properties of a $\mathcal{PT}$-symmetric scattering system. In particular, it presents the properties of the transfer matrix $\mathbf{M}$ and the scattering matrix $\mathbf{S}$ under $\mathcal{PT}$-transformation, under which a $\mathcal{PT}$-symmetric scatterer is shown to exhibit exotic behaviour such as, unidirectional unitary transmission, spontaneous $\mathcal{PT}$-symmetry breaking and simultaneous coherent perfect absorber-lasing operation. Moreover, this chapter also presents the generalised conservation relationship for an asymmetric left-right response and provides a criterion for describing $\mathcal{PT}$-symmetry breaking in a scattering system.

Following the study of a $\mathcal{PT}$-symmetric scattering system in the previous chapter, Chapter 4 focuses on a one-dimensional (1D) $\mathcal{PT}$-symmetric Bragg grating. The chapter overviews the dispersion properties of passive Bragg gratings and compares them to the $\mathcal{PT}$-symmetric Bragg gratings. For the case of a $\mathcal{PT}$ Bragg grating, the impact of the gain/loss upon the transmission and reflection spectra is analysed. Furthermore the asymmetric scattering phenomena depending on the direction of the incident wave is studied. Moreover, the phase transition of $\mathcal{PT}$-symmetry is demonstrated showing how the gain/loss parameter breaks the $\mathcal{PT}$-symmetry of the system. Finally, the spectral singularity of the scattering system associated with the simultaneous coherent perfect absorber-lasing (CPAL) operation state is also shown.

In order to model a $\mathcal{PT}$-symmetric structure within a realistic material framework, Chapter 5 provides a simple practical realistic gain/loss material model which is dispersive and saturable. A frequency domain model of such a dispersive and saturable model is presented. Moreover this chapter also details the time-domain Transmission-line modelling (TLM) method in one-dimension. The *telegrapher* equa-

tion is introduced and shown to give an analogue representation of Maxwell's equations in the electromagnetic field theory as a lumped-element electrical circuit. Subsequently, a numerical TLM method is developed based on this analogy using the bilinear $\mathcal{Z}$-transformation formulation. Moreover, a gain material satisfying the Kramers-Kronig relations is described and implemented in the TLM method. Finally, the implemented TLM gain material model is validated for two study cases, namely for a linear and saturable gain.

In Chapter 6 the impact of dispersion in a realistic causal gain/loss material model, which satisfies the Kramers-Kronigs relations, upon the spectral behaviour of a $\mathcal{PT}$-Bragg grating (PTBG) is investigated. This chapter will show the application and validity of the numerical time-domain TLM method to model a realistic dispersive PTBG based on a typical GaAs material. This chapter shows that dispersion put a practical limit in the operation of a $\mathcal{PT}$-symmetric Bragg grating. Nevertheless, the chapter demonstrates a novel application of a PTBG for a switching application in the time-domain.

Chapter 7 further investigates the properties of a $\mathcal{PT}$-symmetric Bragg grating by including non-linear behaviour in the material model. First, the 1D-TLM model is developed further to also include a non-linear property of material. A realistic dispersive and non-linear Duffing material model is used for the purpose of modelling. Employing the enhanced TLM model, which includes both a dispersive-saturable gain/loss material model and a non-linear-dispersive Duffing model, the performance of non-linear $\mathcal{PT}$-symmetric Bragg grating structures are investigated. Two variants of non-linear $\mathcal{PT}$-Bragg grating structures are considered in this chapter. The chapter further investigates the impact of non-linearity in the operation of such structures in a realistic scenario when the gain/loss material is dispersive and saturable. Two applications exploiting this combined ($\mathcal{PT}$-symmetric and non-linearity) behaviour are also demonstrated as a memory device and a logic gate device.

In Chapter 8 the formulation of 2-dimensional (2D) TLM model is presented. This chapter serves as a prelude to the modelling of $\mathcal{PT}$-symmetric structures in the 2D spatial domain. In particular, the chapter extends the implementation of the digital filter design of a realistic dispersive and saturable gain/loss model which was used to model a realistic $\mathcal{PT}$-symmetric Bragg grating in the previous chapters.

Chapter 9 investigates the fundamental properties of the $\mathcal{PT}$-resonant system based on two coupled whispering gallery resonators within the context of both realistic material properties and practical operating constraints. In particular the chapter will discuss how practical dispersive property of gain and loss material that satisfy the Kramers-Kronig relationship affects the performance of microcavity-based $\mathcal{PT}$-resonant structure. Theoretical background for an isolated circular resonator is also overviewed. An exact analytical model based on the Boundary Integral Equation (BIE) method is developed to calculate the characteristic frequencies of $\mathcal{PT}$-symmetric microresonators.

Chapter 10 considers the extension of the $\mathcal{PT}$-symmetric coupled microresonator structure studied in the previous chapter as a finite periodic Parity Time chain made of resonant dielectric cylinders. The main case studied in this chapter is a $\mathcal{PT}$-chain on which a more general case of $\mathcal{PT}$ symmetry is achieved by modulating both the real and imaginary parts of the material refractive index along the resonator chain. The band-structure of the finite $\mathcal{PT}$ resonator chains is compared to infinite case in order to understand the complex interdependence of the Bloch phase and the amount of the gain/loss in the system that causes the $\mathcal{PT}$ symmetry to break.

Finally Chapter 11 gives a summary and the conclusions of this thesis and discusses possibilities for further developments based on this work.

References

[1.1] C. M. Bender and S. Boettcher, "Real spectra in non-hermitian hamiltonians having PT symmetry," Phys. Rev. Lett. **80**, 5243–5246 (1998).

[1.2] C. M. Bender, D. C. Brody, and H. F. Jones, "Complex extension of quantum mechanics," Phys. Rev. Lett. **89**, 270401 (2002).

[1.3] Q.-H. Wang, S.-Z. Chia, and J.-H. Zhang, "PT symmetry as a generalization of Hermiticity," J. Phys. A Math. Theor. **43** (2010).

[1.4] C. M. Bender, "Introduction to PT-symmetric quantum theory," Contemp. Phys. **46**, 277–292 (2005).

[1.5] C. M. Bender, "Making sense of non-Hermitian Hamiltonians," Reports Prog. Phys. **70**, 947–1018 (2007).

[1.6] C. M. Bender, S. Boettcher, and P. N. Meisinger, "PT-symmetric quantum mechanics," J. Math. Phys. **40**, 2201 (1999).

[1.7] A. Mostafazadeh, "Pseudo-Hermiticity for a class of nondiagonalizable Hamiltonians," J. Math. Phys. **43**, 6343 (2002).

[1.8] M. Znojil, "Exact solution for Morse oscillator in PT-symmetric quantum mechanics," Phys. Lett. A **264**, 108–111 (1999).

[1.9] B. Bagchi, C. Quesne, and M. Znojil, "Generalized continuity equation and modified normalization in PT-symmetric quantum mechanics," Mod. Phys. Lett. A **16**, 2047–2057 (2001).

[1.10] A. Mostafazadeh, "Pseudo-Hermitian representation of quantum mechanics," Int. J. Geom. Methods Mod. Phys. **07**, 1191–1306 (2010).

[1.11] L. Chang, X. Jiang, S. Hua, C. Yang, J. Wen, L. Jiang, G. Li, G. Wang, and M. Xiao, "Paritytime symmetry and variable optical isolation in activepassive-coupled microresonators," Nat. Photonics **8**, 524–529 (2014).

[1.12] A. Regensburger, C. Bersch, M.-A. Miri, G. Onishchukov, D. N. Christodoulides, and U. Peschel, "Parity-time synthetic photonic lattices," Nature **488**, 167–71 (2012).

[1.13] T. Kottos, "Optical physics: Broken symmetry makes light work," Nat. Phys. **6**, 166–167 (2010).

[1.14] P. D. Mannheim, "Making the case for conformal gravity," Found. Phys. **42**, 388–420 (2012).

[1.15] D. Dizdarevic, D. Dast, D. Haag, J. Main, H. Cartarius, and G. Wunner, "Cusp bifurcation in the eigenvalue spectrum of PT-symmetric Bose-Einstein condensates," Phys. Rev. A **91**, 033636 (2015).

[1.16] R. Gutöhrlein, J. Schnabel, I. Iskandarov, H. Cartarius, J. Main, and G. Wunner, "Realizing PT-symmetric BEC subsystems in closed Hermitian systems," J. Phys. A Math. Theor. **48**, 335302 (2015).

[1.17] F. Single, H. Cartarius, G. Wunner, and J. Main, "Coupling approach for the realization of a PT-symmetric potential for a Bose-Einstein condensate in a double well," Phys. Rev. A **90**, 042123 (2014).

[1.18] F. Bagarello and G. Pantano, "Pseudo-Fermions in an electronic loss-gain circuit," Int. J. Theor. Phys. **52**, 4507–4518 (2013).

[1.19] J. Schindler, Z. Lin, J. M. Lee, H. Ramezani, F. M. Ellis, and T. Kottos, "PT-symmetric electronics," J. Phys. A Math. Theor. **45**, 444029 (2012).

[1.20] J. Schindler, A. Li, M. C. Zheng, F. M. Ellis, and T. Kottos, "Experimental study of active LRC circuits with PT symmetries," Phys. Rev. A **84**, 040101 (2011).

[1.21] C. M. Bender, B. K. Berntson, D. Parker, and E. Samuel, "Observation of PT phase transition in a simple mechanical system," Am. J. Phys. **81**, 173 (2013).

[1.22] X. Zhu, H. Ramezani, C. Shi, J. Zhu, and X. Zhang, "PT-Symmetric Acoustics," Phys. Rev. X **4**, 031042 (2014).

[1.23] R. Fleury, D. Sounas, and A. Alù, "An invisible acoustic sensor based on parity-time symmetry," Nat. Commun. **6**, 5905 (2015).

[1.24] C. Poli, M. Bellec, U. Kuhl, F. Mortessagne, and H. Schomerus, "Selective enhancement of topologically induced interface states in a dielectric resonator chain," Nat. Commun. **6**, 6710 (2015).

[1.25] S. Bittner, B. Dietz, U. Günther, H. L. Harney, M. Miski-Oglu, A. Richter, and F. Schäfer, "PT symmetry and spontaneous symmetry breaking in a microwave billiard," Phys. Rev. Lett. **108**, 024101 (2012).

[1.26] S. Longhi, "Invisibility in PT-symmetric complex crystals," J. Phys. A Math. Theor. **44**, 485302 (2011).

[1.27] H. F. Jones, "Analytic results for a PT -symmetric optical structure," J. Phys. A Math. Theor. **45**, 135306 (2012).

[1.28] M. Kulishov, J. M. Laniel, N. Bélanger, J. Azaña, and D. V. Plant, "Nonreciprocal waveguide Bragg gratings," Opt. Express **13**, 3068–78 (2005).

[1.29] J. Čtyroký, V. Kuzmiak, and S. Eyderman, "Waveguide structures with antisymmetric gain/loss profile," Opt. Express **18**, 21585–21593 (2010).

[1.30] Z. Lin, H. Ramezani, T. Eichelkraut, T. Kottos, H. Cao, and D. N. Christodoulides, "Unidirectional invisibility induced by PT-symmetric periodic structures," Phys. Rev. Lett. **106**, 213901 (2011).

[1.31] K. G. Makris, R. El-Ganainy, and D. N. Christodoulides, "Beam dynamics in PT symmetric optical lattices," Phys. Rev. Lett. **100**, 103904 (2008).

[1.32] H. Benisty, A. Degiron, A. Lupu, A. D. Lustrac, S. Forget, M. Besbes, G. Barbillon, A. Bruyant, S. Blaize, and G. Lérondel, "Implementation of PT symmetric devices using plasmonics : Principle and applications," Opt. Express **19**, 3567–3578 (2011).

[1.33] R. El-Ganainy, K. G. Makris, D. N. Christodoulides, and Z. H. Musslimani, "Theory of coupled optical PT-symmetric structures," Opt. Lett. **32**, 2632–2634 (2007).

[1.34] C. E. Rüter, K. G. Makris, R. El-Ganainy, D. N. Christodoulides, M. Segev, and D. Kip, "Observation of paritytime symmetry in optics," Nat. Phys. **6**, 192–195 (2010).

[1.35] L. Razzari and R. Morandotti, "Optics: Gain and loss mixed in the same cauldron," Nature pp. 8–9 (2012).

[1.36] Z. Musslimani, K. Makris, R. El-Ganainy, and D. N. Christodoulides, "Optical solitons in PT periodic potentials," Phys. Rev. Lett. **100**, 030402 (2008).

[1.37] H. Ramezani, T. Kottos, R. El-Ganainy, and D. N. Christodoulides, "Unidirectional nonlinear PT-symmetric optical structures," Phys. Rev. A **82**, 043803 (2010).

[1.38] F. Nazari, M. Nazari, and M. K. Moravvej-Farshi, "A 2x2 spatial optical switch based on PT-symmetry," Opt. Lett. **36**, 4368–70 (2011).

[1.39] A. A. Sukhorukov, Z. Xu, and Y. S. Kivshar, "Nonlinear suppression of time reversals in PT-symmetric optical couplers," Phys. Rev. A **82**, 043818 (2010).

[1.40] Y. N. Joglekar, C. Thompson, D. D. Scott, and G. Vemuri, "Optical waveguide arrays: Quantum effects and PT symmetry breaking," Eur. Phys. J. Appl. Phys. **63**, 30001 (2013).

[1.41] A. Regensburger, M.-A. Miri, C. Bersch, J. Näger, G. Onishchukov, D. N. Christodoulides, and U. Peschel, "Observation of defect states in PT-symmetric optical lattices," Phys. Rev. Lett. **110**, 223902 (2013).

[1.42] M. Kulishov, B. Kress, and R. Slavík, "Resonant cavities based on Parity-Time-symmetric diffractive gratings," Opt. Express **21**, 68–70 (2013).

[1.43] M. Greenberg and M. Orenstein, "Optical unidirectional devices by complex spatial single sideband perturbation," IEEE J. Quantum Electron. **41**, 1013–1023 (2005).

[1.44] S. Phang, A. Vukovic, H. Susanto, T. M. Benson, and P. Sewell, "Ultrafast optical switching using paritytime symmetric Bragg gratings," J. Opt. Soc. Am. B **30**, 2984–2991 (2013).

[1.45] S. Longhi, "Optical realization of relativistic non-hermitian quantum mechanics," Phys. Rev. Lett. **105**, 013903 (2010).

[1.46] S. Longhi, "PT-symmetric laser absorber," Phys. Rev. A **82**, 031801 (2010).

[1.47] S. Phang, A. Vukovic, H. Susanto, T. M. Benson, and P. Sewell, "Impact of dispersive and saturable gain/loss on bistability of nonlinear parity-time Bragg gratings," Opt. Lett. **39**, 2603–6 (2014).

[1.48] A. Lupu, H. Benisty, and A. Degiron, "Switching using PT symmetry in plasmonic systems: positive role of the losses," Opt. Express **21**, 192–195 (2013).

[1.49] H. Benisty, C. Yan, A. Degiron, and A. Lupu, "Healing near-PT-symmetric structures to restore their characteristic singularities: Analysis and examples," J. Light. Technol. **30**, 2675–2683 (2012).

[1.50] A. A. Zyablovsky, A. P. Vinogradov, A. V. Dorofeenko, A. A. Pukhov, and A. A. Lisyansky, "Causality and phase transitions in PT-symmetric optical systems," Phys. Rev. A **89**, 033808 (2014).

[1.51] S. Phang, A. Vukovic, T. M. Benson, H. Susanto, and P. Sewell, "A versatile all-optical parity-time signal processing device using a Bragg grating induced using positive and negative Kerr-nonlinearity," Opt. Quantum Electron. **47**, 37–47 (2015).

[1.52] J. Čtyroký, "Dispersion properties of coupled waveguides with loss and gain: a full-vectorial analysis," Opt. Quantum Electron. **46**, 465–475 (2014).

[1.53] S. Longhi and L. Feng, "PT-symmetric microring laser-absorber," Opt. Lett. **39**, 5026–9 (2014).

[1.54] M. Greenberg and M. Orenstein, "Unidirectional complex grating assisted couplers." Opt. Express **12**, 4013–8 (2004).

[1.55] B. Baum, H. Alaeian, and J. Dionne, "A parity-time symmetric coherent plasmonic absorber-amplifier," J. Appl. Phys. **117**, 063106 (2015).

[1.56] B. Peng, S. K. Ozdemir, S. Rotter, H. Yilmaz, M. Liertzer, F. Monifi, C. M. Bender, F. Nori, and L. Yang, "Loss-induced suppression and revival of lasing." Science **346**, 328–32 (2014).

[1.57] L. Ge, Y. D. Chong, and a. D. Stone, "Conservation relations and anisotropic transmission resonances in one-dimensional PT-symmetric photonic heterostructures," Phys. Rev. A - At. Mol. Opt. Phys. **85**, 1–10 (2012).

[1.58] H. Hodaei, M.-A. Miri, M. Heinrich, D. N. Christodoulides, and M. Khajavikhan, "Parity-time-symmetric microring lasers," Science (80-.). **346**, 975–978 (2014).

[1.59] J. J. Monz, L. Sánchez-Soto, J. Monzón, and J. J. Monz, "Invisibility and PT symmetry: A simple geometrical viewpoint," Symmetry (Basel). **6**, 396–408 (2014).

[1.60] H. Alaeian and J. a. Dionne, "Parity-time-symmetric plasmonic metamaterials," Phys. Rev. A **89**, 033829 (2014).

[1.61] L. Feng, Z. J. Wong, Y. Wang, X. Zhang, R.-M. R.-M. Ma, Y. Wang, X. Zhang, R.-M. R.-M. Ma, Y. Wang, and X. Zhang, "Single-mode laser by parity-time symmetry breaking," Science **346**, 972–975 (2014).

[1.62] B. Peng, a. K. Özdemir, F. Lei, F. Monifi, M. Gianfreda, G. L. Long, S. Fan, F. Nori, C. M. Bender, and L. Yang, "Paritytime-symmetric whispering-gallery microcavities," Nat. Phys. **10**, 394–398 (2014).

[1.63] A. Mostafazadeh, "Semiclassical analysis of spectral singularities and their applications in optics," Phys. Rev. A **84**, 023809 (2011).

[1.64] C. Y. Huang, R. Zhang, J. L. Han, J. Zheng, and J. Q. Xu, "Type-II perfect absorption and amplification modes with controllable bandwidth in combined PT-symmetric and conventional Bragg-grating structures," Phys. Rev. A **89**, 023842 (2014).

[1.65] N. X. A. Rivolta and B. Maes, "Diffractive switching by interference in a tailored PT-symmetric grating," J. Opt. Soc. Am. B **32**, 1330 (2015).

[1.66] S. Nixon, L. Ge, and J. Yang, "Stability analysis for solitons in PT-symmetric optical lattices," Phys. Rev. A **85**, 023822 (2012).

[1.67] G. Harari, Y. Plotnik, M. A. Bandres, Y. Lumer, M. C. Rechtsman, and M. Segev, "Topological insulators in PT-Symmetric lattices," in "CLEO 2015," (2015), p. FTh3D.3.

[1.68] H. Nolting, G. Sztefka, and J. Čtyroký, "Wave propagation in a waveguide with a balance of gain and loss," in "Integr. Photonics Res.", (OSA, Boston, Massachusetts, 1996), 4930, pp. 76–80.

[1.69] A. Ruschhaupt, F. Delgado, and J. G. Muga, "Physical realization of -symmetric potential scattering in a planar slab waveguide," J. Phys. A. Math. Gen. **38**, L171–L176 (2005).

[1.70] S. Phang, A. Vukovic, T. M. Benson, S. Creagh, P. Sewell, and G. Gradoni, "Saturable and dispersive parity-time symmetric directional coupler: A transmission-line modelling study," in "16th Int. Conf. Transparent Opt. Networks," (IEEE, Graz, Austria, 2014), pp. 1–6.

[1.71] S. Phang, A. Vukovic, S. C. Creagh, T. M. Benson, P. D. Sewell, and G. Gradoni, "Parity-time symmetric coupled microresonators with a dispersive gain/loss," Opt. Express **23**, 11493 (2015).

[1.72] L. Feng, Y.-l. Xu, W. S. Fegadolli, M.-h. Lu, J. E. B. Oliveira, V. R. Almeida, Y.-F. Chen, and A. Scherer, "Experimental demonstration of a unidirectional reflectionless parity-time metamaterial at optical frequencies." Nat. Mater. **12**, 108–13 (2013).

[1.73] H. Hodaei, M.-a. Miri, M. Heinrich, D. N. Christodoulides, and M. Khajavikhan, "PT-symmetric microring lasers: Self-adapting broadband mode-selective resonators," arXiv Prepr. arXiv 1405.2103 p. 12 (2014).

[1.74] L. Feng, M. Ayache, J. Huang, Y.-L. Xu, M.-H. Lu, Y.-F. Chen, Y. Fainman, and A. Scherer, "Nonreciprocal light propagation in a silicon photonic circuit," Science (80-.). **333**, 729–733 (2011).

[1.75] Y. D. Chong, L. Ge, and a. D. Stone, "PT-symmetry breaking and laser-absorber modes in optical scattering systems," Phys. Rev. Lett. **106**, 093902 (2011).

[1.76] S. Longhi, "Bloch oscillations in complex crystals with PT symmetry," Phys. Rev. Lett. **103**, 1–4 (2009).

[1.77] A. E. Siegman, *Lasers* (University Science Book, Palo Alto, CA, 1986).

[1.78] L. D. Landau, J. S. Bell, M. J. Kearsley, L. P. Pitaevskii, E. M. Lifshitz, and J. B. Sykes, *Electrodynamics of continuous media* (Elsevier, London, England, 1984), 2nd ed.

[1.79] M. Bass, G. Li, and E. van Stryland, *Handbook of optics vol. 4* (McGraw Hill, New York, NY, 2010), 3rd ed.

2

Electromagnetism and Matter

Fundamental theories of electromagnetism, which form the foundation of the work described in this thesis, are presented in this chapter. The chapter starts with a description of the time-varying and the Helmholtze-quation for electromagnetic field and introduces the concept of the time causal properties of matter. This chapter also defines the scattering matrix formalism which describes a multi-port optical network system. The concept of reciprocity is described and found to place a symmetry condition on the scattering matrix. Finally, the concept of causal material properties is elaborated and gives the Kramers-Kronig conditions which relate the real and imaginary parts of the dielectric permittivity.

* * *

2.1 Basic Theory of Electromagnetism

2.1.1 Maxwell's Equations for Time-Varying Electromagnetic Field

Year 2015 is marked as the International Year of Light to recognise the advancement of light based technologies since the description of light as electromagnetic wave phenomena 150 years ago by James C. Maxwell in 1865 [2.1]. Formulated by James C. Maxwell in 1861 [2.2], Maxwell's equations are the embodiment of a hundred years of theoretical and experimental work previously done by Johann Carl Friedrich Gauss, André-Marie Ampère, Hans Christian Ørsted, Heinrich Lenz, Michael Faraday, Oliver Heaviside and many others [2.3–2.5]. Maxwell's equations are a complete set of equations describing the dynamics of macroscopic electromagnetic phenomenon. They can be expressed in two forms, i.e. in integral and differential form. Although the integral form of Maxwell's equations may provide a more in-depth understanding of the underlying physical phenomena, they are often analytically solvable only for canonically shaped objects [2.6]. Meanwhile, supported by the development of advanced computing technologies, the differential form provides mathematical advantages to naturally discretise any non-standard problem both in spatial and time domains to be solved numerically [2.5,2.7]. The curl pair of Maxwell's equations in the differential form is given as,

$$\begin{bmatrix} \nabla \times \boldsymbol{H} \\ -\nabla \times \boldsymbol{E} \end{bmatrix} = \begin{bmatrix} \boldsymbol{J_e} \\ \boldsymbol{M} \end{bmatrix} + \frac{\partial}{\partial t} \begin{bmatrix} \boldsymbol{D} \\ \boldsymbol{B} \end{bmatrix} \tag{2.1}$$

where the description of each quantity, including their units in an SI system, is given in Table 2.1. It is important to note that in the time-domain formulation of the Maxwell's equation (2.1), all the vector field quantities $\boldsymbol{E}$, $\boldsymbol{H}$, $\boldsymbol{J_e}$, $\boldsymbol{D}$, and $\boldsymbol{B}$ are real functions of both position and time, i.e. $\boldsymbol{E} = \boldsymbol{E}(x, y, z; t)$ in a Cartesian

Table 2.1 | Symbol and unit notation of electromagnetics quantities

Symbol	Unit	Name
$\boldsymbol{E}$	V/m	Electric field vector
$\boldsymbol{D}$	C/m^2	Electric flux density vector
$\boldsymbol{P_e}$	C/m^2	Dielectric polarisation vector
$\boldsymbol{H}$	A/m	Magnetic field vector
$\boldsymbol{B}$	Wb/m^2	Magnetic flux density vector
$\boldsymbol{J_e}$	A/m^2	Electric current density vector
$\boldsymbol{M}$	V/m^2	Magnetic current density vector
ε	F/m	Electric permittivity
ε_0	F/m	Free-space permittivity
$\bar{\varepsilon}$	–	Relative permittivity
χ_e	–	Dielectric susceptibility
σ	S/m	Electrical conductivity
μ	H/m	Magnetic permeability
μ_0	H/m	Free-space permeability

coordinate system. Moreover, as the focus of the thesis will be on applying Maxwell's equations in the optical regime where non-magnetic materials are considered, the magnetic current density is negligible, i.e. $\boldsymbol{M} = 0$ is assumed throughout this thesis.

From (2.1), it can be seen that the rate of change of the electric flux density $\boldsymbol{D}$ in time excites the generation of magnetic field $\boldsymbol{H}$ in space, while the rate of change of the magnetic flux density $\boldsymbol{B}$ generates the electric field $\boldsymbol{E}$ implying that the dynamics of electric and magnetic fields in space and time are coupled. This coupling is related to the macroscopic response of the electric and magnetic properties of a material to the applied electromagnetic field, which is given by the so called constitutive

relations. For an homogeneous and isotropic material the constitutive relationships in the time-domain are given by [2.4,2.8–2.10],

$$\boldsymbol{J_e} = \sigma(t) * \boldsymbol{E}, \tag{2.2}$$

$$\boldsymbol{D} = \varepsilon_0 \boldsymbol{E} + \varepsilon_0 \chi_e(t) * \boldsymbol{E}, \tag{2.3}$$

$$\boldsymbol{B} = \mu \boldsymbol{H}. \tag{2.4}$$

where the electromagnetic properties of the material, (σ, ε, ε_0, χ_e, μ, μ_0), are also described in Table 2.1. Moreover for photonic applications in the THz regime, it is typical to assume a non-magnetic material, i.e. ($\mu = \mu_0$); henceforth a non-magnetic material is assumed in this thesis. Note that $*$ in (2.2) and (2.3) denotes the time-domain convolution operator which is defined as [2.8–2.10],

$$f(t) * \boldsymbol{E}(t) = \int_0^\infty f(\tau)\boldsymbol{E}(t-\tau)d\tau \tag{2.5}$$

where the time-varying function $f(t)$ can be of $\sigma(t)$ or $\chi_e(t)$. The convolution operation of (2.5) suggests that $\boldsymbol{D}(t)$ and $\boldsymbol{J}(t)$ are non-local functions of time; as such the field-matter response at time t depends on the field response at times other than t.

Another important theorem in electromagnetism, associated with the conservation of energy, is the Poynting theorem. The Poynting theorem is obtained directly as a result of imposing vector identities on (2.1) and is given as [2.3–2.5,2.7,2.11],

$$\oiint_{\Omega} (\boldsymbol{E} \times \boldsymbol{H}) \cdot d\mathbf{S} + \iiint_{V} \left[\boldsymbol{E} \cdot \boldsymbol{J}_e + \boldsymbol{H} \cdot \frac{\partial \boldsymbol{B}}{\partial t} + \boldsymbol{E} \cdot \frac{\partial \boldsymbol{D}}{\partial t} \right] dv = 0 \tag{2.6}$$

The interpretation of (2.6) is that the power dissipated and the rate of change of energy stored in a closed volume V are related to the net electromagnetic energy flowing into the volume V through the closed surface Ω. The energy density influx

is commonly referred to as the Poynting vector $\boldsymbol{S}$, i.e.

$$\boldsymbol{S} = \boldsymbol{E} \times \boldsymbol{H} \tag{2.7}$$

In this work, a general interpretation of the Poynting vector $\boldsymbol{S}$ is that the magnitude of the Poynting vector $|\boldsymbol{S}|$ denotes the instantaneous energy fluxes (also known as instantaneous intensity) in units of power per unit area, Watts/m^2, and that the direction of $\boldsymbol{S}$ signifies the direction of the propagating field [2.5,2.12,2.13].

2.1.2 Boundary Conditions

In the preceding section, the curl formulae form of Maxwell's equations have been defined in the time domain. The time-varying form is capable of describing the instantaneous electric and magnetic response at any point in space and time and is fundamental in the development of the time-domain numerical method (Transmission-Line Modelling Method) which is described in Chapter 5. It is important, however, to note that the curl formulae of Maxwell's equations are valid only in a continuous medium. In the presence of a material discontinuity solutions to Maxwell's equations also need to satisfy appropriate boundary conditions depend on the geometrical structure of the system considered.

The response of the field at the interface discontinuity of different materials can be described by the divergence formulae of Maxwell's equations which for the time-varying field and in a source-free region are given by [2.5,2.7],

$$\nabla \cdot \boldsymbol{D} = 0, \tag{2.8}$$

$$\nabla \cdot \boldsymbol{B} = 0. \tag{2.9}$$

Applying Gauss's law to (2.8) at the boundary of two different media denoted by

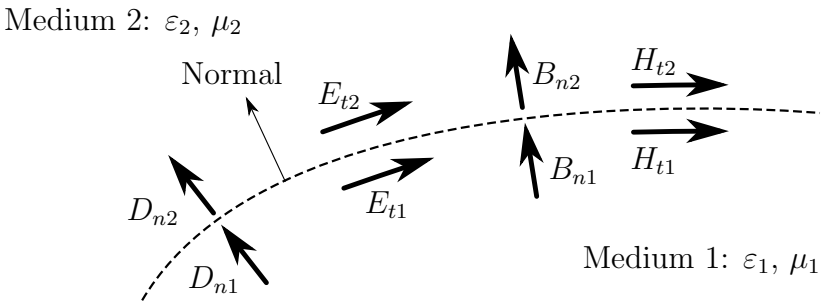

Figure 2.1 | Boundary condition of magnetic and electric field quantities at the interface of two different media. Adapted from [2.3–2.5,2.7,2.12–2.14].

ε_1, and μ_1 and ε_2, and μ_2 as shown in Fig. 2.1, it can be shown that the normal components of electric field density D_n are continuous [2.5,2.7], i.e.

$$D_{n1} = D_{n2}. \tag{2.10}$$

This implies that the normal components of the electric fields E_n are not continuous. Meanwhile upon an application of Stoke's integral theorem on (2.1) within an infinitesimal region around the interface, it can be shown that the tangential components of the electric field are always continuous at the interface [2.3–2.5,2.7, 2.12–2.14],

$$E_{t1} = E_{t2}. \tag{2.11}$$

The boundary conditions for $\boldsymbol{B}$ and $\boldsymbol{H}$ may be obtained in an analogous way and are given as [2.3–2.5,2.7,2.12–2.14],

$$B_{n1} = B_{n2} \tag{2.12}$$

$$H_{t1} = H_{t2} \tag{2.13}$$

The relations (2.10) to (2.13) are illustrated in Fig. 2.1. It is important to note that the boundary conditions decribed here are valid in a source-free interface only; hence they ignore surface current and surface charge densities which can occur in the case

of interfaces with metallic or magnetic materials [2.3–2.5,2.7,2.12–2.14].

2.1.3 Helmholtz Equation for Time-Harmonic Electromagnetics

In the previous subsection, Maxwell's equations in the time-domain have been defined, together with boundary conditions to be satisfied at the interface between different media. It was briefly introduced that solving Maxwell's equations subject to appropriate boundary conditions is enough to describe an electromagnetic problem. This concept will be elaborated further in Section 5.3.1 with the description of the time-domain numerical (the Transmission-Line Modelling) method that is used in the work described in this thesis to solve the Maxwell's equation numerically in the time-domain. This section will focus on the formalisation of the dynamics of an electromagnetic field in the frequency domain. This formalism gives a nice description of the response of the electromagnetic field in the presence of matter, known as the Helmholtz wave equation for electromagnetics. As such, it will be shown that the Helmholtz equation relates the electrical properties of a material in the frequency domain to the phase and attenuation (or gain) constants of the propagating electromagnetic field.

Consider the expansion of the temporal function as a Fourier series of monochromatic plane waves. As such the time-domain dependent vector fields $\boldsymbol{E}$, $\boldsymbol{H}$, $\boldsymbol{J}_e$, $\boldsymbol{D}$, and

$\boldsymbol{B}$ can be expressed as a cosine phasor component,

$$\begin{aligned}
\boldsymbol{H}(x,y,z;t) &= \mathrm{Re}\left[\boldsymbol{\mathcal{H}}(x,y,z)\mathrm{e}^{j\omega t}\right] \\
\boldsymbol{B}(x,y,z;t) &= \mathrm{Re}\left[\boldsymbol{\mathcal{B}}(x,y,z)\mathrm{e}^{j\omega t}\right] \\
\boldsymbol{E}(x,y,z;t) &= \mathrm{Re}\left[\boldsymbol{\mathcal{E}}(x,y,z)\mathrm{e}^{j\omega t}\right] \\
\boldsymbol{D}(x,y,z;t) &= \mathrm{Re}\left[\boldsymbol{\mathcal{D}}(x,y,z)\mathrm{e}^{j\omega t}\right] \\
\boldsymbol{J_e}(x,y,z;t) &= \mathrm{Re}\left[\boldsymbol{\mathcal{J}}_e(x,y,z)\mathrm{e}^{j\omega t}\right]
\end{aligned} \tag{2.14}$$

In this thesis, the notation in (2.14) is used throughout, so that a Roman letter is used to denote field quantities in the time domain whilst calligraphic letters are used for the quantities in frequency domain.

By applying the Fourier expansion to Maxwell's curl equations, (2.1), the frequency domain Maxwell's equations in matrix form are given by

$$\begin{bmatrix} \nabla \times \boldsymbol{\mathcal{H}} \\ -\nabla \times \boldsymbol{\mathcal{E}} \end{bmatrix} = \begin{bmatrix} \boldsymbol{\mathcal{J}_e} \\ 0 \end{bmatrix} + j\omega \begin{bmatrix} \boldsymbol{\mathcal{D}} \\ \boldsymbol{\mathcal{B}} \end{bmatrix}, \tag{2.15}$$

where in (2.15) the magnetic current density $\boldsymbol{\mathcal{M}}$ which appeared in (2.1) has been assumed to be zero. Moreover, the constitutive relations in frequency domain are given by,

$$\begin{aligned}
\boldsymbol{\mathcal{J}}_e &= \mathcal{F}\left\{\sigma_e(t)\right\}\boldsymbol{\mathcal{E}}, \\
\boldsymbol{\mathcal{D}} &= \varepsilon_0\boldsymbol{\mathcal{E}} + \varepsilon_0\mathcal{F}\left\{\chi_e(t)\right\}\boldsymbol{\mathcal{E}}, \\
\boldsymbol{\mathcal{B}} &= \mu_0\boldsymbol{\mathcal{H}}.
\end{aligned} \tag{2.16}$$

Here, $\mathcal{F}$ is used to denote the Fourier transformation operation. Since the time-variation component has been assumed to be of the form $\mathrm{e}^{j\omega t}$, see (2.14), the Fourier

transformation is given by,

$$\mathcal{F}\{f(t)\} \equiv f(\omega) = \int_0^\infty f(t)\mathrm{e}^{-j\omega t}dt, \tag{2.17}$$

where $\omega = 2\pi f$ denotes the angular frequency in rad/s. Note that the Fourier transformation given in (2.17) is assumed for a causal system, i.e.

$$f(t)\begin{cases} = 0, & \text{if } t < 0 \\ \neq 0, & \text{if } t > 0 \end{cases}$$

Substituting the constitutive relation (2.16) into Maxwell's equations, (2.15), in the frequency domain, and solving simultaneously for $\boldsymbol{\mathcal{H}}$ and $\boldsymbol{\mathcal{E}}$, results in the Helmholtz equation for the field $\boldsymbol{\Psi}$ as,

$$\nabla^2\boldsymbol{\Psi} - \gamma^2\boldsymbol{\Psi} = 0, \tag{2.18}$$

where $\boldsymbol{\Psi}$ can be either of the $\boldsymbol{\mathcal{H}}$ or $\boldsymbol{\mathcal{E}}$ field and the propagation constant γ is defined as,

$$\gamma^2 = -\omega^2\mu_0\varepsilon. \tag{2.19}$$

The electrical properties of the material can be expressed in the frequency domain by using the complex dielectric constant,

$$\varepsilon(\omega) = \varepsilon_0\left(1 + \chi_e(\omega) - j\frac{\sigma_e(\omega)}{\varepsilon_0\omega}\right), \tag{2.20}$$

It is noted that throughout this thesis, the notation ε is used to denote the dielectric permittivity while $\bar{\varepsilon}$ is used to denote the dimensionless relative permittivity,

$$\bar{\varepsilon} = \frac{\varepsilon}{\varepsilon_0}$$

It follows from (2.19) that the propagation constant γ is also complex and it is thus defined as,

$$\gamma = \alpha + j\beta \tag{2.21}$$

where,

$$\alpha = \text{attenuation (or amplification) constant in } (\text{m}^{-1})$$
$$\beta = \text{phase constant in (rad/m)}.$$

For propagation in free-space, the light velocity is given by [2.5,2.7],

$$c_0 = \frac{\omega}{\beta_0} = \frac{1}{\sqrt{\mu_0 \varepsilon_0}} \tag{2.22}$$

It is emphasised here that, the subscript "0" is used to denote the free-space properties throughout this thesis. It is worth commenting that in optics, the phase constant β is also alternatively known as the wave-number $k = k_0 n_{\text{eff}}$, where k_0 and n_{eff} represent the free-space wave-number and effective refractive index, respectively.

The Poynting theorem in the time-harmonic form is expressed as [2.4,2.5],

$$\oiint_{\Omega} \boldsymbol{\mathcal{S}} \cdot d\boldsymbol{s} + \iiint_{V} \left[\frac{1}{2}(\boldsymbol{\mathcal{J}}_{\boldsymbol{e}} \cdot \boldsymbol{\mathcal{E}}^*) + j\omega \frac{1}{2}(\boldsymbol{\mathcal{B}} \cdot \boldsymbol{\mathcal{H}}^* - \boldsymbol{\mathcal{D}} \cdot \boldsymbol{\mathcal{E}}^*) \right] dv = 0 \tag{2.23}$$

and the Poynting vector in the time-harmonic form is given as,

$$\boldsymbol{\mathcal{S}} = \frac{1}{2} \text{Re} \left\{ \boldsymbol{\mathcal{E}} \times \boldsymbol{\mathcal{H}}^* \right\} \tag{2.24}$$

where "*" is the conjugation operator.

2.2 Optical Network Theory

The solution of Maxwell's equations for a specific given boundary condition gives a complete description of the electromagnetic response at any point in space and time, and is effective in describing the underlying physical properties of waveguiding and cavity structures [2.5,2.12,2.15]. However in most practical situations, it is desirable to have a macro model in which the system need only be described at its input and output ports. This macro model of an arbitrary system is usually referred to as optical network theory and was originally developed for application to microwave network analysis [2.3,2.5,2.7]. This section will focus on the description of a macro model known as the scattering matrix formalism. In this model, an optical network is considered as a scattering system which couples the incoming and outgoing light signal between port channels.

2.2.1 The Scattering Matrix Formalism

Examples of optical network systems are depicted Fig. 2.2 where, Fig. 2.2(a) shows the two-port system of a waveguide grating, Fig. 2.2(b) shows a circular cavity being coupled with two waveguides and Fig. 2.2(c) illustrates the six-port network of a multimode interference coupler (MMI). Conceptually the structures here can be seen as an arbitrary "black box" system enclosed by surface boundary Ω with definite input/output port channels as illustrated in Fig. 2.3. The input/output waveguide ports are assumed to be lossless and linear and to support a finite number of propagating modes.

Now, consider the system depicted in Fig. 2.3. The figure illustrates a "black-box" model to represent an N-port optical network system. The system is bounded by the boundary Ω and communicates to other confined systems by the input/output ports which support both incoming and outgoing signals. The incoming and out-

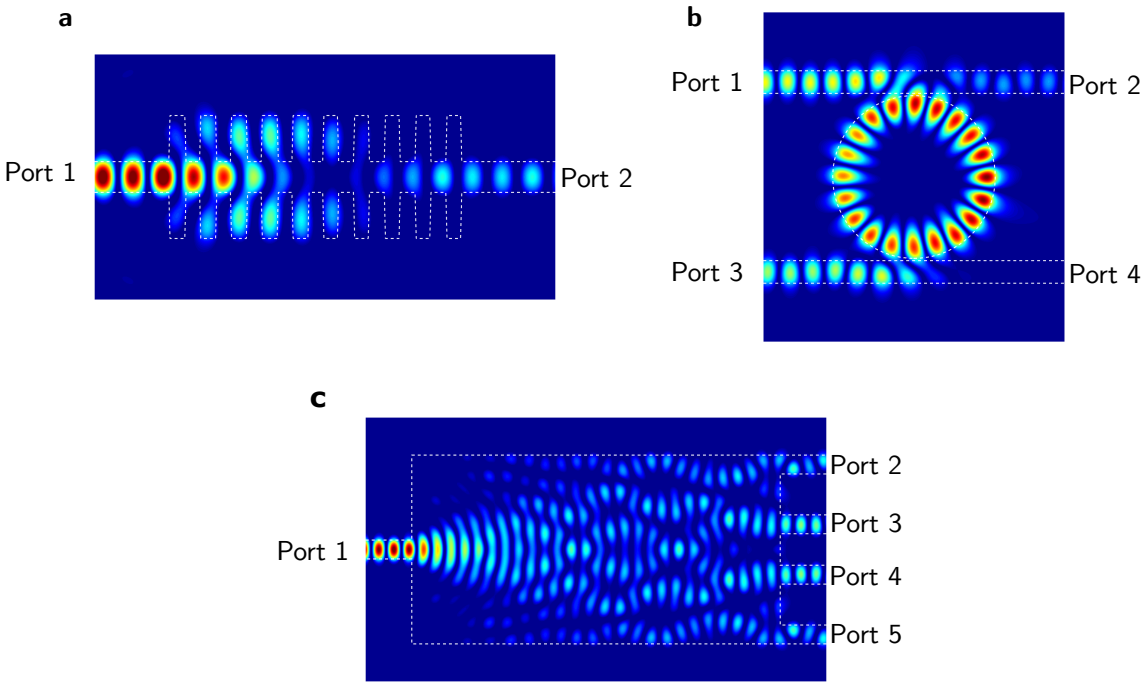

Figure 2.2 | Illustrative examples of optical network circuits. (**a**) Two ports waveguides gratings system, **(b)** coupled whispering-gallery mode resonant cavity with four input/output ports, **(c)** one to four multi-mode interference coupler. These illustrative results were obtained using the Transmission-line modelling (TLM) method.

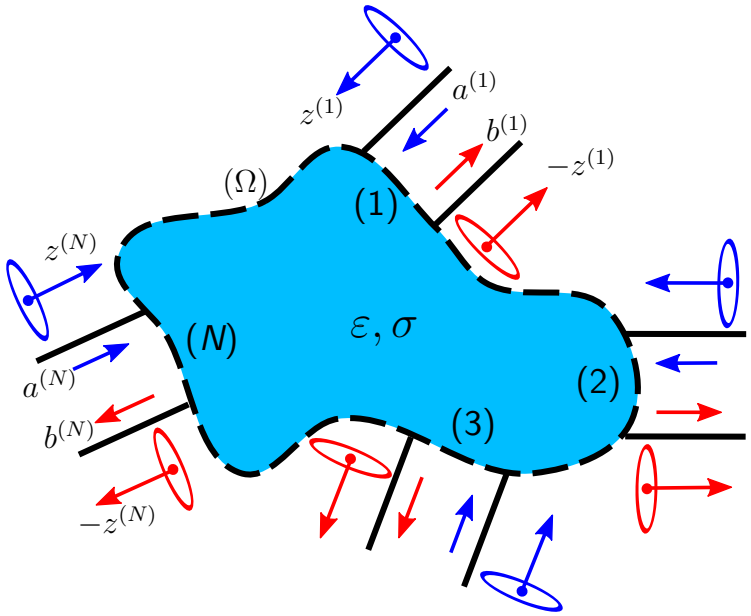

Figure 2.3 | Schematic illustration of an N-port optical network system

going mode amplitudes at port-n, where $1 \leq n \leq N$, are denoted by $a^{(n)}$ and $b^{(n)}$ respectively. Each individual port is assumed to have its independent coordinate system which are illustrated for the case of incoming and outgoing modes. One can expand the transverse field in terms of all supported modes in each individual port [2.12,2.15]. So, for example, consider that port-n can support $\mathcal{N}$ propagating modes; it follows that the transverse electric and magnetic field at the port-n can be expressed as,

$$\begin{aligned} \boldsymbol{\mathcal{E}}_{\boldsymbol{T}}^{(n)}(x,y,z) &= \sum_{m\in\mathcal{N}} \left(a_m^{(n)} \mathrm{e}^{-j\beta_m^{(n)} z} + b_m^{(n)} \mathrm{e}^{j\beta_m^{(n)} z} \right) \mathbf{e}_{\boldsymbol{T},m}(x,y) \\ \boldsymbol{\mathcal{H}}_{\boldsymbol{T}}^{(n)}(x,y,z) &= \sum_{m\in\mathcal{N}} \left(a_m^{(n)} \mathrm{e}^{-j\beta_m^{(n)} z} - b_m^{(n)} \mathrm{e}^{j\beta_m^{(n)} z} \right) \mathbf{h}_{\boldsymbol{T},m}(x,y) \end{aligned} \tag{2.25}$$

In (2.25), each port has its own local coordinate axis (x, y, z), with z assumed to be the propagation axis and (x, y) the transverse plane. Moreover, here the incoming propagation is assumed in the form of $\mathrm{e}^{-j\beta_m z}$ whilst the outgoing propagation is $\mathrm{e}^{j\beta_m z}$. The $\mathbf{e}_{\boldsymbol{T},m}(x,y)$ and $\mathbf{h}_{\boldsymbol{T},m}(x,y)$ denote the transverse mode dependence of a particular guided mode m which are comprised of a suitable set of vector orthogonal function in the transverse plane (x, y). For the case of lossless modes, the following orthogonality property is valid,

$$\iint\limits_{\Omega^{(n)}} \left(\mathbf{e}_{\boldsymbol{T},m} \times \mathbf{h}_{\boldsymbol{T},m'}^{*} \right) \cdot \hat{\boldsymbol{z}} dS = \begin{cases} 2, & \text{if } m = m' \\ 0, & \text{if } m \neq m' \end{cases} \tag{2.26}$$

where $\Omega^{(n)}$ denotes the a surface normal to propagation direction $\hat{\boldsymbol{z}}$ located at the port-n. As such the net-power flow at the opening of port-n can be calculated by (2.24) and is given by

$$P = \frac{1}{2} \iint\limits_{\Omega^{(n)}} \left(\boldsymbol{\mathcal{E}}_{\boldsymbol{T}}^{(n)} \times \boldsymbol{\mathcal{H}}_{\boldsymbol{T}}^{(n)*} \right) \cdot \hat{\boldsymbol{z}} dS = \left| a_m^{(n)} \right|^2 - \left| b_m^{(n)} \right|^2 . \tag{2.27}$$

Exploiting the fact that the propagating mode m exists only on the associate waveg-

uide port-n; the expansion (2.25), which is valid on the port-n, can be generalised to the whole boundary Ω by extending the modal field as [2.12,2.15,2.16],

$$\text{generalised modal field } (n,m) = \begin{cases} \text{original field on port-}n \\ 0 \text{ elsewhere.} \end{cases}$$

As such, the whole set of local modal expansions, specific to the various ports, can be condensed into a single expansion as

$$\begin{aligned} \boldsymbol{\mathcal{E}}_T(x,y,z) &= \sum_{\mu\in\mathcal{M}} \left(a_\mu e^{-j\beta_\mu z} + b_\mu e^{j\beta_\mu z}\right) \mathbf{e}_{T,\mu}(x,y) \\ \boldsymbol{\mathcal{H}}_T(x,y,z) &= \sum_{\mu\in\mathcal{M}} \left(a_\mu e^{-j\beta_\mu z} - b_\mu e^{j\beta_\mu z}\right) \mathbf{h}_{T,\mu}(x,y). \end{aligned} \tag{2.28}$$

In (2.28), μ stands for the composite notation (n,m) and $\mathcal{M}$ is used to denote the total number of propagating modes supported on all waveguides, i.e. the union of $\mathcal{N}$ for all ports.

Furthermore, considering the system associated with Fig. 2.3 to be *linear, time independent* and *isolated*, i.e. energy can only enter and leave only through the ports, the outgoing wave b_μ is completely determined by the inward wave a_μ. The relation between the outgoing and the ingoing wave can be related by a scattering matrix as [2.3,2.4,2.12,2.15,2.16],

$$\boldsymbol{b} = \mathbf{S} \cdot \boldsymbol{a}, \tag{2.29}$$

where, the incoming wave amplitude vector $\boldsymbol{a}$, the outgoing wave amplitude vector

$\boldsymbol{b}$, and the scattering matrix $\mathbf{S}$ are in the form of,

$$\begin{pmatrix} b_1 \\ b_2 \\ b_3 \\ \vdots \\ b_\mu \end{pmatrix} = \begin{bmatrix} S_{11} & S_{12} & S_{13} & \cdots & S_{1\nu} \\ S_{21} & S_{22} & S_{23} & \cdots & S_{2\nu} \\ S_{31} & S_{32} & S_{33} & \cdots & S_{3\nu} \\ \vdots & \vdots & \vdots & \ddots & \vdots \\ S_{\mu 1} & S_{\mu 2} & S_{\mu 3} & \cdots & S_{\mu\mu} \end{bmatrix} \begin{pmatrix} a_1 \\ a_2 \\ a_3 \\ \vdots \\ a_\mu \end{pmatrix}. \tag{2.30}$$

From (2.30), it can be seen that the diagonal elements of the $\mathbf{S}$-matrix, i.e. $S_{\mu\mu}$ are the reflection coefficients of mode μ back to the respective mode, and the non-diagonal elements $S_{\mu\nu}$ give the transmission coefficient from mode μ to mode ν.

2.2.2 Lorentz Reciprocity Theorem

In the previous subsection, a "black-box" representative model was developed to describe an optical network by the scattering matrix formulation. It can be seen from (2.30) that the outgoing wave amplitude $\boldsymbol{b}$ depends only on the incoming wave $\boldsymbol{a}$. As such it can be argued that there can be only one solution of $\boldsymbol{b}$ for a given $\boldsymbol{a}$ because if there exists another solution for a given incoming wave $\boldsymbol{a}$, denoted for instance by $\boldsymbol{b}'$, the difference of these waves $(\boldsymbol{b} - \boldsymbol{b}')$ will imply that there is energy leaking from (or added to) the system which violates the underlying assumption of the model [2.4,2.12,2.15,2.16]. This suggests that there is a fundamental property of $\mathbf{S}$ that it is independent of the incoming wave amplitude $\boldsymbol{a}$. The following discussion on the reciprocity theorem in this subsection follows the argumentation in [2.16] which shows the validity of the reciprocity theorem in a system with complex refractive indices.

For this reason, now consider the time-harmonic Maxwell's equations for two different states, namely state-(1) and state-(2). In practice, these two different states can be achieved by, for example, changing the configuration of the incoming amplitude

$\boldsymbol{a}$. As such, Maxwell's equations for these two different state configurations are expressed as,

$$\left.\begin{aligned} \nabla \times \boldsymbol{\mathcal{H}}_1 &= \sigma \boldsymbol{\mathcal{E}}_1 + j\omega\varepsilon_0(1+\chi_e)\boldsymbol{\mathcal{E}}_1 \\ -\nabla \times \boldsymbol{\mathcal{E}}_1 &= j\omega\mu_0 \boldsymbol{\mathcal{H}}_1 \end{aligned}\right\} \quad \text{for state-(1)} \tag{2.31}$$

and

$$\left.\begin{aligned} \nabla \times \boldsymbol{\mathcal{H}}_2 &= \sigma \boldsymbol{\mathcal{E}}_2 + j\omega\varepsilon_0(1+\chi_e)\boldsymbol{\mathcal{E}}_2 \\ -\nabla \times \boldsymbol{\mathcal{E}}_2 &= j\omega\mu_0 \boldsymbol{\mathcal{H}}_2 \end{aligned}\right\} \quad \text{for state-(2).} \tag{2.32}$$

By solving both (2.31) and (2.32) simultaneously, it can found that the electric and magnetic field of the different state systems are related by the so-called Lorentz reciprocity relation, which in a source-free system is expressed by,

$$\nabla \cdot (\boldsymbol{\mathcal{E}}_1 \times \boldsymbol{\mathcal{H}}_2 - \boldsymbol{\mathcal{E}}_2 \times \boldsymbol{\mathcal{H}}_1) = 0 \tag{2.33}$$

or in the integral form, obtained from (2.33) by applying Gauss' divergence law on a volume enclosed by a closed surface $\boldsymbol{\Omega}$, as,

$$\iint_{\Omega} (\boldsymbol{\mathcal{E}}_1 \times \boldsymbol{\mathcal{H}}_2 - \boldsymbol{\mathcal{E}}_2 \times \boldsymbol{\mathcal{H}}_1)\, d\boldsymbol{\Omega} = 0 \tag{2.34}$$

It is important to note that the reciprocity relation (2.33) or (2.34) is valid for materials with gain or loss but not in the case of magneto-optical, non-linear and time-dependent materials [2.3–2.6,2.10,2.12,2.15,2.16].

In order to see the implication of Lorentz reciprocity to the scattering matrix $\mathbf{S}$,

consider the two states in terms of input and scattered wave amplitudes as,

$$\left.\begin{aligned} \boldsymbol{\mathcal{E}}_1 &= \sum_{\mu} a_{1,\mu}\mathbf{e}_\mu + \sum_{\nu} b_{1,\nu}\mathbf{e}_\nu \\ \boldsymbol{\mathcal{H}}_1 &= \sum_{\mu} a_{1,\mu}\mathbf{h}_\mu - \sum_{\nu} b_{1,\nu}\mathbf{h}_\nu \end{aligned}\right\} \quad \text{for state-(1)} \tag{2.35}$$

and

$$\left.\begin{aligned} \boldsymbol{\mathcal{E}}_2 &= \sum_{\mu} a_{2,\mu}\mathbf{e}_\mu + \sum_{\nu} b_{2,\nu}\mathbf{e}_\nu \\ \boldsymbol{\mathcal{H}}_2 &= \sum_{\mu} a_{2,\mu}\mathbf{h}_\mu - \sum_{\nu} b_{2,\nu}\mathbf{h}_\nu \end{aligned}\right\} \quad \text{for state-(2).} \tag{2.36}$$

Applying the reciprocity relation (2.34), to both (2.35) and (2.36) it can be shown that [2.3,2.12,2.15,2.16],

$$2\sum_{\mu}\sum_{\nu}(b_{1,\nu}a_{2,\mu} - a_{1,\mu}b_{2,\nu}) \iint_{\Omega} \mathbf{e}_\mu \times \mathbf{h}_\nu \; d\boldsymbol{\Omega} = 0. \tag{2.37}$$

Moreover, because the waveguide ports are assumed lossless, the transverse field vector are real function in (x, y) as a result the orthogonality condition of guided modes [2.4,2.15,2.16],

$$\iint_{\Omega} \mathbf{e}_\mu \times \mathbf{h}_\nu \; d\boldsymbol{\Omega} = \begin{cases} 1, & \text{if } \mu = \nu \\ 0, & \text{if } \mu \neq \nu \end{cases},$$

equation (2.37) can be simplified and represented in matrix form as,

$$\begin{aligned} \sum_{\mu}(b_{1,\mu}a_{2,\mu} - a_{1,\mu}b_{2,\mu}) &= \boldsymbol{b}_1^T\boldsymbol{a}_2 - \boldsymbol{a}_1^T\boldsymbol{b}_2 \\ &= \boldsymbol{a}_1^T\mathbf{S}^T\boldsymbol{a}_2 - \boldsymbol{a}_1^T\mathbf{S}\;\boldsymbol{a}_2 = 0 \end{aligned} \tag{2.38}$$

where, the superscript T denotes the transpose operation. An important conclusion from (2.38) is that Lorentz reciprocity requires the scattering matrix of an optical

system to be symmetric, i.e.

$$\mathbf{S} = \mathbf{S}^T \tag{2.39}$$

when the system is comprised of linear, non-magnetic, and time independent materials.

2.3 Kramers-Kronig Relationship

Section 2.1.1 introduced the fact that the field-matter response is a non-local function of time which depends on the temporal material response as,

$$\boldsymbol{D}(t) = \chi_e(t) * \boldsymbol{E}(t) = \int_0^\infty \chi_e(\tau)\boldsymbol{E}(t-\tau)d\tau \tag{2.40}$$

Equation (2.40) suggests that the interaction of electric field $\boldsymbol{E}$ with the material function $\chi_e(t)$ at any instant t is dependent on the $\boldsymbol{E}$ that existed at earlier times. It is important to note that since $\boldsymbol{E}$ is a real quantity, the material response $\chi_e(t)$ has to be real too. The dielectric susceptibility in the frequency domain is obtained by Fourier transformation and is given by,

$$\chi_e(\omega) = \int_0^\infty \chi_e(t)\mathrm{e}^{-j\omega t}dt. \tag{2.41}$$

Here, the causality principle has been enforced, i.e. $\chi_e(t) = 0$ for $t < 0$. In general the frequency domain dielectric susceptibility is a complex parameter,

$$\chi_e(\omega) = \chi_e'(\omega) + j\chi_e''(\omega), \tag{2.42}$$

where, χ_e' and χ_e'' are the real and imaginary parts of the dielectric susceptibility respectively.

We now see the implications of imposing the causality principle to the Fourier transformation. First, it can be shown that from (2.41) that, dielectric susceptibility has to satisfy, i.e.,

$$\chi_e(-\omega) = \chi_e^*(\omega), \tag{2.43}$$

meaning that the real part of the susceptibility is an even function, whilst the imaginary part is an odd function, of frequency, i.e.

$$\begin{aligned} \chi_e'(-\omega) &= \chi_e'(\omega) \\ \chi_e''(-\omega) &= -\chi_e''(\omega). \end{aligned} \tag{2.44}$$

Moreover by definition[‡], $\chi_e(\omega)$ has to be a single-valued complex function and analytic (having no singularities) in the lower half-plane of the complex frequency plane, $\omega = \omega' + j\omega''$. Hence, for $\omega'' < 0$ the integration in (2.41) converges as it includes the exponentially decaying factor $\mathrm{e}^{\omega'' t}$, whilst in the upper half-plane the definition in (2.41) is invalid as the integration diverges.

From (2.41), it can be shown that the Kramers-Kronig relations are given as [2.5, 2.6,2.10],

$$\begin{aligned} \chi_e'(\omega) &= \frac{1}{\pi}\ \text{p.v.} \int_{-\infty}^{\infty} \frac{\chi_e''(\Omega)}{\Omega - \omega} d\Omega \\ \chi_e''(\omega) &= -\frac{1}{\pi}\ \text{p.v.} \int_{-\infty}^{\infty} \frac{\chi_e'(\Omega)}{\Omega - \omega} d\Omega \end{aligned} \tag{2.45}$$

The Kramers-Kronig relations (2.45) imply that any material with non-zero imaginary part of susceptibility $|\chi_e''(\omega)| > 0$ has to be dispersive. Moreover the causality

[‡]The existence of the Fourier tranform of a function f together with its inverse transform, requires f to be a single-valued and continuous function [2.17,2.18]

condition requires the material susceptibility function $\chi_e(\omega)$ to be analytical in the bottom half-plane of the complex frequency plane, so that any singularity in the $\chi_e(\omega)$ function has to be located in the upper half-plane [2.10]. A full derivation of the Kramers-Kronig relations is given in the Appendix A.

References

[2.1] J. Maxwell, "A dynamical theory of the electromagnetic field," Phil. Trans. R. Soc. **155**, 459–512 (1865).

[2.2] J. Maxwell, "On physical lines of force," Philos. Mag. **90**, (11)161–175; 281–291; 338–348;(12)12–24; 85–95 (1861).

[2.3] S. Ramo, J. R. Whinnery, and T. V. Duzer, *Fields and Waves in Communication Electronics* (John Wiley, 1999), 3rd ed.

[2.4] K. Zhang and D. Li, *Electromagnetic Theory for Microwaves and Optoelectronics* (Springer, 2008), 2nd ed.

[2.5] C. A. Balanis, *Advanced Engineering Electromagnetics: Traditions v. 2* (John Wiley, NJ, 2012), 2nd ed.

[2.6] R. E. Collin, *Field Theory of Guided Waves* (IEEE Press, New York, NY, 1991), 2nd ed.

[2.7] D. M. Pozar, *Microwave Engineering* (John Wiley, New York, NY, 2011), 4th ed.

[2.8] J. Paul, C. Christopoulos, and D. Thomas, "Generalized material models in TLM .II. Materials with anisotropic properties," IEEE Trans. Antennas Propag. **47**, 1528–1534 (1999).

[2.9] J. Paul, C. Christopoulos, and D. Thomas, "Generalized material models in TLM .I. Materials with frequency-dependent properties," IEEE Trans. Antennas Propag. **47**, 1528–1534 (1999).

[2.10] L. D. Landau, J. S. Bell, M. J. Kearsley, L. P. Pitaevskii, E. M. Lifshitz, and J. B. Sykes, *Electrodynamics of Continuous Media* (Elsevier, London, England, 1984), 2nd ed.

[2.11] A. Yariv and P. Yeh, *Photonics: Optical Electronics in Modern Communications* (Oxford University Press, New York, NY, 2007), 6th ed.

[2.12] H. A. Haus, *Waves and Fields in Optoelectronics* (Prentice-Hall, New Jersey, 1983).

[2.13] J.-M. Liu, *Photonic Devices* (Cambridge University Press, Cambridge, 2005).

[2.14] K. Iizuka, *Elements of Photonics, Vol II* (John Wiley, New York, NY, 2002).

[2.15] C. Vassallo, *Optical Waveguide Concepts* (Elsevier, New York, NY, 1991), 1st ed.

[2.16] D. Jalas, A. Petrov, M. Eich, W. Freude, S. Fan, Z. Yu, R. Baets, M. Popović, A. Melloni, J. D. Joannopoulos, M. Vanwolleghem, C. R. Doerr, and H. Renner, "What is and what is not an optical isolator," Nat. Photonics **7**, 579–582 (2013).

[2.17] E. Kreyszig, *Advanced Engineering Mathematics* (John Wiley, New York, NY, 2011), 10th ed.

[2.18] G. B. Arfken, H. J. Weber, and F. E. Harris, *Mathematical Methods for Physicists: A Comprehensive Guide* (Academic Press, Amsterdam, 2012), 7th ed.

3

Parity-Time Symmetric Scattering System

The concept of $\mathcal{PT}$-symmetric photonics as a translation of the $\mathcal{PT}$-symmetric Hamiltonian problem in quantum mechanics is introduced in this chapter. The chapter studies the spectral properties of a $\mathcal{PT}$-symmetric scattering system. In particular, it presents the properties of the transfer matrix $\mathbf{M}$ and the scattering matrix $\mathbf{S}$ under $\mathcal{PT}$-transformation, under which a $\mathcal{PT}$-symmetric scatterer is shown to exhibit exotic behaviour such as, unidirectional unitary transmission, spontaneous $\mathcal{PT}$-symmetry breaking and simultaneous coherent perfect absorber-lasing operation. Moreover, this chapter also presents the generalised conservation relationship for an asymmetric left-right response and provides a criterion for describing $\mathcal{PT}$-symmetry breaking in a scattering system.

* * *

3.1 Parity and Time-Reversal ($\mathcal{PT}$) Symmetry

In order to understand the concept of Parity and Time ($\mathcal{PT}$) symmetric structures in photonics, it is natural to review some fundamental theorems and postulates in Quantum Mechanics (QM) in which the $\mathcal{PT}$-symmetric problem was firstly defined. In QM, it is well-known that the behaviour of a particle is described by the so-called Schrödinger equation, the time-independent form of which is given by [3.1,3.2],

$$\hat{H}\psi = E\psi, \tag{3.1}$$

where ψ denotes the scalar time-independent wavefunction which is a function of position, i.e. $\psi(x, y, z)$ in the Cartesian coordinate system, E refers to the energy corresponding to the state described by the wave function ψ and $\hat{H}$ denotes the Hamiltonian operator and has important roles as summarised below [3.3–3.5]:

1. To determine the energy eigenstates E which essentially are the solution of (3.1). It implies that the energy eigenstates E are the result of the action described by $\hat{H}$ applied on the state vector ψ. Moreover, considering that E is a physically measurable quantity, it is essential for E to be real.

2. Within the context of the time-domain Schrödinger equation,

$$\hat{H}\psi(x, y, z; t) = \mathrm{i}\hbar\frac{\partial}{\partial t}\psi(x, y, z; t), \tag{3.2}$$

   the Hamiltonian has a role to describe the time evolution of the state vector ψ which is the time-domain solution of (3.2). To avoid confusion, in this subsection the complex number notation ($\mathrm{i} = -j$) is used as is customary in most of Quantum Mechanics textbooks [3.1,3.2].

3. The Hamiltonian incorporates symmetry properties into the theory. In QM the Hamiltonian may exhibit continuous symmetries, such as time and spa-

tial translation, and discrete symmetries, such as parity inversion and time-reversal invariance [3.3–3.5]. For example if the Hamiltonian is commute with the parity inversion symmetry, the Hamiltonian is said to be parity inversion invariant.

The Hamiltonian $\hat{H}$ is expressed in terms of the position $\mathbf{x}$ and momentum $\hat{\mathbf{p}}$ operator as,

$$\hat{H} = \hat{\mathbf{p}}^2 + V(\mathbf{x}) \tag{3.3}$$

where, $\hat{\mathbf{p}}$ and $V(\mathbf{x})$ denotes the linear momentum operator and potential energy function of a particle, respectively. The linear momentum operator is imaginary and anti-symmetric, defined as $\hat{\mathbf{p}} = -\mathrm{i}\nabla$. It follows that $\hat{\mathbf{p}}^2 = -\nabla^2$ is real and symmetric (Hermitian) and therefore *if* the potential function $V(\mathbf{x})$ is a real function in space, it can be guaranteed that all the energy states E are also real with the Hamiltonian $\hat{H}$ satisfying,

$$\hat{H} = \hat{H}^\dagger, \tag{3.4}$$

where $\dagger$ denotes a Hermitian adjoint operation which in matrix form denotes a combined transpose and complex conjugation operation

As suggested by Bender and Boettcher [3.5], although the Hermitian condition (3.4) is *sufficient* to ensure all possible energy states to be completely real, it is not *necessary*. In [3.3–3.5], it is further shown that a weaker symmetry than Hermiticity (3.4) may lead to real eigenvalues E, and this weaker symmetry is denoted as a *Parity* ($\mathcal{P}$) and *Time* ($\mathcal{T}$) symmetric Hamiltonian. As such the Hamiltonian $\hat{H}$ is invariant under the $\mathcal{PT}$ transformation,

$$\mathcal{PT}\hat{H}\mathcal{TP} = \hat{H}, \tag{3.5}$$

where the parity operator $\mathcal{P}$ is defined as a linear operator which inverts space and momentum, and the time-reversal operator $\mathcal{T}$ is an operator which reverses time, i.e. $t \to -t$. The transformations performed by the parity and time-reversal operators are defined as [3.3–3.8],

$$\mathcal{P} : \mathbf{x} \to -\mathbf{x} \quad ; \quad \hat{\mathbf{p}} \to -\hat{\mathbf{p}} \tag{3.6}$$

$$\mathcal{T} : j \to -j \quad ; \quad \mathbf{x} \to \mathbf{x} \quad ; \quad \hat{\mathbf{p}} \to -\hat{\mathbf{p}}. \tag{3.7}$$

As such, it can be shown that a $\mathcal{PT}$-symmetric Hamiltonian in Quantum Mechanics is achieved when the potential function satisfies [3.3–3.8],

$$\mathcal{PT}V(\mathbf{x})\mathcal{TP} = V^*(-\mathbf{x}) = V(\mathbf{x}). \tag{3.8}$$

where $*$ denotes the conjugation operation. The $\mathcal{PT}$-symmetric condition (3.8) implies that the energy potential $V(\mathbf{x})$ is a complex function where the real part is an even function and the imaginary part is an odd function in space.

3.2 Photonics System Analogue of Quantum Mechanics $\mathcal{PT}$-Symmetric Hamiltonian

In contrast to the Schrödinger equation in Quantum Mechanics, in optics the dynamics of an electromagnetic field is defined by the Helmholtz equation (2.18). For the electric field, the Helmholtz equation is given as,

$$\nabla^2 \boldsymbol{\mathcal{E}} + \frac{\omega^2}{c_0^2} \bar{\varepsilon}(\mathbf{x}) \boldsymbol{\mathcal{E}} = 0 \tag{3.9}$$

where $\bar{\varepsilon}(\mathbf{x})$ is the relative permittivity of the material and is a function of space $\mathbf{x}$, such that it can be expressed in the form of,

$$\bar{\varepsilon}(\mathbf{x}) = \bar{\varepsilon}_b + \Delta\bar{\varepsilon}(\mathbf{x}) \tag{3.10}$$

In (3.10), $\bar{\varepsilon}_b$ denotes the homogeneous background material relative permittivity on which the spatial modulation $\Delta\varepsilon(\mathbf{x})$ occurs. By substituting, the permittivity profile function (3.10) to (3.9), the Helmholtz equation can also be formulated as [3.9],

$$\left\{\nabla^2 + \frac{\omega^2}{c_0^2}\Delta\bar{\varepsilon}(\mathbf{x})\right\}\boldsymbol{\mathcal{E}} = -\frac{\omega^2}{c_0^2}\bar{\varepsilon}_b\boldsymbol{\mathcal{E}} \tag{3.11}$$

By comparing (3.11) and (3.1), it can be seen that the time-harmonic Helmholtz equation of wave dynamics, albeit multicomponent, is isomorphic with the time-independent Schrödinger (3.1). The comparison of the Schrödinger and Helmholtz equations is summarised in Table 3.1. Based on this analogy, it can be shown that $\mathcal{PT}$-symmetric photonic structure has a dielectric profile that satisfies,

$$\bar{\varepsilon}(\mathbf{x}) = \bar{\varepsilon}^*(-\mathbf{x}) \quad \text{or} \quad n(\mathbf{x}) = n^*(-\mathbf{x}) \tag{3.12}$$

so that the real part of permittivity (or refractive index) is an even function and the imaginary part of the permittivity (or refractive index) is an odd function of

Table 3.1 | Comparison of the Helmholtz and Schrödinger equations [3.10].

	Quantum Mechanics	Electromagnetics
Field	$\Psi(\mathbf{x},t) = \psi(\mathbf{x})\mathrm{e}^{\mathrm{i}Et/\hbar}$	$\boldsymbol{E}(\mathbf{x};t) = \mathrm{Re}\,[\boldsymbol{\mathcal{E}}(\mathbf{x})\mathrm{e}^{j\omega t}]$
Eigenvalue problem	$\hat{H}\psi = E\psi$	$\hat{\Theta}\boldsymbol{\mathcal{E}} = -(\frac{\omega}{c_0})^2\varepsilon_b\boldsymbol{\mathcal{E}}$
Hamiltonian	$\hat{H} = \hat{\mathbf{p}}^2 + V(\mathbf{x})$	$\hat{\Theta} = \nabla^2 + (\frac{\omega}{c_0})^2\Delta\bar{\varepsilon}(\mathbf{x})$

space,

$$\varepsilon'(-\mathbf{x}) = \varepsilon'(\mathbf{x}) \tag{3.13}$$

$$\varepsilon''(-\mathbf{x}) = -\varepsilon''(\mathbf{x}). \tag{3.14}$$

As such (3.14) implies that a $\mathcal{PT}$-symmetric structure in photonic requires the presence of both gain and loss in the system.

3.3 $\mathcal{PT}$-Symmetric Scattering System

In the previous section, the Helmholtz equation is shown to be isomorphic with the Schrödinger equation. Photonic system in particular offers a practical platform for realisation as a $\mathcal{PT}$-symmetric system by a judicious composition material so that, the dielectric material parameter satisfies (3.12), i.e. the real part of the dielectric material parameter is a even function, whist the imaginary part is an odd function in space. This section focuses on a one-dimensional (1D) $\mathcal{PT}$-symmetric scatterer, where modulation of dielectric permittivity (or refractive index) occurs only along one axis, i.e. $n^*(x) = n(-x)$.

3.3.1 Generalised Conservation Relations

For definiteness, consider a 1D $\mathcal{PT}$-symmetric structure schematically illustrated in Fig. 3.1. The structure has a length L with a refractive index profile satisfying the $\mathcal{PT}$-symmetric condition in the longitudinal direction, i.e. $n^*(x) = n(-x)$, and is embedded in a lossless background material of refractive index n_b. In Fig. 3.1, the incoming a and outgoing b wave amplitudes are denoted for both the left and right sides, using a similar notation to that defined previously in (2.28). The transversal-

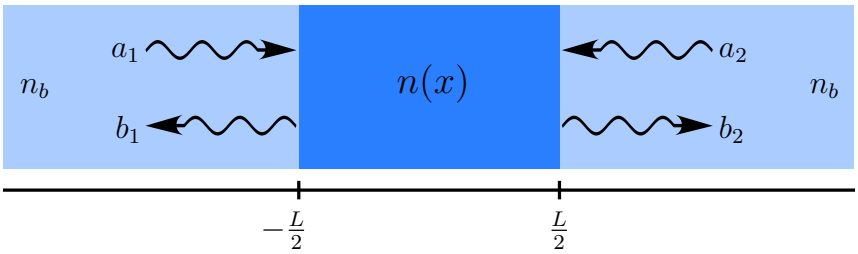

Figure 3.1 | Schematic illustration of a one-dimensional scattering system.

components of the electric field on each port can be expanded as,

$$\mathcal{E}_T(x) = \begin{cases} a_1 e^{j\beta x} + b_1 e^{-j\beta x} & \text{for}: \ x < -\frac{L}{2} \\ a_2 e^{j\beta x} + b_2 e^{-j\beta x} & \text{for}: \ x > \frac{L}{2} \end{cases} \tag{3.15}$$

As such the wavescattering can be modelled by the **S**-matrix as,

$$\begin{bmatrix} b_1 \\ b_2 \end{bmatrix} = \mathbf{S} \begin{bmatrix} a_1 \\ a_2 \end{bmatrix} \quad \text{where,} \quad \mathbf{S} = \begin{bmatrix} r_L & t_R \\ t_L & r_R \end{bmatrix} \tag{3.16}$$

and the quantities in the **S**-matrix are defined as,

t_L : effective transmission coefficient for left incidence,

t_R : effective transmission coefficient for right incidence,

r_L : effective reflection coefficient for left incidence,

r_R : effective reflection coefficient for right incidence.

Based upon the Lorentz reciprocity theorem for linear and non-magnetic materials, see Section 2.2.2, a further reduction in the **S**-matrix can be attained based on the reciprocality of left and right transmission coefficients, $t_L = t_R \equiv t$, as,

$$\mathbf{S} = \begin{bmatrix} r_L & t \\ t & r_R \end{bmatrix} \tag{3.17}$$

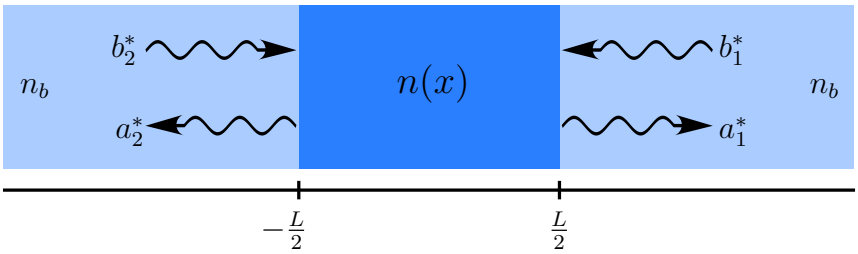

Figure 3.2 | $\mathcal{PT}$-transformed scattering system. The original system before $\mathcal{PT}$-symmetry transformation is illustrated in Fig. 3.1.

From (3.16) and (3.17), the transfer matrix[‡] **M**-matrix associated with Fig. 3.1, which relates the left and right wave amplitudes, could be constructed as:

$$\begin{bmatrix} a_1 \\ b_1 \end{bmatrix} = \mathbf{M} \begin{bmatrix} b_2 \\ a_2 \end{bmatrix} \quad \text{where,} \quad \mathbf{M} \equiv \begin{bmatrix} \frac{1}{t} & -\frac{r_R}{t} \\ \frac{r_L}{t} & t - \frac{r_L r_R}{t} \end{bmatrix}. \tag{3.18}$$

Moreover since the structure is $\mathcal{PT}$-symmetric, the $\mathcal{PT}$-transformed solutions should also be solutions of the Helmholtz equation. As such, Fig. 3.2 depicts the $\mathcal{PT}$ transformed solution of the original problem in Fig. 3.1. The $\mathcal{PT}$-transformed solutions are expressed as,

$$\mathcal{PT}\left\{\mathcal{E}_T(x)\right\} = \begin{cases} b_2^* e^{j\beta x} + a_2^* e^{-j\beta x} & \text{for}: \; x < -\frac{L}{2} \\ b_1^* e^{j\beta x} + a_1^* e^{-j\beta x} & \text{for}: \; x > \frac{L}{2} \end{cases}$$

The corresponding **M**-matrix formulation is now given by,

$$\begin{bmatrix} b_2^* \\ a_2^* \end{bmatrix} = \mathbf{M}^{(\mathcal{PT})} \begin{bmatrix} a_1^* \\ b_1^* \end{bmatrix}. \tag{3.19}$$

By a direct comparison of (3.18) and (3.19), the corresponding $\mathcal{PT}$-transformed matrix **M** is [3.7,3.8,3.11,3.12],

$$\mathbf{M} \xrightarrow{\mathcal{PT}} \mathbf{M}^{(\mathcal{PT})} \equiv \mathbf{M}^{-1*} \tag{3.20}$$

[‡]For the detailed formulation and definition of the transfer matrix method, see Appendix B

Since the structure is $\mathcal{PT}$-symmetric invariant, it can be deduced that,

$$\mathbf{M} = \mathbf{M}^{-1*} \tag{3.21}$$

Exploiting the fact that $\det(\mathbf{M}) = 1$, see (B.4) in Appendix B, it can be shown that,

$$M_{11} = M_{22}^{*} \quad \text{and} \quad \mathrm{Re}[M_{12}] = \mathrm{Re}[M_{21}] \equiv 0.$$

Using these relations, the $\mathbf{M}$-matrix can be parameterised as,

$$\mathbf{M} = \begin{bmatrix} A & -jB \\ jC & A^{*} \end{bmatrix} \quad \text{where} \quad \{B, C\} \in \mathbb{R}. \tag{3.22}$$

Here, each entry of the $\mathbf{M}$-matrix is defined as,

$$\begin{aligned} A &= \frac{1}{t} = t^{*} - \frac{r_L^{*} r_R^{*}}{t^{*}}, \\ B &= -j\frac{r_R}{t} = j\frac{r_R^{*}}{t^{*}}, \\ C &= -j\frac{r_L}{t} = j\frac{r_L^{*}}{t^{*}}. \end{aligned} \tag{3.23}$$

By further exploitation of $\det(\mathbf{M}) = 1$ on (3.22), the *generalised conservation relation* is formulated as [3.7,3.8,3.11,3.12],

$$1 - |t|^2 = r_L r_R^{*} = r_L^{*} r_R \tag{3.24}$$

From (3.24) the generalised conservation relation can also be expressed in terms of the transmittance $T = |t|^2$ and reflectance $R_{L,R} = |r_{L,R}|^2$ coefficients as [3.7,3.8, 3.11,3.12],

$$|1 - T| = \sqrt{R_L R_R} \tag{3.25}$$

Generally, the conservation relation (3.25) implies that one the following cases may occur:

1. For the case of $T < 1$, (3.25) reduces to $T + \sqrt{R_L R_R} = 1$. It can be seen that $\sqrt{R_L R_R}$ replaces the conventional R in the case of an orthogonal system. It follows that when $T < 1$ the scattering of a single incident wave from one side of the structure yields to a loss of power flux [3.7]. This operation is referred to throughout this thesis as *sub-unitary transmission* operation.

   Moreover, from (3.24) one can evaluate the phase relation between the left and right reflected light. Consider that the reflected signal from left side is of the form of $r_L = |r_L|e^{j\phi_L}$ and from the right side is of the form $r_R = |r_R|e^{j\phi_R}$. From (3.24) it can be found that the phase for the left and right reflected signal is related by $\phi_L = \phi_R$.

2. For the case of $T > 1$, (3.25) reduces to $T - \sqrt{R_L R_R} = 1$. In this case, a single incident beam yields to a *super-unitary transmission* with the phase relation between left and right reflected waves as $\phi_L - \phi_R = \pi$.

3. For the case of $T = 1$, (3.25) reduces to $\sqrt{R_L R_R} = 0$ which implies that the product of the left and right reflectances must be zero. Such an operation is typically accomplished by having no reflection from one side of the structure. This particular operation case is referred to as *unidirectionally invisible* operation.

To sum up, throughout this work the term *sub-unitary transmission* refers to the first case of $T < 1$, *super-unitary transmission* refers to the second case of $T > 1$ and *unidirectionally invisible operation* refers to the third case of $T = 1$.

3.3.2 Spontaneous Symmetry Breaking in a $\mathcal{PT}$ Scattering System

The relationship between the incoming and outgoing waves in an optical network is well-described by using the scattering matrix **S**. The formal description and definition of the **S**-matrix was presented in Section 2.2.1 and this section will focus on investigating the spectral properties of the **S**-matrix associated with the $\mathcal{PT}$-symmetric scattering system depicted in Fig. 3.1.

It is well-understood that for any linear passive structure, i.e. no gain and loss, the **S**-matrix is unitary [3.13–3.17],

$$\mathbf{S}^{\dagger} = \mathbf{S}^{-1}, \tag{3.26}$$

where † denotes the transpose and conjugation operation. The unitary relation (3.26) puts a strict condition that the eigenvalues s_n of the **S**-matrix have to be unimodular, i.e.

$$|s_n| = 1. \tag{3.27}$$

Hence, for a passive structure, power is conserved with no net-amplification or dissipation.

However, in the case when a gain or/and lossy element is present, as is the case in $\mathcal{PT}$-symmetric structures, the spectral behaviour of the **S**-matrix is non-trivial. It will be shown shortly that the $\mathcal{PT}$-symmetric structure may undergo a *phase transition* from a power conserving operation, with no net-amplification or dissipation, to a non-conserving system. Hence, consider the scattering matrix formulation

associated with Fig. 3.1 expressed as,

$$\begin{bmatrix} b_1 \\ b_2 \end{bmatrix} = \mathbf{S} \begin{bmatrix} a_1 \\ a_2 \end{bmatrix} \quad \text{where,} \quad \mathbf{S} = \begin{bmatrix} r_L & t \\ t & r_R \end{bmatrix} \tag{3.28}$$

where the ingoing and outgoing field amplitudes (a and b) for each individual port can also be expressed compactly[‡] as,

$$\mathcal{E}_T(x) = \sum_{n=1}^{2} [a_n \mathrm{e}^{-j\beta_n x} + b_n \mathrm{e}^{j\beta_n x}] \tag{3.29}$$

Following similar reasoning to that employed in Section 3.3.1, a $\mathcal{PT}$-symmetric scattering system should support the $\mathcal{PT}$-transformed solution on each port, which is

$$\mathcal{PT}\left\{\mathcal{E}_T(x)\right\} = \sum_{n=1}^{2} [(\mathcal{PT}a_n)\mathrm{e}^{j\beta_n x} + (\mathcal{PT}b_n)\mathrm{e}^{-j\beta_n x}] \tag{3.30}$$

As such the following scattering formulation is also valid,

$$\mathcal{PT} \begin{bmatrix} a_1 \\ a_2 \end{bmatrix} = \mathbf{S}\mathcal{PT} \begin{bmatrix} b_1 \\ b_2 \end{bmatrix} \tag{3.31}$$

where in the matrix formulation the operators $\mathcal{P}$ and $\mathcal{T}$ are defined as

$$\mathcal{P} = \begin{bmatrix} 0 & 1 \\ 1 & 0 \end{bmatrix} \quad \text{and} \quad \mathcal{T} = \mathcal{K} \tag{3.32}$$

where $\mathcal{K}$ is the conjugation operation. As such, by comparing (3.28) and (3.31), it can be found that the scattering matrix $\mathbf{S}$ obeys the following $\mathcal{PT}$-symmetric transformation,

$$\mathcal{PT}\mathbf{S}\mathcal{PT} = \mathbf{S}^{-1}. \tag{3.33}$$

[‡]Using the same notation as that introduced in Section 2.28.

For convenience, consider the parameterised **S**-matrix using (3.23) as,

$$\mathbf{S} = \frac{1}{A}\begin{bmatrix} jC & 1 \\ 1 & jB \end{bmatrix} \quad \text{where,} \quad \{B, C\} \in \mathbb{R}. \tag{3.34}$$

By direct calculation, the eigenvalues s_n, with $n = \{1, 2\}$ can be expressed as [3.7],

$$s_1, s_2 = \frac{j}{2A}\left[(B + C) \pm \sqrt{(B - C)^2 - 4}\right] \quad \text{where,} \quad \{B, C\} \in \mathbb{R}. \tag{3.35}$$

Since the parameters B and C are real numbers, it can be deduced that one of the following cases may happen,

1. For the case of $(B - C)^2 < 4$, the eigenvalues are

$$s_1, s_2 = \frac{j}{2A}\left[(B + C) \pm j\sqrt{4 - (B - C)^2}\right] \quad \text{where,} \quad \{B, C\} \in \mathbb{R}, \tag{3.36}$$

and the corresponding eigenvectors are,

$$\boldsymbol{\psi}_1, \boldsymbol{\psi}_2 = \begin{pmatrix} 2 + j\left[(C - B) \pm j\sqrt{4 - (B - C)^2}\right] \\ 2 + j\left[(B - C) \pm j\sqrt{4 - (B - C)^2}\right] \end{pmatrix} \quad \text{for:} \quad s_1, s_2 \tag{3.37}$$

From (3.36), it can be found by direct calculation that the eigenvalues are unimodular, i.e. $|s_n| = 1$. This implies that, for this case, power is conserved thus there is no net amplification nor dissipation. Note that, in this case, the eigenvectors themselves are $\mathcal{PT}$-symmetric as the $\mathcal{PT}$-operation transforms the eigenvectors back to themselves,

$$\boldsymbol{\psi}_1, \boldsymbol{\psi}_2 \xrightarrow{\mathcal{PT}} \boldsymbol{\psi}_1, \boldsymbol{\psi}_2 \tag{3.38}$$

This particular operation case is referred to as the $\mathcal{PT}$-*symmetric phase*.

2. For the case of $(B-C)^2 > 4$, the eigenvalues are

$$s_1, s_2 = \frac{j}{2A}\left[(B+C) \pm \sqrt{(B-C)^2-4}\right] \quad \text{where,} \quad \{B, C\} \in \mathbb{R}, \tag{3.39}$$

with the corresponding eigenvectors as,

$$\boldsymbol{\psi}_1, \boldsymbol{\psi}_2 = \begin{pmatrix} 2 + j\left[(C-B) \pm \sqrt{(B-C)^2-4}\right] \\ 2 + j\left[(B-C) \pm \sqrt{(B-C)^2-4}\right] \end{pmatrix} \quad \text{for:} \quad s_1, s_2, \tag{3.40}$$

and the transformed solution is

$$\mathcal{PT}\left\{\boldsymbol{\psi}_1, \boldsymbol{\psi}_2\right\} = \begin{pmatrix} 2 + j\left[(C-B) \mp \sqrt{(B-C)^2-4}\right] \\ 2 + j\left[(B-C) \mp \sqrt{(B-C)^2-4}\right] \end{pmatrix} \quad \text{for:} \quad s_1, s_2.$$

Hence, it can be seen that, in this case, the eigenvectors are not $\mathcal{PT}$-symmetric but the pair satisfies the $\mathcal{PT}$-transformation, by transforming to each other,

$$\boldsymbol{\psi}_1, \boldsymbol{\psi}_2 \xrightarrow{\mathcal{PT}} \boldsymbol{\psi}_2, \boldsymbol{\psi}_1 \tag{3.41}$$

Exploiting the symmetry properties of the $\mathcal{PT}$-symmetric $\mathbf{S}$-matrix (3.33), it can be deduced that the pair of eigenvalues are reciprocally conjugate, i.e.

$$s^*_{1,2} s_{2,1} = 1 \tag{3.42}$$

which implies in general that if $|s_1| > 1$ then $|s_2| < 1$. Operation in this case is denoted as the *$\mathcal{PT}$-broken symmetry phase*.

3. The case of $(B-C)^2 = 4$, is the case when both of the above cases are true. In this case, one can find that the eigenvalues are degenerate, as

$$s_1 = s_2 \equiv \frac{j}{2A}(B+C) = \pm j\frac{|A|}{A} \quad \text{where,} \quad \{B, C\} \in \mathbb{R}, \tag{3.43}$$

with the associated eigenvectors,

$$\boldsymbol{\psi}_1 = \boldsymbol{\psi}_2 \equiv \begin{pmatrix} 1 \pm j \\ 1 \mp j \end{pmatrix} \quad \text{for:} \quad s_1, s_2 \tag{3.44}$$

This particular point is referred to as the *$\mathcal{PT}$-breaking point*.

It has been shown that the eigenvalues of the **S**-matrix characterise the operational phase of a $\mathcal{PT}$-symmetric system. As such when the eigenvalues are unimodular, the system is in the $\mathcal{PT}$-symmetric phase whilst if the eigenvalues are reciprocal conjugate the system is in the $\mathcal{PT}$-broken symmetry phase. However, a simpler criterion can be obtained by evaluating the value of $(B - C)^2$ using the identities given in (3.23). The criterion of $\mathcal{PT}$-symmetry phases can be expressed in terms of the transmittance and reflectance coefficients as [3.7],

$$\frac{R_L + R_R}{2} - T \begin{cases} < 1, & \text{for : } \mathcal{PT}\text{-}symmetric\ phase, \\ = 1, & \text{for : } \mathcal{PT}\text{-}symmetry\ breaking\ point, \\ > 1, & \text{for : } \mathcal{PT}\text{-}broken\ symmetric\ phase, \end{cases} \tag{3.45}$$

where, $T = |t|^2$ denotes the transmittance and $R_{L,R} = |r_{L,R}|^2$ denotes the reflectance coefficients for the incident wave arriving from the left or the right of the structure, respectively.

3.3.3 Simultaneous Coherent Perfect Absorber and Lasing

A simultaneous lasing and absorbing action in a $\mathcal{PT}$-symmetric scatterer was noted in [3.7,3.8,3.11,3.12]. In order to understand the properties of this operation, first consider a laser system. In a laser system, the structure emits light even in the absence of an injected signal beam hence $a_1 = a_2 = 0$ whilst $\{b_1, b_2\} \to \infty$. Imposing this solution upon the **M**-matrix (3.18) means that the entry $M_{11} = 0$. On the

other hand, if a structure behaves as a coherent prefect absorber (CPA), there is no scattered wave $b_1 = b_2 = 0$ whilst $\{a_1, a_2\} \neq 0$, and this requires the entry $M_{22} = 0$. In practice, the conditions $M_{11} = 0$ and $M_{22} = 0$ do not coincide at the same frequency, hence the system is either lasing or absorbing, but not both.

However, in a $\mathcal{PT}$-symmetric structure the condition (3.21) does allow this to happen as $M_{11} = M_{22} = 0$ can occur generically at the same frequency. Moreover, since $\det(\mathbf{M}) = 1$, it can be further shown that,

$$M_{11} = M_{22} = 0 \quad \text{and} \quad M_{12}, M_{21} \neq 0, \tag{3.46}$$

which implies that transmission and reflection from the both sides are such that,

$$|t| \to \infty \quad \text{and} \quad |r_L|, |r_R| \to \infty, \tag{3.47}$$

and their phase can be calculated from (3.18) as,

$$\phi_R + \phi_L = 2\phi_t \tag{3.48}$$

where, ϕ_L and ϕ_R denote the phase for the reflected wave for the signal incident from left and right side for the structure respectively whilst ϕ_t is the phase of the transmitted wave.

The scenario of (3.47) can only occur in the $\mathcal{PT}$-broken symmetry phase, i.e. operation case 2 described in Section 3.3.2. This implies that one of the eigenvalues of the $\mathbf{S}$-matrix is $|s_1| \to 0$ whilst the other one is $|s_2| \to \infty$, noting that the product of them should remain unity (3.42). This physically means that the structure has both lasing and coherent perfect absorber(CPA) states simultaneously. Such operation is referred to as *simultaneous coherent perfect absorber-lasing*(CPAL) operation. Since $|\det(\mathbf{S})| = |s_1 s_2|$, one can also interpret that CPAL occurs when the poles and zeros of the $\mathbf{S}$-matrix coalesce in the real frequency axis.

In order to see how CPAL operation occurs, consider 2 incident beams where one is incident from the left and the other from the right side of the $\mathcal{PT}$-scatterer, i.e.

$$\begin{aligned} a_1 &= 1 \\ a_2 &= \mathrm{e}^{j\theta} \end{aligned} \tag{3.49}$$

In (3.49), the left incident a_1 has been taken as a reference beam incident whilst the right incident a_2 has an equal amplitude to a_1 but it differs in phase by θ. As such in practice θ could be varied with respect to the reference beam a_1.

It can be found from (3.28) that the intensity on the left and right side of the structure are given by [3.7],

$$I_L \propto |b_1|^2 = |t|^2 \left(1 + \left|\frac{r_L}{t}\right|^2 + 2\left|\frac{r_L}{t}\right| \cos(\phi_L - \phi_t - \theta)\right) \tag{3.50}$$

$$I_R \propto |b_2|^2 = |t|^2 \left(1 + \left|\frac{r_R}{t}\right|^2 + 2\left|\frac{r_R}{t}\right| \cos(\phi_R - \phi_t + \theta)\right) \tag{3.51}$$

where I_L and I_R denotes the left and right emitted intensities respectively. Moreover, from (3.18), the phases of the transmitted and reflected beams are related by $\phi_L + \phi_R = 2\phi_t$; as such the intensity at each port can also be expressed as,

$$I_{L,R} \propto |b_{1,2}|^2 = |t|^2 \left(1 + \left|\frac{r_{L,R}}{t}\right|^2 + 2\left|\frac{r_{L,R}}{t}\right| \sin\theta\right) \tag{3.52}$$

For the particular case when $|t|, |r_L|$ and $|r_R| \to \infty$, (3.52) can be reduced to,

$$I_{L,R} \propto 2|t|^2\Delta \quad \text{where,} \quad \Delta = 1 + \sin\theta \tag{3.53}$$

It can be seen from (3.53) that CPA operation can only occur for the particular value of $\Delta = 0$ while lasing happens in the more general case $\Delta \neq 0$. In practice, to observe CPA one needs to first acquire the lasing operation of the $\mathcal{PT}$-structure, i.e. when $T \to \infty$, for the given operation frequency f_{op} and the gain/loss parameter. Subsequently a second incident beam at the same frequency is launched from the

opposite side of the structure while varying the phase of the second beam with respect to the first beam. The CPA operation is achieved when the total scattered field is zero. It is noted also that in practice once the structure enters the lasing state, the structure operates in an unstable regime and usually the behaviour is non-linear.

3.4 Summary

This chapter outlines the isomorphism between the Schrödinger equation for the wave-function in quantum mechanics and the Helmholtz equation for electromagnetic field in photonics. As such the concept of a $\mathcal{PT}$-symmetric Hamiltonian in quantum mechanics can be well translated into the photonics system by having a $\mathcal{PT}$-symmetric profile of dielectric material properties.

Furthermore, this chapter also investigates the spectral behaviour of a $\mathcal{PT}$-symmetric scattering system. As such, it is shown that a $\mathcal{PT}$-symmetric photonic scattering system satisfies a more general conservation relation which relates the asymmetric response between ports. Moreover, this chapter shows that a $\mathcal{PT}$-symmetric scattering system may undergo a spontaneous $\mathcal{PT}$-symmetry breaking. The breaking of $\mathcal{PT}$-symmetry is marked by a degeneracy of the eigenvalues of the scattering matrix, with the $\mathcal{PT}$-symmetric phase is defined by unimodular eigenvalues but not in $\mathcal{PT}$-broken symmetry phase. Lastly, this chapter describes the operation of a simultaneous lasing and coherent perfect absorber in a $\mathcal{PT}$-symmetric scattering system.

References

[3.1] N. Zettili, *Quantum Mechanics: Concepts and Applications* (John Wiley, New York, NY, 2009), 2nd ed.

[3.2] A. Yariv, *Quantum Electronics* (John Wiley, New York, NY, 1989), 3rd ed.

[3.3] C. M. Bender, "Introduction to PT-symmetric quantum theory," Contemp. Phys. **46**, 277–292 (2005).

[3.4] C. M. Bender, "Making sense of non-Hermitian Hamiltonians," Reports Prog. Phys. **70**, 947–1018 (2007).

[3.5] C. M. Bender and S. Boettcher, "Real spectra in non-hermitian hamiltonians having PT symmetry," Phys. Rev. Lett. **80**, 5243–5246 (1998).

[3.6] A. Mostafazadeh, "Invisibility and PT symmetry," Phys. Rev. A - At. Mol. Opt. Phys. **87**, 012103 (2013).

[3.7] L. Ge, Y. D. Chong, and A. D. Stone, "Conservation relations and anisotropic transmission resonances in one-dimensional PT-symmetric photonic heterostructures," Phys. Rev. A - At. Mol. Opt. Phys. **85**, 1–10 (2012).

[3.8] Y. D. Chong, L. Ge, and A. D. Stone, "PT-symmetry breaking and laser-absorber modes in optical scattering systems," Phys. Rev. Lett. **106**, 093902 (2011).

[3.9] S. Longhi, "Invisibility in PT-symmetric complex crystals," J. Phys. A Math. Theor. **44**, 485302 (2011).

[3.10] J. D. Joannopoulos, S. G. Johnson, J. N. Winn, and R. D. Meade, *Photonic Crystals: Molding the Flow of Light* (Princeton University Press, Oxford, 2008), 2nd ed.

[3.11] S. Longhi, "PT-symmetric laser absorber," Phys. Rev. A **82**, 031801 (2010).

[3.12] A. Mostafazadeh, "Spectral singularities of complex scattering potentials and infinite reflection and transmission coefficients at real energies," Phys. Rev. Lett. **102**, 220402 (2009).

[3.13] F. A. Benson and T. M. Benson, *Fields, Waves and Transmission Lines* (Springer, Amsterdam, 1991).

[3.14] S. Ramo, J. R. Whinnery, and T. V. Duzer, *Fields and Waves in Communication Electronics* (John Wiley, 1999), 3rd ed.

[3.15] D. M. Pozar, *Microwave Engineering* (John Wiley, New York, NY, 2011), 4th ed.

[3.16] H. A. Haus, *Waves and Fields in Optoelectronics* (Prentice-Hall, New Jersey, 1983).

[3.17] R. E. Collin, *Field Theory of Guided Waves* (IEEE Press, New York, NY, 1991), 2nd ed.

4

Parity-Time Symmetric Bragg Grating

Following the study of a $\mathcal{PT}$-symmetric scattering system in the previous chapter, this chapter focuses on an one-dimesional (1D) $\mathcal{PT}$-symmetric Bragg grating. The chapter overviews the dispersion properties of passive Bragg gratings and compares them to the $\mathcal{PT}$-symmetric Bragg gratings. For the case of a $\mathcal{PT}$ Bragg grating, the impact of the gain/loss on the transmission and reflection spectra is analysed which features the asymmetric scattering phenomena depending on the direction of the incident wave. Moreover, the phase transition of $\mathcal{PT}$-symmetry is demonstrated showing how the gain/loss parameter breaks the $\mathcal{PT}$-symmetry of the system. Finally, the spectral singularity of the scattering system associated with the simultaneous coherent perfect absorber-lasing (CPAL) operation state is also shown.

* * *

4.1 Introduction

The dispersion properties of optical structures with periodic refractive index modulation have been first studied more than 200 years ago [4.1]. The main feature of these periodic structures is the highly-frequency-selectivity reflection depending on the periodicity of the structure known as Bragg diffraction. The structures became a hot topic fuelled by the first experimental demonstration [4.2,4.3] of fibre based Bragg gratings and the observation of non-linear behaviour of photosensitive effects in such structures in the 90s' [4.4,4.5].

It is noted that the first fabrication and experimental work on a Bragg grating was done by Hill and Meltz in 1978 [4.5] utilising the photosensitive effect of Germanium doped silica Ge−Si fibres. In the experiment, an intense Argon-ion laser beam was launched into a Ge−Si fibre from which they observed about 4% reflectivity. However, the reflectivity was gradually increasing in time and reached about 90% after several minutes [4.5] implying that the grating was fully formed. The formation of grating in this technique can be understood as follows: upon the incident laser beam into the fibre, a standing-wave was formed due to a superposition of forward and backward propagating wave reflected by the partial mirror formed by the fibre-air interface at both ends of the structure. Subsequently, GeO defects are formed due to a prolonged exposure of the high intensity periodically-localised field within the fibre core, so forming the grating.

Although the single-beam internal technique was successfully applied to fabricate Bragg gratings, its application was limited since the resulting grating operates at the same frequency as the laser beam used to make it. Subsequently, several other methods were developed to overcome this limitation which offer flexibility on grating periodicity and fabrication ease, such as the dual-beam holographic technique [4.5] and the phase mask by photolithographic method [4.6,4.7]. In addition, different chemical and physical treatments such as *hydrogen loading* [4.8] and *flame brushing*

[4.9] were introduced, which are applied prior radiation in order to enhance the refractive index modulation strength Δn of the grating; a Δn of the order of 10^{-2} could be obtained by hydrogen loading treatment.

In terms of applications, conventional Bragg gratings have been used for a large variety of applications, mainly in optical communications as dispersion compensators [4.10,4.11], wavelength-selectors [4.12,4.13], band-rejection filters [4.14], fibre taps [4.15], erbium doped fibre lasers [4.16,4.17], cascade Raman amplifiers [4.18], fibre mode converters, switching and signal processing devices. Other applications such as bio-chemical sensors and optical memory device with improved performance have also been reported [4.19].

The study of $\mathcal{PT}$-Bragg gratings (PTBGs) is motivated by the introduction of a $\mathcal{PT}$-symmetric refractive index profile [4.20,4.21]. Intriguing features of PTBG such as unidirectional loss-induced invisibility [4.20,4.21] and asymmetric response depending on the direction of incident beam [4.20,4.21] have been reported both theoretically and experimentally. Motivated by the unique spectral behaviour of the PTBG, novel functionality for applications, such as switching [4.20–4.23], optical logic [4.24–4.26], memory devices [4.24,4.27], lasers [4.28–4.31], coherent-perfect absorber (CPA) [4.32–4.35], dense wavelength division multiplexing (DWDM) device [4.24] are enabled.

Throughout this chapter, an *idealised* PTBG, comprised of non-dispersive and linear media is considered by using an exact transfer-matrix (T-matrix) method [4.36]. Details of the formulation and implementation of the T-matrix method can be found in Appendix B.

4.2 Spectral Properties of a Passive Bragg Grating

A Bragg grating has refractive index variation along the propagation direction which leads to a collective reflection and transmission from the interfaces of the different dielectric media. In the case of a Bragg grating, this collective process of reflection and transmission is enhanced by the presence of a regular periodicity. The grating considered in this section has piecewise constant layers of refractive index $n = n_{\text{avg}} \pm \Delta n'$, where n_{avg} is the average refractive index, and $\Delta n'$ is the modulation of the real parts of the refractive index. The grating is surrounded by a background material of average refractive index $n_b = n_{\text{avg}}$ and has a total length of $N\Lambda$, where Λ is the length of one unit cell and N is the number of periods. This structure is illustrated in Fig. 4.1.

The operation of a Bragg grating is based on the Bragg reflection in which the periodical modulation of refractive index along the propagation direction intensifies the collective interaction between the forward and backward propagation wave. The superposition of these two propagating waves leads to a very high reflectivity at a certain frequency at which the strongest mode coupling occurs. The condition for the strongest coupling is referred to as the Bragg condition and occurs at the Bragg frequency f_B,

$$f_B = \frac{c_0}{2n_{\text{avg}}\Lambda}. \tag{4.1}$$

From (4.1), it can be seen that the Bragg frequency depends on the physical period length Λ of the grating and the average refractive index n_{avg} of the grating, with c_0 denotes the speed of light in the free-space.

In practice, the strength of the Bragg grating, which defines the steepness and the

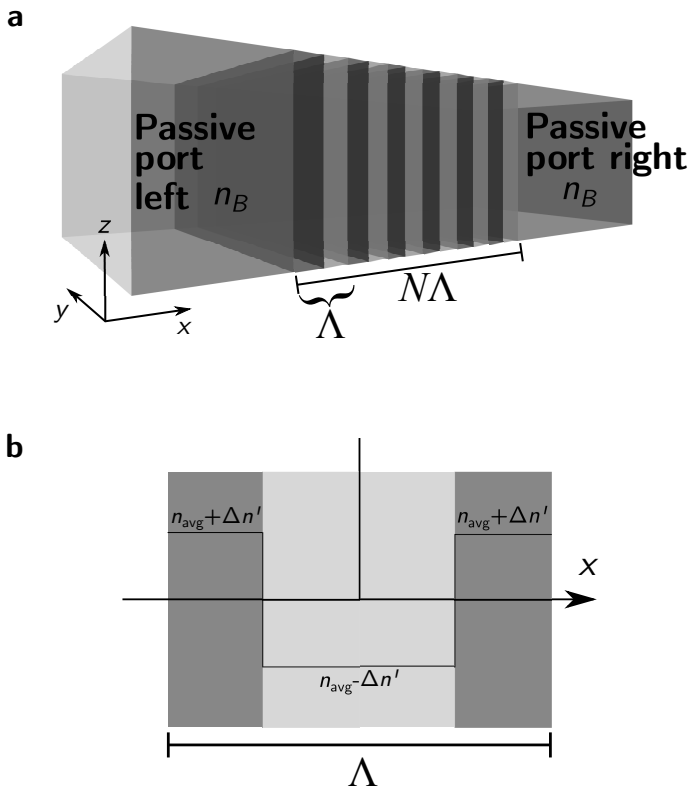

Figure 4.1 | Schematic of a passive Bragg grating structure. (**a**) Passive grating comprised of N-number of unit cells in a background material n_B, (**b**) single unit cell of the grating with 2 slightly different refractive indices $n_{\text{avg}} + \Delta n'$ and $n_{\text{avg}} - \Delta n'$.

width of the transmission and reflection spectra, depends on the number of unit cells N and the depth of modulation $\Delta n'$. To demonstrate this, a Bragg grating is designed for a Bragg frequency of $f_B = 336.845$ THz ($\lambda_B = 0.89$ μm) and is surrounded by a background material having a refractive index of $n_b = 3.5$. By assuming that the average refractive index corresponds to the background material, the physical length of a unit cell of the grating can be calculated by (4.1), i.e. $\Lambda = 0.127$ μm.

Figure 4.2 shows (a) the transmitted and (b) the reflected power spectra calculated using the T-matrix method for different numbers of unit cells N and different depths of modulation $\Delta n'$. It can be seen that, in all cases, a stop-band is formed and centred at $f = f_B$. The total power of the scattered wave is conserved, i.e. $T+R = 1$. Furthermore, Fig. 4.2 shows that the steepness of the transmission and reflection

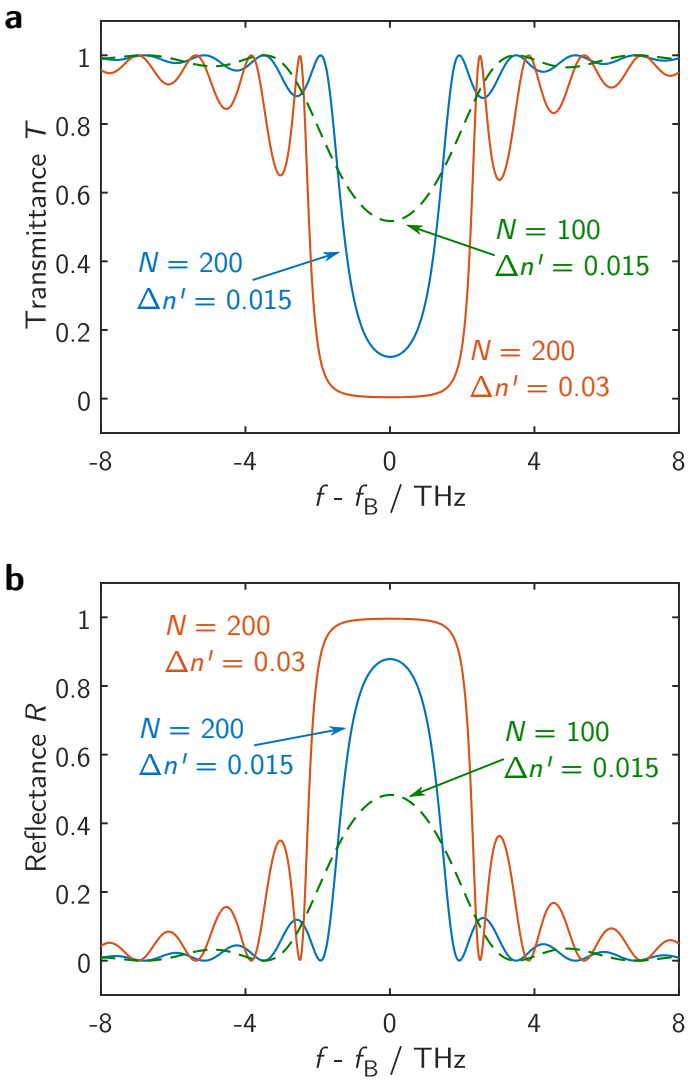

Figure 4.2 | (a) Transmittance and (b) reflectance spectra of a passive Bragg grating.

spectra is dependent on the number of unit cells N, such that an increase in N leads to a steeper spectral response. The width of the transmission and reflection spectra is controlled by the depth of modulation of the real part refractive index $\Delta n'$. Moreover since the dielectric material is passive, the scattering matrix is unitary ($\mathbf{S}^{-1} = \mathbf{S}^{\dagger}$), which implies that the system has the same reflection when excited from the left or the right sides of the grating.

4.3 Bragg Grating with a $\mathcal{PT}$-Symmetric Refractive Index Modulation

In this section, a $\mathcal{PT}$-symmetric refractive index modulation profile is introduced to the Bragg grating to form a $\mathcal{PT}$-symmetric Bragg grating (PTBG) structure. In particular, this section will be focused on the study of the effect of the $\mathcal{PT}$-symmetric phase transition and the spectral singularity on the operation of the PTBG. Special attention will be given to different kinds of transmission, i.e. the sub-unitary, super-unitary and unitary transmissions which were described in Subsection 3.3.1.

The $\mathcal{PT}$-symmetric refractive index modulation requires that the real part of the refractive index is an even function of position and the imaginary part of the refractive index, which represents gain and loss, is an odd function of position. The $\mathcal{PT}$-symmetric Bragg grating (PTBG) considered has piecewise constant layers of refractive index $n = (n_{\text{avg}} \pm \Delta n') \pm jn''$, where n_{avg} is the average refractive index, and $\Delta n'$ and n'' are the modulations of the real and imaginary parts of the refractive index, respectively. The grating is surrounded by a background material of average refractive index $n_b = n_{\text{avg}}$ and has total length of $N\Lambda$, where Λ is the length of one unit cell and N is the number of unit cells. This is schematically illustrated in Fig. 4.3.

For definiteness, consider a PTBG with a depth of real part modulation of $\Delta n' = 0.02$ that is designed with a Bragg frequency $f_B = 336.845$ THz ($\lambda_B = 0.89$ μm) and that the a number of periods of $N = 200$. Moreover, the background material and the average refractive index of the structure are designed to correspond to the refractive index of commonly used GaAs material, i.e. $n_b = n_{\text{avg}} = 3.5$. Using (4.1), the pitch length of a single unit cell of the grating could be calculated as $\Lambda = 0.127$ μm. The transmittance and reflectance for both left and right incident waves are plotted in Fig. 4.4 for an increasing value of gain/loss parameter, i.e.

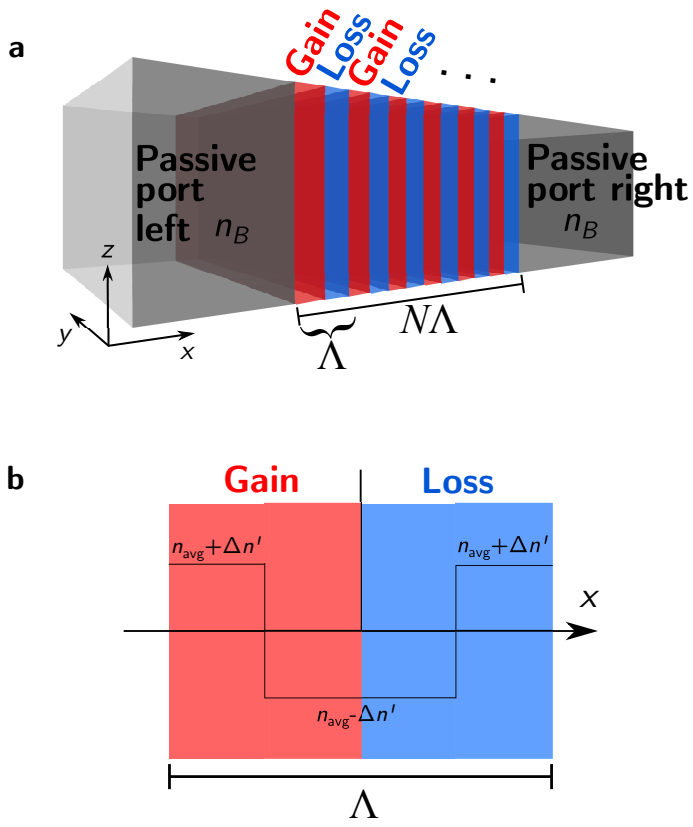

Figure 4.3 | Schematic of a $\mathcal{PT}$-Bragg grating structure. (**a**) Grating composed of N unit cell in a background material n_B, (**b**) single unit cell of the grating with 2 slightly different refractive indices $n_{\text{avg}} + \Delta n'$ and $n_{\text{avg}} - \Delta n'$. Red coloured sections denote gain while the lossy sections are coloured blue.

$n'' = 0$, 0.0041, 0.015, 0.02, 0.022 and 0.02429.

The Lorentz reciprocity theorem, described in Subsection 2.2.2, states that the **S**-matrix of a linear, non-magnetic and time-independent system is symmetric. It implies that the linear $\mathcal{PT}$-symmetric Bragg grating (PTBG), studied in this chapter, has the same transmittance for left and right incidence. As such the transmittances are denoted only as transmittance T and are shown in the top panel of Fig. 4.4. The reflectances, however, are different for left and right incidence and are denoted by R_L and R_R, respectively, and displayed in the middle and bottom row of Fig. 4.4.

The transmittance and reflectance of a passive grating has been discussed in detail in

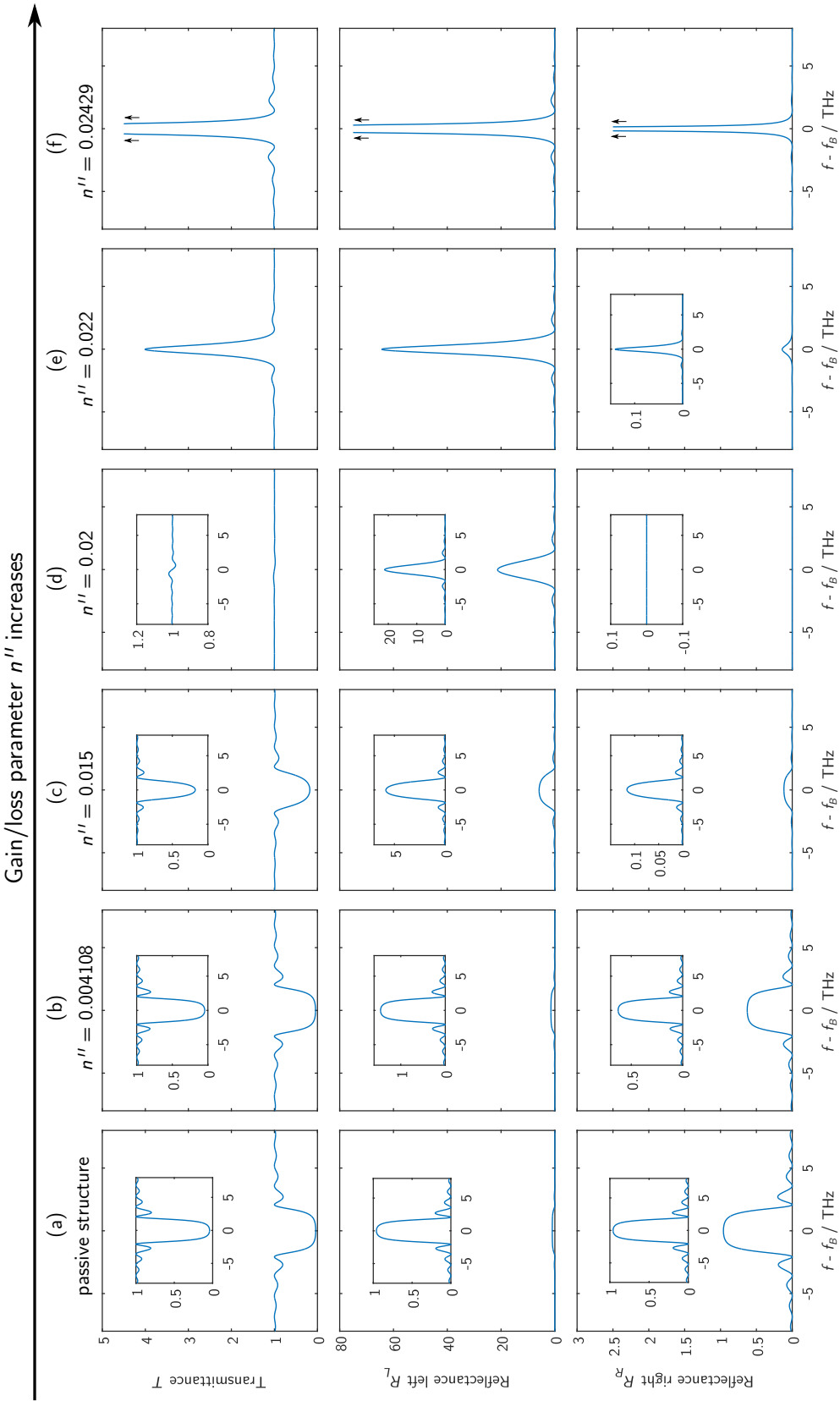

Figure 4.4 | Transmittance and reflectance spectra of a PTBG. The transmittance T, reflectance for the left and right incident waves (R_L and R_R respectively) are displayed in the top, middle and bottom panels respectively. Six different values of gain/loss parameter $n'' = 0$, 0.0041, 0.015, 0.02, 0.022 and 0.02429 are considered. The insets show amplified details of spectra.

the previous section. As the gain/loss parameter n'' is introduced to the system, the reflectance for left incidence differs from the reflectance for right incidence. Looking at the transmittance spectra, in the top panel of Fig. 4.4, it can be seen that as the gain/loss parameter n'' increases the transmission band-gap reduces and almost *unitary transmission* ($T = 1$) occurs at $n'' = 0.02$, with a further increase of n'' from this point leading to *super-unitary* transmission ($T > 1$) spectra.

The reflectance for the left incident wave R_L is shown in the middle panel of Fig. 4.4. It can be seen that as the gain/loss parameter n'' increases, the reflectance from the left side R_L also increases. Meanwhile, the reflectance for the right incident wave R_R behaves differently in that as the gain/loss parameter increases the right reflectance decreases and reaches almost no reflection $R_R = 0$ for all frequencies at $n'' = 0.02$. Operation for gain/loss parameters above this point leads to $R_R > 0$.

It is important to note that for the particular gain/loss parameter of $n'' = \Delta n' = 0.02$, the transmittance is unity ($T = 1$) for all frequencies, and the grating is almost reflectionless for the right incident wave ($R_R = 0$) whilst the left incident wave experiences amplified reflection ($R_L > 1$). This particular operation at $n'' = \Delta n'$ is also known as unidirectional invisible operation [4.21], since the PTBG is invisible when it is excited from one side (right) but not the other (left).

Finally, consider the transmittance T and reflectances (R_L and R_R) for the case when the gain/loss parameter $n'' = 0.02429$, shown in Fig. 4.4(f). For this particular value of gain/loss parameter, the value of T, R_L and R_R approach infinity at the Bragg frequency $f = f_B$. This particular singularity at $f = f_B$ is associated with the simultaneous coherent perfect absorber-lasing (CPAL) operation point. The properties of the CPAL point are discussed in detail in Subsection 3.3.3. It is important to note that, in practice, once the PTBG enters a lasing state, operating at or above the CPAL point, the system is in an unstable regime since the power inside the structure is increasing exponentially. Therefore, controllable practical applications

of the PTBG are constrained to be before the CPAL operation point.

In Subsection 3.3.1, it has been shown that in a $\mathcal{PT}$-symmetric scattering system a more general conservation relationship, see (3.25), which relates both asymmetric left and right responses is applied. This is reproduced again here:

$$|1 - T| = \sqrt{R_L R_R}. \tag{4.2}$$

In order to show the validity of (4.2), the top row of Fig. 4.5 depicts the difference between the left and the right hand side of (4.2). It can be seen from the top panel of Fig. 4.5 that the difference is zero throughout the spectra for an increasing value of gain/loss parameter n'' which implies that the general conservation relation is satisfied in a $\mathcal{PT}$-symmetric Bragg grating structure.

Moreover, it is also discussed in Subsection 3.3.2 that a $\mathcal{PT}$-symmetric scattering system may undergo a spontaneous symmetry breaking which could be observed by the magnitude of the eigenvalues of the **S**-matrix or by a simpler condition defined by the $\mathcal{PT}$-symmetry transition criterion, given in (3.45). Consider the middle panel of Fig. 4.5. This part of the figure shows the magnitude of the eigenvalue of the **S**-matrix, denoted by $|s_n|$ where $n \in \{1, 2\}$, and bottom panel depicts the $\mathcal{PT}$-symmetry transition criterion of (3.45) as a function of frequency for different gain/loss parameter n''.

Now consider the middle panel of Fig. 4.5 which shows the magnitude of the eigenvalues of the **S**-matrix, i.e. $|s_n|$ on a semi-log scale for different gain/loss parameters n''. It can be seen from the middle panel of Fig. 4.5(a) that the eigenvalues of the passive grating are unimodular $|s_{1,2}| = 1$ throughout the frequency spectrum, implying that the **S**-matrix is orthogonal. However, as the gain/loss is introduced into the system the **S**-matrix is no longer Hermitian but will be in either the $\mathcal{PT}$-symmetry or $\mathcal{PT}$-broken-symmetry phase. As such, in the $\mathcal{PT}$-symmetry phase the eigenvalue

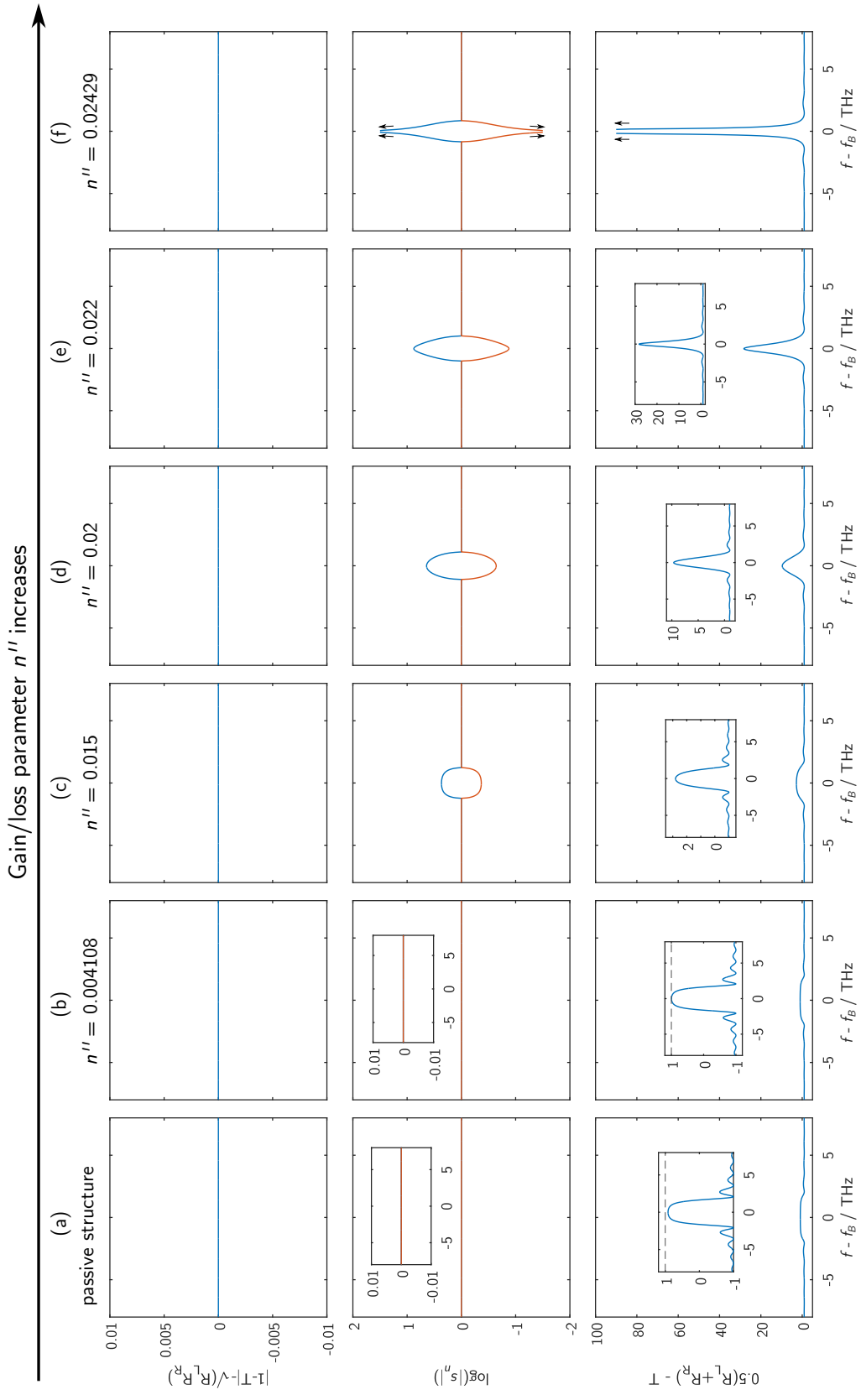

Figure 4.5 | Spectral behaviour of $\mathcal{PT}$-symmetric Bragg grating. (Top panel) the difference between the left and right terms of the general conservation relations. (Middle panel) The magnitude of the eigenvalue of the **S**-matrix. (Bottom panel) the $\mathcal{PT}$-phase transition criterion.

is unimodular $|s_{1,2}| = 1$ whilst in the $\mathcal{PT}$-broken-symmetry phase the *product of the eigenvalues* is unimodular, i.e. $s^*_{1,2}s_{2,1} = 1$. Therefore it can be seen from Fig. 4.5(b) that for a gain/loss parameter value of $n'' = 0.004108$, the PTBG operates in the $\mathcal{PT}$-symmetric phase throughout the frequency range considered. However from Fig. 4.5(c-f) it can be observed that for larger values of n'', the PTBG could operate under the $\mathcal{PT}$-symmetry phase and $\mathcal{PT}$-broken-symmetry phase, depending on the operational frequency f. It is important to note that since the coupling between the forward and backward propagating waves is strongest at the Bragg frequency f_B, the $\mathcal{PT}$-symmetry will be firstly broken at the Bragg frequency and then spread within the band-gap of the grating.

The transition from the $\mathcal{PT}$-symmetric phase to the $\mathcal{PT}$-broken-symmetry can be clearly observed by studying the $\mathcal{PT}$-transition criterion of (3.45). For the operation in the $\mathcal{PT}$-symmetric phase the criterion is $\frac{1}{2}(R_L + R_R) - T < 1$ whilst for operation in the broken-symmetry phase, the criterion is $\frac{1}{2}(R_L + R_R) - T > 1$. It is noted that operation at the criterion of $\frac{1}{2}(R_L + R_R) - T = 1$ is denoted by the $\mathcal{PT}$-symmetric breaking point operation.

The bottom panel of Fig. 4.5 plots the criterion $\frac{1}{2}(R_L + R_R) - T$ for different values of gain/loss parameter n''; the insets depict the detail of the criterion value with the dashed line denoting the $\frac{1}{2}(R_L+R_R)-T = 1$ value. It can be seen that for the passive grating structure, the criterion value is below 1 throughout the frequency spectrum. As the gain/loss parameter value increases, the criterion value also increases. It is noted that at the particular value of $n'' = 0.004108$, the criterion value at the Bragg frequency is just touching the dashed line. It implies that the value of gain/loss parameter $n'' = 0.004108$ indicates the initial $\mathcal{PT}$-symmetry breaking which occurs at the Bragg frequency and which is followed by other frequencies within the band-gap region proximity.

It is important to inspect the operation at the gain/loss parameter value of $n'' =$

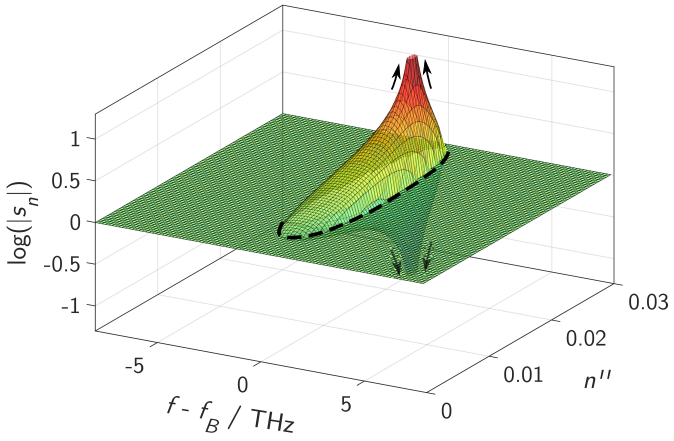

Figure 4.6 | Magnitude of the eigenvalues of the S-matrix. Plotted in a semi-log scale as a function of frequency and for different gain/loss parameter n''

0.02429, depicted by Fig. 4.5(f). Although the PTBG exhibits CPAL operation, the $\mathcal{PT}$-system satisfies the general conservation relationship. Furthermore, the eigenvalues of the **S**-matrix show a strong singularity at the Bragg frequency f_B with one of the eigenvalues approaching infinity whilst the other approaches zero. This implies that the structure supports both lasing and coherent-perfect-absorber operation simultaneously at the same operating frequency and at the same gain/loss parameter value. The singularity signatures also observed in Fig. 4.5(f, bottom panel) where the criterion at the Bragg frequency is also approaching infinity.

In order to study the $\mathcal{PT}$-symmetry phase transition process, Fig. 4.6 depicts the magnitude of the eigenvalues of the **S**-matrix on a semi-log scale as a function of both gain/loss parameter and the operating frequency f. For this figure, the PTBG considered is the same as that presented in Fig. 4.4 and Fig. 4.5. It can be seen from this figure that, as a passive grating, i.e. with no gain/loss, the eigenvalues are uni-modular. However, as the gain/loss increases, the $\mathcal{PT}$-symmetry starts to break which initially happens at f_B for the gain/loss parameter value of $n'' = 0.004108$. For a further increase of gain/loss in the system, more $\mathcal{PT}$-symmetry breaking is observed. The black dashed line in this figure denotes the value of $\frac{1}{2}(R_L + R_R) - T = 1$, i.e. the $\mathcal{PT}$-symmetry breaking point. Furthermore

this figure demonstrates that $\mathcal{PT}$-symmetry breaking occurs at a frequency located within the band-gap region of the grating. It can be explained since propagation of a wave at a frequency outside of the band-gap experiences almost no dispersion, and the interaction between the forward and the backward propagation wave is negligible. Moreover, this figure also shows the singularity point of the eigenvalues of the **S**-matrix, with one eigenvalue approaching infinity whilst the other approaches zero. Operation at this singular point is associated with the CPAL point which is depicted in more detail in Fig. 4.5(f). It is important to note that in practice as the structure reaches the CPAL point the system becomes unstable as it is now operating as a laser cavity, hence that operation beyond the CPAL point leads to unstable operation.

4.4 Summary

To summarise, this chapter overviewed the dispersion properties and the impact of design parameters, such as number of unit cells N and depth of modulation $\Delta n'$, on the transmission and reflection spectra of a passive Bragg grating. As such, it was shown that a passive Bragg grating operates as a band-stop structure centred at the Bragg frequency, which parameter depends on the design parameters of average refractive index and physical length of a unit cell Λ.

Subsequently, the chapter studied the transmission and reflection spectra of a $\mathcal{PT}$-symmetric Bragg grating. It was demonstrated that a $\mathcal{PT}$-Bragg grating has an asymmetric scattering response depending on the direction of the incoming incident wave. Moreover, the possible operation of the so-called unidirectional invisibility operation which occurs when the modulation of the real part of the refractive index is equal to the modulation of the gain/loss parameter of the refractive index, $\Delta n' = n''$ was also shown. This chapter also demonstrated the $\mathcal{PT}$-symmetry transition

process, which was studied in two ways, first by investigating the magnitude of the eigenvalues of the scattering matrix **S** and secondly by the $\mathcal{PT}$-phase transition criterion given in Section 3.45. Moreover, the PTBG was shown to exhibit the spectral singularity operation which is associated with the simultaneous coherent perfect absorber-lasing (CPAL) operation state. The signature of the CPAL state is marked by the singularities in the eigenvalues of the **S**-matrix and the $\mathcal{PT}$-phase transition criterion.

References

[4.1] M. Born and E. Wolf, *Principles of Optics: Electromagnetic Theory of Propagation, Interference and Diffraction of Light* (Cambridge University Press, Cambridge, 1999), 7th ed.

[4.2] K. Hill, Y. Fujii, D. Johnson, and B. Kawasaki, "Photosensitivity in optical fiber waveguides: Application to reflection filter fabrication," Appl. Phys. Lett. **32**, 647–649 (1978).

[4.3] B. S. Kawasaki, K. O. Hill, D. C. Johnson, and Y. Fujii, "Narrow-band Bragg reflectors in optical fibers," Opt. Lett. **3**, 66 (1978).

[4.4] D. K. W. Lam and B. K. Garside, "Characterization of single-mode optical fiber filters," Appl. Opt. **20**, 440 (1981).

[4.5] G. Meltz, W. W. Morey, and W. H. Glenn, "Formation of Bragg gratings in optical fibers by a transverse holographic method," Opt. Lett. **14**, 823 (1989).

[4.6] D. Anderson, V. Mizrahi, T. Erdogan, and A. White, "Production of in-fibre gratings using a diffractive optical element," Electron. Lett. **29**, 566 (1993).

[4.7] K. O. Hill, B. Malo, F. Bilodeau, D. C. Johnson, and J. Albert, "Bragg gratings fabricated in monomode photosensitive optical fiber by UV exposure through a phase mask," Appl. Phys. Lett. **62**, 1035 (1993).

[4.8] P. Lemaire, R. Atkins, V. Mizrahi, and W. Reed, "High pressure H2 loading as a technique for achieving ultrahigh UV photosensitivity and thermal sensitivity in GeO2 doped optical fibres," Electron. Lett. **29**, 1191 (1993).

[4.9] F. Bilodeau, B. Malo, J. Albert, D. C. Johnson, K. O. Hill, Y. Hibino, M. Abe, and M. Kawachi, "Photosensitization of optical fiber and silica-on-silicon/silica waveguides," Opt. Lett. **18**, 953 (1993).

[4.10] K. O. Hill, "Aperiodic distributed-parameter waveguides for integrated optics," Appl. Opt. **13**, 1853 (1974).

[4.11] N. Doran, K. Sugden, I. Bennion, and J. Williams, "Fibre dispersion compensation using a chirped in-fibre Bragg grating," Electron. Lett. **30**, 985–987 (1994).

[4.12] I. Baumann, J. Seifert, W. Nowak, and M. Sauer, "Compact all-fiber add-drop-multiplexer using fiber Bragg gratings," IEEE Photonics Technol. Lett. **8**, 1331–1333 (1996).

[4.13] D. Johnson, K. Hill, F. Bilodeau, and S. Faucher, "New design concept for a narrow-band wavelength-selective optical tap and combiner," Electron. Lett. **23**, 668 (1987).

[4.14] A. Vengsarkar, P. Lemaire, J. Judkins, V. Bhatia, T. Erdogan, and J. Sipe, "Long-period fiber gratings as band-rejection filters," J. Light. Technol. **14**, 58–65 (1996).

[4.15] G. Meltz, W. W. Morey, and W. H. Glenn, "In-fiber Bragg grating tap," in "Opt. Fiber Commun.", (OSA, Washington, D.C., 1990), p. TUG1.

[4.16] R. Kashyap, R. Wyatt, and R. Campbell, "Wideband gain flattened erbium fibre amplifier using a photosensitive fibre blazed grating," Electron. Lett. **29**, 154 (1993).

[4.17] C. Giles, T. Erdogan, and V. Mizrahi, "Simultaneous wavelength-stabilization of 980-nm pump lasers," IEEE Photonics Technol. Lett. **6**, 907–909 (1994).

[4.18] G. Ball, W. Morey, and J. Waters, "Nd3+ fibre laser utilising intra-core Bragg reflectors," Electron. Lett. **26**, 1829 (1990).

[4.19] K. Hill and G. Meltz, "Fiber Bragg grating technology fundamentals and overview," J. Light. Technol. **15**, 1263–1276 (1997).

[4.20] M. Kulishov, J. M. Laniel, N. Bélanger, J. Azaña, and D. V. Plant, "Nonreciprocal waveguide Bragg gratings," Opt. Express **13**, 3068–78 (2005).

[4.21] Z. Lin, H. Ramezani, T. Eichelkraut, T. Kottos, H. Cao, and D. N. Christodoulides, "Unidirectional invisibility induced by PT-symmetric periodic structures," Phys. Rev. Lett. **106**, 213901 (2011).

[4.22] S. Phang, A. Vukovic, H. Susanto, T. M. Benson, and P. Sewell, "Ultrafast optical switching using paritytime symmetric Bragg gratings," J. Opt. Soc. Am. B **30**, 2984–2991 (2013).

[4.23] F. Nazari, M. Nazari, and M. K. Moravvej-Farshi, "A 2x2 spatial optical switch based on PT-symmetry," Opt. Lett. **36**, 4368–70 (2011).

[4.24] M. Kulishov, B. Kress, and R. Slavík, "Resonant cavities based on Parity-Time-symmetric diffractive gratings," Opt. Express **21**, 68–70 (2013).

[4.25] S. Phang, A. Vukovic, T. M. Benson, H. Susanto, and P. Sewell, "A versatile all-optical parity-time signal processing device using a Bragg grating induced using positive and negative Kerr-nonlinearity," Opt. Quantum Electron. **47**, 37–47 (2015).

[4.26] C. Y. Huang, R. Zhang, J. L. Han, J. Zheng, and J. Q. Xu, "Type-II perfect absorption and amplification modes with controllable bandwidth in combined PT-symmetric and conventional Bragg-grating structures," Phys. Rev. A **89**, 023842 (2014).

[4.27] S. Phang, A. Vukovic, H. Susanto, T. M. Benson, and P. Sewell, "Impact of dispersive and saturable gain/loss on bistability of nonlinear parity-time Bragg gratings," Opt. Lett. **39**, 2603–6 (2014).

[4.28] B. Peng, . K. Ozdemir, S. Rotter, H. Yilmaz, M. Liertzer, F. Monifi, C. M. Bender, F. Nori, and L. Yang, "Loss-induced suppression and revival of lasing." Science **346**, 328–32 (2014).

[4.29] S. Longhi and L. Feng, "PT-symmetric microring laser-absorber," Opt. Lett. **39**, 5026–9 (2014).

[4.30] M. Brandstetter, M. Liertzer, C. Deutsch, P. Klang, J. Schöberl, H. E. Türeci, G. Strasser, K. Unterrainer, and S. Rotter, "Reversing the pump dependence of a laser at an exceptional point." Nat. Commun. **5**, 4034 (2014).

[4.31] L. Feng, Z. J. Wong, Y. Wang, X. Zhang, R.-M. R.-M. Ma, Y. Wang, X. Zhang, R.-M. R.-M. Ma, Y. Wang, and X. Zhang, "Single-mode laser by parity-time symmetry breaking," Science **346**, 972–975 (2014).

[4.32] L. Chang, X. Jiang, S. Hua, C. Yang, J. Wen, L. Jiang, G. Li, G. Wang, and M. Xiao, "Paritytime symmetry and variable optical isolation in activepassive-coupled microresonators," Nat. Photonics **8**, 524–529 (2014).

[4.33] Y. D. Chong, L. Ge, and A. D. Stone, "PT-symmetry breaking and laser-absorber modes in optical scattering systems," Phys. Rev. Lett. **106**, 093902 (2011).

[4.34] L. Ge, Y. D. Chong, and A. D. Stone, "Conservation relations and anisotropic transmission resonances in one-dimensional PT-symmetric photonic heterostructures," Phys. Rev. A - At. Mol. Opt. Phys. **85**, 1–10 (2012).

[4.35] S. Longhi, "PT-symmetric laser absorber," Phys. Rev. A **82**, 031801 (2010).

[4.36] R. E. Collin, *Field Theory of Guided Waves* (IEEE Press, New York, NY, 1991), 2nd ed.

5

Transmission-Line Modelling of Active Photonic Medium

The chapter starts with an overview of a simplified gain and loss material model typically used to model erbium-doped active material. The *telegrapher's* equation is introduced and shown to give an analogue representation of Maxwell's equations in the electromagnetic field theory as a lumped-element electrical circuit. Subsequently, a time-domain numerical method namely the Transmission-line modelling (TLM) is developed based upon this analogy using the bilinear transformation formulation. By using the digital filter approach, simple realistic dispersive and saturable gain (or loss) material is implemented within the time-domain TLM model. Finally, the implemented TLM gain (or loss) material model is validated for two cases, i.e. a linear and saturable gain.

* * *

5.1 A Realistic Gain (or Loss) Medium Model

Light amplification phenomena can be explained using the concept of energy levels and the transitions of electrons between the energy levels [5.1–5.3]. To elaborate the concept of gain by the mechanism of electron transition between different energy levels, consider a three-energy-level model, illustrated in Fig. 5.1.

The three-energy-level model, illustrated Fig. 5.1, is a simplified model which is typically used to describe light amplification phenomena in an erbium-doped optical amplifier [5.2–5.5]. In such a configuration, there are three energy levels denoted by E_1, E_2 and E_3, with E_1 being the lowest energy level. The level E_3 is typically a collection of closely spaced energy levels in comparison to the discrete levels E_1 and E_2.

The amplification process starts with an upward transition of electrons from E_1 to E_3 by an external pumping beam. Almost immediately, electron transitions between the closely spaced energy levels in E_3 as well as from E_3 to E_2 occur. These rapid transitions are usually associated with phonon and non-radiative transition. Meanwhile, the large energy gap between E_2 and E_1 causes a transition between these energy levels while emitting light. Additionally E_1 and E_2 are discrete levels, hence the emitted photons has a distinct energy $E_2 - E_1$.

During the transition from E_2 to E_1, two kinds of emission occur, namely stimulated and spontaneous emissions. The stimulated emission occurs because of an induced downward transition by an incoming light signal frequency which is matched to the energy gap, i.e. $E_2 - E_1$. This emission is usually almost instantaneous, thus produces a coherent light amplification. Meanwhile the spontaneous emission happens regardless the presence of incoming signal and is typically slow and in a random manner, thus the emitting light is not coherent and in random directions and polarisation. In practice, the spontaneous emission causes noise problems in optical

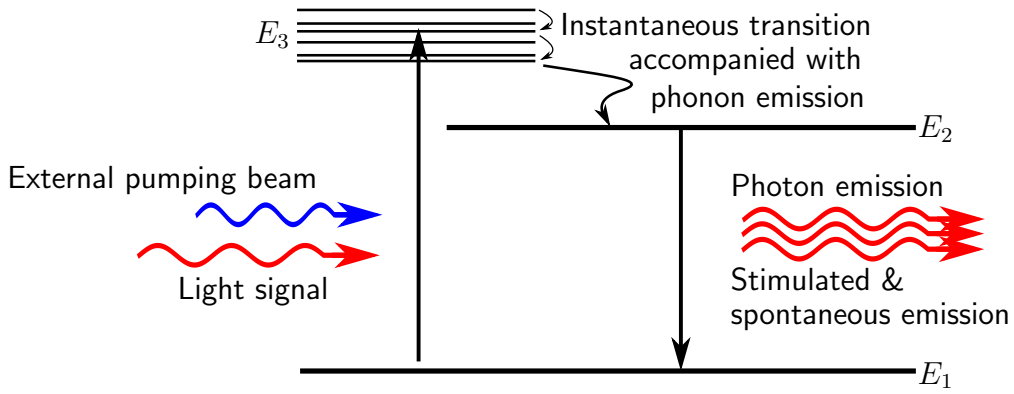

Figure 5.1 | Light amplification by population inversion. Thee-energy levels of an atomic system, denoted by E_1, E_2 and E_3 with E_1 the lowest and E_3 is the highest energy level. Adapted from [5.1–5.4].

amplifier applications [5.2].

For the case when the electron transition between E_2 and E_1 is considered to be *homogeneous*, the electron response to the incoming light is characterised by the same atomic transitional angular frequency ω_σ and the same time relaxation parameter τ. In such an homogeneous system, the time relaxation parameter τ models the time required by the electrons to come to rest after transition, which is responsible for the finite material response described previously in Section 2.3. The finite material response introduces a broadening in the spectrum of the emitted light in the shape of Lorentzian lineshape function.

A macroscopic model of the homogeneously broadened gain medium can conveniently be modelled through the electrical conductance of the medium as [5.6],

$$\sigma_e(I,\omega) = \mathbb{S}(I)\frac{\sigma_0}{2}\left[\frac{1}{1+j(\omega-\omega_\sigma)\tau} + \frac{1}{1+j(\omega+\omega_\sigma)\tau}\right] \tag{5.1}$$

where, ω_σ denotes the atomic transitional angular frequency, τ is the atomic relaxation time parameter, and σ_0 is related to the conductivity peak value that is set by the pumping level at ω_σ. The saturation coefficient $\mathbb{S}$ is non-linear in nature as a consequence of the finite number of electrons available in the case of large incident

signal and is given as [5.2,5.5–5.7],

$$\mathbb{S}(I) = \frac{1}{1 + (I/I_{sat})}. \tag{5.2}$$

In the case of a small incident signal, variation of the saturation coefficient is typically negligible. The value of the saturation intensity I_{sat} is highly dependent on the detail of structure and material [5.8].

Overall, the frequency domain relative dielectric permittivity (2.20) is given by,

$$\varepsilon_r(\omega, I) = 1 + \chi_e(\omega) - j\mathbb{S}(I)\frac{\sigma_0}{2\varepsilon_0\omega}\left[\frac{1}{1 + j(\omega - \omega_\sigma)\tau} + \frac{1}{1 + j(\omega + \omega_\sigma)\tau}\right]. \tag{5.3}$$

It is important to note that the material model given by (5.3) satisfies the Kramers-Kronig relations by the fact that a change in the imaginary part causes the real part of the dielectric constant to be dispersive and it meets the analytic condition of the Fourier transform that all singularities of the model are located in the upper half-plane of the complex frequency plane.

In order to associate the conductivity model given in (5.3) with the resulting gain, assume that the dielectric susceptibility is constant and real, i.e. $\chi_e(\omega) = \chi_e$ and consider the case of small signal gain. The relative permittivity can then be simplified as,

$$\varepsilon_r(\omega) = 1 + \chi_e + \frac{\sigma_e''(\omega)}{\varepsilon_0\omega} - j\frac{\sigma_e'(\omega)}{\varepsilon_0\omega}, \tag{5.4}$$

where, the frequency domain (small signal) conductivity has been considered in the form of $\sigma_e(\omega) = \sigma_e'(\omega) + j\sigma_e''(\omega)$, so that the real and imaginary parts of the

conductivity are given by,

$$\begin{aligned}\sigma_e'(\omega) &= \sigma_0 \frac{1+(\omega_\sigma^2+\omega^2)\tau^2}{\{1+(\omega_\sigma^2-\omega^2)\tau^2\}^2+4\omega^2\tau^2}, \\ \sigma_e''(\omega) &= \sigma_0 \frac{(\omega\tau)\{-1+(\omega_\sigma^2-\omega^2)\tau^2\}}{\{1+(\omega_\sigma^2-\omega^2)\tau^2\}^2+4\omega^2\tau^2}.\end{aligned} \tag{5.5}$$

In the refractive index formalism, the propagation constant in (2.19) can also be expressed as,

$$\gamma = \alpha + j\beta = j\frac{\omega}{c_0}n(\omega) \tag{5.6}$$

where, the complex frequency-domain refractive index is defined as,

$$n(\omega) \equiv n'(\omega) + jn''(\omega) = \sqrt{\varepsilon_r(\omega)} \tag{5.7}$$

Consequently, the phase constant (β) and gain (α) depend only on the real and imaginary parts of the refractive index respectively as,

$$\alpha = -\frac{\omega}{c_0}n''(\omega), \tag{5.8}$$

$$\beta = \frac{\omega}{c_0}n'(\omega). \tag{5.9}$$

By assuming propagation in the $+z$ direction in the form $\mathrm{e}^{-\gamma z}$, it can be seen from (5.5), (5.6) and (5.8) that gain is achieved by having $\sigma_0 < 0$.

It is also important to note that the three-level system, illustrated in Fig. 5.1, also describes light absorption phenomena. From Fig. 5.1, it can be seen that in the absence of external pumping beam, most of the electrons are at E_1 and the incoming light signal induces an upward transition from E_1 to E_2. The upward transition induces loss at the corresponding frequency of the appropriate energy $E_2 - E_1$. Mathematically, this induced absorption loss can be modelled by (5.3) by having $\sigma_0 > 0$.

5.2 The Transmission-Line Theory

This section presents the manifestation of Maxwell's equations describing propagating electromagnetic fields in circuit theory, which becomes the underlying concept of the time-domain electromagnetic modelling scheme on which the Transmission-line modelling (TLM) method is based.

In order to exemplify the analogous principle, consider the two-wire transmission-line shown in Fig. 5.2. Figure 5.2 schematically shows a section of transmission line with length Δx with voltage V across the wires and a propagating current I (top) for which the equivalent circuit is represented by the lumped components of inductor (L), capacitor (C) and conductance (G) (bottom).

Applying the Kirchhoff voltage and current conservation laws to the bottom circuit of Fig. 5.2, the voltage V and current I are described by the coupled partial differential equations [5.9],

$$-\frac{\partial I(x,t)}{\partial x}\Delta x = GV(x,t) + C\frac{\partial V(x,t)}{\partial t} \tag{5.10}$$

$$-\frac{\partial V(x,t)}{\partial x}\Delta x = L\frac{\partial I(x,t)}{\partial t} \tag{5.11}$$

Equations (5.10) and (5.11) are commonly known as the *Telegrapher equations*. Assuming the steady-state, the solution of the coupled PDEs is assumed to take the form of,

$$V(x,t) = \bar{v}(x)e^{j\omega t} \tag{5.12}$$

$$I(x,t) = \bar{i}(x)e^{j\omega t} \tag{5.13}$$

Equations (5.10) and (5.11) can be solved simultaneously to give the travelling wave

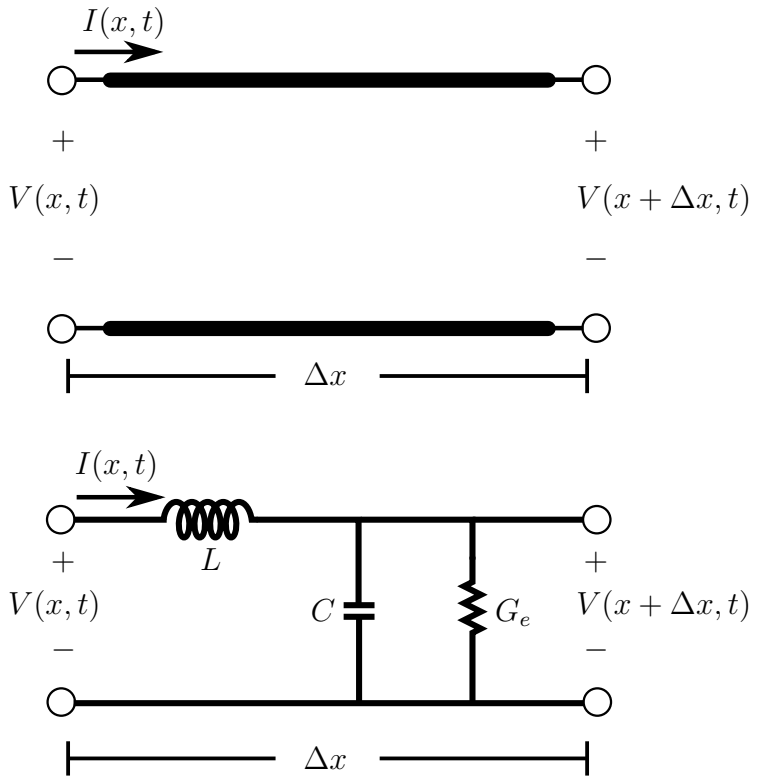

Figure 5.2 | Schematic illustration of a transmission-line section. (top) A section of length Δx of two wire transmission-line; (below) The circuit representation of the transmission-line lumped-elements of inductor L, capacitor C and conductance G_e.

equations,

$$\frac{d\psi(x)}{dx^2} - \gamma^2\psi(x) = 0 \tag{5.14}$$

where, $\psi(x)$ can be either $\bar{v}(x)$ or $\bar{i}(x)$, and γ denotes the propagation constants which are defined as

$$\gamma = \pm\sqrt{\left(j\omega\frac{L}{\Delta x}\right)\left(\frac{G}{\Delta x} + j\omega\frac{C}{\Delta x}\right)} \tag{5.15}$$

Equation (5.15) signifies that the solution to (5.14) is comprised of two wave travelling in $+x$ and $-x$ direction as,

$$\begin{aligned}\bar{v}(x) &= v_0^+ \mathrm{e}^{-\gamma x} + v_0^- \mathrm{e}^{\gamma x} \\ \bar{i}(x) &= i_0^+ \mathrm{e}^{-\gamma x} + i_0^- \mathrm{e}^{\gamma x}\end{aligned} \tag{5.16}$$

Note that here, we have adopt $e^{-\gamma x}$ to represent propagation in the $+x$ direction and $e^{\gamma x}$ for propagation in the $-x$ direction. By solving (5.10) and (5.16) simultaneously the characteristic impedance Z_{TL} of the transmission line (Fig. 5.2) can be defined as,

$$\frac{v_0^+}{i_0^+} = -\frac{v_0^-}{i_0^-} = Z_{TL} = \sqrt{\frac{j\omega L}{G + j\omega C}}\,. \tag{5.17}$$

Meanwhile, from (2.1), Maxwell's equations for a one-dimensional wave propagating in the x-direction with the electric field polarised in y-direction and the magnetic field in z-direction are,

$$-\frac{\partial H_z}{\partial x} = J_{ey} + \frac{\partial(\varepsilon E_y)}{\partial t} \tag{5.18}$$

$$-\frac{\partial E_y}{\partial x} = \mu_0 \frac{\partial H_z}{\partial t} \tag{5.19}$$

In this context, the Maxwell's equations have again been assumed for non-magnetic material ($\mu = \mu_0$) which is typical of optical materials.

By comparing (5.10)-(5.11) with (5.18)-(5.19), the equivalences of the field and the transmission-line theory can be obtained and are summarised in Table 5.1, along with the corresponding symbol notation and units. Note that the negative signs on the magnetic field (H) and current (I) equality are due to the fact that clockwise current direction has been adopted.

5.3 Transmission-Line Modelling of Gain Medium

In this section, the concept and methodologies of the time-domain Transmission-line modelling (TLM) numerical method is introduced. The alternative approach of the TLM method based on the bilinear $\mathcal{Z}$-transformation formulation will also

Table 5.1 | Equivalences of the field and transmission-line quantities [5.10,5.11].

Field theory			Transmission line theory			
Quantity	Symbol	unit	Quantity	Symbol	unit	Equivalences
Electric field	E	[V/m]	Voltage	V	[V]	$E \leftrightarrow -\frac{V}{\Delta x}$
Magnetic field	H	[A/m]	Current	I	[A]	$H \leftrightarrow -\frac{I}{\Delta x}$
Permittivity	ε	[F/m]	Capacitance	C	[F]	$\varepsilon \leftrightarrow \frac{C}{\Delta x}$
Permeability	μ_0	[H/m]	Inductance	L	[H]	$\mu_0 \leftrightarrow \frac{L}{\Delta x}$
Conductivity	σ	[S/m]	Conductance	G_e	[S]	$\sigma \leftrightarrow \frac{G_e}{\Delta x}$

be described and shown to be suited for modelling of material with dispersion and non-linear properties [5.11–5.14].

5.3.1 TLM: Concept and Methodology

Having established the analogous formulation of electrodymamics in dielectic media and the scattering of voltages and currents in within the transmission-line model, this section presents a simulation technique of electodynamics best-known as the transmission-line modelling (TLM) method [5.10–5.18]. The TLM method is a time-domain numerical model based upon the analogous principle between the propagating electromagnetic field and voltage impulses travelling on an interconnected mesh of transmission lines [5.10–5.18]. In its simplest, 1D, case the TLM discretises the problem of interest into sections of length Δx, represented by a transmission line model as is illustrated in Fig. 5.2 [5.10–5.18].

At the conceptual level, the TLM simulation can be distinguished by the 3+1 main block processes illustrated in Fig. 5.3. Before the calculations, one needs to define the simulation conditions which include excitation sources, geometry and material

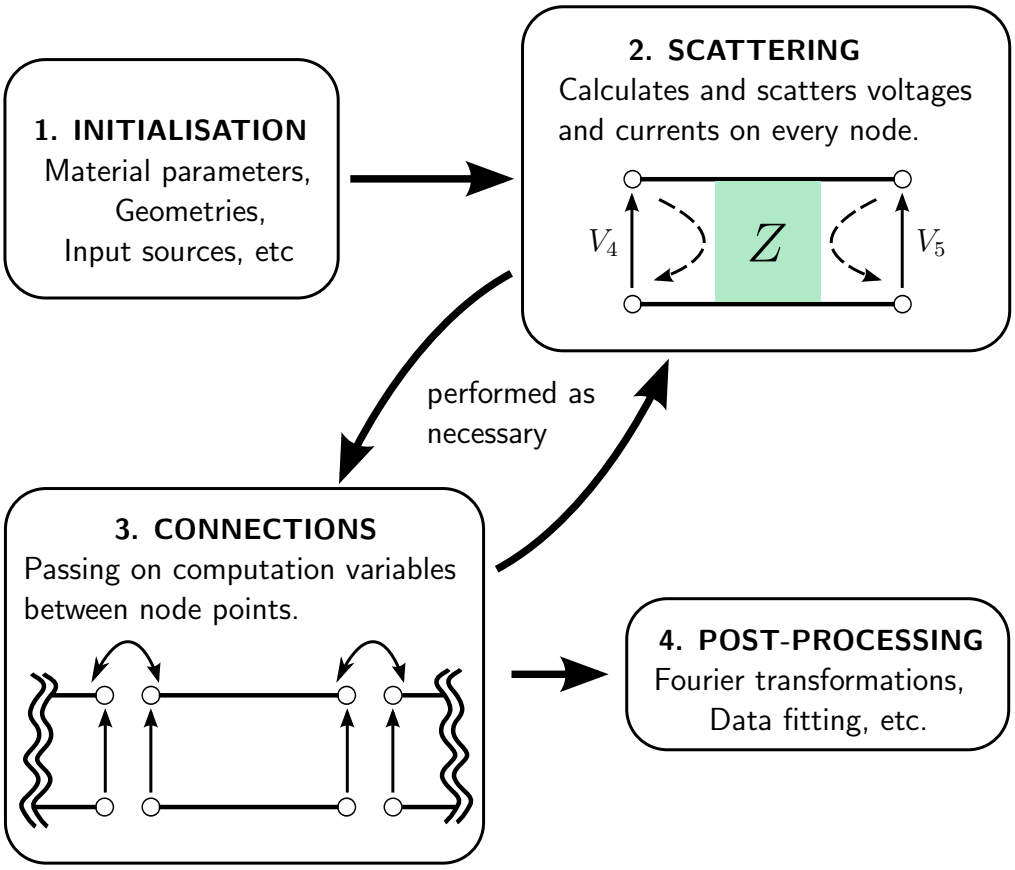

Figure 5.3 | Schematic illustration of a TLM simulation. Adapted from [5.10].

parameters of structures. Based upon the specified simulation conditions the TLM calculation is performed starting with a scattering process. In the scattering process, each TLM node receives the incoming voltage pulses from the neighbouring nodes and scatters them depending on the material defined on each node (this process is detailed in Subsection 5.3.2). The output of the scattering process is the set of scattered voltage pulses, these scattered voltage pulses need to be communicated to the adjacent nodes by the connection process. The connection process mimics the propagation of voltages by passing on each scattered voltage pulse to the adjacent nodes. The iterative scattering-connection process is repeated as many times as is needed to simulate the propagation of voltage pulses between all the TLM nodes in the problem space. After all the scattering-connection processes, the TLM simulation is ended with data collections and post-processing. The post-processing of the time-domain data may include data-fitting, Fourier transformations and complex

eigenvalue extractions.

In this thesis, an alternative TLM formulation using bilinear $\mathcal{Z}$-transformation of Maxwell's equations approach is employed [5.11–5.14,5.18]. In this approach, the TLM is formulated using less of an electical analogy but more of transmission-line characteristics and a $\mathcal{Z}$-transformation of Maxwell's equations [5.11–5.14,5.18]. In particular, this approach offers flexibility in the implementation of dispersive and non-linear material properties [5.11–5.14,5.16–5.18].

5.3.2 Scattering Process

Maxwell's equations (2.1) for a one-dimensional problem with the electric field polarisation in the y-direction are,

$$-\frac{\partial}{\partial x}\begin{bmatrix} H_z \\ E_y \end{bmatrix} = \begin{bmatrix} \sigma_e * E_y \\ 0 \end{bmatrix} + \frac{\partial}{\partial t}\begin{bmatrix} \varepsilon_0(E_y + \chi_e * E_y) \\ \mu_0 H_z \end{bmatrix} \tag{5.20}$$

In (5.20), the curl Maxwell's equations are displayed in a compact matrix notation, where $*$ denotes the time-domain convolution operator.

Utilising the field-circuit equivalences (See Table 5.1), the circuit form of (5.20) is illustrated by Fig. 5.4 and the Telegrapher equation is formulated as,

$$-\frac{\partial}{\partial x}\Delta x\begin{bmatrix} I_z \\ V_y \end{bmatrix} = \begin{bmatrix} G_e * V_y \\ 0 \end{bmatrix} + \frac{\partial}{\partial t}\begin{bmatrix} C_0\,(V_y + \chi_e * V_y) \\ L_0 I_z \end{bmatrix}, \tag{5.21}$$

By introducing the following normalisation transformation,

$$\begin{aligned} x \to X\Delta x \quad &| \quad \partial x \to \Delta x \partial X, \\ t \to T\Delta t \quad &| \quad \partial t \to \Delta t \partial T \end{aligned} \tag{5.22}$$

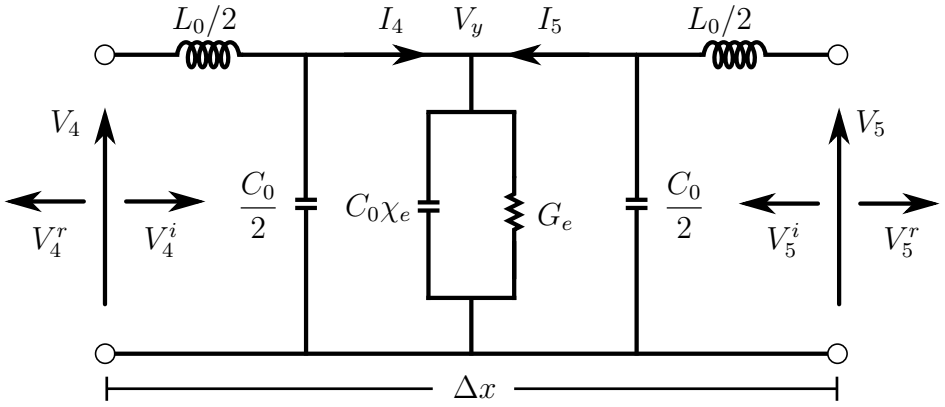

Figure 5.4 | Lumped-component circuit form of (5.21). Build based upon the equivalences of Maxwell's curl and transmission-line telegrapher's equations. Adapted from [5.10–5.14,5.18].

where X and T are dimensionless variables. Equation (5.21) can be simplified further as a single unit operation (volt) as,

$$-\frac{\partial}{\partial X}\begin{bmatrix} i_z \\ V_y \end{bmatrix} = \begin{bmatrix} g_e * V_y \\ 0 \end{bmatrix} + \frac{\partial}{\partial T}\begin{bmatrix} V_y \\ i_z \end{bmatrix} + \frac{\partial}{\partial T}\begin{bmatrix} \chi_e * V_y \\ 0 \end{bmatrix}. \tag{5.23}$$

Here, the normalised conductivity and current parameters are defined as $g_e = G_e Z_{\mathrm{TL}}$ and $i_z = I_z Z_{\mathrm{TL}}$, where Z_{TL} denotes the characteristic impedance of the transmission-line and has been adopted to correspond to the properties in free-space, hence $Z_{\mathrm{TL}} = \sqrt{L_0/C_0}$ and $\Delta x = c_0 \Delta t$ where $c_0 = 1/\sqrt{\varepsilon_0 \mu_0}$.

By utilising the travelling-wave format [5.11–5.14,5.18],

$$-\frac{\partial i_z}{\partial X} - \frac{\partial V_y}{\partial T} = 2V_4^i + 2V_5^i - 2V_y, \tag{5.24}$$

$$-\frac{\partial V_y}{\partial X} - \frac{\partial i_z}{\partial T} = 2V_4^i - 2V_5^i - 2i_y, \tag{5.25}$$

where V_4^i and V_5^i denote the incident impulses coming from the left and right respectively, as illustrated in Fig. 5.4. The travelling-wave form of (5.23) in the Laplace-domain is given as,

$$2\begin{bmatrix} V_y^r \\ i_z^r \end{bmatrix} \equiv 2\begin{bmatrix} V_4^i + V_5^i \\ V_4^i - V_5^i \end{bmatrix} = 2\begin{bmatrix} V_y \\ i_z \end{bmatrix} + \begin{bmatrix} g_e V_y \\ 0 \end{bmatrix} + \bar{s}\begin{bmatrix} p_{ey} \\ 0 \end{bmatrix}. \tag{5.26}$$

In (5.26), the convolution operator $*$, which appeared in (5.23), has been transform to a simple multiplication in the frequency domain and $p_{ey} = \chi_e V_y$ denotes the normalised dielectric polarisation. Note that the normalised Laplacian operator is $\bar{s} = \partial/\partial T$. Performing a bilinear $\mathcal{Z}$-transform of the normalised Laplacian operation [5.11–5.14,5.18],

$$\bar{s} \xrightarrow{\mathcal{Z}} 2\left(\frac{1-z^{-1}}{1+z^{-1}}\right), \tag{5.27}$$

equation (5.26) becomes in $\mathcal{Z}$-domain,

$$2\begin{bmatrix} V_y^r \\ i_z^r \end{bmatrix} = 2\begin{bmatrix} V_y \\ i_z \end{bmatrix} + \begin{bmatrix} g_e V_y \\ 0 \end{bmatrix} + 2\left(\frac{1-z^{-1}}{1+z^{-1}}\right)\begin{bmatrix} p_{ey} \\ 0 \end{bmatrix}. \tag{5.28}$$

Equation (5.28) is suited for material modelling with dispersive and nonlinear properties, which are modelled through the dielectric polarisation p_{ey} and the conductivity g_e. Right after obtaining the voltage V_y and current i_z quantities, the new scattered voltage impulses can obtained by [5.10–5.14,5.18],

$$\begin{aligned} V_4^r &= V_y - V_4^i \\ V_5^r &= V_y - V_5^i \end{aligned} \tag{5.29}$$

and be communicated to the neighbouring nodes during the connection process.

5.3.3 Internodal Connection Process

In the connection process, the new calculated reflected voltage impulses will become the incident voltages of the next time step. Hence, the reflected voltages of node X at time step T become the new incident voltage impulses of the neighbouring nodes at

the time iteration step $T+1$. This process can be expressed as [5.11–5.14,5.18],

$$\underset{T}{\begin{bmatrix} V_4[X] \\ V_5[X] \end{bmatrix}^r} \rightarrow \underset{T+1}{\begin{bmatrix} V_5[X-1] \\ V_4[X+1] \end{bmatrix}^i} \tag{5.30}$$

where, $[X-1]$ and $[X+1]$ denote the adjacent nodes on the left and right side, respectively.

5.3.4 Digital Filter Formulation of Active Material Model

In this Subsection, a digital filter is designed based on the material model described in the previous section. The purpose of designing a digital filter of the material model is to facilitate the implementation of the frequency-domain material model within the time-domain TLM method as a feed-back system.

The gain (or loss) material model given in (5.1) can be conveniently expressed in the Laplace domain as,

$$\sigma_e(I,s) = \mathbb{S}(I)\sigma_0 \left[\frac{K_1 s + (K_1)^2}{s^2 + 2K_1 s + (K_2)^2}\right], \tag{5.31}$$

where the constants K_1 and K_2 are defined as,

$$K_1 = \frac{1}{\tau} \quad \text{and} \quad K_2 = \frac{1+(\omega_\sigma \tau)^2}{\tau^2}.$$

Using the normalisation procedure introduced in Subsection 5.3.2, the material model of (5.31) in the TLM form can be expressed as,

$$g_e(I,s) = \mathbb{S}(I)g_0 \left[\frac{K_1 s + (K_1)^2}{s^2 + 2K_1 s + (K_2)^2}\right], \tag{5.32}$$

and by performing the bilinear $\mathcal{Z}$-transformation on the Laplacian operator as,

$$g_e(I,z) = \mathbb{S}(I) g_0 \left[\frac{K_3 + z^{-1}(K_4) + z^{-2}(K_5)}{K_6 + +z^{-1}(K_7) + +z^{-2}(K_8)} \right], \tag{5.33}$$

where, the constants in (5.33) are given by,

$$K_3 = 2K_1\Delta t + (K_1\Delta t)^2 \quad ; \quad K_4 = 2(K_1\Delta t)^2 \tag{5.34}$$

$$K_5 = -2K_1\Delta t + (K_1\Delta t)^2 \quad ; \quad K_6 = 4 + 4K_1\Delta t + K_2(\Delta t)^2 \tag{5.35}$$

$$K_7 = -8 + 2K_2(\Delta t)^2 \quad ; \quad K_8 = 4 - 4K_1\Delta t + K_2(\Delta t)^2 \tag{5.36}$$

Furthermore, any system with a causal response can always be described as a feedback system whose current response depends on a past event. Hence it can be shown that [5.13,5.18] ,

$$(1 + z^{-1}) g_e = g_{e0} + z^{-1}(g_{e1} + \bar{g}_e(z)), \tag{5.37}$$

where the constants g_{e0} and g_{e1} and the causal response $\bar{g}_e(z)$ are given by,

$$\begin{aligned} g_{e0} &= g_s \left(\frac{K_3}{K_6} \right), \\ g_{e1} &= 0, \\ \bar{g}_e(z) &= \frac{b_0 + z^{-1}b_1 + z^{-2}b_2}{1 - z^{-1}(-a_1) - z^{-2}(-a_2)}, \end{aligned} \tag{5.38}$$

with the corresponding constants being defined as,

$$\begin{aligned}
g_s &= g_0 \left(\frac{1}{1 + (I/I_{sat})} \right), \\
b_0 &= g_s \left(\frac{K_3}{K_6} \right) \left(\frac{K_3 + K_4}{K_3} - \frac{K_7}{K_6} \right), \\
b_1 &= g_s \left(\frac{K_3}{K_6} \right) \left(\frac{K_4 + K_5}{K_3} - \frac{K_8}{K_6} \right), \\
b_2 &= g_s \left(\frac{K_3}{K_6} \right) \left(\frac{K_5}{K_3} \right), \\
a_1 &= \frac{K_7}{K_6}, \\
a_2 &= \frac{K_8}{K_6}.
\end{aligned} \tag{5.39}$$

5.3.5 Implementation of Digital Filter

In this subsection, the digital filter for a gain (or loss) material (5.37) is implemented within the TLM method in the one-dimensional regime described in section 5.3.2. For convenience, the first row of (5.28) is reproduced here,

$$2V_y^r = 2V_y + g_e V_y + 2 \left(\frac{1 - z^{-1}}{1 + z^{-1}} \right) p_{ey} \tag{5.40}$$

After multiplying both sides by $(1 + z^{-1})$ and rearranging, (5.40) can also be expressed as,

$$(2V_y^r - 2V_y) + z^{-1}(2V_y^r - 2V_y) = (1 + z^{-1}) g_e V_y + 2(1 - z^{-1}) p_{ey} \tag{5.41}$$

Substituting the digital filter for the conductivity given in (5.37), and by further assuming the case of linear and dispersionless dielectric polarisation $p_{ey} = \chi_{e\infty} V_y$, (5.41) reduces to

$$2V_y^r + z^{-1}(S_{ey}) = K_{e2} V_y, \tag{5.42}$$

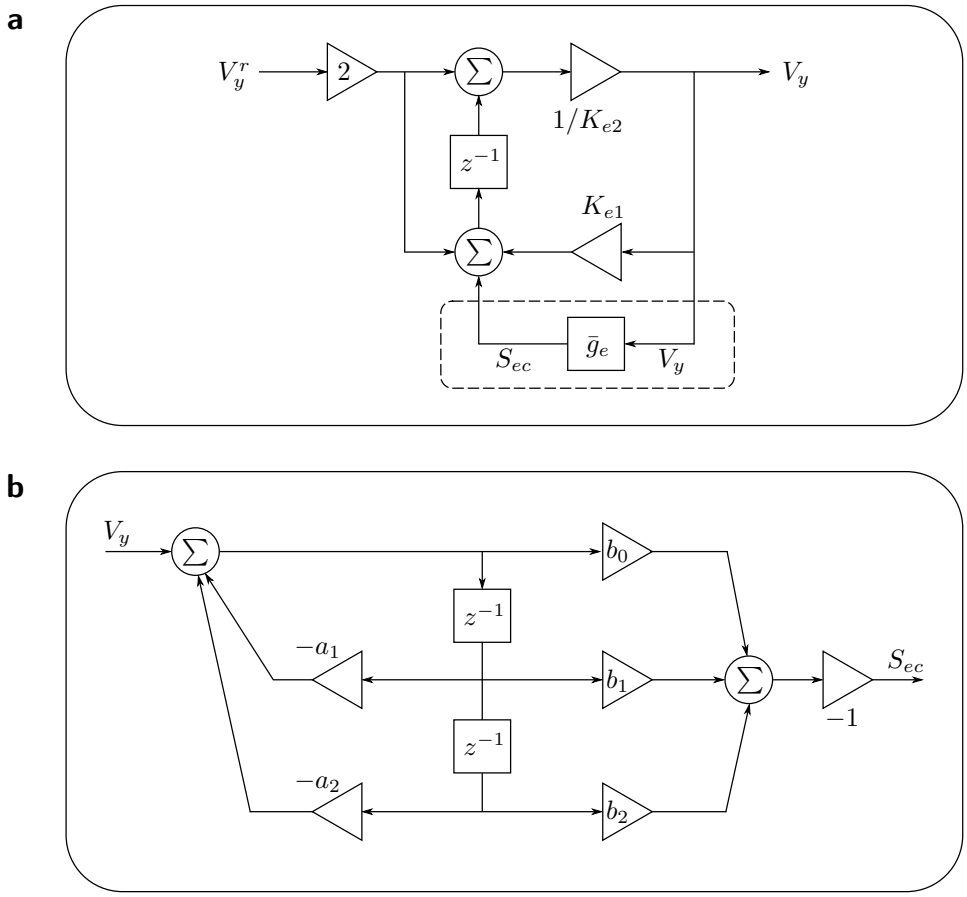

Figure 5.5 | Signal flow diagram modelling gain material in TLM algorithm. (**a**) Overall signal flow diagram from the incoming voltage impulses V_y^r to the resulting nodes voltage V_y. (**b**) Detail field updating scheme of conductivity model of gain material which is marked in the dashed box in (**a**).

where the cumulative past response is given by,

$$\begin{aligned} S_{ey} &= 2V_y^r + K_{e1}V_y + S_{ec}, \\ S_{ec} &= -\bar{g}_e V_y, \end{aligned} \tag{5.43}$$

with the constants K_{e1} and K_{e2} defined as,

$$\begin{aligned} K_{e1} &= -(2 + g_{e1} - 2\chi_{e\infty}), \\ K_{e2} &= 2 + g_{e0} - 2\chi_{e\infty}, \end{aligned} \tag{5.44}$$

and g_{e0}, g_{e1} and $\bar{g}_e$ are as in (5.38).

The signal flow diagram of system (5.42) is illustrated in Fig. 5.5(a), the subsystem defining the conductivity digital filter system (within the dashed line box) is detailed in Fig. 5.5(b). It is also noted here that, for the case of a saturable gain (or loss) model, the saturation coefficient $\mathbb{S}(I)$ is updated as follows: if $|V_y|$ at the time-step T is greater than $|V_y|$ at $T-1$ at the same location in space, then $\mathbb{S}(I)$ is updated using the last value of $|V_y|$. However, if $|V_y|$ has decreased from its previous value, it is not updated; hence $\mathbb{S}(I)$ remains based on the most recent peak value. In this manner, intensity feedback in the time-domain retains, as much as possible, its frequency domain meaning [5.6]. Thus the time-averaged intensity I can be calculated by (2.24) which, for a one-dimension problem is reduced to,

$$I = \frac{1}{2}\frac{E_y^2}{\eta} = \frac{1}{2}\frac{V_y^2}{\eta \Delta x^2}, \quad \text{where} \quad \eta = \frac{\eta_0}{n'} \tag{5.45}$$

where $\eta_0 = \sqrt{\mu_0/\varepsilon_0}$ is the free-space impedance of a normally incident wave and n' is the real-part of the refractive index.

5.3.6 Validations

This section demonstrates the accuracy of the implemented gain model for both low-signal gain amplification and strong-signal amplification where gain saturation dominates.

For the small-signal gain case - the TLM model will be validated using the structure illustrated in Fig. 5.6 which is based on GaAs material with $\chi_{e\infty} = 11.8881$ [5.6]. It is noted that for validation purposes in this subsection, a constant value of dielectric constant as given in [5.6] is used, in the following chapter, such as in Chapter 7, a more realistic dispersive and non-linear dielectric material model will be developed and used. By injecting current into the centre region of length $L = 5$ μm, this region becomes active. The gain region is assumed to have a conductivity

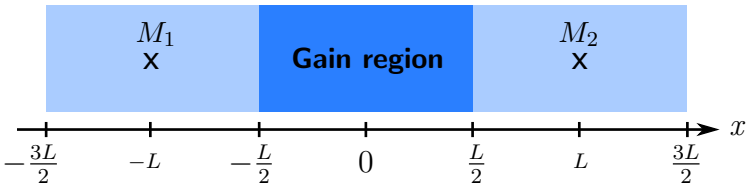

Figure 5.6 | Schematic illustration of the validating structure. The 1D structure used for the validation of the gain material model implemented in the TLM method and relevant coordinate axis.

$\sigma_0 = -5000$ S/m, atomic transition angular frequency $\omega_\sigma = 2\pi(336.845)$ rad/ps and time relaxation parameter $\tau = 0.07$ ps [5.6]. Furthermore, for small-signal amplification the gain can be assumed to be linear and unsaturable ($\mathbb{S} = 1$). As such by assuming a linear gain medium, the TLM calculation can be validated with one obtained by using the exact T-matrix model. Detail on the implementation of the T-matrix method is given in Appendix B.

The TLM simulation is conditioned as follow: a single Gaussian pulse function modulated at $f = \omega_\sigma/(2\pi)$ with Full-Width Half Magnitude (FWHM) 20 fs was launched from the left side of the structure before the gain region. The simulation was performed with a spatial discretisation $\Delta x = \lambda_0/(50n)$ and run for 3 ps, which ensured that all of the signal had passed through the structure and provided a sufficient frequency-domain resolution.

Two separate TLM simulations were under-taken. The first simulation was performed without the gain region and acts as a reference. The second simulation serves as the main simulation, where the gain region is present. In both simulations, two sets of time-domain data (electric field in this case) were recorded at M_1 and M_2 monitor points. From the first simulation, the recorded data at M_1, namely $E_{y,1}$, was reserved as the incident signal and the other one, at M_2, namely $E_{y,2}$, was used as a reference to calculate the phase change of the transmitted signal for the case when the gain region is present. The second simulation included the gain region and was monitored at M_2, namely $E_{y,3}$. As such, the transmittance T and phase

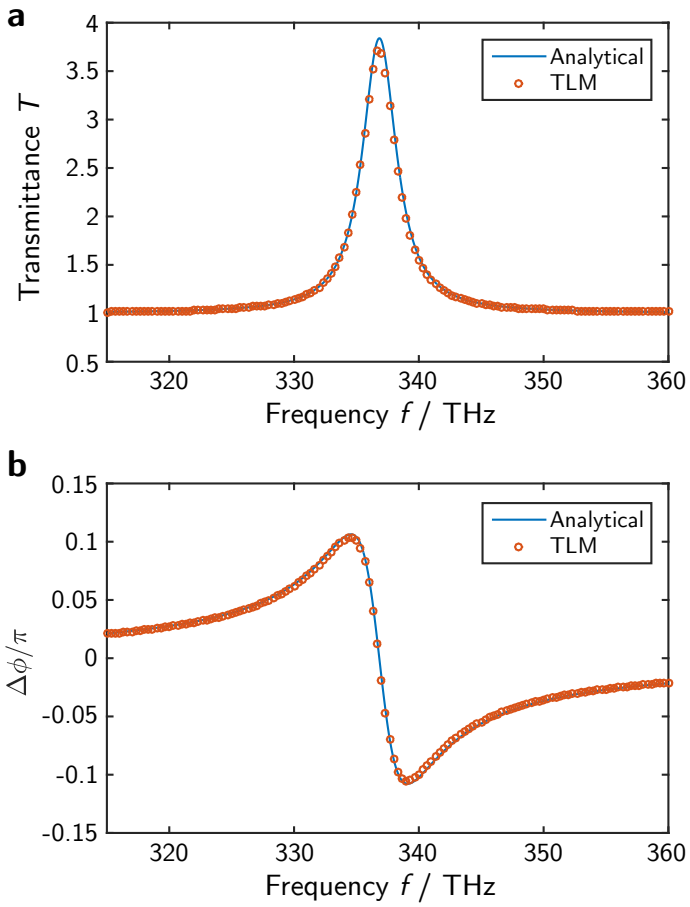

Figure 5.7 | Transmittance and phase difference of signal passing through gain medium. Results of the first validation case of linear GaAs material, i.e. $\mathbb{S} = 1$ calculated by the TLM and the analytical T-matrix method. (**a**) The transmittance and (**b**) the phase difference of the transmitted signal observed at the monitor point M_2 plotted as a function of frequency.

difference $\Delta\phi$ can be calculated as,

$$T = \frac{|\mathcal{E}|^2_{y,3}}{|\mathcal{E}|^2_{y,1}} \quad \text{and} \quad \Delta\phi = \angle\left(\frac{\mathcal{E}_{y,3}}{\mathcal{E}_{y,2}}\right),$$

where $\mathcal{E}_{y,1}$ $\mathcal{E}_{y,2}$ and $\mathcal{E}_{y,3}$ denote the Fourier transformed $E_{y,1}$, $E_{y,2}$ and $E_{y,3}$ data respectively. $\angle$ denotes the argument of a complex number.

Figure 5.7(a) compares the transmittance of the structure illustrated in Fig. 5.6 as a function of frequency from the TLM simulation and the analytical transfer-matrix (T-matrix) method. The transmittance indicates an amplification of the incident

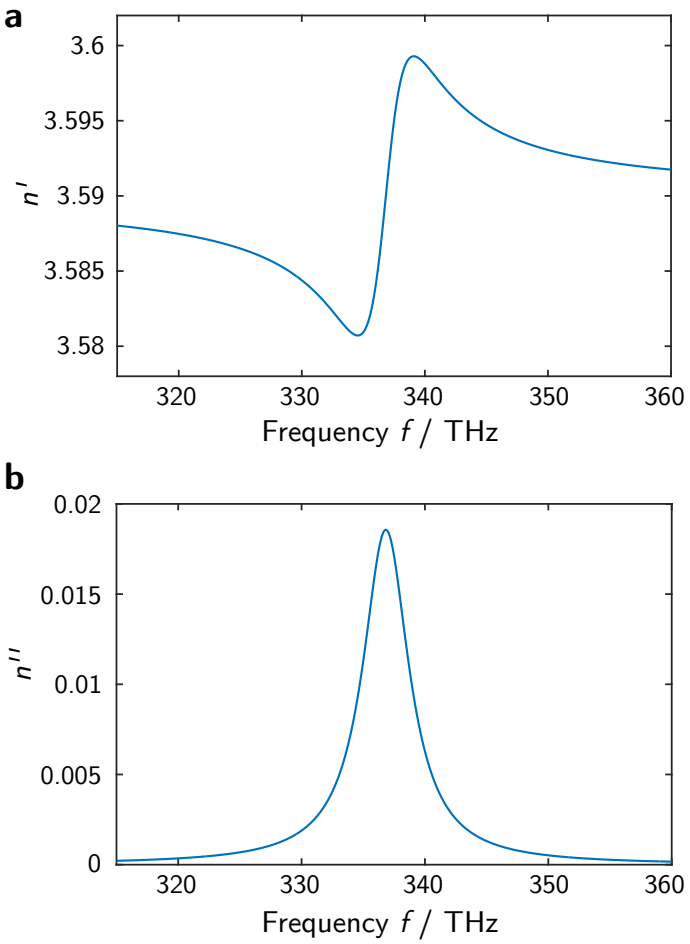

Figure 5.8 | Complex refractive index of the gain GaAs material. (**a**) The real part of the refractive index and (**b**) the imaginary part of the refractive index of the gain region material. The gain region material parameter used are conductivity parameter $\sigma_0 = -5000$ S/m, atomic transition angular frequency $\omega_\sigma = 2\pi(336.845)$ rad/ps and time relaxation parameter $\tau = 0.07$ ps, as used in [5.6].

light with a Lorentzian line-shape and a maximum amplification of almost 4 times at $f = 336.85$ THz. The phase difference $\Delta\phi$ is plotted in Fig. 5.7(b) as a function of frequency. It can be seen from Fig. 5.7 that the TLM simulation results agree with the results calculated by the analytical T-matrix method.

To provide a better understanding of the result given in Fig. 5.7, the dispersion of the gain region is now examined. By substituting all the parameters in (5.3) for the material defined above, Figs. 5.8(a,b) show the real part and the imaginary part refractive index as a function of frequency, respectively. Figure 5.8(a) shows

that the real part of the refractive index is dispersive so that the value of n' varies between 3.58 and 3.6. It is also important to note that there is zero phase change at the atomic transitional frequency $f_\sigma = \omega_\sigma/(2\pi)$, as the light is amplified coherently at this frequency. The imaginary part of the refractive index depicted in Fig. 5.8(b) is shown to be positive with a Lorentzian lineshape; this signifies that the maximum amplification occurs at $f_\sigma = \omega_\sigma/(2\pi)$ with the peak value of $n''(f_\sigma) = 0.0186$.

Comparing Fig. 5.7(a) with Fig. 5.8(b), it can be seen that the amplified signal follows the profile of the imaginary part of the refractive index, n''; this is reflected by the maximum amplification which happens at $f = 336.85$ THz and is associated with the peak of n'', that is $f_\sigma = \omega_\sigma/(2\pi)$. From Fig. 5.7(b), it can be seen that $\Delta\phi$ is positive for $f < 336.85$ THz whilst it is negative for $f > 336.85$ THz. This can be explained by examining the variation of real part of refractive index given in Fig. 5.8(a). It can be seen from Fig. 5.8(a) that for $f < 336.85$ THz the real part of the refractive index n' is smaller than that of the background material, whist it is higher than that of the background for $f > 336.85$ THz. This causes light signal with $f < 336.85$ THz to propagate faster, which gives rise to a positive $\Delta\phi$, while for $f > 336.85$ THz the light propagates slower, which results in a negative $\Delta\phi$.

For the strong-signal gain case - the model used for validation is a simple Fabry-Perot laser cavity based on GaAs material. The Fabry-Perot cavity is comprised of a section of GaAs gain region ($\chi_{e\infty} = 11.8881$) of length $L = 12.4$ μm, as illustrated in Fig. 5.6, but within an air ($n_b = 1$) background. The gain material parameters used are $\omega_\sigma = 2\pi(336.845)$ rad/ps, $\tau = 0.07$ ps and saturation intensity $I_{sat} = 65.2 \times 10^7$ W/m^2 [5.6]. As such, two partial mirrors are formed at the GaAs and air interface on both sides of the GaAs gain region.

Figure 5.9 depicts the electric field E_y monitored at M_2 as a function of time for the case of a gain region with a conductivity $\sigma_0 = -7000$ S/m, which corresponds to an imaginary part of the refractive index, calculated by (5.7), of $n''(f_\sigma) = 0.02604$.

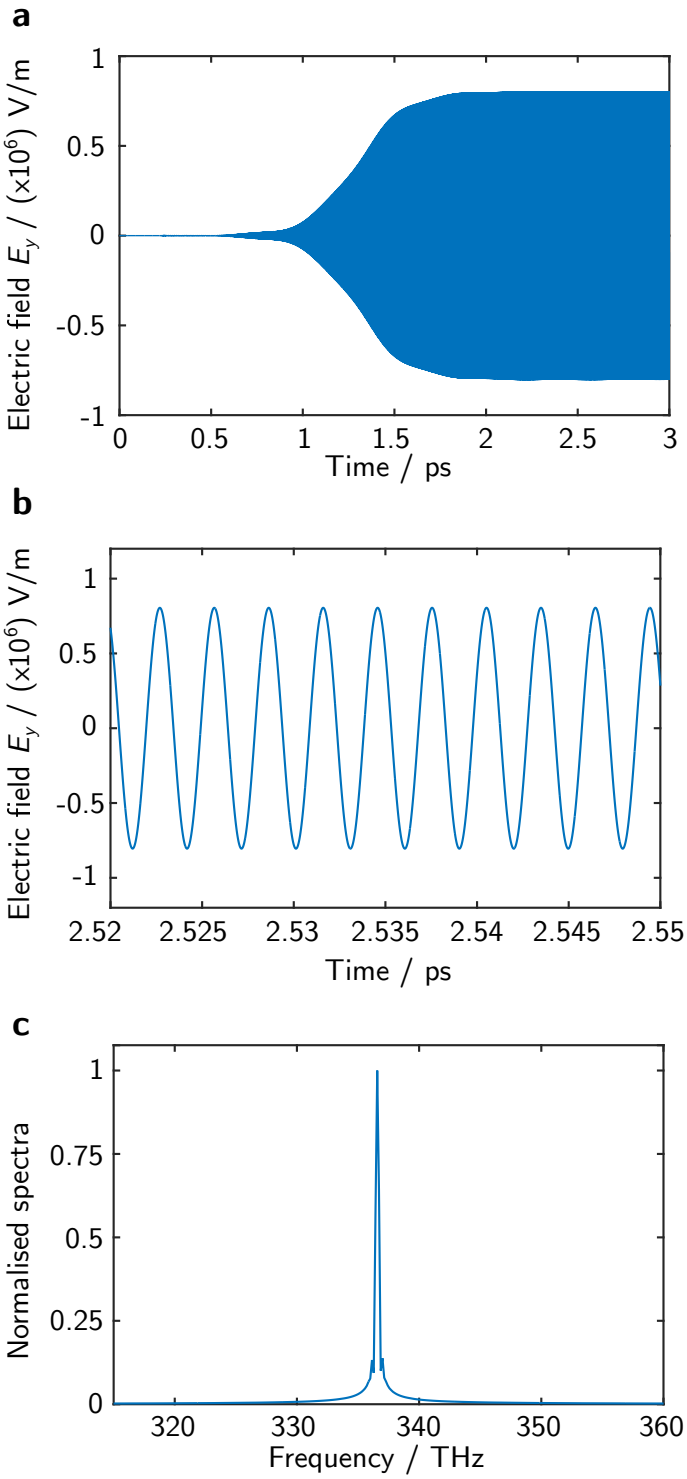

Figure 5.9 | Second validation study of strong-signal gain material model. (**a**) Transmitted electric field amplitude as a function time recorded at M_2 and (**b**) the enlarged view of the electric field E_y between a 0.03 ps window at the steady state. Part (**c**) is the normalised spectrum of the time-domain TLM result.

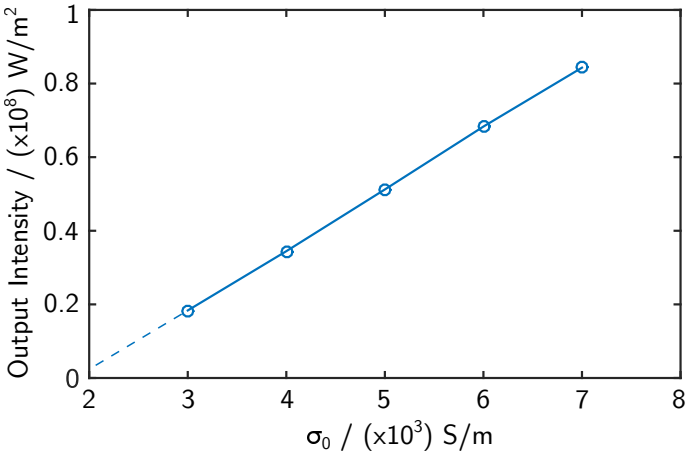

Figure 5.10 | The dependence of the output intensity on the conductivity σ_0 parameter. The output intensity is calculated at the steady state. Dashed line is the extrapolation.

In the TLM simulation, a Gaussian pulse (FWHM 20 ps) modulated at $f = \omega_\sigma/2\pi$ with a peak intensity of $0.01\%I_{sat}$, is launched from the left side of the cavity. It can be seen from Fig. 5.9(a) that the electric field increases rapidly and saturates after 2 ps as the gain saturates. Figure 5.9(b) shows the enlarged electric field amplitude over a 0.03 ps window after the steady-state is reached. Furthermore, Fig. 5.9(c) depicts the Fourier transformation of the time-domain data and confirms that lasing occurs at $f = 336.85$ THz, which corresponds to the atomic transitional frequency of the gain region.

In order to investigate the impact of the conductivity σ_0 parameter on the laser performance, several TLM simulations were undertaken for smaller values of the σ_0 parameter. The output intensity monitored at the steady-state is plotted in Fig. 5.10 for different σ_0 parameters. From Fig. 5.10, it can be seen that the output intensity varies linearly. A similar profile was also reported in [5.6]. Further extrapolation shows that laser threshold occurs at $\sigma_0 \approx -1800$ S/m.

For the case of no material loss, the threshold gain required to achieve lasing could

be obtained analytically by [5.2,5.5,5.6],

$$\alpha_{\text{th}} = \frac{1}{2L}\ln(R) \tag{5.46}$$

where, R is the reflection coefficient of the GaAs-air interface and L is the length of the gain region. For the Fabry-Perot configuration described above, the minimum gain required to achieve lasing is $\alpha_{\text{th}} = -0.046147 \times 10^6$ m^{-1} or the corresponding conductivity $\sigma_{0,\text{th}} = -1759$ S/m, which is calculated by (5.8). Therefore, it can be seen that the gain threshold obtained from the TLM simulations agrees pretty well with the theoretically predicted value.

5.4 Summary

A simple realistic gain (or loss) material model based on three-energy level concept has been presented. In this chapter it was shown that a realistic material with gain (or loss) is dispersive. It was further shown that under small-signal excitation, a linear gain can be used by assuming $\mathbb{S} = 1$ but not for the strong-signal excitation case, mimicking the finite number of electrons available as in practical material.

Subsequently, a transmission-line theory was presented which shows the conceptual equivalences between the propagation of electromagnetic waves and the scatter-propagation of voltage pulses. Based on these equivalences, the time-domain numerical Transmission-Line Model (TLM) based on the alternative bilinear $\mathcal{Z}$-transform was developed for the one-dimensional case. It was shown that this method is well-suited to a dispersive and non-linear material model. Moreover in order to implement the frequency-domain gain (or loss) material model, a digital filter was designed to model a feed-back system and implemented within the TLM model. This chapter was finalised by the validation of the implemented model, which was shown to have a good agreement with the analytically calculated results.

References

[5.1] A. Yariv, *Quantum Electronics* (John Wiley, New York, NY, 1989), 3rd ed.

[5.2] A. Yariv and P. Yeh, *Photonics: Optical Electronics in Modern Communications* (Oxford University Press, New York, NY, 2007), 6th ed.

[5.3] K. Iizuka, *Elements of Photonics, Vol II* (John Wiley, New York, NY, 2002).

[5.4] B. E. A. Saleh and M. C. Teich, *Fundamentals of Photonics* (John Wiley, New York, NY, 2007), 2nd ed.

[5.5] J.-M. Liu, *Photonic Devices* (Cambridge University Press, Cambridge, 2005).

[5.6] S. C. Hagness, R. M. Joseph, and A. Taflove, "Subpicosecond electrodynamics of distributed Bragg reflector microlasers: Results from finite difference time domain simulations," Radio Sci. **31**, 931–941 (1996).

[5.7] A. E. Siegman, *Lasers* (University Science Book, Palo Alto, CA, 1986).

[5.8] M. Robertson, Private communication, October 2015.

[5.9] D. M. Pozar, *Microwave Engineering* (John Wiley, New York, NY, 2011), 4th ed.

[5.10] C. Christopoulos, *The Transmission-Line Modeling Method TLM* (IEEE Press, Piscataway, 1995).

[5.11] J. Paul, "Modelling of general electromagnetic material properties in TLM," Ph.D. thesis, University of Nottingham (1998).

[5.12] J. Paul, C. Christopoulos, and D. Thomas, "Generalized material models in TLM - part III: materials with nonlinear properties," IEEE Trans. Antennas Propag. **50**, 997–1004 (2002).

[5.13] J. Paul, C. Christopoulos, and D. Thomas, "Generalized material models in TLM - part I: Materials with frequency-dependent properties," IEEE Trans. Antennas Propag. **47**, 1528–1534 (1999).

[5.14] J. Paul, C. Christopoulos, and D. Thomas, "Time-domain modelling of negative refractive index material," Electron. Lett. **37**, 1–2 (2001).

[5.15] W. Hoefer, "The transmission-line matrix method–theory and applications," IEEE Trans. Microw. Theory Tech. **33**, 882–893 (1985).

[5.16] V. Janyani, A. Vukovic, and J. Paul, "The development of TLM models for nonlinear optics," Microw. Rev. **10**, 35–42 (2004).

[5.17] V. Janyani, A. Vukovic, J. D. Paul, P. Sewell, and T. M. Benson, "Time domain simulation in photonics: A comparison of nonlinear dispersive polarisation models," Opt. Quantum Electron. **37**, 3–24 (2005).

[5.18] J. Paul, C. Christopoulos, and D. Thomas, "Generalized material models in TLM - part II: Materials with anisotropic properties," IEEE Trans. Antennas Propag. **47**, 1528–1534 (1999).

6

All-Optical Switching Device Using a Parity-Time Symmetric Bragg Grating

This chapter investigates the impact of dispersion on the spectral behaviour of a $\mathcal{PT}$-Bragg grating (PTBG) when a realistic causal gain/loss material model, which satisfied the Kramers-Kronigs relations, is used. The application and validity of the numerical time-domain TLM method to model a realistic dispersive PTBG based on GaAs-based material is investigated. Furthermore, the chapter will also demonstrate the real-time switching application of the PTBG.

* * *

6.1 Introduction

In Chapter 4, the spectral properties of a $\mathcal{PT}$-symmetric Bragg grating (PTBG) were investigated. One of the key findings in Chapter 4 is that a PTBG has unique asymmetric scattering response, as such the response for the left incident signal is different from that of the right incident signal. In particular, it was highlighted that it is possible to engineer an interesting unidirectional invisibility operation under certain parameter conditions, where by a total unity transmission with no reflection from one side and amplified reflection from the other side is achieved. Moreover, Chapter 4 also shows the coherent perfect absorber-Laser (CPAL) operation point; operation at and beyond this point yields to an unstable operation.

Meanwhile, in Chapter 5 the operation concept of gain (or loss) material, which is the ingredient of $\mathcal{PT}$-symmetric material, is studied. It was shown that the amplification (or dissipation) process is related to the stimulated emission which may happen due to a population inversion process. As with any other physical phenomena, the emission process is constrained by the so-called causality condition. As such a realistic causal material with gain (or loss) has to be dispersive, which is the conclusion obtained from the Kramers-Kronig relationship which was introduced in Subsection 2.3.

This chapter will investigate the impact of material dispersion upon the spectral performance of a PTBG. Moreover, this chapter will also demonstrate an application of a PTBG as temporal switching device. In order to observe the temporal behaviour of a PTBG the time-domain Transmission-Line Modelling (TLM) method, equipped with the dispersive gain/loss material model, is used. Details on the implementation and numerical scheme of the TLM method were given in Chapter 5.

6.2 Impact of Dispersive Gain/Loss Medium on the Performance of a $\mathcal{PT}$-Bragg Grating

Consider the PTBG illustrated in Fig. 6.1. The structure is embedded in a background material with a refractive index $\bar{\varepsilon}_b$ and has a total length of $N\Lambda$, where Λ denotes the physical length of an unit cell and N is the total number of unit cells. The relative permittivity distribution in a single unit cell, $\bar{\varepsilon}(x)$, along the propagation direction x, shown in Fig. 6.1, can be expressed as,

$$\bar{\varepsilon}(x,\omega) = \begin{cases} \bar{\varepsilon}_b + \Delta\bar{\varepsilon}' - j\dfrac{\sigma_e(\omega)}{\varepsilon_0\omega}, & x < \dfrac{\Lambda}{4} \\ \bar{\varepsilon}_b - \Delta\bar{\varepsilon}' - j\dfrac{\sigma_e(\omega)}{\varepsilon_0\omega}, & \dfrac{\Lambda}{4} \leq x < \dfrac{\Lambda}{2} \\ \bar{\varepsilon}_b - \Delta\bar{\varepsilon}' + j\dfrac{\sigma_e(\omega)}{\varepsilon_0\omega}, & \dfrac{\Lambda}{2} \leq x < \dfrac{3\Lambda}{4} \\ \bar{\varepsilon}_b + \Delta\bar{\varepsilon}' + j\dfrac{\sigma_e(\omega)}{\varepsilon_0\omega}, & \dfrac{3\Lambda}{4} \leq x < \Lambda \end{cases} \tag{6.1}$$

where, $\Delta\bar{\varepsilon}'$ denotes the constant modulation of the real part of the dielectric permittivity and ε_0 denotes the free-space permittivity. The material conductivity σ_e is a function of frequency as was given in (5.1) and reproduced here for convenience,

$$\sigma_e(\omega) = \frac{|\sigma_0|}{2}\left[\frac{1}{1+j(\omega-\omega_\sigma)\tau} + \frac{1}{1+j(\omega+\omega_\sigma)\tau}\right]. \tag{6.2}$$

In (6.2), ω_σ denotes the atomic transitional angular frequency, τ is the dipole relaxation time, and σ_0 is related to the conductivity peak value that is set by the pumping level at ω_σ. Physical interpretation of these parameters is discussed in Chapter 5. It is important to note that in (6.2), the absolute value of peak conductivity σ_0 is considered. As such from (6.1), it can be seen that the first two sections of the PTBG have gain while the other two sections are lossy. Moreover, it is a common practice in optics to denote dielectric material properties using the complex

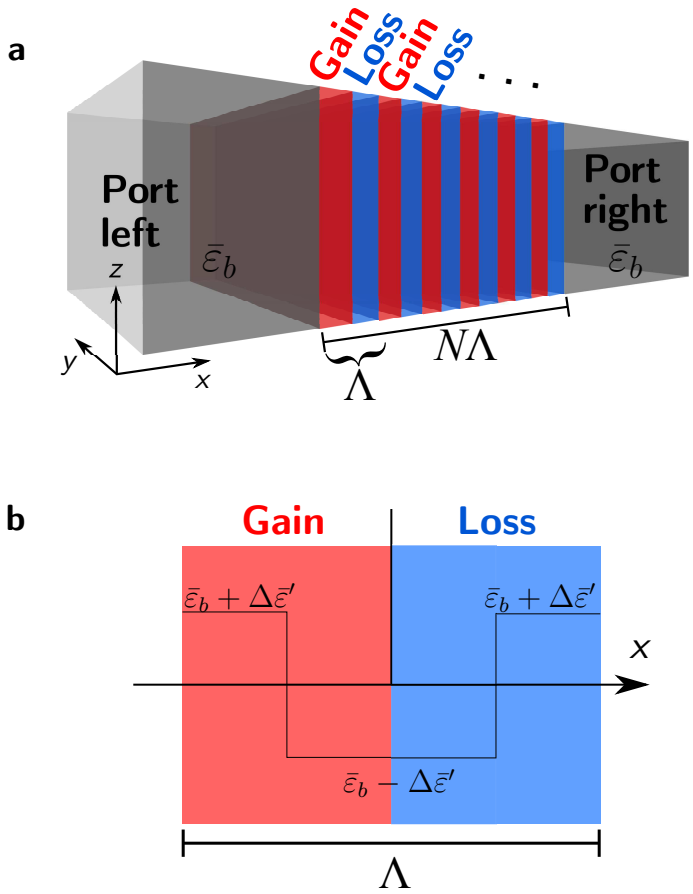

Figure 6.1 | Schematic of $\mathcal{PT}$-Bragg grating structure. (**a**) N-number of period grating in a background material $\bar{\varepsilon}_b$, (**b**) single unit cell of the grating with 2 slightly different dielectric constants $\bar{\varepsilon}_b + \Delta\bar{\varepsilon}'$ and $\bar{\varepsilon}_b - \Delta\bar{\varepsilon}'$.

refractive index, $n = n' + jn''$ which is related to the complex dielectric permittivity by $n = \sqrt{\bar{\varepsilon}(\omega)}$. It is important to note that in this section a small incident signal is considered, hence the saturation effect is negligible and $\mathbb{S} = 1$.

For definiteness, consider a PTBG made of GaAs-based material with the following material parameters used throughout this chapter: the background dielectric constant $\bar{\varepsilon}_b = (3.625)^2$ and modulation of the real-part of dielectric constant $\Delta\bar{\varepsilon}' = (0.02)^2$ as used in [6.1]. The parameter related to the gain/loss material used is similar to that reported in [6.2], in which the atomic transition angular frequency $\omega_\sigma = 2\pi(336.85)$ rad/ps, and time relaxation parameter $\tau = 0.1$ ps. It is here noted that in practice a small change in the dielectric constant $\Delta\bar{\varepsilon}'$ can be achieved by

adjusting a small amount of Ga by Al as in [6.3–6.5]. The PTBG is designed as follows: the grating has $N = 200$ and the Bragg frequency is centred at the atomic transitional frequency $f_B = 336.85$ THz. It follows that the physical length of an unit cell, calculated by (4.1), is $\Lambda = 112.7$ nm.

It is emphasised here that the gain/loss considered in this chapter is different to that in Chapter 4. In Chapter 4 the gain/loss parameter n'' is non-dispersive. In this chapter the gain/loss parameter is dispersive and causal, as such the gain/loss is a function of frequency and the gain/loss causes the real part of the dielectric constant to be dispersive. To quantify, the amount of gain/loss, the gain/loss parameter used is the imaginary part of the refractive index at the atomic transitional frequency which in this case has been associated with the Bragg frequency so that $n''(\omega_\sigma/(2\pi)) = n''(f_B)$. The value of $n''(f_B)$ can be calculated directly by substituting $\omega \to (2\pi f_B)$ to (5.5) and (5.4).

The performance of the PTBG is depicted in Fig. 6.2 for different values of gain/loss. Figure 6.2 considers the transmittance, T, and reflectance for the left, R_L, and right, R_R, incidence for increasing values of gain/loss parameter for (a) a passive structure, (b-f) $n''(f_B) = 0.0045$, 0.015, 0.02, 0.022 and 0.0245. The transmittance T, reflectance left R_L and reflectance right R_R are depicted on the top, middle and bottom panel, respectively. It is noted that the transmission for both left and right incidence, is the same, as for a reciprocal system, and is shown here as T. In contrast to the non-dispersive PTBG structure, depicted in Fig. 4.4, it can be seen from the top panel of Fig. 6.2(d) that for a dispersive PTBG system the unidirectional operation occurs only at a single point. Moreover, the reflectance for left incidence R_L, increases as the gain/loss parameter increases, although in the dispersive case most amplification of R_L occurs at the f_B. A further look at the first five panels on the bottom row of Fig. 6.2, reveals that in general R_R decreases as the gain/loss parameter $n''(f_B)$ increases. In addition, Fig. 6.2(f) shows that for $n''(f_B) = 0.0245$ both transmittance and reflectance approach infinity regardless of the direction of

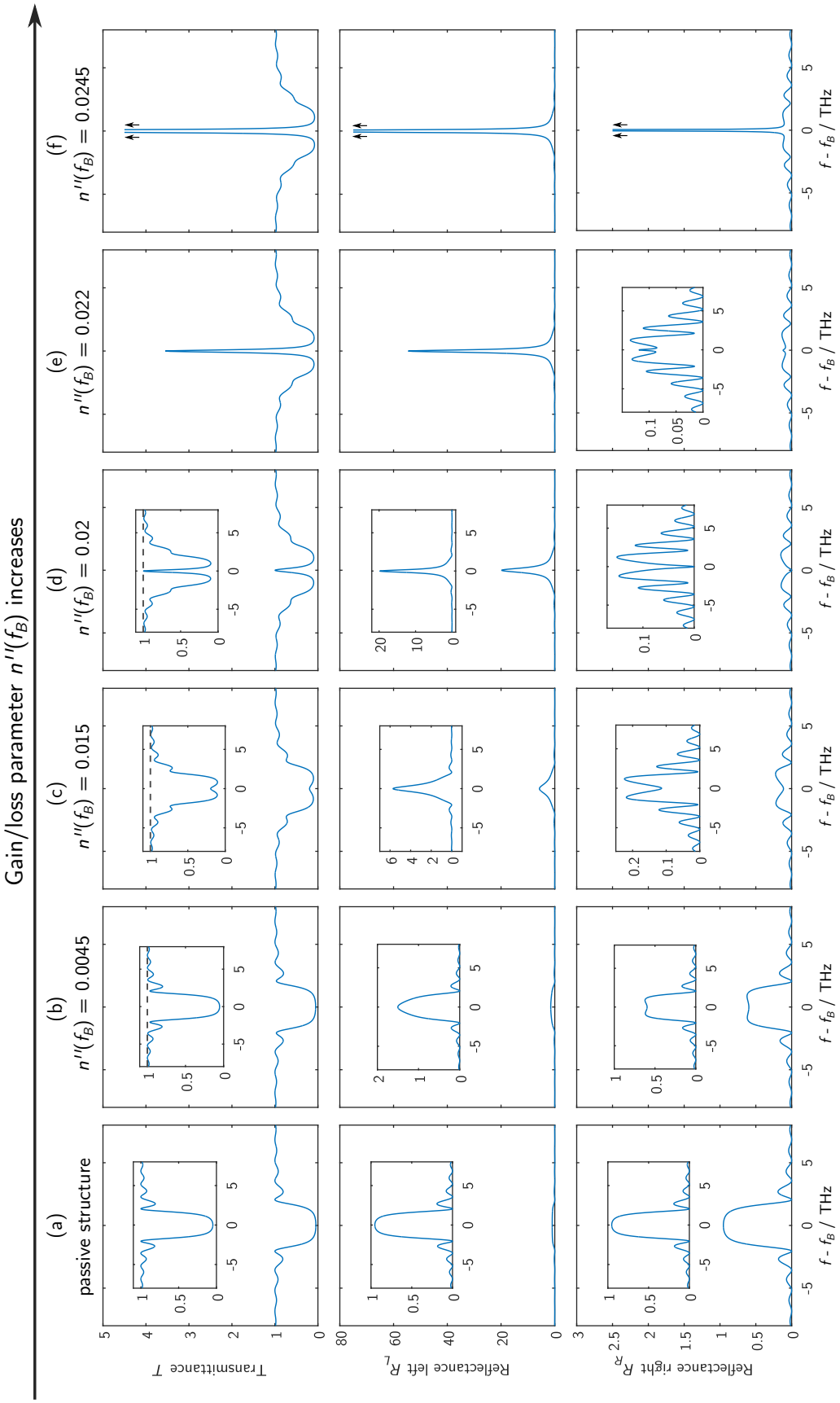

Figure 6.2 | The impact of dispersive gain/loss parameter on the performance of PTBG. The transmittance T, reflectance for the left R_L and right incident R_R are displayed at the top, middle and bottom panel respectively. Six different value of gain/loss parameter: passive structure, $n''(f_B) = 0.0045$, 0.015, 0.02, 0.022 and 0.0245 are considered. The inset shows the magnified spectra.

incidence; operation at this point is related to the CPAL operation case where the spectral singularity occurs.

To further analyse the impact of dispersion upon the spectral performance of the PTBG, Fig. 6.3 plots the conservation relations (4.2) and the magnitude of the eigenvalue of the scattering matrix **S** for different gain/loss parameters as in Fig. 6.2. It was discussed before in Section 4.3 that a $\mathcal{PT}$-symmetric scattering system has to satisfy the generalised conservation relation (4.2) so that the difference between the left and right hand-sides of the equation remains zero. In the dispersive PTBG system, the top panel of Fig. 6.3 shows that the generalised conservation relation only valid at a single frequency f_B.

The bottom panels of Fig. 6.3 show the magnitude of the eigenvalues of the scattering matrix $|s_n|$ where $n = \{1, 2\}$. As a reminder, it was discussed in more detail in Subsections 3.3.2 and Section 4.3 that a $\mathcal{PT}$-symmetric scattering system may undergo a spontaneous symmetry breaking as the gain/loss parameter increases. These different symmetry phases are determined by the magnitude of the eigenvalues of the **S**-matrix, so that in the symmetric phase the eigenvalues are unimodular ($|s_n| = 1$) while in the broken-symmetry phase the eigenvalue is not-unimodular. In the non-dispersive PTBG structure, see Fig. 4.5, it was shown that the eigenvalues of the **S**-matrix are unimodular until a certain value of gain/loss parameter, with operation beyond this point leading to a splitting in the value of $|s|$ which is depicted as "egg-shaped" spectra. In the dispersive PTBG system, it can be seen from the bottom panels of Fig. 6.3 that the eigenvalues are in general not-unimodular even with a small gain/loss parameter; it, however, can be seen in detail from the inset of Fig. 6.3(b, bottom) that at a frequency f_B the eigenvalues are still unimodular for $n'' = 0.0045$. It implies that even with a small amount of gain/loss, the $\mathcal{PT}$-symmetry can occur *only* at a single frequency f_B. From Fig. 6.3(f, bottom), it can be seen that there exists a spectral singularity, which is related to the CPAL point operation, that also appeared in Fig. 6.2 as the transmittance and reflectance

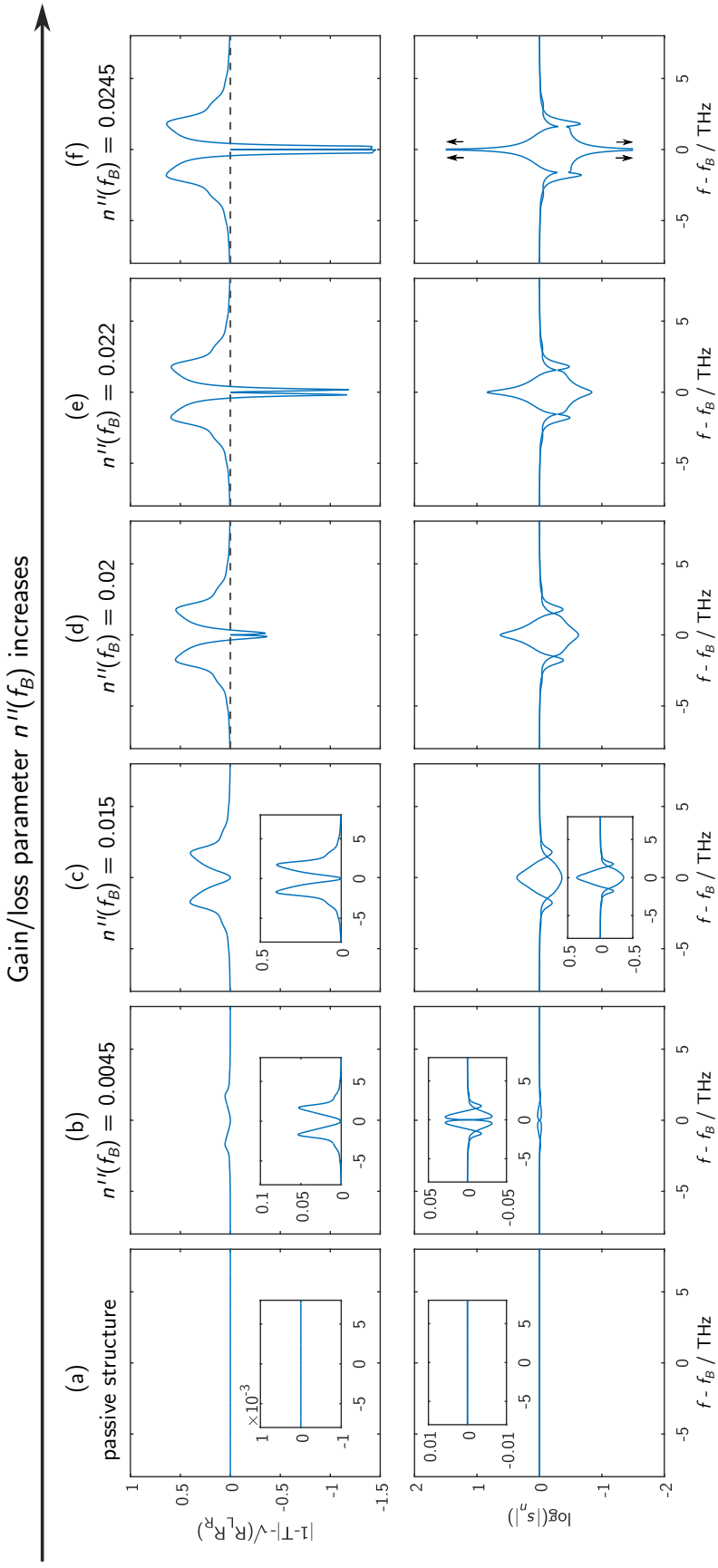

Figure 6.3 | The spectral behaviour of a dispersive PTBG. The top panels show the difference between the left and right terms of generalised conservation relation and the bottom panels show the magnitude of the eigenvalues of the scattering matrix $\mathbf{S}$. Six different value of gain/loss parameters are considered (**a**) passive structure, (**b-f**) $n''(f_B) = 0.0045$, 0.015, 0.02, 0.022 and 0.0245. The insets show the magnified spectra.

coefficients approach infinity.

In order to understand the reason why the $\mathcal{PT}$-symmetric behaviour is only observed at a single isolated frequency in the PTBG structure with a dispersive causal gain/loss medium, recall that a $\mathcal{PT}$-symmetric structure requires a spatially modulated dielectric constant, (See (3.13) and (3.14)), which reproduced below,

$$\bar{\varepsilon}'(-x) = \bar{\varepsilon}'(x), \tag{6.3}$$

$$\bar{\varepsilon}''(-x) = -\bar{\varepsilon}''(x). \tag{6.4}$$

That is, the real part of permittivity has to be an even function in space while the imaginary part is an odd function in space and both condition occur *independently of frequency*. On the other hand, one also needs to consider that the material permittivity has to satisfy the Kramers-Kronig relations[‡], so that the modified Kramers-Kronig is now given by:

$$\varepsilon'(\omega, x) = \varepsilon_0 + \frac{1}{\pi}\ \text{p.v.} \int_{-\infty}^{\infty} \frac{\varepsilon''(\Omega, x)}{\Omega - \omega} d\Omega, \tag{6.5}$$

$$\varepsilon''(\omega, x) = -\frac{1}{\pi}\ \text{p.v.} \int_{-\infty}^{\infty} \frac{\varepsilon'(\Omega, x)}{\Omega - \omega} d\Omega. \tag{6.6}$$

Considering operation at a real frequency ω and substituting $x \to -x$, (6.5) becomes,

$$\varepsilon'(\omega, -x) = \varepsilon_0 + \frac{1}{\pi}\ \text{p.v.} \int_{-\infty}^{\infty} \frac{\varepsilon''(\Omega, -x)}{\Omega - \omega} d\Omega. \tag{6.7}$$

Further, substituting the condition (6.4) into (6.7), it can be shown that

$$\varepsilon'(\omega, -x) = \varepsilon_0 - \frac{1}{\pi}\ \text{p.v.} \int_{-\infty}^{\infty} \frac{\varepsilon''(\Omega, -x)}{\Omega - \omega} d\Omega, \tag{6.8}$$

[‡]Derived in Appendix A

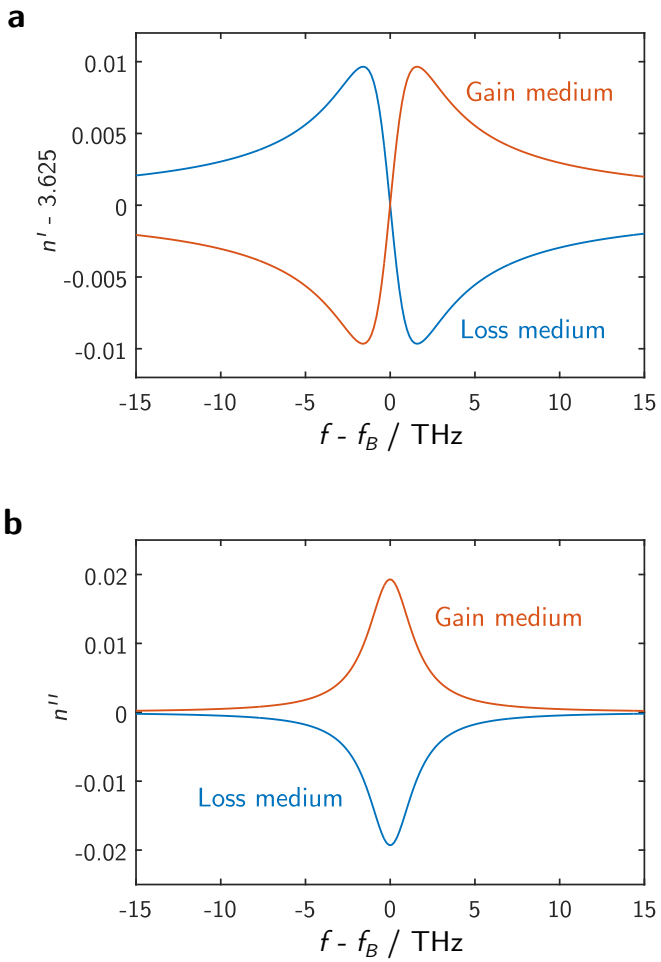

Figure 6.4 | Gain and loss profile of the dispersive gain/loss material model operating at the unidirectional invisibility point. (**a**) The real part and (**b**) the imaginary part of the refractive index.

from which follows the condition of

$$\text{p.v.} \int_{-\infty}^{\infty} \frac{\varepsilon''(\Omega, -x)}{\Omega - \omega} d\Omega = 0. \tag{6.9}$$

Equation (6.9) means that the $\mathcal{PT}$-symmetric condition (6.3) and (6.4) can not be satisfied for an *infinite* frequency interval except for the case of $\varepsilon'(\omega, x) = \varepsilon_0(\omega, x)$ and $\varepsilon''(\omega, x) = 0$, hence a continuous medium without gain (or loss). The conditions (6.3) and (6.4) can, however, be satisfied at a single frequency associated with the resonant behaviour of the medium. Consider the homogeneous gain/loss material model given by (5.3) which are plotted in Fig. 6.4.

Figure 6.4 depicts the real part and the imaginary part of the refractive index of (6.4) using the material parameter of $\bar{\varepsilon} = 1 + \chi_e = (3.625)^2$, atomic transition angular frequency $\omega_\sigma = 2\pi(336.85)$ rad/ps, and time relaxation parameter $\tau = 0.1$ ps, the conductivity peak $\sigma_0 = 211.65$ S/m. These are the same material parameters used to generate Fig. 6.2 and Fig. 6.3. The refractive index of the gain medium is presented with a red line while the refractive index of the loss medium is plotted with a blue line. Figure 6.4(a) shows the impact of generating gain/loss in a medium. It can be seen from this figure that the real part of the refractive index is modulated in the frequency domain, i.e. dispersive.

Meanwhile, the frequency dependence of the imaginary part of the refractive index is depicted in Fig. 6.4(b). It can be seen from this figure that the gain/loss is dispersive, so that a different operation frequency leads to a different gain/loss. It is noted that the notation $n'' < 0$ corresponds to loss while $n'' > 0$ corresponds to gain. For this figure the value of σ_0 has been set to generate a gain/loss parameter $n''(f_B) = 0.02$, i.e. the unidirectional invisibility operation depicted in Fig. 6.2(d). It can be seen from 6.4(a) and 6.4(b) that the $\mathcal{PT}$-symmetric refractive index profile (6.3) and (6.4) can only be satisfied at a single frequency of f_B, i.e. when the modulation of the real part of the refractive index is zero.

6.3 Time-domain Modelling of PTBG Using the TLM Method

This section demonstrates the application of the Transmission-Line Modelling (TLM) method to model the dispersive PTBG structure in the time-domain. It is well-known that in modelling a continuous medium using the TLM method a mesh discretisation condition $\Delta x \leqslant \lambda/10$, where λ is the wavelength inside the medium, is a rule of thumb used to obtain an accurate simulation [6.6]. However in modelling

a deep *sub-wavelength* periodic structure with different materials, like the case of a PTBG structure, the mesh discretisation condition $\Delta x = \lambda/10$ is not enough to provide an accurate representation of the multi-layered structure [6.7,6.8].

In order to demonstrate the dependence between the accuracy of the TLM method to model a PTBG structure with the discretisation parameter, the spectral performance of a PTBG under unidirectional invisibility operation is shown in Fig. 6.5. The unidirectional operation point here refers to the operation when the real part modulation of the refractive index is equal to the gain/loss parameter. The analytical calculation using the Transfer-matrix (T-matrix) method at this operation point is displayed in Fig. 6.2(d).

Figure 6.5(a-c) shows the transmittance T, reflectance left R_L and reflectance right R_R of PTBG operating at the unidirectional invisibility point. The PTBG structure for the TLM simulation is designed and made using the same material parameters as described in Section 6.2 and is set to operate at the unidirectional invisibility point, i.e. the peak conductivity $|\sigma_0| = 211.65$ S/m is used. Moreover, the TLM simulation is excited using a single Gaussian pulse function modulated at $f = f_B$ with FWHM 20 ps. Different mesh discretisation parameters are used, i.e. $\Delta x = \lambda/24$ and $\lambda/96$ where λ is the wavelength in the medium $\lambda = \lambda_0/n_b$, to demonstrate the impact of discretisation on the spectra of the scattered light. The TLM simulation is run for 9 ps, which ensured that all of the signal has passed through the structure and provided a sufficient frequency-domain resolution. The frequency domain response is obtained by Fourier transformation of the time-domain signal. For reference, results from the analytic T-matrix method are included in the figure.

Consider the frequency response of the TLM simulation with $\Delta x = \lambda/24$, plotted with the green lines. It can be seen from Fig. 6.5 that the spectral response for this case is shifted to a lower frequency compared to the analytical results, this shifting is usually referred to as a *red-shifting* error. The occurrence of the red-shifting

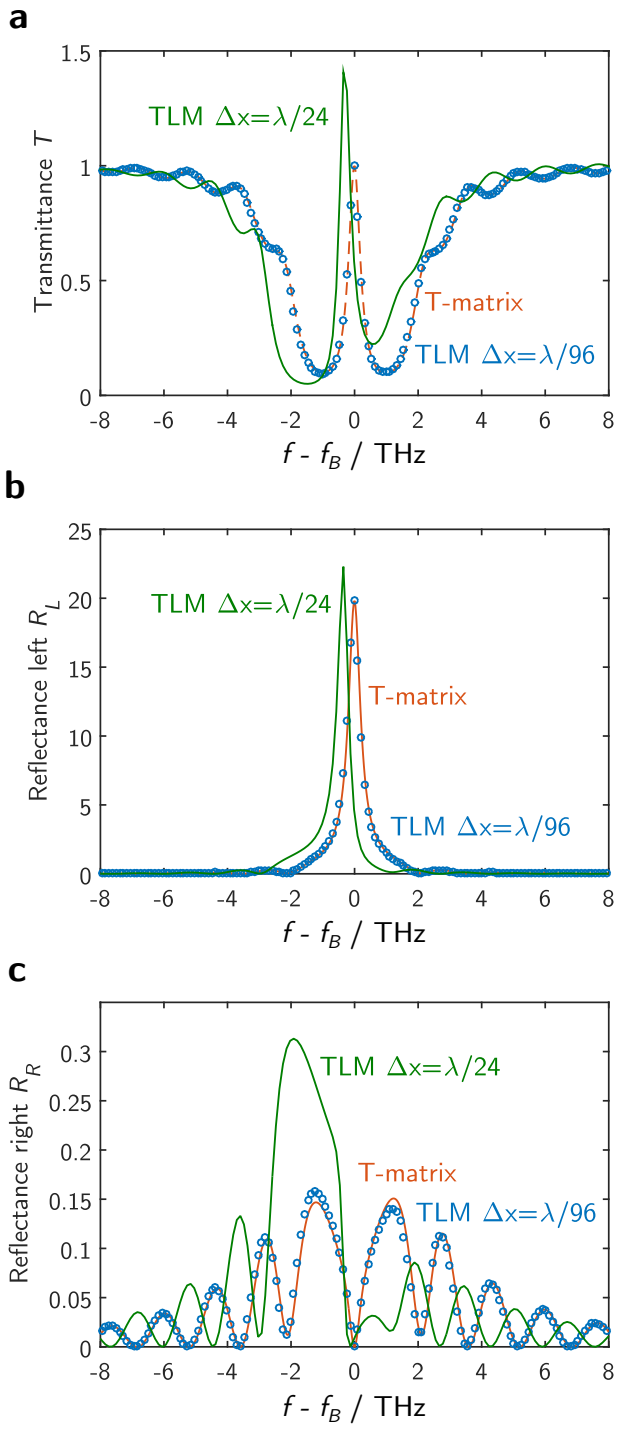

Figure 6.5 | The impact of TLM mesh discretisation on the spectral response of a PTBG. The (**a**) transmittance, (**b**) reflectance left R_L and (**c**) reflectance right R_R of PTBG with dispersive gain/loss. For reference results from the analytic T-matrix method is also included.

error can be explained as a result of increased numerical dispersion created by the unphysical spatial discretisation process; this is a well-known source of error in any numerical method involving spatial discretisation [6.6,6.7,6.9]. Moreover, it can be seen that when Δx is not fine enough, not only is the spectra red-shifted, but the amplitudes are also modified significantly.

Now, consider the spectral response for the TLM simulation with $\Delta x = \lambda/96$ which is plotted by the blue coloured circle bullet points. The spectral response for this mesh discretisation parameter agrees well with the analytical result both in frequency and in amplitude. It can be seen that modelling a PTBG using the TLM method requires a fine discretisation parameter Δx in order to guarantee the accuracy of the TLM simulation. For that reason, a discretisation parameter of $\Delta x = \lambda/96$ will be used in the next section to demonstrate a switching application of a PTBG by using the TLM method.

6.4 A Temporal Optical Switch Using the $\mathcal{PT}$-Symmetric Bragg Grating

This section investigates the transient and dynamic behaviour of a $\mathcal{PT}$-Bragg grating where the gain is suddenly introduced into parts of the system. Practically, it can be done by suddenly turning on a gain pumping current or optical beam while masking the loss region. The PTBG considered in this section is as described in Fig. 6.1 and studied in the previous section.

The structure is excited with a continuous wave (CW) of constant amplitude at the Bragg frequency $f = f_B$. The choice of input signal amplitude ensures that the $\mathcal{PT}$-Bragg grating operates in the linear regime, i.e. the effect of gain saturation is negligible, $\mathbb{S} = 1$.

The scenario that is modelled is as follows: initially, the Bragg grating is assumed to be uniformly lossy $n''(f_B) = -0.02$, i.e. the gain pumping is off, throughout for a 5 ps duration, under which conditions the Bragg grating has a stop band centred at the Bragg frequency f_B. After the 5 ps duration, the gain is introduced as might be achieved practically by turning on the gain pumping in the gain section while masking the loss sections. After another 5 ps the same temporal switching pattern is then repeated.

Figure 6.6 shows the time-domain response for the input-normalised transmitted and reflected signal of the PTBG optical switch for the left and right excitations. Figure 6.6(a) shows the input-normalised incident signal, (b and c) the transmitted and reflected signal when the grating is excited from the left and (d and e) the transmitted and reflected signal when the grating is excited from the right. It can be seen that the transmitted signal switches from nearly 0 to ≈ 1 over a transient period of less than 1 ps.

Figure 6.6(c and e) show that the reflected signal for left incidence has increased in the presence of gain but that the reflected signal for the right incident has sharply reduced to almost zero. The time-domain simulation results confirm that when the gain pumping beam is turned on, the grating transforms to a PTBG operating at the unidirectional invisibility point, and when excited from the right, its response will change from purely reflective to all transmitting and thus exhibit a switch-like behaviour. It is also emphasized that this is achieved when the grating is operated at the Bragg frequency f_B with a background medium of n_b and is the first demonstration of a temporal $\mathcal{PT}$-Bragg grating switch using a numerical time-domain code [6.10]. Moreover, Fig. 6.6 demonstrates that switching on gain in the grating in the real-time triggers a switch-like response from the grating.

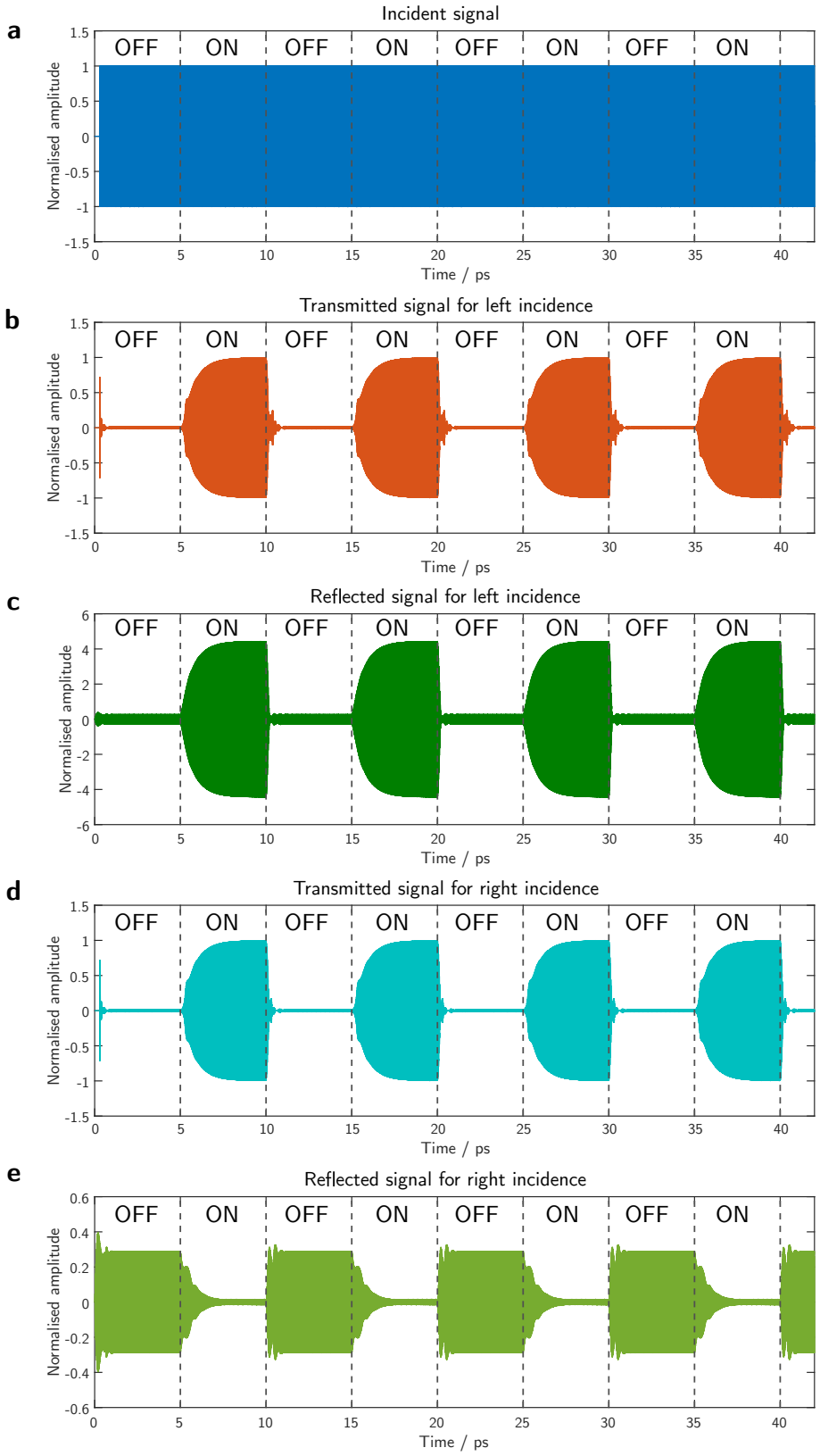

Figure 6.6 | Switching application of PTBG in time-domain. Time-domain response of the (**a**) incident signal, (**b**) transmitted signal amplitude, (**c**) reflected signal amplitude for left incidence, (**d**) transmitted signal amplitude and (**e**) reflected signal amplitude for right incidence.

6.5 Summary

The chapter demonstrated the impact of dispersion on the performance of a PTBG when realistic causality properties of gain/loss medium are considered. It was shown that the dispersion causes the $\mathcal{PT}$-symmetric condition to be satisfied only at a single frequency and hence the $\mathcal{PT}$-symmetry behaviour, including $\mathcal{PT}$-symmetry transition, unidirectional invisibility and spectral singularity, can only be observed at a single frequency.

Moreover, the chapter demonstrated the application of the numerical TLM time-domain method to model $\mathcal{PT}$-Bragg gratings with a dispersive and causal gain material model in time-domain. The results presented shown that an optical switch can be engineered by suddenly switching on the gain pumping in the grating and ensuring that the grating is operating in the linear regime. The switching operation is possible when the grating operates at the unidirectional invisibility point and is excited from the right side with total transmission and almost zero back reflection.

References

[6.1] S. Phang, A. Vukovic, H. Susanto, T. M. Benson, and P. Sewell, "Impact of dispersive and saturable gain/loss on bistability of nonlinear parity-time Bragg gratings," Opt. Lett. **39**, 2603–6 (2014).

[6.2] S. C. Hagness, R. M. Joseph, and A. Taflove, "Subpicosecond electrodynamics of distributed Bragg reflector microlasers: Results from finite difference time domain simulations," Radio Sci. **31**, 931–941 (1996).

[6.3] S. Adachi, "Optical dispersion relations for GaP, GaAs, GaSb, InP, InAs, InSb, Al xGa1-xAs, and In1-xGaxAs yP1-y," J. Appl. Phys. **66**, 6030–6040 (1989).

[6.4] J. Aitchison, D. Hutchings, J. Kang, G. Stegeman, and a. Villeneuve, "The nonlinear optical properties of AlGaAs at the half band gap," IEEE J. Quantum Electron. **33**, 341–348 (1997).

[6.5] D. E. Aspnes, S. M. Kelso, R. A. Logan, and R. Bhat, "Optical properties of AlxGa1x As," J. Appl. Phys. **60**, 754 (1986).

[6.6] C. Christopoulos, *The Transmission-Line Modeling Method TLM* (IEEE Press, Piscataway, 1995).

[6.7] V. Janyani, J. Paul, A. Vukovic, T. Benson, and P. Sewell, "TLM modelling of nonlinear optical effects in fibre Bragg gratings," IEE Proc. - Optoelectron. **151**, 185 (2004).

[6.8] S. Phang, A. Vukovic, H. Susanto, T. Benson, and P. Sewell, "Time domain modeling of all-optical switch based on PT-symmetric Bragg grating," in "29th Annu. Rev. Prog. Appl. Comput. Electromagn.", (Applied Computational Electromagnetics Society, Monterey, CA, 2013), pp. 693–698.

[6.9] A. Taflove and S. C. Hagness, *Computational Electrodynamics: The Finite-Difference Time-Domain Method* (Artech House, New York, NY, 2005), 3rd ed.

[6.10] S. Phang, A. Vukovic, H. Susanto, T. M. Benson, and P. Sewell, "Ultrafast optical switching using paritytime symmetric Bragg gratings," J. Opt. Soc. Am. B **30**, 2984–2991 (2013).

7

Non-Linear and Dispersive Parity-Time Bragg Grating for Optical Signal Processing Applications

This chapter focuses on the impact of non-linearity in a realistic scenario when the gain/loss medium within the PT-Bragg Grating (PTBG) is dispersive and saturable. For that reason, the TLM model will be extended further to include a non-linear material model. The chapter demonstrates the bistable properties of a PTBG and studies the impact of the interplay between the non-linearity and saturation properties of gain/loss material. The interplay of non-linearity and $\mathcal{PT}$-behaviour is investigated on two different types of Bragg grating structures. Furthermore, practical applications of non-linear PTBG as a memory and logical gate device are also demonstrated.

* * *

7.1 TLM Model for Non-Linear Medium

The alternative formulation of the TLM method based upon the $\mathcal{Z}$-transformation has been developed to model a realistic dispersive gain/loss model in Chapter 6. This section will extend the TLM model further to also include the non-linear property of a material.

As found in practice, the interaction between light and matter is non-linear. These non-linear interactions are usually manifested in various physical phenomena, such as: optical rectification, Pockels effect, optical Kerr effect, photo-thermal effect, two-photon absorption, etc [7.1–7.3]. In most cases, non-linear interactions can be classified as second-order or third-order non-linearity effects. It is worth commenting that although there are higher orders of non-linearity, they are very small and typically ignored [7.1–7.3].

Various mathematical models have been developed to incorporate these non-linearity effects within a numerical framework [7.4–7.6]. As for Kerr-type non-linearity it usually has been assumed that the non-linearity interaction is non-causal [7.1–7.4]. In this thesis, a dispersive and causal non-linear material model, namely the Duffing material model [7.6–7.12], is implemented within the TLM method. The non-linear Duffing material model has been extensively used to model a particular class of non-linear dispersive materials accurately and with no-instabilities [7.6,7.10–7.13].

7.1.1 Duffing Model of Non-Linear Medium

It is known that material response to an electromagnetic excitation is non-linear. Mathematically, the non-linear interactions can be described by the polarisation of the material which behaves in a non-linear manner in the presence of strong optical electric field [7.1–7.4,7.14,7.15]. As such one can expand the dielectric polarisation

in terms of its linear and non-linear terms as [7.4,7.14],

$$\boldsymbol{P}_e = \underbrace{\chi_{eL}|\boldsymbol{E}|}_{\boldsymbol{P}_L} + \underbrace{\chi_e^{(2)}|\boldsymbol{E}|^2 + \chi_e^{(3)}|\boldsymbol{E}|^3 + \cdots}_{\boldsymbol{P}_{NL}} \tag{7.1}$$

In (7.1), $\boldsymbol{P}_L$ denotes the linear polarisation while $\boldsymbol{P}_{NL}$ represents the non-linear dielectric polarisation interaction, which may include different orders of non-linearity. Consider that the non-linear polarisation $\boldsymbol{P}_{NL}$ is modelled through the Duffing polarisation $\boldsymbol{P_D}$ [7.6,7.7,7.10–7.13],

$$\frac{\partial^2 \boldsymbol{P_D}}{\partial t^2} + 2\delta\frac{\partial \boldsymbol{P_D}}{\partial t} + \omega_{0D}^2 \boldsymbol{P_D} f_D\left(\boldsymbol{P_e}\right) = \varepsilon_0 \Delta\chi_{e0}\omega_{0D}^2 \boldsymbol{E} \tag{7.2}$$

where, $\boldsymbol{P_D}$ and $\boldsymbol{E}$ are the Duffing non-linear polarisation and electric field vector quantities which are both functions of space and time. The parameters ω_{0D} and δ are related to the Duffing polarisation angular resonant frequency and the damping constant, $\Delta\chi_{e0}$ denotes the dielectric susceptibility measured at the zero frequency (DC). The function $f_D\left(\boldsymbol{P_e}\right)$ denotes the non-linear terms of the Duffing polarisation which depend on the total dielectric polarisation $\boldsymbol{P_e}$. The application of the Duffing equation to model non-linear material properties has been extensively analysed and shown to be superior to the Kerr model of a non-linear material [7.6–7.13]. It is mainly due to the fact that the Duffing model incorporate both the non-linear and dispersive nature of the material response and thus is closer to realistic material properties [7.6,7.8–7.13].

For the case of a one-dimensional problem, with the electric field polarised in the y-direction, the Duffing equation (7.2) can be simplified to,

$$\frac{\partial^2 P_{Dy}}{\partial t^2} + 2\delta\frac{\partial P_{Dy}}{\partial t} + \omega_{0D}^2 P_{Dy} f_D\left(P_{ey}\right) = \varepsilon_0 \Delta\chi_{e0}\omega_{0D}^2 E_y. \tag{7.3}$$

For the particular case of $f_D\left(P_{ey}\right) = 1$, the Duffing polarisation is linear and dispersive with a Lorentzian type of dispersion and, by performing a Fourier transformation

the complex dielectric permittivity, can be obtained as,

$$\varepsilon(\omega) = \frac{\mathcal{P}_{Dy}}{\mathcal{E}_y} = \frac{\Delta\chi_{e0}\omega_{0D}^2}{2j\delta\omega + (\omega_{0D}^2 - \omega^2)}\varepsilon_0, \quad \text{when} \quad f_D = 1. \tag{7.4}$$

In (7.4) the field quantities $\mathcal{P}_{Dy}$ and $\mathcal{E}_y$ are the Fourier transformed Duffing polarisation P_{Dy} and electric field E_y which are both complex.

For the more general case of non-linear problem, $f_D\left(P_{ey}\right) \neq 1$, different non-linear functions $f_D\left(P_{ey}\right)$ have been used and analysed such as in [7.6,7.8–7.13],

$$\text{Exponential non-linearity}: \quad f_D\left(P_{ey}\right) = e^{\alpha|P_{ey}|^2}, \tag{7.5}$$

$$\text{Polynomial non-linearity}: \quad f_D\left(P_{ey}\right) = 1 + \alpha|P_{ey}|^2, \tag{7.6}$$

where, α denotes the Duffing non-linearity parameter, so that $\alpha = 0$ defines the linear case. It is important to note that the polynomial non-linearity function (7.6) is an approximation of the exponential non-linear function (7.5). It can be seen that by expanding the exponential function in a Taylor's series,

$$e^x = \sum_{k=0}^{\infty} \frac{x^k}{k!} = 1 + x + \frac{x^2}{2!} + \frac{x^3}{3!} + \cdots, \tag{7.7}$$

the polynomial non-linearity function (7.6) is only the first two terms of the Taylor expansion of the exponential non-linearity (7.5). This approximation is valid only for small values of P_{ey}. Furthermore, the polynomial approximation of the Duffing non-linear polarisation shows an association with the Kerr-type non-linearity.

Hence, consider the Kerr non-linear effect which is typically expressed as the instantaneous perturbation of the real part of the refractive index as

$$n(t) = n_L \pm n_2 I(t), \tag{7.8}$$

where n_L denotes the constant linear refractive index which is the total of the asymp-

totic contribution at DC and infinity, $n_L = \sqrt{\chi_{e\infty} + \Delta\chi_{e0} + 1}$. The Kerr non-linear constant n_2 is given in units of $\mathrm{m}^2/\mathrm{Watt}$. The parameter I is the instantaneous intensity which is given previously by (5.45) and reproduced here,

$$I = \frac{1}{2}\frac{E_y^2}{\eta}, \quad \text{where} \quad \eta = \frac{\eta_0}{n_L}. \tag{7.9}$$

where $\eta_0 = \sqrt{\mu_0/\varepsilon_0}$ is the free-space impedance of a normal propagating electromagnetic waves. The total dielectric polarisation in the presence of instantaneous Kerr non-linearity is,

$$P_{ey} = \varepsilon_0(n^2(t) - 1)E_y \tag{7.10}$$

which can be approximated by,

$$P_{ey} \approx \varepsilon_0(n_L^2 - 1)E_y + 2\varepsilon_0 n_L n_2 I E_y, \quad \text{since} \quad (n_2 I)^2 \to 0. \tag{7.11}$$

Expanding the linear refractive index, the dielectric polarisation can be expressed as,

$$P_{ey} = \varepsilon_0 \left(\chi_{e\infty} + \Delta\chi_{e0}\right) E_y + 2\varepsilon_0 n_L n_2 I E_y \tag{7.12}$$

By substituting the intensity I defined in (7.9) to (7.12) and comparing it to (7.1), the dielectric susceptibility can be obtained as,

$$\chi_{eL} = (\chi_{e\infty} + \Delta\chi_{e0})\varepsilon_0, \tag{7.13}$$

$$\chi_e^{(3)} = \frac{(\chi_{e\infty} + \Delta\chi_{e0} + 1)\, n_2}{\eta_0}\varepsilon_0, \tag{7.14}$$

where, $\chi_e^{(3)}$ denotes the Kerr non-linear susceptibility constant.

In order to find the association between the Duffing non-linearity and the Kerr non-linearity, consider a dispersion-less non-linear Duffing polarisation by substituting

$\partial P_{Dy}/\partial t \to 0$ into (7.3). The dielectric polarisation can be obtained as,

$$f_D(P_{ey})P_D = \varepsilon_0 \Delta\chi_{e0} E_y \tag{7.15}$$

By substituting the polynomial approximation for non-linear polarisation (7.6) it can be shown that,

$$P_{ey} + \alpha P_{ey}^2 (P_{ey} - P_\infty) = \varepsilon_0(\chi_{e\infty} + \Delta\chi_{e0})E_y, \tag{7.16}$$

where $P_\infty = \varepsilon_0 \chi_{e\infty} E_y$ is the asymptotic polarisation contribution at the infinity. By direct comparison of (7.16) and (7.12), the relation between the Duffing non-linear parameter α and the Kerr non-linear parameter n_2 at the small-signal excitation can be found as,

$$\alpha = -\frac{n_L^2 n_2}{\varepsilon_0^2 \eta_0 (\chi_{e\infty} + \Delta\chi_{e0})^2 \Delta\chi_{e0}} \quad \text{where,} \quad n_L^2 = \chi_{e\infty} + \Delta\chi_{e0} + 1 \tag{7.17}$$

For comparison, the total dielectric polarisation P_{ey} is plotted as a function of electric field E_y in Fig. 7.1 for (a) positive sign and (b) negative sign of Kerr non-linearity. In Fig. 7.1(a,b) the dielectric polarisation is plotted for three functions of non-linearity, i.e. Kerr non-linearity, exponential and polynomial Duffing non-linearity. The linear polarisation, $P_{ey} = \varepsilon_0(\chi_{e\infty} + \Delta\chi_{e0})E_y$, is plotted for reference. Material parameters typical of GaAs-based material are used [7.16], with DC dielectric susceptibility $\chi_{e0} = 7.5$, susceptibility at infinity $\chi_{e\infty} = 2.5$ and the Kerr non-linear parameter $n_2 = 2 \times 10^{-17}$ m^2/W [7.17–7.19].

It can be seen from Fig. 7.1 that, for both the cases of positive and negative values of n_2, for a small signal excitation the non-linear polarisation response for all three different functions of non-linearity agree very well. However as electric field excitation increases the non-linear dielectric polarisation responses start to deviate. For the positive Kerr parameter from Fig. 7.1(a) it can be seen that the Duffing

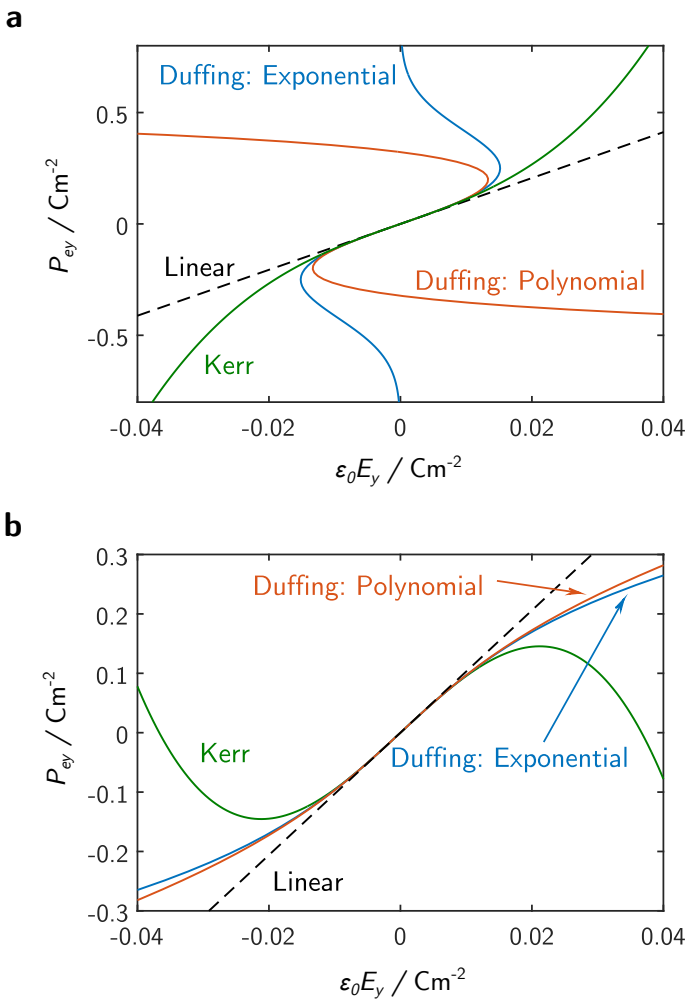

Figure 7.1 | Non-linear relation between dielectric polarisation P_{ey} and electric field E_y. (**a**) Posivitive and (**b**) negative sign of Kerr non-linear parameter n_2 are considered. Three different non-linearities such as, Kerr non-linear polarisation and Duffing with exponential and polynomial non-linear polarisation are considered.

with exponential non-linearity and polynomial have very different responses. It is important to note that the polarisation for the Duffing non-linearity with positive Kerr parameter is double valued for both exponential and polynomial non-linearity. This may cause instability when used in a numerical code at high signal excitation intensity, however such high intensity is beyond a practical setting [7.10–7.12].

For the negative Kerr parameter n_2 the dielectric polarisation plotted in Fig. 7.1(b) shows that for strong-signal excitation the polarisation with the Duffing non-linearity saturates. On the other hand the Kerr non-linearity does not saturate for strong-

signal excitation which can cause instablilities in the numerical implementation [7.10–7.12].

Throughout this thesis, the Duffing model with exponential non-linearity is used considering the fact that the polynomial non-linearity is an approximation of the exponential non-linearity in the small signal limit.

7.1.2 Implementation of Non-Linear Duffing Material Within the TLM Framework in $\mathcal{Z}$-Domain

In this subsection, the digital filter design of Duffing non-linear polarisation model (7.3) is developed and implemented within the TLM algorithm. The 1D Duffing polarisation equation is reproduced below,

$$\frac{\partial^2 P_{Dy}}{\partial t^2} + 2\delta \frac{\partial P_{Dy}}{\partial t} + \omega_{0D}^2 P_{Dy} f_D\left(P_{ey}\right) = \varepsilon_0 \Delta \chi_{e0} \omega_{0D}^2 E_y \tag{7.18}$$

After normalisation of the electromagnetic quantities (described in Subsection 5.3.2), the normalised Duffing model is given by,

$$\frac{\partial^2 p_{Dy}}{\partial T^2} + K_{D1} \frac{\partial p_{Dy}}{\partial T} + K_{D2} p_{Dy} f_D\left(p_{ey}\right) = K_{D3} V_y \tag{7.19}$$

where, p_{Dy} is the normalised Duffing polarisation and is defined by $p_{Dy} = -\dfrac{P_{Dy}\Delta x}{\varepsilon_0}$. The dimensionless constants in (7.19) are defined as,

$$\begin{aligned} K_{D1} &= 2\delta\Delta t, \\ K_{D2} &= \left(\omega_{0D}\Delta t\right)^2, \\ K_{D3} &= \Delta\chi_{e0}\left(\omega_{0D}\Delta t\right)^2. \end{aligned}$$

where, δ and ω_{0D} are the Duffing polarisation damping and angular resonant frequency respectively, and Δt is the TLM time-step. By an application of the bilinear $\mathcal{Z}$-transform on the normalised Duffing model,

$$\frac{\partial}{\partial T} \rightarrow 2\frac{1-z^{-1}}{1+z^{-1}},$$

and after some re-arrangement, the Duffing model in the $\mathcal{Z}$-domain is given by,

$$p_{Dy}K_{D4} + p_{Dy}K_{D2}f_D\left(p_{ey}\right) + z^{-1}S_{D1} = K_{D3}V_y, \tag{7.20}$$

where,

$$K_{D4} = \left(4 + 2K_{D1}\right), \tag{7.21}$$

$$S_{D1} = \left[p_{Dy}\left(-8 + 2K_{D2}f_D\right) - 2K_{D3}V_y\right] + z^{-1}S_{D2}, \tag{7.22}$$

$$S_{D2} = \left[p_{Dy}\left(4 - 2K_{D1} + K_{D2}f_D\right) - K_{D3}V_y\right]. \tag{7.23}$$

The normalised non-linear Duffing exponential function is given by,

$$f_D\left(p_{ey}\right) = e^{\alpha|p_{ey}|^2} \tag{7.24}$$

with the Duffing non-linear parameter α as given in (7.17). The main result of this section is the transcendental non-linear polarisation (7.20) which will be solved simultaneously within the TLM scheme by an iteration method.

For this reason, the 1D-TLM scattering equation (5.40), is reproduced below as,

$$2V_y^r = 2V_y + g_eV_y + 2\left(\frac{1-z^{-1}}{1+z^{-1}}\right)p_{ey} \tag{7.25}$$

Upon substituting the normalised expanded dielectric polarisation,

$$p_{ey} = p_\infty + p_{Dy} = \chi_{e\infty}V_y + p_{Dy}. \tag{7.26}$$

and multiplying both side by $(1+z^{-1})$, (7.25) can also be expressed as,

$$2\left(V_y^r - V_y\right)\left(1+z^{-1}\right) = \left(1+z^{-1}\right) g_e V_y + 2\left(1-z^{-1}\right)\left(\chi_{e\infty} V_y + p_{Dy}\right) \tag{7.27}$$

By substituting the dispersive conductivity model (5.37), (7.27) becomes

$$\begin{aligned} 2\left(V_y^r - V_y\right)\left(1+z^{-1}\right) = \\ \left\{g_{e0} + z^{-1}(g_{e1} + \bar{g}_e(z))\right\} V_y + 2\left(1-z^{-1}\right)\left(\chi_{e\infty} V_y + p_{Dy}\right). \end{aligned} \tag{7.28}$$

By grouping the present and past variables in (7.28), it can be shown that

$$2V_y^r + z^{-1}\left(2V_y^r + K_{e1} V_y - \bar{g}_e(z) V_y + 2p_{Dy}\right) = K_{e2} V_y + 2p_{Dy}, \tag{7.29}$$

where the constants are defined as,

$$K_{e1} = -(2 + g_{e1} - 2\chi_{e\infty}), \tag{7.30}$$

$$K_{e2} = 2 + g_{e0} + 2\chi_{e\infty}. \tag{7.31}$$

By further calling the sum of all the past variables in (7.29) as,

$$S_{ey} = 2V_y^r + K_{e1} V_y + S_{ec} + 2p_{Dy} \tag{7.32}$$

$$S_{ec} = -\bar{g}_e(z) V_y \tag{7.33}$$

Equation (7.29) can be simplified further as,

$$K_{e2} V_y + 2p_{Dy} = 2V_y^r + z^{-1} S_{ey} \tag{7.34}$$

The equations (7.34) and (7.20) are two coupled equations with two unknown vari-

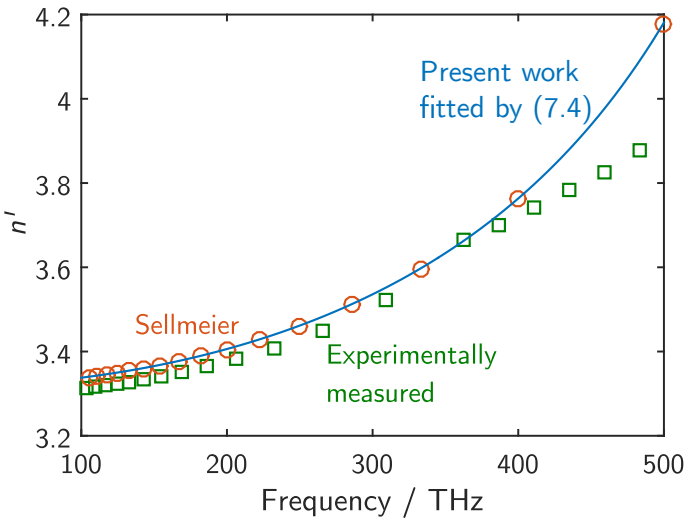

Figure 7.2 | Refractive index profile of GaAs-based material. The experimentally measured (square bullets) refractive index of GaAlAs based alloy material from [7.21,7.22], Sellmeier model (circle bullets) for typical GaAs-based material taken from [7.23] and the present model (solid line) using (7.4).

ables V_y and p_{Dy},

$$\begin{cases} K_{e2}V_y + 2p_{Dy} = 2V_y^r + z^{-1}S_{ey} \\ K_{D3}V_y = p_{Dy}K_{D4} + p_{Dy}K_{D2}f_D + z^{-1}S_{D1} \end{cases}$$

which are now ready to be solved simultaneously for p_{Dy} by an iterative method, e.g. either the Newthon-Rhapson or Bi-section methods [7.20]. The nodal voltage V_y can be subsequently obtained by substituting the solved p_{Dy} back into (7.34).

7.2 Bistability of a Non-linear Bragg Grating

This section demonstrates the application of the TLM method with the non-linear Duffing model to simulate the bistablity property of a Bragg grating based on GaAs material. In this section, a non-linear Bragg grating is first studied to familiarise the reader with the concept of non-linear operation and its modelling procedures.

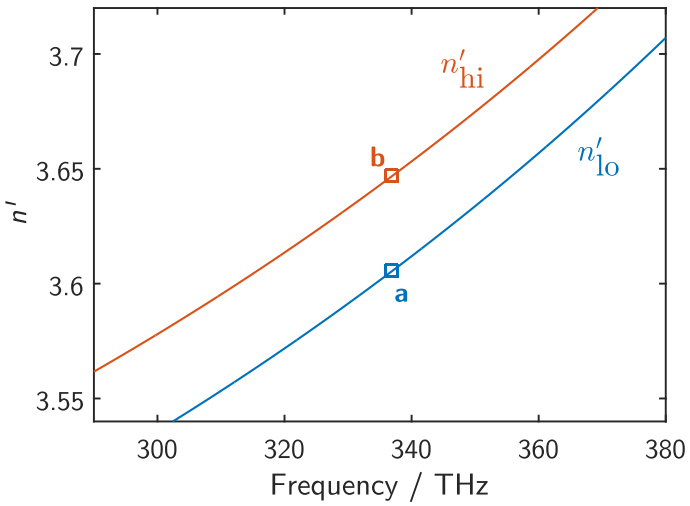

Figure 7.3 | Refractive index of 2 slightly different refractive index GaAs materials.

The material dispersion (7.4) is used to model a GaAs-based material. Figure 7.2 plots the experimentally measured refractive index of AlGaAs-based alloy reported in [7.21,7.22], the approximate Sellmeier model of typical GaAs material taken from [7.23] and the fitted refractive index obtained by using (7.4). For modelling purposes, the material dispersion (7.4) is fitted to the approximate Sellmeier model of typical GaAs taken from [7.23] for the frequency range of interest of around 337 THz. From that process the following constants are obtained: dielectric susceptibility at infinity $\chi_{e\infty} = 2.5$, the Duffing material parameter $\Delta\chi_{e0} = 7.5$, $\delta = 0.0923$ rad/ps and $\omega_{0D} = 4614.4$ rad/ps.

Furthermore in order to create a grating with two slightly different refractive indices, a variant of GaAs-based material with a higher refractive index is assumed to be obtained by adjusting the concentration of Ga-Al within the $\mathrm{Al_xGa_{1\text{-}x}As}$ alloy is varied as was done in [7.22]. In Fig. 7.3, the real part of the refractive indices are depicted within the frequency range of interest; the higher refractive index profile is denoted by n'_{hi} while the lower refractive index denoted by n'_{lo}. It can be seen from Fig. 7.3 that n'_{hi} has a higher refractive index with parallel profile to that n'_{lo}; this parallel spectral profile is a typical behaviour when there is only a small change in the Al-Ga concentration ratio, as is reported in [7.22]. For modelling purposes, the

parameters used to generate of both n'_{hi} and n'_{lo} profiles are summarised in Table 7.1.

Based on these two variants of GaAs-based materials, a non-linear Bragg grating is designed and modelled. For a clearer picture, Fig. 7.4 illustrates the structure considered which is embedded in a background material with a linear and dispersionless refractive index n_b. The structure has a total length of $N\Lambda$, where Λ denotes the physical length of an unit cell of the grating and N is the total number of unit cells. The refractive index in a single period, n_G, along the propagation direction x shown in Fig. 7.4, can be expressed as,

$$n_G(x,\omega,I,t) = \begin{cases} n_{\text{hi}}(\omega) + n_2 I(x,t), & x < \dfrac{\Lambda}{4} \\ n_{\text{lo}}(\omega) + n_2 I(x,t), & \dfrac{\Lambda}{4} \leq x < \dfrac{\Lambda}{2} \\ n_{\text{lo}}(\omega) + n_2 I(x,t), & \dfrac{\Lambda}{2} \leq x < \dfrac{3\Lambda}{4} \\ n_{\text{hi}}(\omega) + n_2 I(x,t), & \dfrac{3\Lambda}{4} \leq x < \Lambda \end{cases} \tag{7.35}$$

It can be seen from (7.35) that the grating is non-linear denoted by the Kerr non-linearity parameter n_2, which is modelled through the Duffing non-linear exponential polarisation as described in the previous section. Parameter I is the input beam intensity calculated by (7.9).

Furthermore, the grating is designed for a Bragg frequency of $f_B = 336.85$ THz

Table 7.1 | Material parameters used to model non-linear Bragg grating.

Parameters	Low refractive index	High refractive index
$\chi_{e\infty}$	2.5	2.8
$\Delta\chi_{e0}$	7.5	7.5
δ (rad/ps)	0.0923	0.0923
ω_{0D} (rad/ps)	4614.4	4614.4

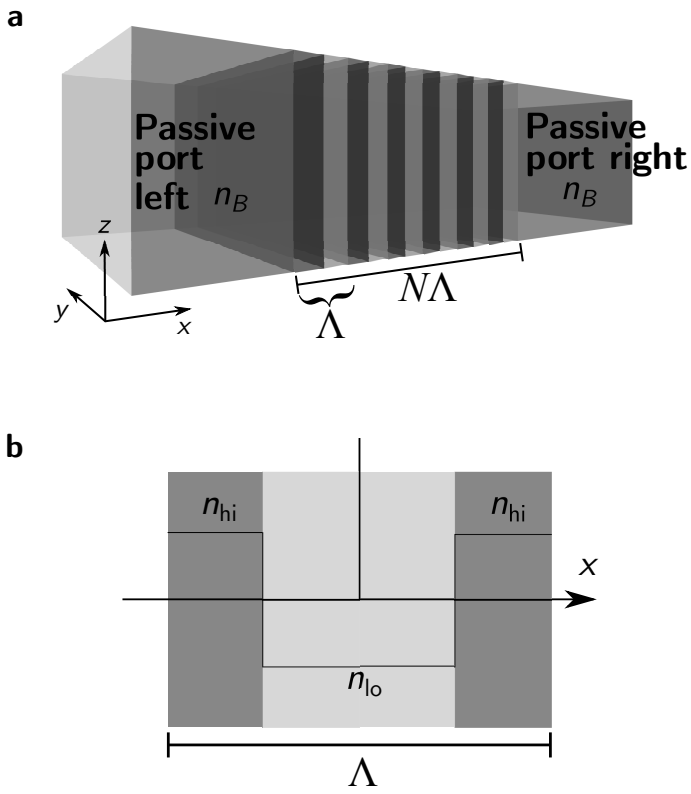

Figure 7.4 | Schematic of passive Bragg grating structure. (**a**) N-number of period passive grating in a background material n_B, (**b**) single unit cell of the grating with refractive index profile.

($\lambda_B = 0.89\ \mu$m). The real part of the low and the high refractive index at this frequency are $n_{\text{lo}}(f_B) = 3.6053$ and $n_{\text{hi}}(f_B) = 3.6466$; these are marked in Fig. 7.3 as points "a" and "b" respectively. As such the average refractive index at f_B is $n_{\text{avg}}(f_B) = \frac{1}{2}(n_{\text{hi}}(f_B) + n_{\text{lo}}(f_B)) = 3.6260$, and is used as the background material refractive index $n_b = 3.6260$. Therefore from (4.1) the physical length of an unit cell can be calculated as $\Lambda = 122.73$ nm. It follows that the modulation of the real part of the refractive index at the Bragg frequency is $\Delta n'(f_B) = \frac{1}{2}(n_{\text{hi}}(f_B) - n_{\text{lo}}(f_B)) = 0.02068$. For this application, 200 periods of unit cells are considered with the Kerr non-linearity parameter $n_2 = 2 \times 10^{-17}$ m^2/Watt as experimentally measured in [7.18,7.19]. The simulations are done by using the TLM method with the non-linear Duffing material model with a spatial discretisation $\Delta x = \lambda_B/96$.

Figure 7.5 shows the transmittance (a) and reflectance (b) of the passive *linear* Bragg

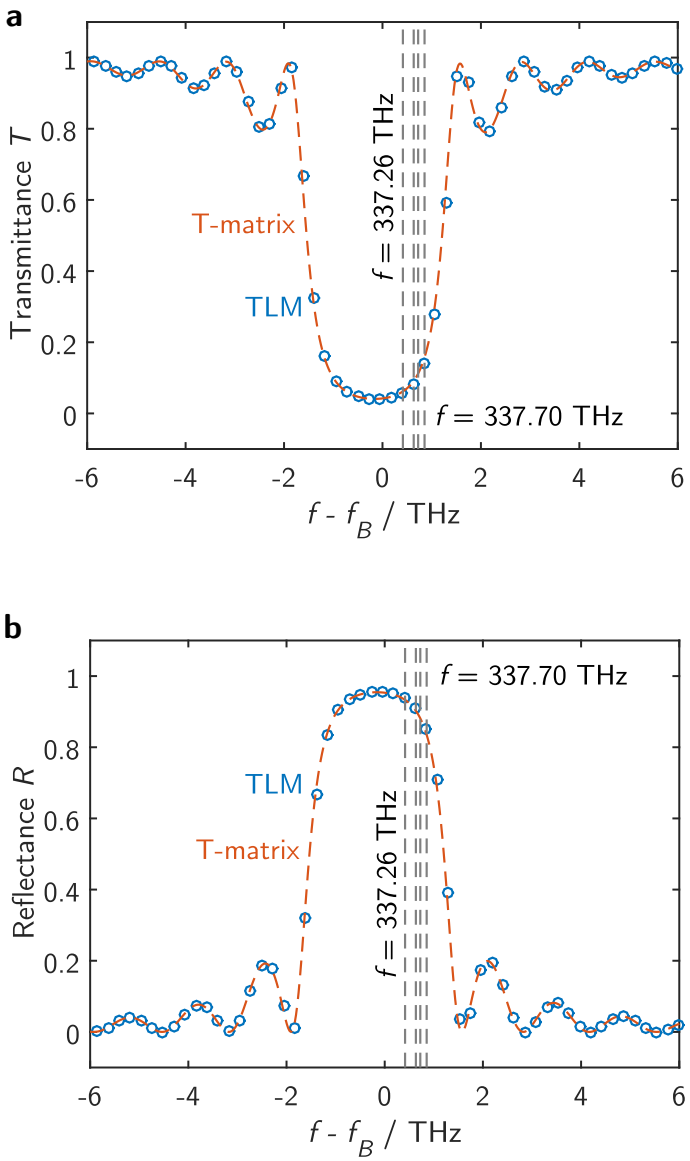

Figure 7.5 | Comparison of the (a) transmitted and (b) reflected spectra of a passive grating calculated by the T-matrix and the TLM method. The dashed lines denotes the different operational frequencies for hysteresis analysis.

grating ($n_2 = 0$) calculated by using the analytical Transfer matrix (T-matrix) method[‡] and the TLM method. It can be seen that the results obtained by the TLM method agree with the ones calculated analytically by using the T-matrix method. In order to investigate the bistable behaviour of the Bragg gratings using the TLM method, 4 different operational frequencies are considered, i.e. $f_{\text{op}} =$

[‡]Detail implementation of T-matrix method is presented in Appendix B

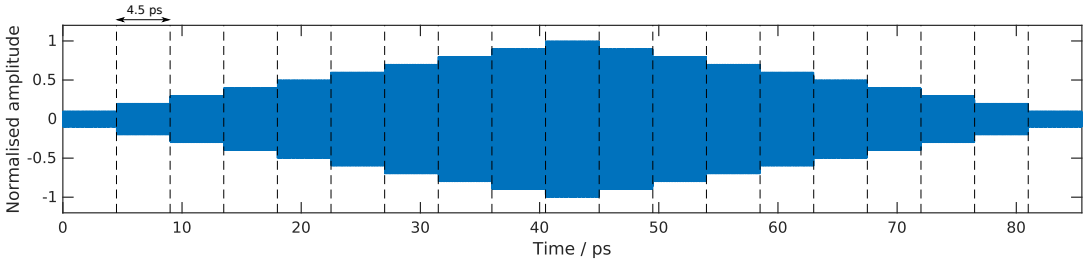

Figure 7.6 | An illustration of input signal used for hysteresis simulation.

337.26, 337.48, 337.57 and 337.70 THz which are located at the right flank of the band-gap; these frequencies are marked in Fig. 7.5 by vertical lines. The reason for operation at the right flank of the band-gap is because in general a positive non-linearity will shift non-linearly the entire transmission spectra to the left (lower frequency), hence it will open a transmission window on the right side of the band-gap [7.10,7.12,7.16,7.24,7.25].

The TLM simulation for hysteresis analysis is conditioned as follows: a Continuous Wave (CW) is excited at operation frequency f_{op}. The intensity of the CW increases after 4.5 ps duration until the desired maximum intensity after which decreases each time after 4.5 ps duration to the initial intensity. The intensity is increased and decreased in a single simulation. An illustrative example of the input signal is presented in Fig. 7.6.

Figure 7.7 shows the bistable behaviour of the transmittance (a) and reflectance (b) of a passive non-linear Bragg gratings operated at four different frequencies, i.e. f_{op} = 337.26, 337.48, 337.57 and 337.70 THz. From Fig. 7.7, it can be seen that the hysteresis for both the transmittance and reflectance occurs at lower input intensity when the grating is operated at higher operational frequency. However as the operation frequency increases, the width and the on/off ratio of the transmission hysteresis reduces. In particular it is important to comment on the hysteresis when the grating is operated at f_{op} = 337.26 THz; it can be seen that the on/off ratio of the hysteresis is significantly reduced compared to the ones operated at other frequencies.

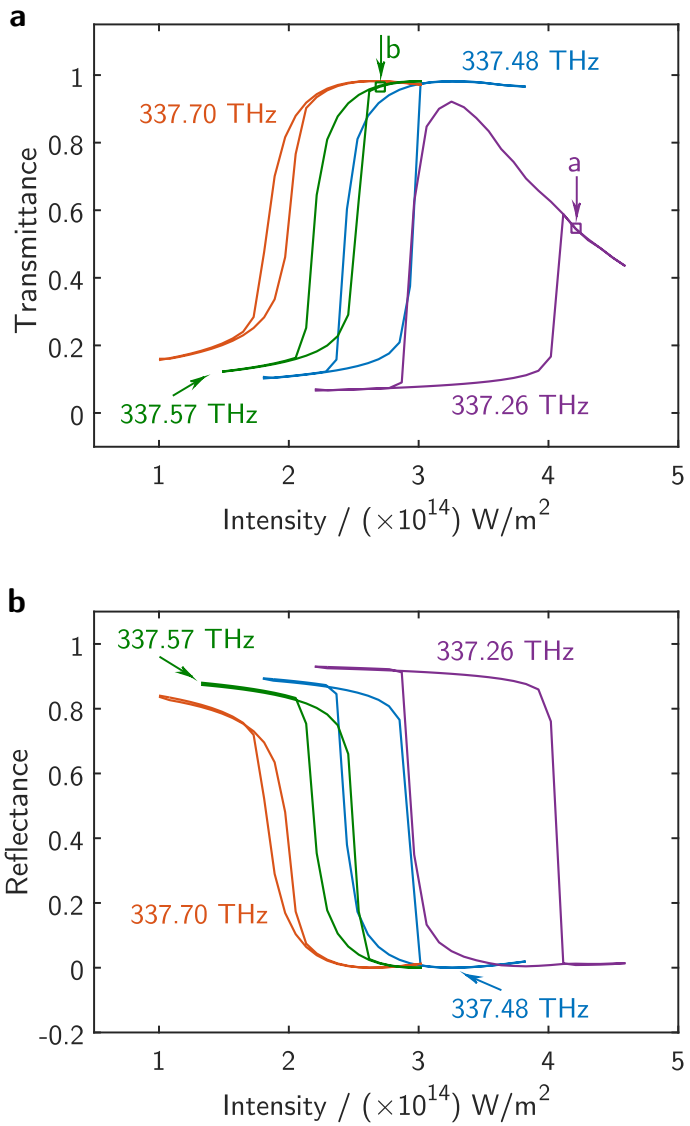

Figure 7.7 | Hysteresis of passive Bragg grating structure. (**a**) Transmittance and (**b**) reflectance as a function of input signal intensity I. For 4 different operational frequencies.

To rationalise this significant change, Fig. 7.8(a) plots the temporal response of transmitted electric field when the structure is operated at $f_{\text{op}} = 337.26$ THz and $I = 4.21 \times 10^{14}$ W/m^2, i.e. at the *on* state; this is indicated by arrow "a" in Fig. 7.7. It can be seen in Fig. 7.8(a) that the transmitted electric field is pulsating in the time-domain. This is because when the grating is operated close to the Bragg frequency, a high intensity signal is required to switch *on* the grating which induces a strong non-linear self-pulsation effect to the incident signal. To get a better insight to the nature of self-pulsation behaviour, the spectrum of the transmitted

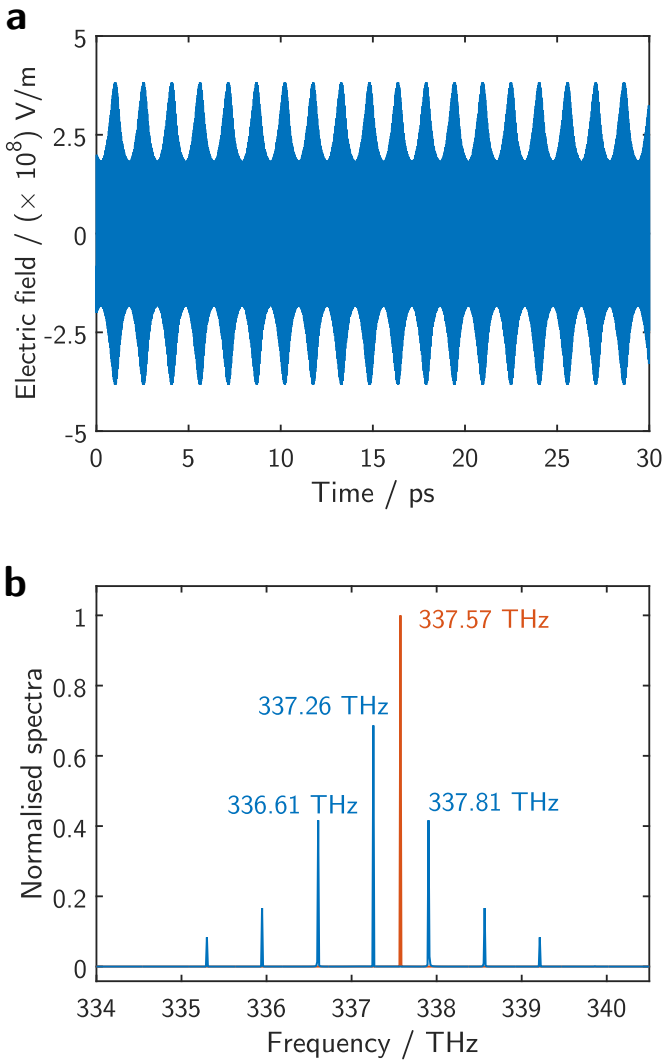

Figure 7.8 | Self-pulsation of the transmitted electric field. (**a**) Temporal and (**b**) frequency response of the transmitted electric field of the passive Bragg grating operated at $f_{\text{op}} = 336.26$ THz with intensity $I = 4.21 \times 10^{14}$ W/m^2, marked by square bullet "a" in Fig. 7.7. Spectra when operated at point "b" included for comparison.

electric field is plotted in Fig. 7.8(b). For comparison the transmission spectrum operated at $f_{\text{op}} = 337.57$ THz and $I = 2.7 \times 10^{14}$ W/m^2, denoted by arrow "b" in Fig. 7.7, is also shown in Fig. 7.8(b). By comparing the transmission spectra of these two operation conditions, it can be seen that there exist a set of longitudinal modes which are spaced at multiples of ∼0.65 THz around the main excitation frequency $f_{\text{op}} = 337.26$ THz when operated at point "a", while the operation at point "b" shows a single peak at $f_{\text{op}} = 337.57$ THz. The significant decrease in the

transmission when operated at point "a" can thus be explained as a result of energy conversion to other frequencies. In practice to exploit the bistable operation of such a structure, the operational frequency is usually set to give a hysteresis that is wide enough for the designated application with pronounced on/off ratio but operated at as lowest an intensity as possible to minimise power usage.

7.3 Non-Linear $\mathcal{PT}$-Bragg Grating

Using the same geometrical design as was described in the previous section, a non-linear $\mathcal{PT}$-Bragg grating (NPTBG) is made by adding both gain and loss at different sections within a unit cell. For this purpose the realistic dispersive and saturable gain/loss model described in Section 5.1 is used to model the gain and loss materials while the Duffing material model is used to model the Kerr non-linearity of the medium. Hence the refractive index in a single period, n_G, along the propagation direction x shown in Fig. 7.9, is now modified as,

$$n_G(x,\omega,I,t)\begin{cases} n_{\text{hi}}(\omega)+n_2 I(x,t)-j\dfrac{c_0}{\omega}\alpha(\omega,I), & x<\dfrac{\Lambda}{4} \\ n_{\text{lo}}(\omega)+n_2 I(x,t)-j\dfrac{c_0}{\omega}\alpha(\omega,I), & \dfrac{\Lambda}{4}\le x<\dfrac{\Lambda}{2} \\ n_{\text{lo}}(\omega)+n_2 I(x,t)+j\dfrac{c_0}{\omega}\alpha(\omega,I), & \dfrac{\Lambda}{2}\le x<\dfrac{3\Lambda}{4} \\ n_{\text{hi}}(\omega)+n_2 I(x,t)+j\dfrac{c_0}{\omega}\alpha(\omega,I), & \dfrac{3\Lambda}{4}\le x<\Lambda \end{cases}, \tag{7.36}$$

where, n_{hi} and n_{lo} are frequency dependent complex high and low refractive indices, respectively, n_2 is the Kerr non-linearity coefficient, I is the input signal intensity and $\pm\alpha$ denotes the gain (-) and loss (+) in the grating lattices that are now both dispersive and saturable. The gain/loss is modelled by the conductivity of the medium that is dispersive and saturable, using the realistic gain/loss conductivity

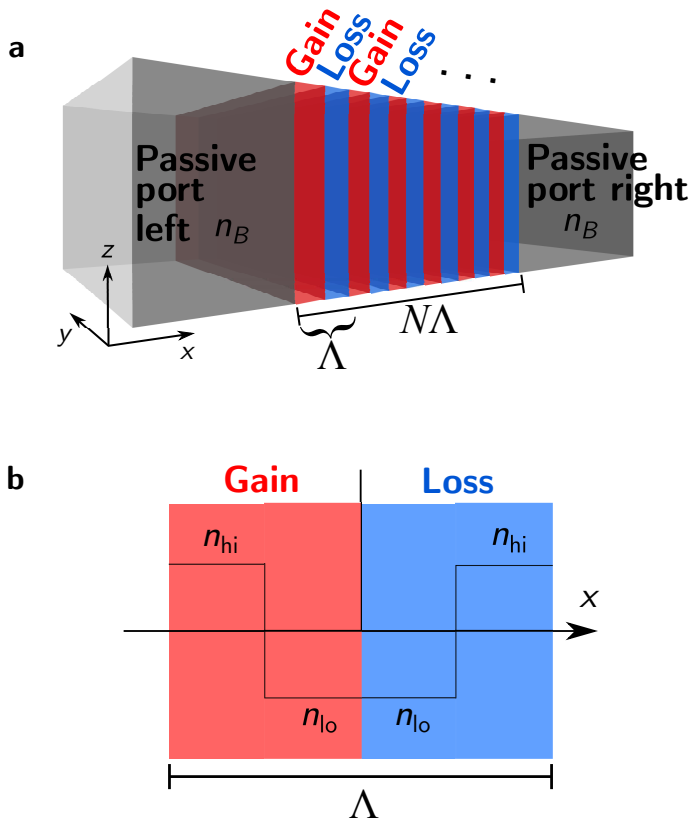

Figure 7.9 | Schematic of a non-linear $\mathcal{PT}$-Bragg grating structure (NPTBG). (**a**) NPTBG with N unit grating cell in a background material n_B, (**b**) single unit cell of the grating with two slightly different refractive indicies n_{hi} and n_{lo}. Red coloured sections denote gain while the blue sections denote lossy lattices.

model described previously in Section 5.1 and reproduced here as,

$$\sigma_e(\omega) = \mathbb{S}(I)\frac{\sigma_0}{2}\left[\frac{1}{1+j(\omega-\omega_\sigma)\tau} + \frac{1}{1+j(\omega+\omega_\sigma)\tau}\right]. \tag{7.37}$$

The gain/loss material parameters σ_0, ω_σ and τ in (7.37) have been described in Section 5.1 in more detail. By using the relation (5.8), between the gain/loss α and the dispersive imaginary part of the refractive index, the peak value of gain/loss parameter α_0 can be defined as

$$\alpha_0 = \frac{\omega_\sigma}{c_0} n''(\omega_\sigma). \tag{7.38}$$

The intensity dependent saturation $\mathbb{S}$ factor denotes the amount of gain/loss under

the influence of strong signal intensity which is expressed as,

$$\mathbb{S}(I) = \frac{1}{1 + \frac{I}{I_{\text{sat}}}} \tag{7.39}$$

where I and I_{sat} are the field intensity and the gain/loss saturation intensity, respectively. Noting that in practice the amount of I_{sat} is dependent on the material treatment during fabrication process [7.26]. For modelling purposes it is assumed that the saturation factor $\mathbb{S}$ varies in the range of $0 < \mathbb{S} < 1$, with $\mathbb{S} \to 1$, i.e. $\frac{I}{I_{\text{sat}}} \to 0$ referring to a non-saturated condition, and $\mathbb{S} \to 0$, i.e. $\frac{I}{I_{\text{sat}}} \to \infty$, referring to a highly saturated condition.

7.3.1 Impact of Saturable Gain/Loss on Bistability of Non-Linear $\mathcal{PT}$-Bragg Grating

For modelling purposes, the gain/loss material parameters are set as follows: the atomic transition frequency of the gain/loss material is set to coincide with the Bragg frequency, i.e. $\omega_\sigma = 2\pi f_B$ with the time relaxation constant $\tau = 0.1$ ps as in [7.5,7.16,7.27,7.28]. The saturation intensity I_{sat} is varied to analyse its impact on the hysteresis.

The first case considered is when the saturation intensity is set at $I_{\text{sat}} = 5 \times 10^{13}$ W/m^2. Figure 7.10 shows (a) transmittance T_L and (c) reflectance R_L for the left incidence case and (b) transmittance T_R and (d) reflectance R_R for the right incident signal as a function of input signal intensity and for different gain and loss parameter α_0. It is noted that for the given variation of input signal intensity, the saturation factor $\mathbb{S}$ varies between $0.125 < \mathbb{S} < 0.77$ although it is emphasized that saturation factor may vary between layers. For comparison, the response of a *passive* non-linear Bragg grating (NBG) (i.e. one without gain and loss, $\alpha_0 = 0$) is depicted by dashed lines.

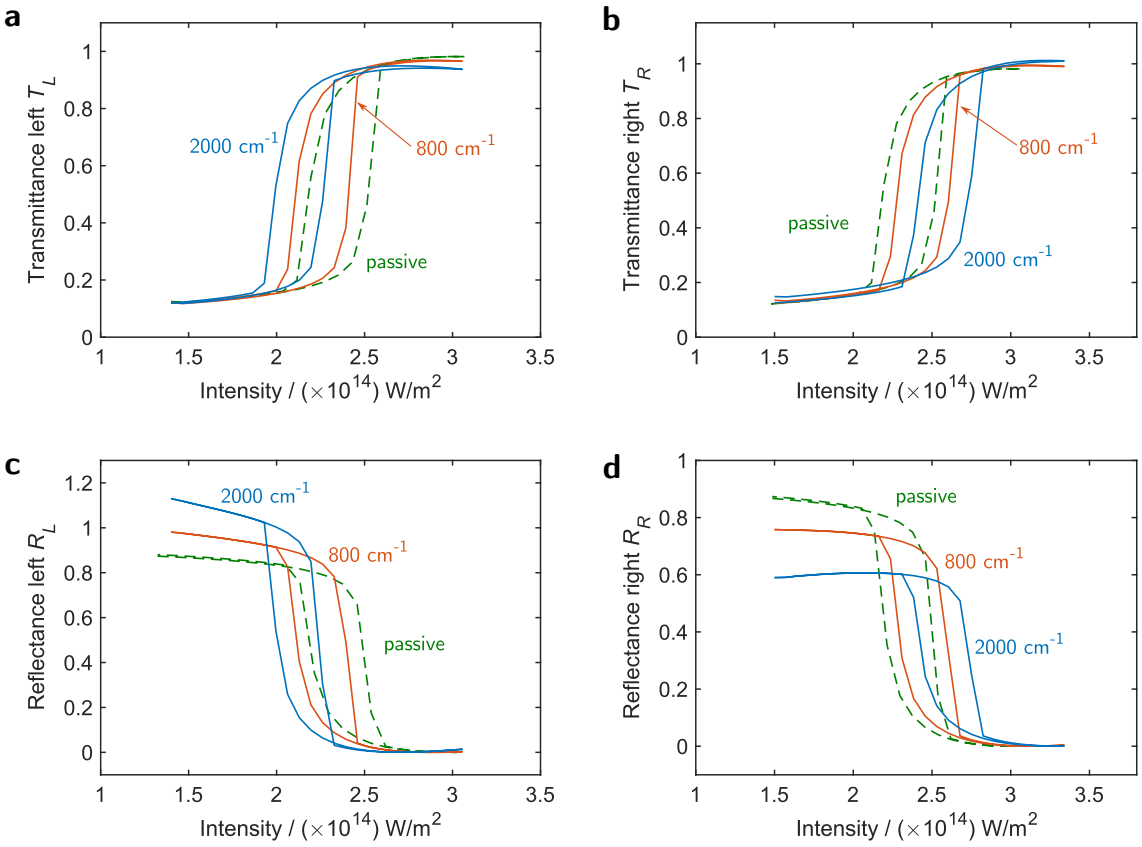

Figure 7.10 | Hysteresis of non-linear PTBG with high saturation intensity gain/loss material. (**a**) Transmittance T_L, (**c**) reflectance R_L, for the light incident from the left, (**b**) transmittance T_R, (**d**) reflectance R_R for the light incident from the right of the grating. Saturation intensity is $I_{\text{sat}} = 5 \times 10^{13}$ W/m^2. Dashed line represents the response of the passive NBG for reference.

As in the previous section, in order to obtain bistable operation the input signal frequency is set to be at the right flank of the band-gap [7.10,7.12,7.16,7.24,7.25], in which a continuous-wave (CW) operating at $f_{\text{op}} = 337.57$ THz is chosen. The hysteresis is obtained by gradually increasing and decreasing the input signal intensity in a single computation. This is repeated for different gain/loss parameters, namely $\alpha_0 = 800$ cm^{-1} and 2000 cm^{-1}.

Figure 7.10(a-d) shows that the NPTBG is bistable for both transmittance and reflectance regardless of the side of incidence (left or right). Figure 7.10(a,c) shows that compared to a non-linear Bragg grating (NBG), the bistability of NPTBG occurs at lower input intensities for the signals incident from the left of the grating and at

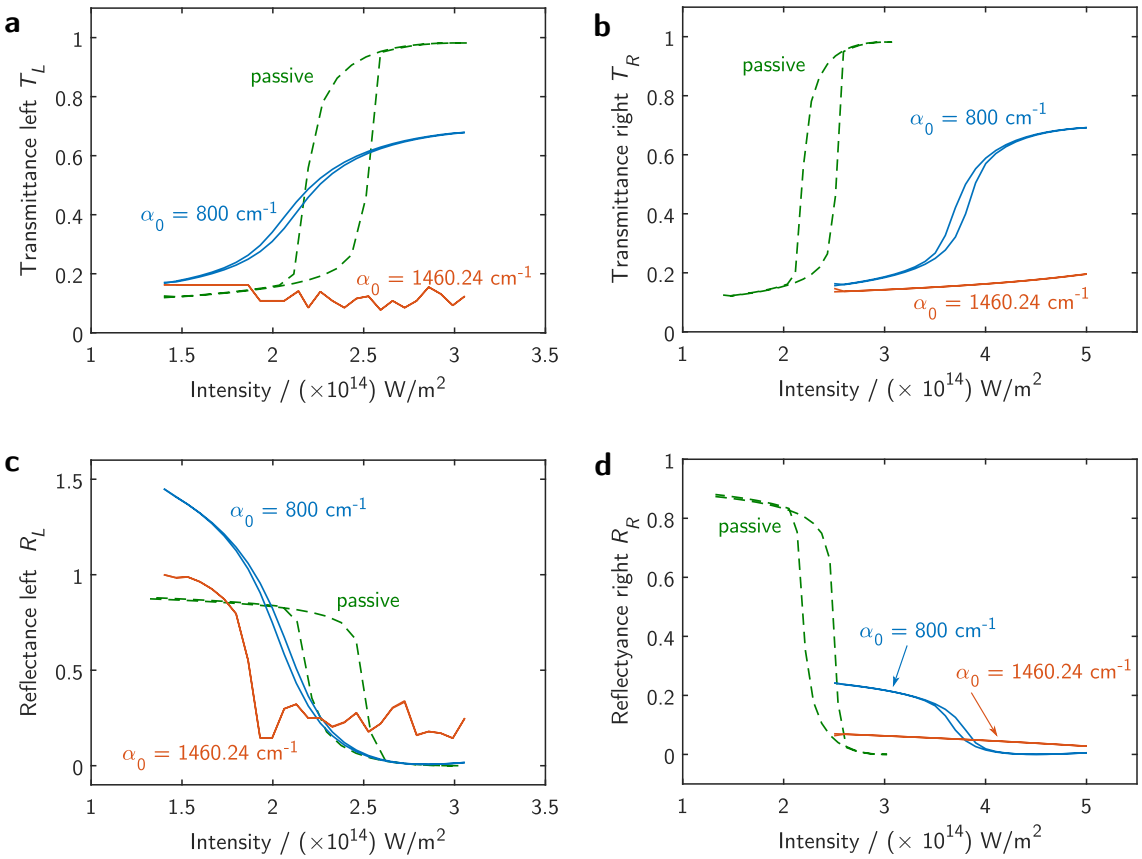

Figure 7.11 | Hysteresis of non-linear PTBG with no saturation effect. (**a**) Transmittance T_L, (**c**) reflectance R_L, for the light incident from the left, (**b**) transmittance T_R, (**d**) reflectance R_R for the light incident from the right of the grating. Dashed line represents the response of the passive NBG for reference.

higher intensity for signals incident from the right side of the grating. It is noted that the transmittances for the left and right incidence are different, $T_L \neq T_R$ as shown in Fig. 7.10(a,b), showing that the NPTBG does not satisfy Lorentzian reciprocity. This is due to the fact that the scattering matrix is no longer a complex-symmetric matrix, $\mathbf{S} \neq \mathbf{S}^T$. Furthermore, it is observed that at high intensity, both R_L and R_R are very low while transmittances are almost unity, implying the behaviour of bidirectionally transparent material at high intensity (Fig. 7.10(c,d)).

When the NPTBG is operated with very low saturation intensity, e.g. $I_{\text{sat}} = 65.2 \times 10^7$ W/m^2, as taken from [7.5,7.27], for the same input field intensity range the saturation factor varies in the range of $1.5 \times 10^{-6} < \mathbb{S} < 20 \times 10^{-6}$. For that case it

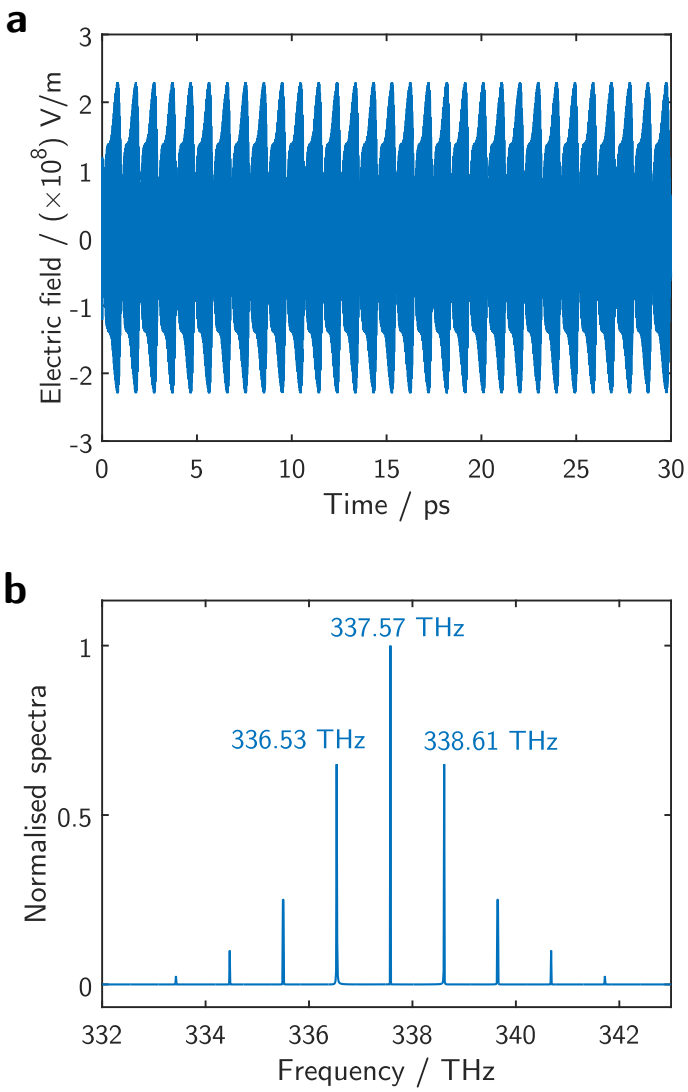

Figure 7.12 | Self-pulsation of transmitted signal from NPTBG. (**a**) Time and (**b**) frequency response of the transmitted electric field of NPTBG at $\alpha_0 = 1460.24$ cm^{-1} with input intensity $I = 2 \times 10^{14}$ W/m^2 and the incident is from the left side of the grating.

is observed that, regardless of the amount of gain and loss in the system, all results overlap with that of the passive NBG (dashed line on Fig. 7.10), i.e $T_L = T_R$ and $R_L = R_R$. This result, which is not shown separately, confirms that when gain and loss saturation intensity are very low, $\mathcal{PT}$-behaviour is inhibited due to the negligible effective gain and loss.

Attention is now focused on the case of no gain/loss saturation, i.e. $\mathbb{S} = 1$. Figure 7.11(a-d) shows that the NPTBG is bistable for both transmittance and reflectance

regardless of the direction of input signal incidence (respectively from left or right side). It is noted that in the absence of gain/loss saturation, $\mathbb{S} = 1$, both the width and on/off ratio of hysteresis reduce as the gain/loss in the grating is increased. Similarly as in Fig. 7.11(a,c), the bistability occurs at lower input intensities for the signals incident from the left of the grating compared to signals incident from the right. Of special interest is when the NPTBG is operated at $\alpha_0 = 1460.24$ cm^{-1} at which the structure loses the hysteresis properties and its responses (transmittance T_L and reflectance R_L) behave erratically. Furthermore, Fig. 7.11(a,b) show that the transmittances for the left and right incidence are different, $T_L \neq T_R$, again confirming that the NPTBG does not satisfy Lorentzian reciprocity.

Figure 7.12 shows the temporal response (a) and frequency content (b) of the transmitted signal for the left incident signal for an input intensity $I = 2 \times 10^{14}$ W/m^2. The results confirms the presence of longitudinal modes that fall within the gain/loss profile of the grating and are spaced at multiples of ∼1.04 THz around the input signal frequency $f = 337.57$ THz. The erratic behaviour of the T_L in Fig. 7.11(a) can thus be explained as a result of the transfer of energy to other frequencies.

Overall, it can be summarised that high saturation intensity (with respect to the Kerr non-linear parameter) is required in order to have an interplay of both non-linear Kerr effect (bistability) and the $\mathcal{PT}$-symmetry. It is however noted that the saturation effect should not be neglected as it is shown that in the absence of saturation light can be amplified greatly within the grating and induce a strong self-pulsation effect which causes dynamic light instability.

7.3.2 Non-Linear $\mathcal{PT}$-symmetric Bragg Grating as an Optical Memory Device

In this subsection, an application of non-linear PTBG as a memory device is demonstrated. Exploiting the interplay of both the $\mathcal{PT}$-symmetric behaviour and the Kerr non-linearity, a memory device can be achieved by considering a gain/loss material with a high saturation intensity as in the case studied in Fig. 7.10.

The NPTBG is operated at $f_{\text{op}} = 337.57$ THz with gain/loss parameter $\alpha_0 = 2000$ cm^{-1} and with a saturation intensity $I_{\text{sat}} = 5 \times 10^{13}$ W/m^2 as in Fig. 7.10. The TLM modelling was undertaken as follows: a CW light signal was excited from the left side of the NPTBG at f_{op}, and the intensity of the CW was varied throughout the simulation to emulate memory *reading*, *writing* and *resetting* operations of memory device. The reading operation is set to be at $I_{\text{read}} = 2.2 \times 10^{14}$ W/m^2, the memory writing operation occurs by increasing the input intensity to $I_{\text{write}} = 2.725 \times 10^{14}$ W/m^2 while the resetting operation is achieved by decreasing the input intensity to $I_{\text{reset}} = 1.5 \times 10^{14}$ W/m^2. During the simulation each process happens for a duration of 10 ps and patterned as read, write, read and reset; the same pattern is then repeated.

Figure 7.13(a) depicts the input signal (electric field) as a function of time, each process is labelled within the figure as *read*, *write* and *reset* over a total simulation time of 120 ps. The transmitted electric field is plotted in Fig. 7.13(b). It can be seen in this figure that initially the memory is in the "0" *null* state. At $t = 10$ ps a "write" operation occurs by increasing the input signal intensity to achieve the "on" state in the hysteresis, to fill the memory storage, denoted by memory "1". After the writing the information, the input signal intensity is reduced to the reading intensity level. It can be seen from Fig. 7.13(b) that the transmitted signal during the reading process with memory "1" ($20 < t < 30$ ps) is higher when compared to when the memory is null "0"($0 < t < 10$ ps). By sending the reset signal (reducing the input

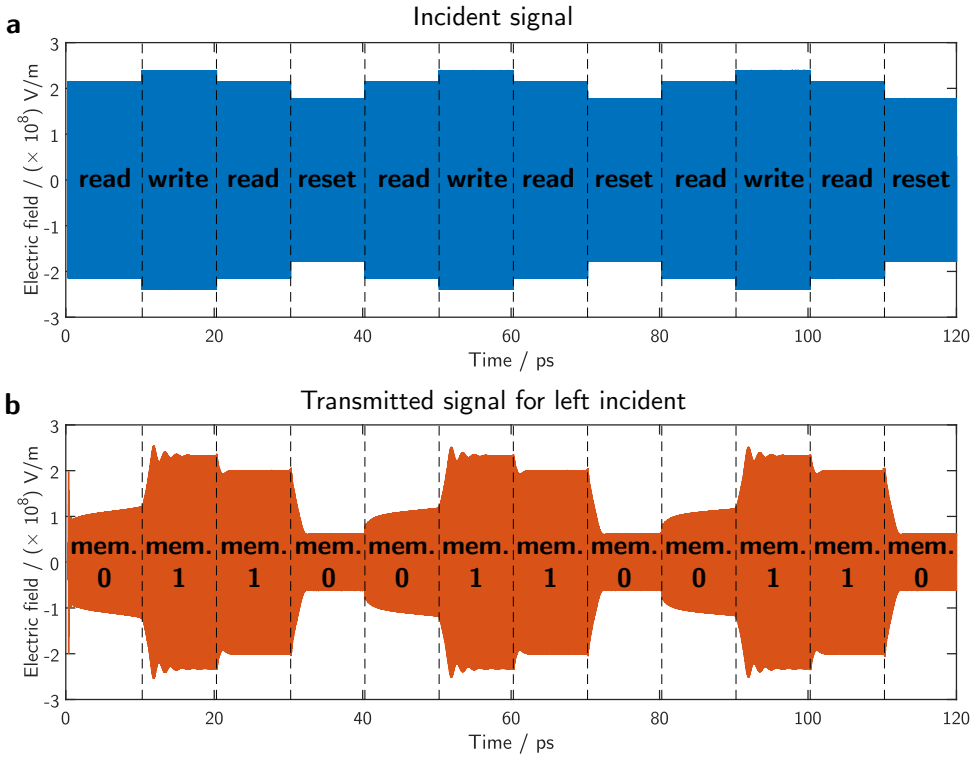

Figure 7.13 | Demonstration of application of NPTBG as a memory device. The electric field of (**a**) the input signal and (**b**) the transmitted signal.

signal intensity), the hysterisis is now at the "off" state; as such the output during the reading process gives a small transmitted signal (memory value reset back to null). Furthermore, Fig. 7.13(b) shows that the write, read and reset operation can be performed many times with reproducible response. By using a NPTBG grating the RAM operation is performed at lower input power compared to that would be resulted for passive non-linear Bragg grating.

7.4 Application of Non-Linear and Dispersive PTBG as Logical-Gate Device

This section considers the design of a non-linear $\mathcal{PT}$-symmetric Bragg grating based on common GaAs-based material for an application as optical logical-gate device.

The Kerr non-linearity of the material is modelled by the Duffing material model. Realistic dispersive and saturable gain/loss are modelled by using the homogeneously broadened gain/loss material model described in Section. 5.1.

7.4.1 Kerr Non-Linearity Induced $\mathcal{PT}$-Bragg Grating (K-NPTBG)

The grating design considered in this section is illustrated in Fig. 7.14. The grating has a total length of $N\Lambda$, where N is the total number of unit cells and Λ is the physical length of an unit cell, and is embedded in a medium with a refractive index n_B. Each unit cell has the same background refractive index and four non-linear layers with alternating positive and negative Kerr non-linearity. This design is inspired by the grating structure studied by Sargent and Brozozowski [7.29], where the grating had an alternating layers of negative and positive Kerr non-linearity, but without the inclusion of gain/loss. The refractive index profile associated with the unit cell, n_G, depicted in Fig. 7.14, can be expressed as,

$$n_G(x,\omega,I,t)\begin{cases} n_{\text{avg}}(\omega)+n_2I(x,t)-j\dfrac{c_0}{\omega}\alpha(\omega,I), & x<\dfrac{\Lambda}{4} \\ n_{\text{avg}}(\omega)-n_2I(x,t)-j\dfrac{c_0}{\omega}\alpha(\omega,I), & \dfrac{\Lambda}{4}<x<\dfrac{\Lambda}{2} \\ n_{\text{avg}}(\omega)-n_2I(x,t)+j\dfrac{c_0}{\omega}\alpha(\omega,I), & \dfrac{\Lambda}{2}<x<\dfrac{3\Lambda}{4} \\ n_{\text{avg}}(\omega)+n_2I(x,t)+j\dfrac{c_0}{\omega}\alpha(\omega,I), & \dfrac{3\Lambda}{4}<x<\Lambda \end{cases}, \tag{7.40}$$

where, n_{avg} represents the base refractive index of the grating as a function of frequency ω, n_2 is the Kerr non-linearity constant, I is the field intensity and $\pm\alpha$ denotes the gain (-) and loss (+) in the grating lattices that is both dispersive and saturable. The gain/loss parameter α is related to the imaginary part of the refractive index n'' by the relation (5.8) given in Section 5.1. It can be seen from (7.40) that the refractive index profile n_G has an intensity modulated real refractive index,

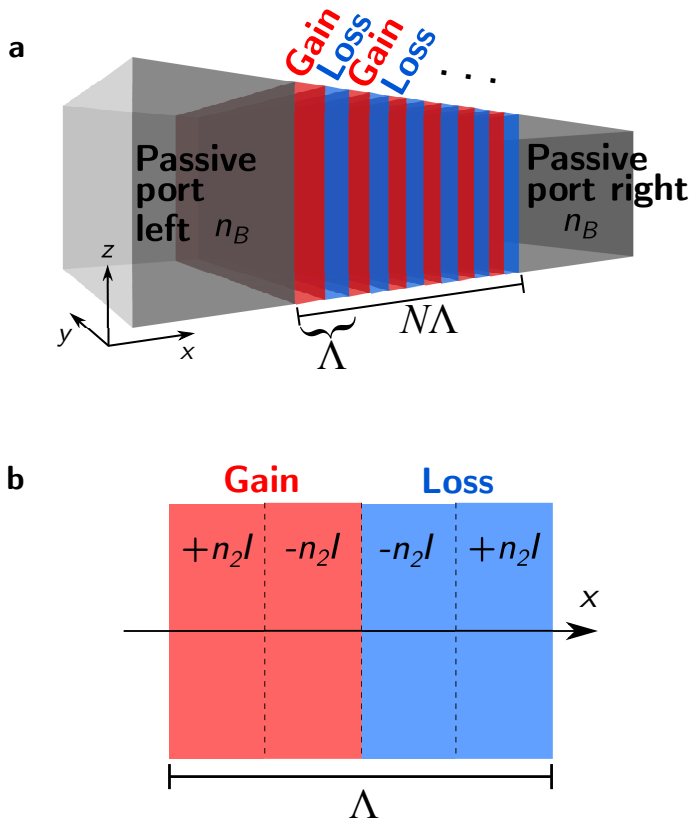

Figure 7.14 | Schematic illustration of Kerr-induced $\mathcal{PT}$-symmetric Bragg grating structure (K-NPTBG). (**a**) N unit cells of the grating embedded in a background material n_B and (**b**) detailed composition of a unit cell of the K-NPTBG

i.e. when the signal intensity is very small ($n_2 I \ll$), there is no modulation of the real part of the refractive index and the grating reduces to only alternating layers with gain and loss. For a strong signal intensity, the refractive index of the grating is modulated by the intensity of the input signal, effectively splitting each layer via the positive and negative Kerr non-linearity. As such grating is referred as Kerr non-linearity induced $\mathcal{PT}$-Bragg grating (K-NPTBG). Throughout the K-NPTBG, the dispersive and intensity dependent media are defined by the Duffing model for dielectric polarisation and is implemented in the TLM method as described in the previous section. Meanwhile the gain/loss sections are modelled by the conductivity of the material which includes the dispersive and saturable properties in the same way as in the previous section.

7.4.2 Intensity Dependent Performance of K-NPTBG

For definiteness the K-NPTBG investigated is based on GaAs material properties and comprises of 200 periods with the following material parameters: $\chi_{e\infty} = 2.65$, $\chi_{e0} = 7.5$, $\omega_{0D} = 4614.4$ rad/ps, and $\delta = 0.0923$ rad/ps. For the present numerical investigation the magnitude of the Kerr non-linearity constant is also taken to be that of GaAs, $|n_2| = 2 \times 10^{-17}\text{m}^2/\text{W}$ [7.18,7.19,7.30] throughout the structure. The gain and loss material parameters are $\tau = 0.1$ ps and $\omega_\sigma = 2116.5$ rad/ps [7.27], while the σ_0 depends on the gain or loss given. The periodicity of K-NPTBG is designed so that the Bragg frequency is at the atomic-transitional frequency, i.e. $f_B = \omega_\sigma/(2\pi) = 336.85$ THz. Using the given material parameters the real part of the refractive index at f_B can be calculated using (7.4), i.e. $n_{\text{avg}}(f_B) = 3.6260$ from which the length per unit cell $\Lambda = 112.73$ nm can be calculated using (4.1). The refractive index of the background material is again taken to be that of GaAs at f_B, i.e. $n_B = 3.626$.

The input beam comprises of two different beams, i.e. a probe beam and a strong pump beam. The pump beam is a continuous wave (CW) and is used to alter the base refractive index of the grating through the Kerr non-linearity. The frequency of the pump beam, f_{pump}, is set to be far from the Bragg frequency, i.e. $f_{\text{pump}} = 200$ THz, hence providing a uniform magnitude of real index modulation throughout the structure due to the Kerr non-linearity [7.29]. The probe beam is a Gaussian pulse modulated at the Bragg frequency f_B and is low in intensity, with its maximum intensity being 1% of the pump beam intensity. Since the probe beam intensity is very low compared to that of the strong pump beam, its effect can be seen as a perturbation to the pump beam and hence the intensity of the pump beam can be considered as the intensity of the input beam.

In order to identify the range of stable operation of the K-NPTBG, the structure is first modelled without the non-linearity ($n_2 = 0$), and the transmittance and re-

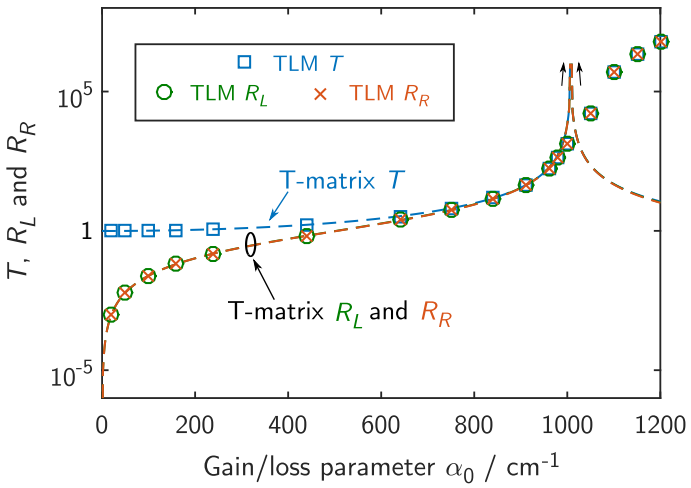

Figure 7.15 | Comparison of the transmission and reflectance of a K-NPTBG as a function of gain/loss parameter α_0. Results are calculated by using the analytical T-matrix and the TLM method.

flectance of PTBG is analysed using both the analytical Transfer matrix (T-matrix) method and the TLM method. The T-matrix method models the linear and dispersive structures. Figure 7.15 shows the response of the PTBG grating assuming that the non-linearity is switched off, i.e. $n_2 = 0$, for different gain/loss parameters. Two sets of results are presented, namely the TLM results that include dispersive material model and saturation; and the T-matrix results for a dispersive material model but no saturation. The saturation intensity is set to $I_{\text{sat}} = 2.5 \times 10^{13}$ W/m^2 and the intensity of the pump and probe beams are set as described with the pump beam intensity of 2.5×10^{11} W/m^2. Figure 7.15 shows the transmittance, T, and reflectance of a K-NPTBG when excited from the left and right of the grating, R_L and R_R respectively, as a function of gain/loss parameter α_0. The results are calculated at the Bragg frequency.

Figure 7.15 depicts that the reflectances of the K-NPTBG with $n_2 = 0$ are the same, $R_L = R_R$, regardless of the side of excitation. This is unlike the PTBG structures studied before, in Chapter 6, where the reflectances are different, and the results imply that this is due to the absence of the phase grating. The TLM results agree well with the T-matrix results for low gain/loss parameter. As gain/loss in

the structure increases, transmittance and reflectance also increase. The T-matrix results show a singularity at $\alpha_0 = 1008$ cm^{-1} which is associated with the coherent-perfect-absorber and laser(CPAL) point, at which the **S**-matrix poles of the linear PTBG cross the real frequency axis [7.31–7.33]. More importantly, as the only difference between the TLM and analytical results is the presence of the saturation in the TLM modes, it is observed that the TLM results do not exhibit a singularity meaning that gain/loss saturation can limit the accumulation of energy inside the grating.

The response of the K-NPTBG grating for different saturation intensities is analysed in Fig. 7.16(a,b) as a function of input intensity for three different cases namely, grating with no gain/loss, $\alpha_0 = 0$, with gain/loss parameter $\alpha_0 = 800$ cm^{-1} and saturation turned off ($\mathbb{S} = 1$), and $\alpha_0 = 800$ cm^{-1} with gain and loss saturation intensity $I_{\text{sat}} = 2.5 \times 10^{13}$ W/m^2. In all cases Kerr non-linearity is present with $|n_2| = 2 \times 10^{17}$ m^2/W. Figure 7.16(a) shows the transmittance, T, which is the same regardless of the side of excitations. For the case $\alpha_0 = 0$, total transmittance $T = 1$ is observed at low intensities but then transmittance gradually decreases to zero at high intensities. This can be explained by the fact that at high input intensities modulation of the refractive index due to Kerr non-linearity becomes dominant and results in the formation of a Bragg grating. Since the structure for the case $\alpha_0 = 0$ is orthogonal (reciprocal and lossless), i.e. $T + R = 1$, it follows that $R \approx 0$ at low intensities and there is an almost-total reflectance $T \approx 1$ at high intensities (Fig. 7.16(b)).

For the case when the K-PTBG is operated with gain/loss parameter $\alpha_0 = 800$ cm^{-1} and no saturation ($\mathbb{S} = 1$), the transmittance slowly increases and then decreases at higher input intensities. Figure 7.16(b) shows that reflectance generally has different responses, $R_L \neq R_R$, depending on the side of excitation, with larger differences occurring at higher input intensities. At the intensity of $I_U = 5.65 \times 10^{14}$ W/m^2, unidirectional invisibility is observed; when $T = 1$, reflectance from the right, R_R,

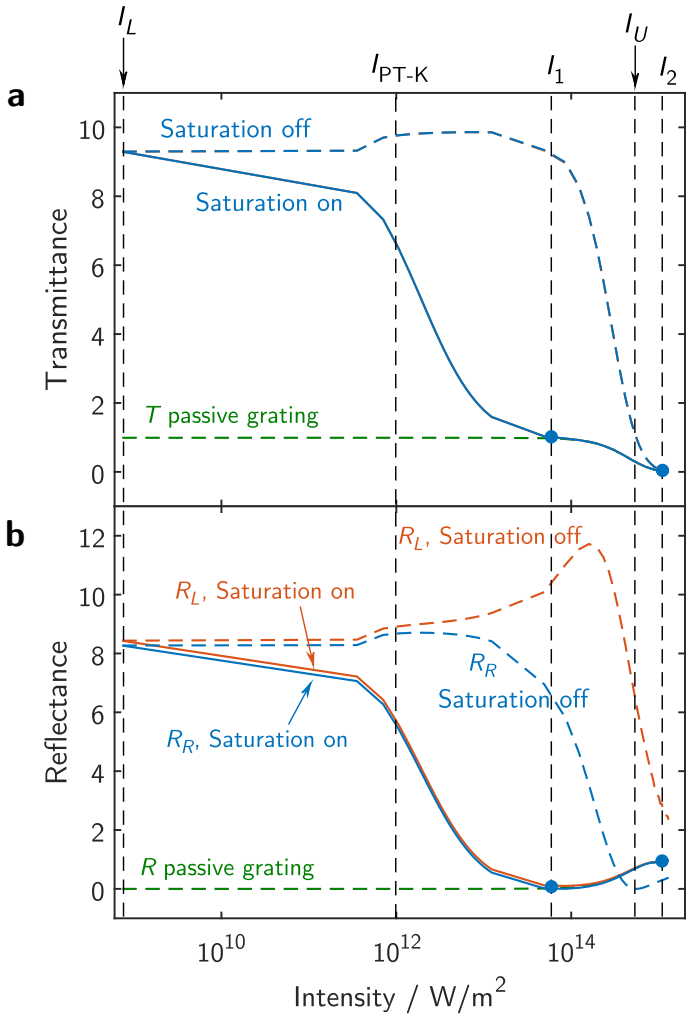

Figure 7.16 | Impact of saturation to the transmittance and reflectance of a non-linear K-NPTBG. (**a**) Transmittance and (**b**) reflectances as a function of input beam intensity for K-PTBG with gain/loss parameter $\alpha_0 = 800$ cm^{-1} with no saturation $\mathbb{S} = 1$; and gain/loss parameter $\alpha_0 = 800$ cm^{-1} with saturation intensity $I_{\text{sat}} = 2.5 \times 10^{13}$ W/m^2. The response of the passive structure $\alpha_0 = 0$ is included for reference.

is at its minimum, but R_L is highly amplified [7.31–7.35]. This condition can be explained by the fact that at higher input intensities, the phase grating is induced by strong Kerr non-linearity causing the reflectances to differ, $R_L \neq R_R$ as observed in a linear PTBG. It is noted that, when there is no saturation, the structure is dominated by $\mathcal{PT}$-symmetry at lower intensities. This shows that for a certain range of intensities ($I_{\text{PT-K}} < I < I_2$) both $\mathcal{PT}$ and non-linear behaviour are present and can be exploited simultaneously. At lower intensities $\mathcal{PT}$-behaviour is dominant,

whereas non-linear dynamics dominate at higher intensities.

In the case of $\alpha_0 = 800$ cm^{-1} and $I_{\text{sat}} = 2.5 \times 10^{13}$ W/m^2, the transmittance decreases as the intensity increases and after $I_1 = 5 \times 10^{13}$ W/m^2 overlaps with the transmittance of a passive non-linear Bragg grating with $\alpha_0 = 0$. Figure 7.16(b) further shows that the reflectances for this case are the same regardless of the side of incidence. Similarly, the reflectances overlap with that of the passive grating structure ($\alpha_0 = 0$) at very high intensities. This can be explained by the fact that saturation reduces the effective gain and loss in the structure, thus prohibiting $\mathcal{PT}$-behaviour at high input intensities. At higher intensities, $I_1 > 5 \times 10^{13}$ W/m^2, the behaviour of the K-NPTBG corresponds to the nonlinear Bragg grating with no gain and loss. Therefore, low saturation intensity causes the gain and loss to saturate early and thus inhibits the asymmetric behaviour $R_L \neq R_R$ of a PTBG.

Now, consider the region where we can manipulate both $\mathcal{PT}$ and non-linear behaviour. Figure 7.17 shows the frequency response, obtained by Fourier transformation of the time-domain signal, for the case in Fig. 7.16 when $\alpha_0 = 800$ cm^{-1} and the gain and loss saturation is turned off ($\mathbb{S} = 1$) for three different input beam intensities, i.e. $I_L = 7 \times 10^8$, $I_U = 5.65 \times 10^{14}$, and $I_2 = 1 \times 10^{15}$ W/m^2, as marked in Fig. 7.16. The intensity of I_U is when the unidirectional invisibility occurs as shown in Fig. 7.16. Results obtained by the T-matrix method are included for reference. Generally the transmittance is the same for the left and right incidence but reflectances differ for input intensities of I_U and I_2. Figure 7.17(a) shows the impact of input beam intensity on the the transmittance spectrum. The transmittance at low input intensity, I_L, fits with the one calculated using the T-matrix method. However, at high input intensity, I_U, i.e., at the unidirectional invisibility operation, almost-total transmittance $T \approx 1$ is observed at the Bragg frequency. Further increase of the input intensity increases the background index modulation even further, which reduces the impact of the gain and loss resulting in a more defined band-gap.

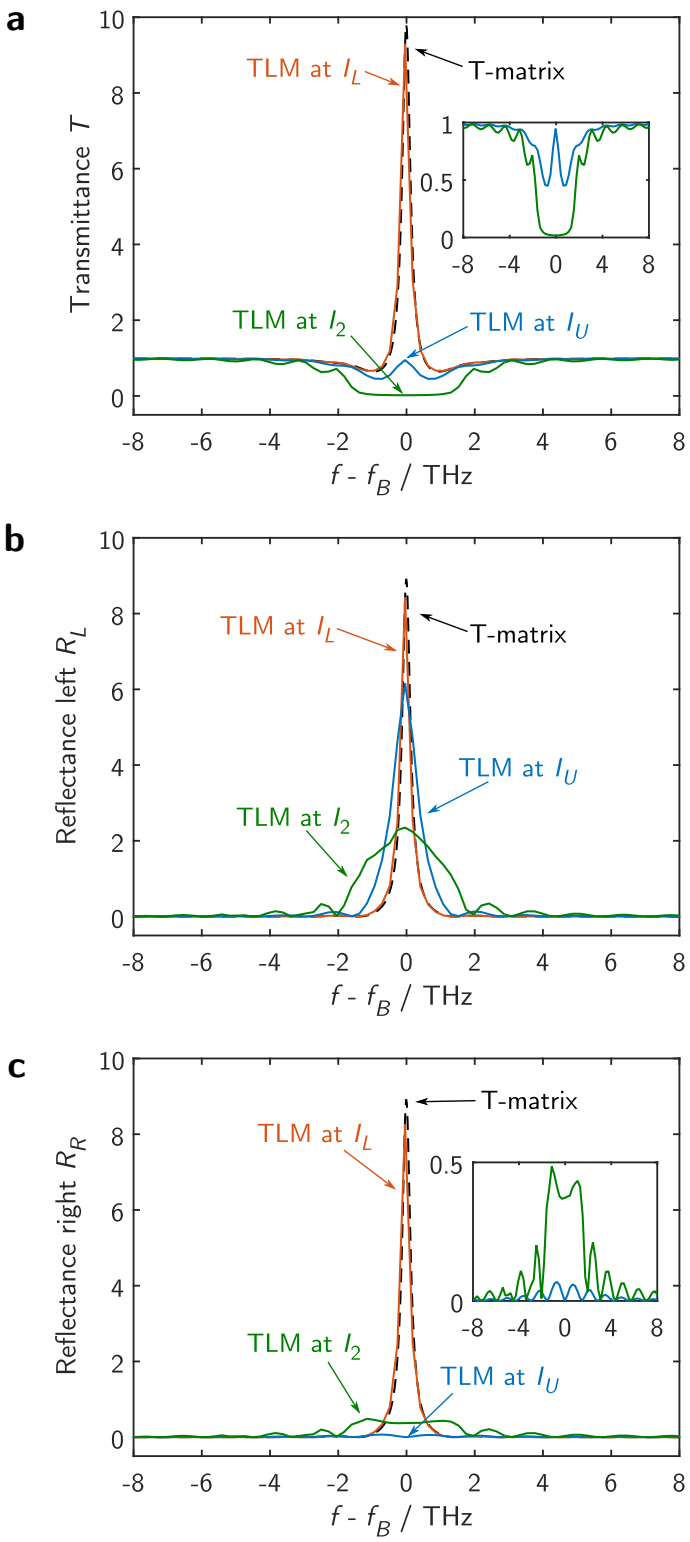

Figure 7.17 | Spectra of the transmitted and reflected probe signal for different input signal intensities. (**a**) Transmittance, (**b**) reflectance R_L for signal incident from left and (**c**) reflectance R_R for signal incident from right side of the grating, for 3 different input intensities namely, $I_L = 7 \times 10^8$, $I_U = 5.65 \times 10^{14}$, and $I_2 = 1 \times 10^{15}$ W/m^2. For all cases the gain/loss saturation is turned off $\mathbb{S} = 1$. For clarity, the insets are showing the magnified spectra.

The reflectances R_L and R_R are shown in Fig. 7.17(b) and Fig. 7.17(c) respectively. For low input intensity, I_L, the TLM calculations agree with the results calculated by the T-matrix method, showing that the structure operates in a linear regime. However, when operated at the unidirectional point with intensity I_U, the reflectances are different, showing that the Kerr non-linearity induced a strong phase grating [7.31,7.34,7.35]. Further increase in input intensity to I_2 reduces the reflectance R_L while increasing the reflectance R_R, which again can be explained by the fact that as the input intensity increases, the Kerr non-linearity induced modulation of the background refractive index becomes more dominant and reduces the impact of gain and loss in the system resulting in a more pronounced band-gap property of the structure.

7.4.3 Intensity Driven All-Optical Logical Gate Device by Kerr Non-linear $\mathcal{PT}$-Bragg Grating

In this section, a potential applications of the K-NPTBG by controlling the level of the pump beam is investigated. The input signal comprises of both aweak probe beam and a strong pump beam. The probe beam is a CW signal operated at the Bragg frequency $f_{\text{probe}} = 336.85$ THz with low intensity and is kept constant throughout the simulation with intensity $I_{\text{probe}} = 1 \times 10^6$ W/m^2. The pump beam is a CW signal operated far from the Bragg frequency at $f_{\text{pump}} = 200$ THz. The intensities of the pump beam are switched between two different values i.e., $I_1 = 5 \times 10^{13}$ W/m^2 and $I_2 = 1 \times 10^{15}$ W/m^2 which are marked in Fig. 7.16(a). The gain/loss has a saturation intensity $I_{\text{sat}} = 2.5 \times 10^{13}$ W/m^2 as in Fig. 7.16.

Figure 7.18(a) shows the pump beam as a function of time, initially turned "off" and then turned "on" to intensity I_1 for a duration of 10 ps, followed by an increase of intensity to I_2 for another 10 ps, and then repeating the same pattern. The probe beam is set to be constant throughout the simulation as shown in Fig. 7.18(b).

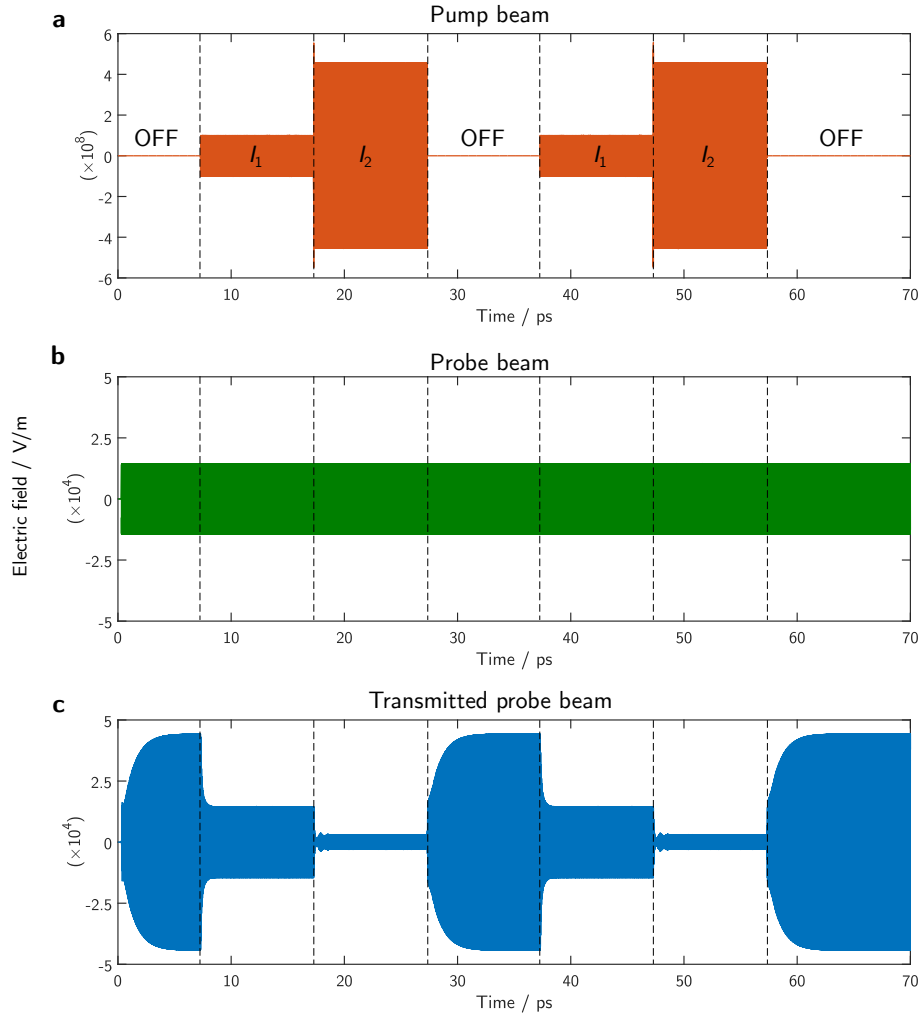

Figure 7.18 | Logical gate operation using K-NPTBG structure. Time domain response of the K-PTBG grating of (**a**) the pump beam, (**b**) the input probe beam and (**c**) the transmitted probe beam.

Figure 7.18(c) shows the transmitted probe field when the grating is excited from the left. It can be seen that when the pump beam is switched off, the probe beam intensity is amplified by almost 10 times. A subsequent increase in the pump beam intensity to I_1 causes a decrease in the transmitted probe beam to the same value as the input probe beam ($T = 1$). When the pump beam intensity is increased to I_2, the transmitted probe field is significantly reduced.

It is important to note that the change in response occurs almost instantaneously, with the longest switching time being 2.5 ps. Figure 7.18(a,c) demonstrates that the

K-NPTBG can potentially be used as an optical amplifier (when the pump beam is turned off), optical switch (by using the pump beam to control the ON/OFF output of the probe beam) or as an optical negation logic gate, i.e. modulation of probe beam by the pump beam whereby the presence of a strong pump beam (logic 1) produces a low probe beam content (logic 0).

7.5 Summary

This chapter described the implementation of a non-linear material property in the TLM model by using the Duffing equation. A realistic GaAs-based material dispersion was fitted to the Duffing model and used throughout to study a non-linear $\mathcal{PT}$-symmetric Bragg grating structure. Two different $\mathcal{PT}$-symmetric Bragg structures were studied in this chapter, namely a simple non-linear $\mathcal{PT}$-Bragg Grating (NPTBG) and Kerr-induced $\mathcal{PT}$-Bragg Grating (K-NPTBG).

For both structures, it was found that gain/loss saturation plays an important role in the exploitation of the non-linear behaviour. A high saturation intensity is essential to allow an interplay between $\mathcal{PT}$-behaviour and Kerr non-linearity behaviour. It is, however, noted that if the saturation effect is neglected, the unbounded gain/loss in the material may cause instability for the high intensity non-linear operations. Furthermore, a low saturation intensity may prohibit the $\mathcal{PT}$-behaviour in high intensity operation where the Kerr non-linearity starts to take effect.

This chapter proposed and demonstrated two applications based on non-linear $\mathcal{PT}$-Bragg gratings, namely a memory device and a logical gate device. The results shown that the non-linear $\mathcal{PT}$-Bragg grating is a promising platform for building a novel optical information processing devices. Moreover it is shown that non-linear $\mathcal{PT}$-symmetric based devices offer more degrees of freedom in their operation, such as gain/loss and input signal intensity, compared to a passive non-linear devices

which can only be manipulated by the input signal intensity.

References

[7.1] K. Iizuka, *Elements of Photonics, Vol II* (John Wiley, New York, NY, 2002).

[7.2] A. Yariv and P. Yeh, *Photonics: Optical Electronics in Modern Communications* (Oxford University Press, New York, NY, 2007), 6th ed.

[7.3] J.-M. Liu, *Photonic Devices* (Cambridge University Press, Cambridge, 2005).

[7.4] R. Joseph and A. Taflove, "FDTD Maxwell's equations models for nonlinear electrodynamics and optics," IEEE Trans. Antennas Propag. **45**, 364–374 (1997).

[7.5] A. Taflove and S. C. Hagness, *Computational Electrodynamics: The Finite-Difference Time-Domain Method* (Artech House, New York, NY, 2005), 3rd ed.

[7.6] J. Paul, C. Christopoulos, and D. Thomas, "Generalized material models in TLM - part III: Materials with nonlinear properties," IEEE Trans. Antennas Propag. **50**, 997–1004 (2002).

[7.7] Fatkhulla Kh. Abdullaev and V. V. Konotop, *Nonlinear Waves: Classical and Quantum Aspects*, vol. 153 of *NATO Science Series II: Mathematics, Physics and Chemistry* (Springer Netherlands, Dordrecht, 2005).

[7.8] A. I. Maimistov and J.-G. Caputo, "Propagation of extremely short pulses in nonresonant media: the total MaxwellDuffing model," Phys. D Nonlinear Phenom. **189**, 107–114 (2004).

[7.9] E. V. Kazantseva, A. I. Maimistov, and J.-G. Caputo, "Reduced Maxwell-Duffing description of extremely short pulses in nonresonant media," Phys. Rev. E **71**, 056622 (2005).

[7.10] V. Janyani, A. Vukovic, and J. Paul, "The development of TLM models for nonlinear optics," Microw. Rev. **10**, 35–42 (2004).

[7.11] V. Janyani, A. Vukovic, J. D. Paul, P. Sewell, and T. M. Benson, "Time domain simulation in photonics: A comparison of nonlinear dispersive polarisation models," Opt. Quantum Electron. **37**, 3–24 (2005).

[7.12] V. Janyani, J. Paul, A. Vukovic, T. Benson, and P. Sewell, "TLM modelling of nonlinear optical effects in fibre Bragg gratings," IEE Proc. - Optoelectron. **151**, 185 (2004).

[7.13] C. Conti, A. Di Falco, and G. Assanto, "Optical parametric oscillations in isotropic photonic crystals," Opt. Express **12**, 823 (2004).

[7.14] A. E. Siegman, *Lasers* (University Science Book, Palo Alto, CA, 1986).

[7.15] B. E. A. Saleh and M. C. Teich, *Fundamentals of Photonics* (John Wiley, New York, NY, 2007), 2nd ed.

[7.16] S. Phang, A. Vukovic, H. Susanto, T. M. Benson, and P. Sewell, "Impact of dispersive and saturable gain/loss on bistability of nonlinear parity-time Bragg gratings," Opt. Lett. **39**, 2603–6 (2014).

[7.17] A. H. Kachare, W. G. Spitzer, and J. E. Fredrickson, "Refractive index of ion-implanted GaAs," J. Appl. Phys. **47**, 4209 (1976).

[7.18] J. Aitchison, D. Hutchings, J. Kang, G. Stegeman, and A. Villeneuve, "The nonlinear optical properties of AlGaAs at the half band gap," IEEE J. Quantum Electron. **33**, 341–348 (1997).

[7.19] C. Paré, A. Villeneuve, P.-A. A. Bélanger, and N. J. Doran, "Compensating for dispersion and the nonlinear Kerr effect without phase conjugation," Opt. Lett. **21**, 459–461 (1996).

[7.20] W. H. Press, S. A. Teukolsky, W. T. Vetterling, and B. P. Flannery, *Numerical Recipes in C++: The Art of Scientific Computing* (Cambridge University Press, Cambridge, 2002), 2nd ed.

[7.21] T. Skauli, P. S. Kuo, K. L. Vodopyanov, T. J. Pinguet, O. Levi, L. A. Eyres, J. S. Harris, M. M. Fejer, B. Gerard, L. Becouarn, and E. Lallier, "Improved dispersion relations for GaAs and applications to nonlinear optics," J. Appl. Phys. **94**, 6447 (2003).

[7.22] D. E. Aspnes, S. M. Kelso, R. A. Logan, and R. Bhat, "Optical properties of AlxGa1x As," J. Appl. Phys. **60**, 754 (1986).

[7.23] M. Bass, G. Li, and E. van Stryland, *Handbook of optics vol. 4* (McGraw Hill, New York, NY, 2010), 3rd ed.

[7.24] A. Suryanto, E. van Groesen, M. Hammer, and H. J. W. M. Hoekstra, "A finite element scheme to study the nonlinear optical response of a finite grating without and with defect," Opt. Quantum Electron. **35**, 313–332 (2003).

[7.25] V. M. Agranovich, S. A. Kiselev, and D. L. Mills, "Optical multistability in nonlinear superlattices with very thin layers," Phys. Rev. B **44**, 10917–10920 (1991).

[7.26] M. Robertson, Private communication, October 2015.

[7.27] S. C. Hagness, R. M. Joseph, and A. Taflove, "Subpicosecond electrodynamics of distributed Bragg reflector microlasers: Results from finite difference time domain simulations," Radio Sci. **31**, 931–941 (1996).

[7.28] S. Phang, A. Vukovic, S. C. Creagh, T. M. Benson, P. D. Sewell, and G. Gradoni, "Parity-time symmetric coupled microresonators with a dispersive gain/loss," Opt. Express **23**, 11493 (2015).

[7.29] L. Brzozowski and E. Sargent, "Optical signal processing using nonlinear distributed feedback structures," IEEE J. Quantum Electron. **36**, 550–555 (2000).

[7.30] S. Lan, A. V. Gopal, K. Kanamoto, and H. Ishikawa, "Ultrafast response of photonic crystal atoms with Kerr nonlinearity to ultrashort optical pulses," Appl. Phys. Lett. **84**, 5124–5126 (2004).

[7.31] S. Phang, A. Vukovic, H. Susanto, T. M. Benson, and P. Sewell, "Ultrafast optical switching using paritytime symmetric Bragg gratings," J. Opt. Soc. Am. B **30**, 2984–2991 (2013).

[7.32] S. Nixon, L. Ge, and J. Yang, "Stability analysis for solitons in PT-symmetric optical lattices," Phys. Rev. A **85**, 023822 (2012).

[7.33] Y. D. Chong, L. Ge, and A. D. Stone, "PT-symmetry breaking and laser-absorber modes in optical scattering systems," Phys. Rev. Lett. **106**, 093902 (2011).

[7.34] M. Kulishov, J. M. Laniel, N. Bélanger, J. Azaña, and D. V. Plant, "Nonreciprocal waveguide Bragg gratings," Opt. Express **13**, 3068–78 (2005).

[7.35] Z. Lin, H. Ramezani, T. Eichelkraut, T. Kottos, H. Cao, and D. N. Christodoulides, "Unidirectional invisibility induced by PT-symmetric periodic structures," Phys. Rev. Lett. **106**, 213901 (2011).

8

The Transmission-Line Model of Electromagnetics in 2D

In this chapter the formulation of a two-dimensional (2D) Transmission-Line Model (TLM) method is presented. In particular, the chapter extends the implementation of the digital filter design of realistic dispersive and saturable gain/loss model which was developed for one-dimensional (1D) in Chapter 5 and was used to model realistic $\mathcal{PT}$-symmetric Bragg gratings previously in Chapter 6.

* * *

8.1 TLM Formalism in 2D Domain

In this thesis, the development of the 2D-TLM model is defined in the Cartesian coordinate system, i.e. (x, y, z). As such Maxwell's equations (2.1) can be expanded to its axis components as,

$$\begin{cases} (\nabla \times \boldsymbol{H}) \cdot \hat{x} &= J_{ex} + \dfrac{\partial D_x}{\partial t} \\ (\nabla \times \boldsymbol{H}) \cdot \hat{y} &= J_{ey} + \dfrac{\partial D_y}{\partial t} \\ (\nabla \times \boldsymbol{H}) \cdot \hat{z} &= J_{ez} + \dfrac{\partial D_z}{\partial t} \end{cases} \tag{8.1}$$

$$\begin{cases} (\nabla \times \boldsymbol{E}) \cdot \hat{x} &= -\dfrac{\partial B_x}{\partial t} \\ (\nabla \times \boldsymbol{E}) \cdot \hat{y} &= -\dfrac{\partial B_y}{\partial t} \\ (\nabla \times \boldsymbol{E}) \cdot \hat{z} &= -\dfrac{\partial B_z}{\partial t} \end{cases} \tag{8.2}$$

where $\hat{x}$, $\hat{y}$ and $\hat{z}$ are unit vector elements in the x, y and z direction and $(\ \cdot\ )$ denotes the vector product. The rest of the field quantities are defined in Table. 2.1.

In 2D, the electromagnetic fields ($E_{x,y,z}$ and $H_{x,y,z}$) are invariant in one direction. For consistency, it is taken to be the z-direction hence,

$$\frac{\partial}{\partial z} \equiv 0. \tag{8.3}$$

Implementation of condition (8.3) within (8.1) and (8.2) leads to two sets of uncoupled Maxwell's equations associated to E_z or H_z. As such an E-type wave has E_z as the primary field component and an H-type wave has H_z as the primary field component throughout this thesis. It is emphasised here that although in several publications in the literature [8.1–8.3], the E-type and H-type waves are also referred to as the TE and TM polarised wave, in this thesis the use of TE and TM notations will be restricted to denote *guided* waves in a waveguide structure.

8.1.1 *E*-Type Wave Nodal Scattering Process

The Maxwell's equations for E-type waves, are given by,

$$\begin{aligned}(\nabla \times \boldsymbol{E}) \cdot \hat{x} &= -\frac{\partial B_x}{\partial t}, \\ (\nabla \times \boldsymbol{E}) \cdot \hat{y} &= -\frac{\partial B_y}{\partial t}, \\ (\nabla \times \boldsymbol{H}) \cdot \hat{z} &= J_{ez} + \frac{\partial D_z}{\partial t}.\end{aligned} \tag{8.4}$$

Upon substituting the constitutive relations (2.2)-(2.4), (8.4) can also be expressed as,

$$\begin{aligned}(\nabla \times \boldsymbol{E}) \cdot \hat{x} &= -\mu_0 \frac{\partial H_x}{\partial t}, \\ (\nabla \times \boldsymbol{E}) \cdot \hat{y} &= -\mu_0 \frac{\partial H_y}{\partial t}, \\ (\nabla \times \boldsymbol{H}) \cdot \hat{z} &= \sigma_e * E_z + \varepsilon_0 \frac{\partial E_z}{\partial t} + \frac{\partial P_{ez}}{\partial t},\end{aligned} \tag{8.5}$$

It is important to note that a non-magnetic material has been assumed in (8.5), $\mu = \mu_0$ and $\boldsymbol{M} = 0$, as it was discussed in Chapter 2. From the transmission-line theory [8.2–8.5] , a 4-port *shunt* transmission line, which is obtained by concatenating the 1D transmission lines (see Fig. 8.1), can be utilised to model the E-type wave propagation. Figure 8.1 depicts the schematic of a single 2D-TLM shunt node in a Cartesian system along with the voltage at each of its 4 ports.

It can be seen from Fig. 8.1 that the shunt node has 4 ports which, for consistency with [8.2,8.3,8.6–8.9], are called ports 8, 9, 10 and 11. Hence the corresponding voltages at these ports are denoted as V_8, V_9, V_{10} and V_{11}. Moreover the differential

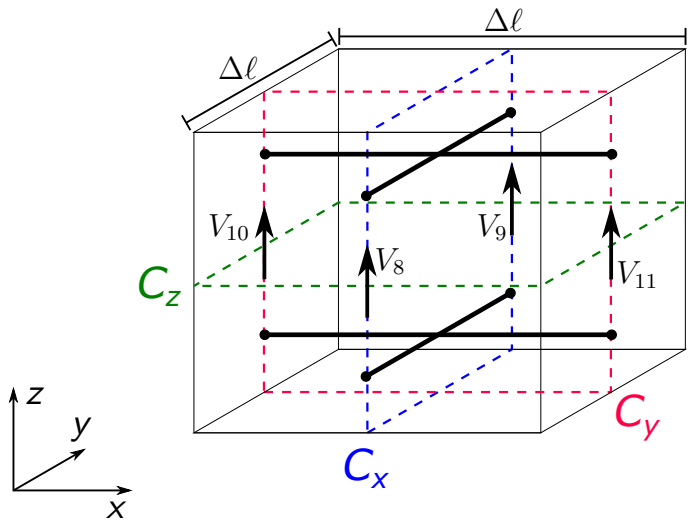

Figure 8.1 | Schematic of 2D-TLM nodes for an E-type wave. A structured TLM meshing paradigm is considered, i.e. rectangle based meshing. Three different integration contour C_x, C_y and C_z are denoted by its normal axis.

operators ∇ and $\partial/\partial t$ can be normalised by $\Delta\ell$ and Δt as (5.22),

$$\begin{cases} \dfrac{1}{\Delta\ell}(\bar{\nabla}\times\boldsymbol{E})\cdot\hat{x} &= -\mu_0\dfrac{1}{\Delta t}\dfrac{\partial H_x}{\partial T} \\ \dfrac{1}{\Delta\ell}(\bar{\nabla}\times\boldsymbol{E})\cdot\hat{y} &= -\mu_0\dfrac{1}{\Delta t}\dfrac{\partial H_y}{\partial T} \\ \dfrac{1}{\Delta\ell}(\bar{\nabla}\times\boldsymbol{H})\cdot\hat{z} &= \sigma_e * E_z + \varepsilon_0\dfrac{1}{\Delta t}\dfrac{\partial E_z}{\partial T} + \dfrac{1}{\Delta t}\dfrac{\partial P_{ez}}{\partial T} \end{cases} \tag{8.6}$$

where, $T \equiv t\Delta t$ and $\bar{\nabla} \equiv \nabla\Delta\ell$ are the (dimensionless) normalised parameters, $\Delta\ell$ denotes the length of the side of an unit cell and Δt denote the time step of the TLM calculation. The relation between $\Delta\ell$ and Δt is discussed below. Furthermore, by implementing the field-circuit equivalences (See Table 5.1), the Maxwell's equations (8.6) can be shown in the circuit form as,

$$\begin{cases} -\dfrac{1}{\Delta\ell^2}(\bar{\nabla}\times\boldsymbol{V})\cdot\hat{x} &= \mu_0\dfrac{1}{Z_{\mathrm{TL}}\Delta\ell\Delta t}\dfrac{\partial i_x}{\partial T}, \\ -\dfrac{1}{\Delta\ell^2}(\bar{\nabla}\times\boldsymbol{V})\cdot\hat{y} &= \mu_0\dfrac{1}{Z_{\mathrm{TL}}\Delta\ell\Delta t}\dfrac{\partial i_y}{\partial T}, \\ \dfrac{1}{Z_{\mathrm{TL}}\Delta\ell^2}(\bar{\nabla}\times\boldsymbol{i})\cdot\hat{z} &= \dfrac{\sigma_e}{\Delta\ell} * V_z + \dfrac{\varepsilon_0}{\Delta\ell\Delta T}\dfrac{\partial V_z}{\partial T} + \dfrac{\varepsilon_0}{\Delta\ell\Delta t}\dfrac{\partial p_{ez}}{\partial T}. \end{cases} \tag{8.7}$$

Since a TLM model based on structured meshing is developed in this thesis, i.e.

rectangular based spatial discretisation in 2D, where $\Delta x = \Delta y = \Delta \ell$, it is customary to define the transmission-line impedance Z_{TL} and the unit transit time Δt to correspond to the properties of wave propagation in free-space with a 45° angle [8.2–8.4,8.6–8.10] as,

$$\begin{aligned} Z_{\mathrm{TL}} &= \frac{\eta_0}{\sin 45^\circ} = \sqrt{2}\,\eta_0, \\ v_{\mathrm{TL}} &= \frac{\Delta \ell}{\Delta t} = \frac{c_0}{\cos 45^\circ} = \sqrt{2}\,c_0, \end{aligned} \tag{8.8}$$

where v_{TL} denotes the velocity of voltage pulse propagation between TLM nodes and $c_0 = 1/\sqrt{\varepsilon_0 \mu_0}$ and $\eta_0 = \sqrt{\mu_0/\varepsilon_0}$ respectively denote the free-space speed of light and the free-space wave impedance of a normal wave propagation. Substituting (8.8) into (8.7), yields

$$\begin{cases} -(\bar{\nabla} \times \boldsymbol{V}) \cdot \hat{x} &= \dfrac{\partial i_x}{\partial T}, \\ -(\bar{\nabla} \times \boldsymbol{V}) \cdot \hat{y} &= \dfrac{\partial i_y}{\partial T}, \\ (\bar{\nabla} \times \boldsymbol{i}) \cdot \hat{z} &= g_e * V_z + 2\dfrac{\partial V_z}{\partial T} + 2\dfrac{\partial p_{ez}}{\partial T}. \end{cases} \tag{8.9}$$

Using the Stokes' theorem to solve the curl operations on the contours C_x, C_y and C_z indicated in Fig. 8.1, leads to

$$\begin{cases} -(V_9 - V_8) &= \dfrac{\partial i_x}{\partial T}, \\ -(V_{10} - V_{11}) &= \dfrac{\partial i_y}{\partial T}, \\ (V_8 + V_9 + V_{10} + V_{11}) &= g_e * V_z + 2\dfrac{\partial V_z}{\partial T} + 2\dfrac{\partial p_{ez}}{\partial T}. \end{cases} \tag{8.10}$$

After transforming the normalised time derivative to the Laplace domain,

$$\begin{cases} -(V_9 - V_8) &= \bar{s} i_x, \\ -(V_{10} - V_{11}) &= \bar{s} i_y, \\ (V_8 + V_9 + V_{10} + V_{11}) &= g_e V_z + 2\bar{s} V_z + 2\bar{s} p_{ez}. \end{cases} \tag{8.11}$$

Utilising the travelling-wave form format [8.2,8.6–8.9] of the port voltage, (8.10) can be expressed as,

$$\begin{cases} -2(V_9^i - V_8^i) & = 2i_x \\ -2(V_{10}^i - V_{11}^i) & = 2i_y \\ 2(V_8^i + V_9^i + V_{10}^i + V_{11}^i) & = g_e V_z + 4V_z + 2\bar{s}p_{ez} \end{cases} \tag{8.12}$$

Equations (8.12) are the governing equations for the TLM nodal voltage calculation which are ready for material implementation. Subsequently, after calculating the nodal field values i_x, i_y and V_z, the new scattered voltage impulses in the condensed TLM nodes can be obtained by [8.2,8.6–8.9],

$$\begin{cases} V_8^r = V_z - i_x - V_9^i \\ V_9^r = V_z + i_x - V_8^i \\ V_{10}^r = V_z + i_y - V_{11}^i \\ V_{11}^r = V_z - i_y - V_{10}^i \end{cases} \tag{8.13}$$

8.1.2 TLM Shunt Nodes Internodal Connection Process

Following the nodal and scattering calculation, the TLM algorithm continues with the internodal connection process. In the connection process, the new calculated reflected voltage impulses are communicated to the adjacent nodes which become the new incident voltage impulses. Hence it can be shown that by performing,

$$\underset{T}{\begin{bmatrix} V_8[X,Y] \\ V_9[X,Y] \\ V_{10}[X,Y] \\ V_{11}[X,Y] \end{bmatrix}^r} \rightarrow \underset{T+1}{\begin{bmatrix} V_9[X,Y-1] \\ V_8[X,Y+1] \\ V_{11}[X-1,Y] \\ V_{10}[X+1,Y] \end{bmatrix}^i} \tag{8.14}$$

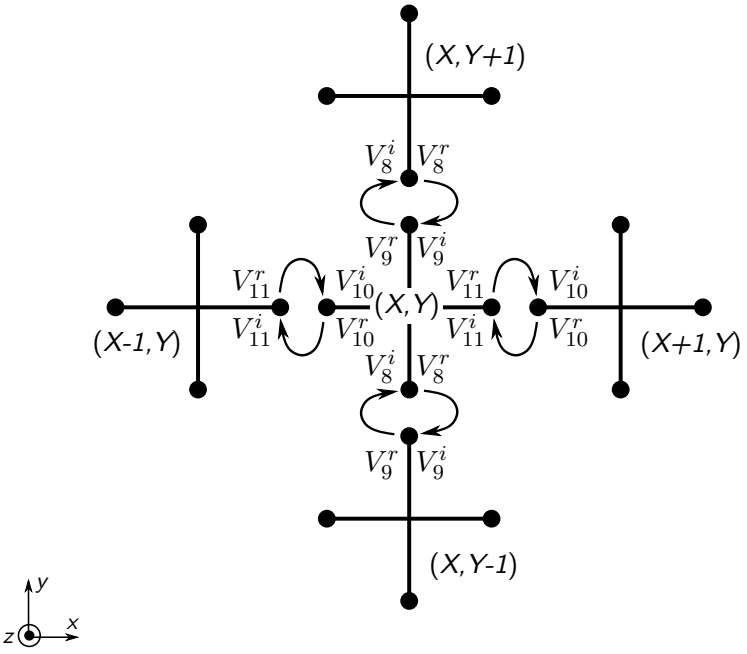

Figure 8.2 | Schematic illustration of TLM connection process.

on every node within the computation window, the information is passed to the neighbouring nodes and in that way mimics the wave propagation in space. This connection process is schematically illustrated in Fig. 8.2 for a node located at (X, Y).

8.1.3 TLM Matched Boundary Condition

The connection processes described in Section 8.1.2 are executed on all nodes within the computation space *except* at the boundary. At the boundary a special treatment is required, according to the application of the simulation. The simplest boundary conditions are PEC and PMC boundary conditions [8.1,8.3]. The PEC boundary condition mimics a termination of the simulation window by a *Perfectly Electric Conducting* wall; hence the voltage at the port next to the boundary is set to zero. This is accomplished by short circuiting the boundary port and the reflected voltage

for such aboundary is,

$$V^r_{\text{on boundary}} = -V^i_{\text{on boundary}} \tag{8.15}$$

Meanwhile the PMC boundary condition stands for *Perfect Magnetic Conductance* wall. Thus the voltage at the port on the boundary is maximum; this is realised by an open circuit at the port on the boundary and the scattered voltage is,

$$V^r_{\text{on boundary}} = V^i_{\text{on boundary}} \tag{8.16}$$

Another kind of important boundary condition is the radiating boundary condition. Different types of radiating boundary condition have been reported for the TLM and the FDTD methods namely, Engquist-Majda Boundary Condition (BC), Higdon BC, Ramahi BC, Berenger's *Perfectly Matched Layer* (PML) scheme [8.1, and references therein]. In this thesis, a simpler matching boundary condition is implemented which gives good approximation of the radiating boundary condition [8.2–8.4,8.6–8.9]. This is accomplished by matching the impedance of the *modelled* material with the impedance of the transmission-line [8.2–8.4,8.6–8.9]. The reflected wave for a matched boundary is given by,

$$V^r_{\text{on boundary}} = \Gamma V^i_{\text{on boundary}}, \tag{8.17}$$

where Γ is the reflection coefficient given as,

$$\Gamma = \frac{Z_{\text{material}} - Z_{\text{TL}}}{Z_{\text{material}} + Z_{\text{TL}}}, \tag{8.18}$$

where the impedance of the material is related to the refractive index of the material, i.e. $Z_{\text{material}} = \eta_0 / n_{\text{material}}$.

8.2 TLM Shunt Node Model for Realistic Gain Medium

In this section, the TLM shunt node model is developed to model the realistic dispersive and saturable gain/loss medium which was previously implemented in the 1D-TLM nodes. Performing the $\mathcal{Z}$-bilinear transformation on the normalised Laplace variable $\bar{s}$,

$$i_x^i = -i_x, \tag{8.19}$$

$$i_y^i = -i_y, \tag{8.20}$$

$$2V_z^i = (4 + g_e)V_z + 2\left(2\frac{1 - z^{-1}}{1 + z^{-1}}\right)\chi_e V_z, \tag{8.21}$$

where for convenience in (8.21) the incoming pulses have been renamed as i_x^i, i_y^i and V_z^i and are given by

$$\begin{aligned} i_x^i &= V_9^i - V_8^i \\ i_y^i &= V_{10}^i - V_{11}^i \\ V_z^i &= V_8^i + V_9^i + V_{10}^i + V_{11}^i \end{aligned}$$

It can be seen from (8.19) and (8.20) that the TLM model for E-type waves and a non-magnetic material has a simple nodal calculation for the transverse field components (i_x and i_y). The material parameters responsible for dielectric modelling χ_e and gain/loss g_e are only found in (8.21) which is responsible for the calculation of electric field V_z. Thus for clarity, consider (8.21) which after multiplying both sides by $(1 + z^{-1})$ and some rearrangement, yields

$$(1 + z^{-1})(2V_z^i - 4V_z) = (1 + z^{-1})g_e V_z + 4(1 - z^{-1})\chi_e V_z \tag{8.22}$$

By substituting the digital filter for conductivity, (5.37), into (8.22) and after some rearrangement, (8.22) becomes

$$2V_z^i + z^{-1}S_{ez} = K_{e2}V_z \tag{8.23}$$

where the accumulated delayed variable S_{ez},

$$\begin{aligned} S_{ez} &= 2V_z^i + K_{e1}V_z + S_{ecz}, \\ S_{ecz} &= -\bar{g}_e V_z, \end{aligned} \tag{8.24}$$

and the constants K_{e1} and K_{e2} are given by,

$$K_{e1} = -(4 + g_{e1} - 4\chi_e), \tag{8.25}$$

$$K_{e2} = 4 + g_{e0} + 4\chi_e. \tag{8.26}$$

It is important to note that constants g_{e0} and g_{e1} are the same as the ones given in (5.38) and are reproduced below,

$$\begin{aligned} g_{e0} &= g_s \left(\frac{K_3}{K_6} \right), \\ g_{e1} &= 0, \\ \bar{g}_e(z) &= \frac{b_0 + z^{-1}b_1 + z^{-2}b_2}{1 - z^{-1}(-a_1) - z^{-2}(-a_2)}. \end{aligned} \tag{8.27}$$

Details of the digital filter design of the conductivity are given in Section 5.3.4. Moreover, the updating scheme for the conductivity S_{ecz} is the same as shown in Fig. 5.5(b). In summary the nodal calculation in the presence of a gain medium is comprised of (8.19), (8.20) and (8.23) which are subsequently followed by the updating scheme (8.24).

8.3 Summary

This chapter has summarised the 2D TLM method for an E-type electromagnetic wave. The alternative 2D TLM algorithm based on the bilinear $\mathcal{Z}$-transformation is used which offers greater flexibility on modelling dispersive material model in comparison of the traditional TLM scheme based on lumped-circuit element. The chapter presented the voltage node scattering, connection and also boundary conditions. Finally the digital filter procedure for implementing a realistic saturable gain (or loss) medium is presented. The 2D TLM model is used in the next chapter to model $\mathcal{PT}$-symmetric resonant structure and real-time analysis.

References

[8.1] A. Taflove and S. C. Hagness, *Computational Electrodynamics: The Finite-Difference Time-Domain Method* (Artech House, New York, NY, 2005), 3rd ed.

[8.2] J. Paul, "Modelling of general electromagnetic material properties in TLM," Ph.D. thesis, University of Nottingham (1998).

[8.3] C. Christopoulos, *The Transmission-Line Modeling Method TLM* (IEEE Press, Piscataway, 1995).

[8.4] V. Janyani, "Modelling of dispersive and nonlinear materials for optoelectronics using TLM," Ph.D. thesis, University of Nottingham (2005).

[8.5] V. Janyani, A. Vukovic, and J. Paul, "The development of TLM models for nonlinear optics," Microw. Rev. **10**, 35–42 (2004).

[8.6] J. Paul, C. Christopoulos, and D. Thomas, "Time-domain modelling of negative refractive index material," Electron. Lett. **37**, 1–2 (2001).

[8.7] J. Paul, C. Christopoulos, and D. Thomas, "Generalized material models in TLM - part II: Materials with anisotropic properties," IEEE Trans. Antennas Propag. **47**, 1528–1534 (1999).

[8.8] J. Paul, C. Christopoulos, and D. Thomas, "Generalized material models in TLM - part I: Materials with frequency-dependent properties," IEEE Trans. Antennas Propag. **47**, 1528–1534 (1999).

[8.9] J. Paul, C. Christopoulos, and D. Thomas, "Generalized material models in TLM - part III: Materials with nonlinear properties," IEEE Trans. Antennas Propag. **50**, 997–1004 (2002).

[8.10] C. A. Balanis, *Advanced Engineering Electromagnetics: Traditions v. 2* (John Wiley, NJ, 2012), 2nd ed.

9

Parity-Time Symmetric Coupled Microresonators With a Realistic Gain/Loss

This chapter investigates the fundamental properties of the $\mathcal{PT}$-resonant system based on two coupled whispering gallery resonators within the contexts both of realistic material properties and practical operating constraints. In particular the chapter will discuss how practical dispersive properties of material gain and loss that satisfy the Kramers-Kronig relationship affect the performance of microcavity-based $\mathcal{PT}$-resonant structures. The theoretical background for an isolated circular resonator is also overviewed. An exact analytical model based on the Boundary Integral Equation (BIE) method is developed to calculate the characteristic frequencies of $\mathcal{PT}$-symmetric microresonators.

* * *

9.1 $\mathcal{PT}$-Symmetric Coupled Microresonators

In this section the theoretical background of a $\mathcal{PT}$-symmetric system based on two coupled microresonators is described. The system, in which both microresonators have radius a and are separated by a gap g, is illustrated schematically in Fig. 9.1. The active and passive microresonators have complex refractive indices n_G and n_L respectively, that are chosen to satisfy the $\mathcal{PT}$-symmetric refractive index condition $n_G = n_L^*$, where * denotes complex conjugate, $n = (n' + jn'')$, and n' and n'' represent the real and imaginary parts of the refractive index. In practice, localised gain might be achieved by means of erbium doping and optical pumping of the active microresonator or electrical pumping with GaAs-based material, while masking the lossy microresonator as in [9.1–9.6]. Both resonators are assumed to be surrounded by air.

The refractive index of dispersive materials is frequency dependent but must also satisfy the causality property between the real and imaginary parts of the material refractive index [9.7,9.8]. The material properties are conveniently modelled by assuming a linear dielectric constant that uses a Lorentzian model for dispersion as described in Section 5.1

$$\varepsilon_r(\omega) = \varepsilon_\infty - j\frac{\sigma_0}{2\varepsilon_0\omega}\left(\frac{1}{1+j(\omega+\omega_\sigma)\tau} + \frac{1}{1+j(\omega-\omega_\sigma)\tau}\right). \tag{9.1}$$

Here ε_∞ denotes the permittivity at infinity, ω_σ denotes the atomic transitional angular frequency, τ is the dipole relaxation time and σ_0 is related to the conductivity peak value that is set by the pumping level at ω_σ. The time variation has been assumed to be of the form $e^{j\omega t}$ and therefore $\sigma_0 > 0$ denotes loss while $\sigma_0 < 0$ denotes gain. The parameter τ controls the degree of dispersion, with $\tau = 0$ corresponding to a dispersion-less system. Throughout this chapter, the frequency-domain refractive index is expressed as $n = \sqrt{\varepsilon_r(\omega)}$ and the material gain/loss parameter is expressed using the imaginary part of the refractive index as $\gamma = \omega n''$.

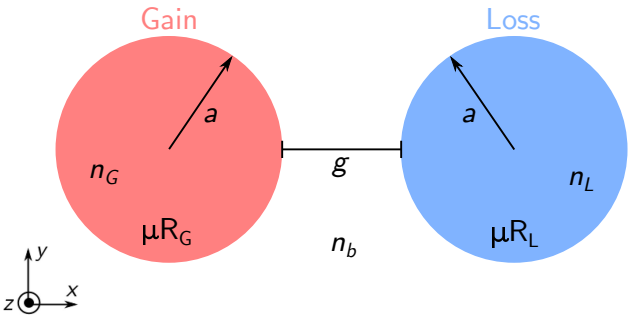

Figure 9.1 | Schematic of $\mathcal{PT}$-symmetric resonators. Microresonators with gain and loss are denoted by μR_G and μR_L, respectively.

9.2 Resonant Frequencies of an Isolated Circular Resonator

Before looking at the coupling problem between two resonators, this section will first overview the solutions of the Maxwell's equations for an isolated cylindrical dielectric resonator with radius a. For convenience, consider Helmholtz equation defined in a cylindrical coordinate system (r, θ, z) for the E-type wave electric field component $\mathcal{E}_z$,

$$\left(\frac{\partial^2}{\partial r^2} + \frac{1}{r}\frac{\partial}{\partial r} + \frac{1}{r^2}\frac{\partial^2}{\partial \theta^2} + \frac{\partial^2}{\partial z^2}\right)\mathcal{E}_z - (k_0 n)^2 \mathcal{E}_z = 0. \tag{9.2}$$

Assuming no variation in the z-direction, as in (8.3), (9.2) can be reduced to,

$$\left(\frac{\partial^2}{\partial r^2} + \frac{1}{r}\frac{\partial}{\partial r} + \frac{1}{r^2}\frac{\partial^2}{\partial \theta^2}\right)\mathcal{E}_z - (k_0 n)^2 \mathcal{E}_z = 0 \tag{9.3}$$

where $k_0 = \omega/c_0$ denotes the free-space wave-number and n is the refractive index of the material. Solution for (9.3) could be obtained by a separation of variables ansats for $\mathcal{E}_z$ [9.9–9.11]. Once the solution for $\mathcal{E}_z$ is obtained the rest of the field components for an E-type wave, $\mathcal{H}_r$ and $\mathcal{H}_\theta$, can directly be obtained by substituting $\mathcal{E}_z$ into

Maxwell's equations,

$$\frac{1}{r}\frac{\partial \mathcal{E}_z}{\partial \theta} = -j\omega\mu_0\mathcal{H}_r, \tag{9.4}$$

$$-\frac{\partial \mathcal{E}_z}{\partial r} = -j\omega\mu_0\mathcal{H}_\theta, \tag{9.5}$$

$$\frac{1}{r}\frac{\partial (r\mathcal{H}_\theta)}{\partial r} - \frac{\partial \mathcal{H}_r}{\partial \theta} = j\omega\varepsilon\mathcal{E}_z. \tag{9.6}$$

Now, consider that the solution of $\mathcal{E}_z$ is comprised of two functions, $R(r)$ and $P(\theta)$ which are independent functions of the radius r and azimuthal parameter θ respectively. Substituting $\mathcal{E}_z(r,\theta) = R(r)P(\theta)$ to (9.3) yields,

$$\frac{d^2P}{d\theta^2} + k_\theta^2 P = 0, \tag{9.7}$$

$$r^2\frac{d^2R}{dr^2} + r\frac{dR}{dr} + (r^2(k_0 n)^2 - k_\theta^2)R = 0. \tag{9.8}$$

These two ordinary differential equations can be solved independently. The solution of (9.7) is,

$$P(\theta) = C_\theta \mathrm{e}^{jk_\theta\theta}. \tag{9.9}$$

Moreover, since $P(\theta)$ has to be periodic in the azimuthal direction, $\theta = \theta + 2m\pi$, it leads to condition that k_θ has to be an integer. Hence (9.9) can be rewritten as,

$$P(\theta) = C_\theta \mathrm{e}^{jm\theta} \quad \text{, where} \quad m = \pm 1, \pm 2, \pm 3, \cdots \tag{9.10}$$

where C_θ is a constant which will be obtained later by enforcing appropriate boundary conditions.

The ordinary differential equation in (9.8) has known solutions named the Bessel function of the first kind J_m and the Bessel function of the second kind Y_m [9.12, 9.13]. The physical condition decides the appropriate solution between the two

possible functions. For instance, the value of the Bessel function of the second kind Y_m approaches negative infinity at 0 and hence is not applicable as part of the solution of (9.8) *inside* the resonator. However *outside* the resonator the field should satisfy radiation condition, the radiating cylindrical function can be either a Hankel function of order m of the first kind ($H_m^{(1)} = J_m + jY_m$) or second kind ($H_m^{(2)} = J_m - jY_m$). The Hankel function of the second kind is chosen here $H_m^{(2)}$ which is representing an outgoing wave, see Appendix C. It follows that the solution to the differential equation (9.8) is,

$$R(r) = \begin{cases} C_r^{\text{in}} J_m(nk_0 r) & \text{for } \; r < a \qquad (9.11a) \\ C_r^{\text{out}} H_m(k_0 r) & \text{for } \; r > a \qquad (9.11b) \end{cases}$$

where for notation simplicity in (9.11b), $H_m^{(2)}$ has been written as H_m and C_r is a constant defined by enforcing the boundary conditions. The total solution $\mathcal{E}_z$ can be found as,

$$\mathcal{E}_z(r,\theta) = \begin{cases} C^{\text{in}} J_m(nk_0 r) \mathrm{e}^{jm\theta} & \text{for } r < a \\ C^{\text{out}} H_m(k_0 r) \mathrm{e}^{jm\theta} & \text{for } r > a \end{cases}, \qquad (9.12)$$

where the constants $C^{\text{in/out}}$ is the product of the two constants contribution, $C^{\text{in/out}} = C_r^{\text{in/out}} C_\theta$. The tangential magnetic field $\mathcal{H}_\theta$ can be obtained directly by substituting (9.12) into (9.5),

$$\mathcal{H}_\theta(r,\theta) = \frac{1}{j\omega\mu_0} \begin{cases} C^{\text{in}} k_0 n J_m'(nk_0 r) \mathrm{e}^{jm\theta} & \text{for } r < a \\ C^{\text{out}} k_0 H_m'(k_0 r) \mathrm{e}^{jm\theta} & \text{for } r > a \end{cases}. \qquad (9.13)$$

Now in order to get the complete solution, the boundary conditions are applied which require that the tangential electric field $\mathcal{E}_z$ and the tangential magnetic field

$\mathcal{H}_\theta$ are continuous at the dielectric boundary, i.e.

$$\begin{aligned} \mathcal{E}_z(a-\delta,\theta) &= \mathcal{E}_z(a+\delta,\theta) \qquad \text{when} \quad \delta \to 0 \\ \mathcal{H}_\theta(a-\delta,\theta) &= \mathcal{H}_\theta(a+\delta,\theta) \qquad \text{when} \quad \delta \to 0 \end{aligned} \tag{9.14}$$

where δ is an infinitesimal distance from the boundary. By applying this condition, it can be found that the interior constants are related to the exterior constants by

$$\frac{C^{\text{in}}}{C^{\text{out}}} = \frac{H_m(k_0 a)}{J_m(n k_0 a)} \tag{9.15}$$

$$\frac{C^{\text{in}}}{C^{\text{out}}} = \frac{H'_m(k_0 a)}{n J'_m(n k_0 a)}. \tag{9.16}$$

Equating (9.15) and (9.16) yields,

$$J_m(a k_0 n) H'_m(a k_0) - n H_m(a k_0) J'_m(a k_0 n) = 0. \tag{9.17}$$

By solving the transcendental equation (9.17) for k_0, the resonant frequency associated with the azimuthal mode m can be obtained as $f_{\text{res}} = k_0 c_0/(2\pi)$.

In contrast to a metallic resonator, where the metal wall provides a high confinement to the field, dielectric resonators are inherently lossy as the dielectric boundary may let the field escape to the surrounding environment typically referred to *radiation losses*. As such the resonant frequencies of a dielectric resonator are complex valued, $f_{\text{res}} = f'_{\text{res}} + j f''_{\text{res}}$. In order to quantify the amount of energy escaping the resonator a *quality factor* Q is used. The Q-factor is defined as the ratio of energy stored to the energy escaping the resonator, and is related to the resonant frequency as [9.14–9.23],

$$Q = \frac{f'_{\text{res}}}{2 f''_{\text{res}}}. \tag{9.18}$$

The Q-factor is an indication of the duration of the transient in the resonator, or in

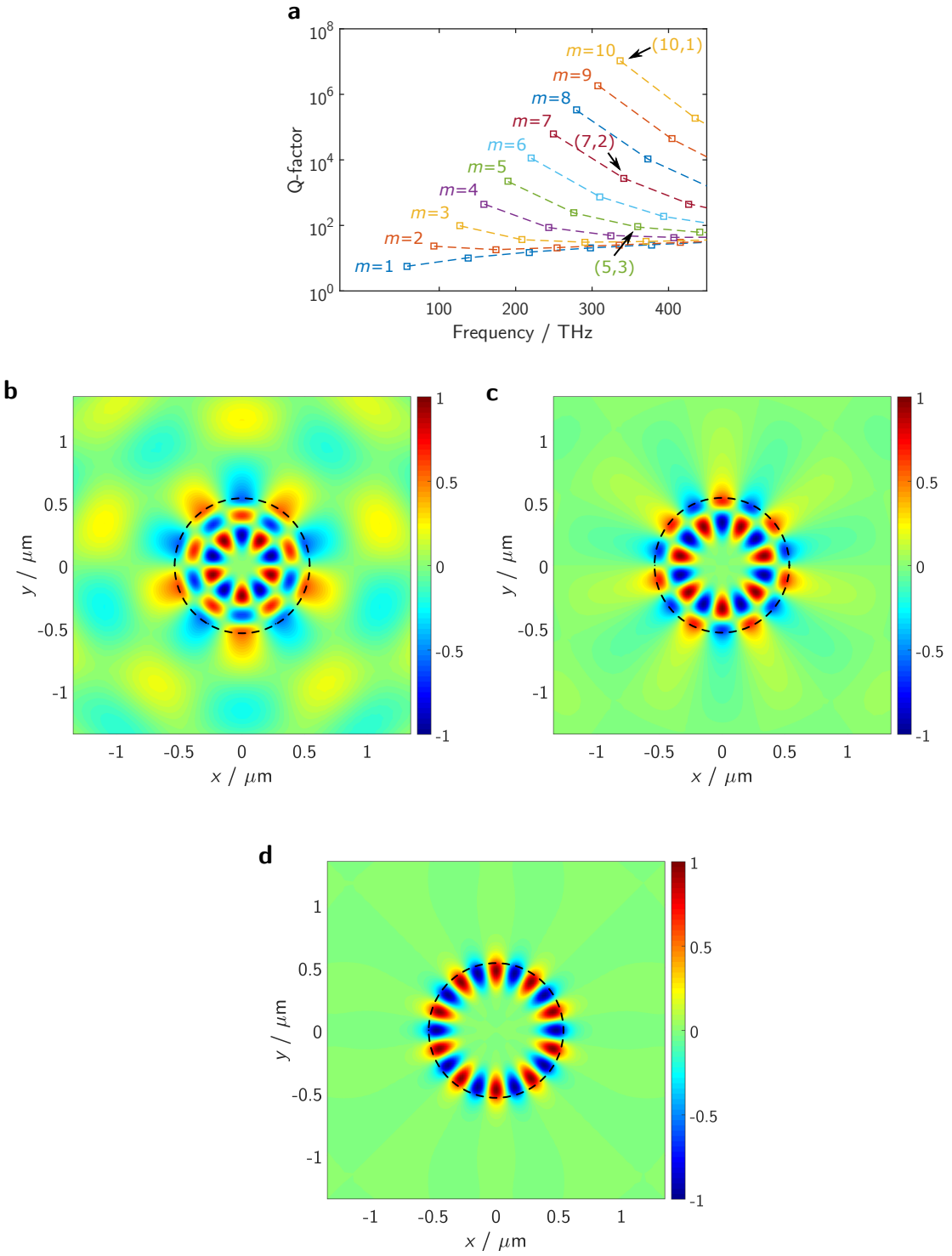

Figure 9.2 | Whispering-gallery modes (WGM) of a cylindrical resonators. (**a**) Resonant frequencies plotted with respect to the Q-factor. Spatial field profile amplitude E_z for (**b**) WGM(5,3), (**c**) WGM(7,2) and (**d**) WGM(10,1). Dashed line denotes the microresonator boundary.

other words when energy is coupled to the resonator, the Q-factor is related to the length of time over which the resonator is capable of holding that energy. Hence, the higher the value of Q-factor the smaller the radiation losses. Moreover, it is important to note that since the time-dependent component has been assumed in the form of $e^{j\omega t}$ and the real part of the resonant frequency f'_{res} is always positive, a *lossy* resonant mode is denoted by $+f''_{\text{res}}$ hence $+Q$-factor and vice-versa for *amplifying* resonant mode.

Figure 9.2 plots the Q-factor of the resonant modes of a circular resonator as a function of the real part of the resonant frequency (a) and field profiles of some of the resonant modes. Results are obtained for a passive circular resonator of radius $a = 0.53775$ μm with a refractive index of a typical GaAs-based material $n = 3.5$ and on air background $n_b = 1$. Figure 9.2(a) shows the resonant frequency for different orders of m between $0 - 450$ THz. It can be seen from the figure that the higher order resonant modes are located at higher frequencies. Moreover, higher order modes have higher Q-factors. It is emphasised here that the resonant frequencies of a resonator are discrete, and in Fig. 9.2(a) they are plotted as square bullet points; the dashed lines merely serve as a guide to the reader.

Figures 9.2(b-d) show the spatial field amplitude profile of E_z obtained by using the TLM method. In the TLM simulation the resonators are excited by an electric dipole located near the boundary, i.e. $0.2a$ from the boundary. The electric dipole is excited with a Gaussian-type pulse modulated at the resonant frequency of the mode of interest, $f_{\text{res}}^{(5,3)} = 359.3125$ THz, $f_{\text{res}}^{(7,2)} = 341.5849$ THz and $f_{\text{res}}^{(10,1)} = 336.8524$ THz with FWHM of 0.4 ps in order to provide a very narrow bandwidth source. The resonant frequencies and the associated Q-factors are marked in Fig. 9.2(a). Note that the mode number (m, n) is used to refer to the azimuthal and the radial order respectively. As such it can be seen from Fig. 9.2(b) that there are five pairs of field maxima and minima in the azimuthal direction and three peaks in the radial

direction. In comparison the Whispering-Gallery Mode (WGM)[‡] (7,2) has 7 pairs of maxima-minima in the azimuthal direction and two peaks in the radial direction: WGM (10,1) (Fig. 9.2(d)) has 10 pairs of maxima-minima in the azimuthal direction and only one peak in the radial direction.

9.3 Analysis of Inter-Resonator Coupling in the Frequency Domain

An analysis of coupling between resonators based on boundary integral methods is now given. This approach is particularly suited to a perturbative approximation of the coupling strength in the weak coupling limit, but also provides an efficient platform for exact calculation when coupling is strong. The calculation is based on an approach used in [9.25] to describe coupling between fully bound states in coupled resonators and optical fibres, but is adapted here to allow for radiation losses. It is also similar to methods used in [9.14,9.15,9.19–9.21].

9.3.1 Notation and Assumptions

The coupled $\mathcal{PT}$-microresonator depicted in Fig. 9.1 is now considered. For consistency the subscripts "G" and "L" are used for variables associated with the gain and lossy resonators respectively. Both resonators have radius a and uniform refractive index, with the electric field polarized along the resonator axis.

From the previous section, it is known that the electric field $\mathcal{E}_z$ takes the form $\psi_L = \dfrac{J_m(n_L k_0 r)}{J_m(n_L k_0 a)} \mathrm{e}^{jm\theta}$ inside the isolated lossy resonator and its normal derivative

[‡]Historically, the term whispering-gallery mode come from an observation by Lord Rayleigh in St Paul's Cathedral, London in which he observes that one's whispers at a point on the cathedral's dome wall can be heard periodically around the dome wall [9.24].

on the boundary of the resonator can be written as

$$a\frac{\partial \psi_L}{\partial n} = F_m^L \psi_L, \tag{9.19}$$

where

$$F_m^L = (n_L k_0 a)\frac{J'_m(n_L k_0 a)}{J_m(n_L k_0 a)}, \tag{9.20}$$

where, k_0 is the free-space wave number and ψ_G and F_m^G are defined similarly for the gain resonator. It is emphasised that for notation simplicity, ψ_L has been adopted to denote the electric field $\mathcal{E}_z$ on the lossy resonator and ψ_G for the electric field $\mathcal{E}_z$ on the gain resonator.

9.3.2 Graf's Addition Theorem

In the next subsection, the coupling of two circular resonators is studied. As a prelude to this, the present subsection will overview Graf's addition theory. Graf's addition theory allows us to displace one cylindrical system of coordinates into another using Bessel function expansion. Consider $\mathscr{F}$, which can be any function from the Bessel function family J, Y, $H^{(1)}$, $H^{(2)}$ or indeed any linear combination of them. The following relation is valid [9.13],

$$\mathscr{F}_m(W)e^{jn\chi} = \sum_{n=-\infty}^{\infty} \mathscr{F}_{m+n}(U)J_n(V)\mathrm{e}^{jn\alpha}, \quad \text{with} \quad U > V \tag{9.21}$$

where in this thesis U, V and W are real numbers defining distances. As such they can be interpreted as the edges of a triangle [9.13] as illustrated in Fig. 9.3.

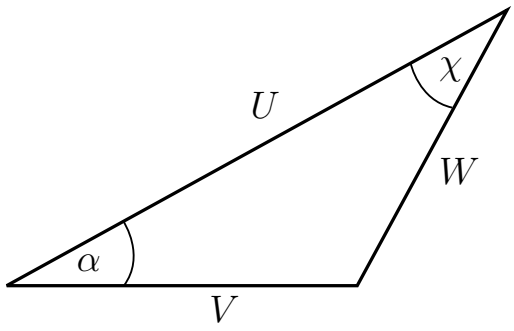

Figure 9.3 | Graf's addition theorem triangle.

9.3.3 Exact Solution Using Boundary-Integral Representation

In this subsection, coupling between two dielectric circular resonators is studied using the Boundary Intergal Equation (BIE) method. Expanding the solution on each resonator boundary as a Fourier series, the solution can be written as

$$\psi_G = \sum_m \varphi_m^G \mathrm{e}^{jm\theta_G} \qquad \text{and} \qquad \psi_L = \sum_m \varphi_m^L \mathrm{e}^{jm\theta_L}, \tag{9.22}$$

in the polar angles θ_G and θ_L centred respectively on the gain and lossy resonators, running in opposite senses in each resonator and zeroed on the line joining the two centres. The corresponding normal derivatives at each boundary can be written as:

$$\frac{\partial \psi_G}{\partial n} = \sum_m \frac{1}{a} F_m^G \varphi_m^G \mathrm{e}^{jm\theta_G} \qquad \text{and} \qquad \frac{\partial \psi_L}{\partial n} = \sum_m \frac{1}{a} F_m^L \varphi_m^L \mathrm{e}^{jm\theta_L}. \tag{9.23}$$

An exact boundary integral representation of the coupled problem is conveniently achieved by applying Green's identities to a region Ω which excludes the resonators, along with an infinitesimally small layer surrounding them (so that the boundaries B_G and B_L of the resonators themselves lie just outside Ω), see Fig. 9.4. In Ω, we assume that the refractive index takes the value $n_0 = 1$, so that the free-space Green

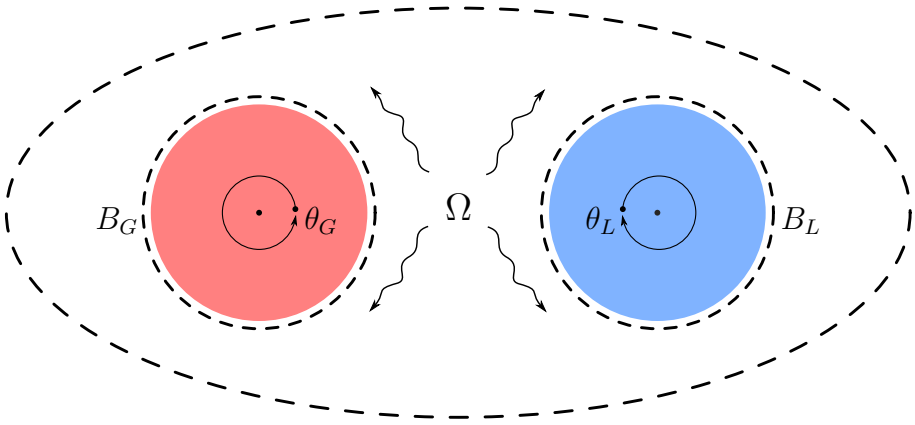

Figure 9.4 | Integration region Ω around the resonators system.

function is, see Appendix C,

$$G_0(\mathbf{x}, \mathbf{x}') = -\frac{j}{4} H_0(k_0|\mathbf{x} - \mathbf{x}'|), \tag{9.24}$$

where $\mathbf{x}$ and $\mathbf{x}'$ are the receiver and the source points and $H_0(z) = J_0(z) - jY_0(z)$ denotes the Hankel function of the second kind (and the solution is assumed to have time dependence $\mathrm{e}^{j\omega t}$). Then, applying Green's identities to the region Ω and assuming radiating boundary conditions at infinity leads to the equation,

$$0 = \int_{B_G + B_L} \left(G_0(\mathbf{x}, \mathbf{x}') \frac{\partial \psi(\mathbf{x}')}{\partial n'} - \frac{\partial G_0(\mathbf{x}, \mathbf{x}')}{\partial n'} \psi(\mathbf{x}') \right) \mathrm{d}s' \tag{9.25}$$

when $\mathbf{x}$ lies on either B_L or B_G (and therefore just outside of Ω).

Using Graf's addition theorem, see Subsection 9.3.2, the Green's function $G_0(\mathbf{x}, \mathbf{x}')$ is expanded analogously in polar coordinates on each boundary. First with respect to the triangle $\mathbf{x}'\ O_L\ \mathbf{x}$ (see Fig. 9.5), it can be shown that,

$$\begin{aligned} H_0(k_0|\mathbf{x} - \mathbf{x}'|) &= \sum_{\ell} H_\ell(k_0 \mathbf{r}') J_\ell(k_0 a) \mathrm{e}^{j\ell(\theta_L - \theta'_L)} \\ &= \sum_{\ell} \left(H_\ell(k_0 \mathbf{r}') \mathrm{e}^{-j\ell\theta'_L} \right) J_\ell(k_0 a) \mathrm{e}^{j\ell\theta_L}. \end{aligned} \tag{9.26}$$

Expanding the term in the bracket in (9.26) with respect to triangle $O_G\ \mathbf{x}'\ O_L$ (see

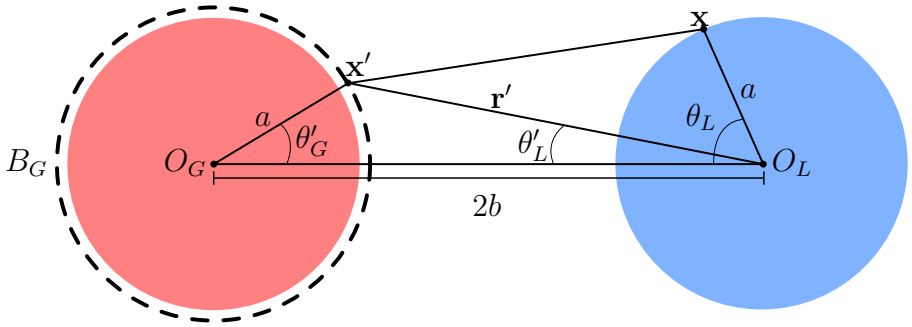

Figure 9.5 | Expansion of the free-space Green's function between the 2-coupled resonators by the Graf's addition theorem. Cross-contribution from the gain resonator to the lossy resonator.

Fig. 9.5), yields

$$H_\ell(k_0\mathbf{r}')\mathrm{e}^{-j\ell\theta'_L} = \sum_{\ell'} H_{\ell+\ell'}(2bk_0)J_{\ell'}(k_0a)\mathrm{e}^{-j\ell'\theta'_G}. \tag{9.27}$$

Substituting (9.27) to (9.26), the Green's function can be expressed as,

$$G_0(\mathbf{x},\mathbf{x}') = -\frac{j}{4}\sum_{\ell}\sum_{\ell'} H_{\ell+\ell'}(2bk_0)J_{\ell'}(k_0a)J_\ell(k_0a)\mathrm{e}^{j\ell\theta_L - j\ell'\theta'_G}, \tag{9.28}$$

with the corresponding normal derivatives of the Green function,

$$\frac{\partial G_0(\mathbf{x},\mathbf{x}')}{\partial n'} = -\frac{jk_0}{4}\sum_{\ell}\sum_{\ell'} H_{\ell+\ell'}(2bk_0)J'_{\ell'}(k_0a)J_\ell(k_0a)\mathrm{e}^{j\ell\theta_L - j\ell'\theta'_G}. \tag{9.29}$$

Then Green's boundary integral on the lossy resonator due to the presence of gain resonator is

$$\int_{B_G}\left(G_0(\mathbf{x},\mathbf{x}')\frac{\partial\psi(\mathbf{x}')}{\partial n'} - \frac{\partial G_0(\mathbf{x},\mathbf{x}')}{\partial n'}\psi(\mathbf{x}')\right)\mathrm{d}s', \tag{9.30}$$

where the first term is calculated by,

$$\begin{aligned}&\int_{B_G} G_0(\mathbf{x},\mathbf{x}')\frac{\partial\psi(\mathbf{x}')}{\partial n'}\mathrm{d}s' \\ &= -\frac{j}{4a}\sum_{m\ell\ell'}\varphi_m^G F_m^G H_{\ell+\ell'}(2bk_0)J_{\ell'}(k_0a)J_\ell(k_0a)\mathrm{e}^{j\ell\theta_L}\oint \mathrm{e}^{j(m-\ell')\theta'_G}d\theta'_G.\end{aligned} \tag{9.31}$$

Due to the orthogonality of the trigonometric function,

$$\oint\sum_{m\ell'}\mathrm{e}^{j(m-\ell')\theta'_G}d\theta'_G = \begin{cases}2\pi & \text{for} \quad m=\ell' \\ 0 & \text{for} \quad m\neq\ell'\end{cases}, \tag{9.32}$$

equation (9.31) can be simplified to,

$$\int_{B_G} G_0(\mathbf{x},\mathbf{x}')\frac{\partial\psi(\mathbf{x}')}{\partial n'}\mathrm{d}s' = -j\frac{\pi}{2a}\sum_{m\ell}\varphi_m^G F_m^G H_{\ell+m}(2bk_0)J_m(k_0a)J_\ell(k_0a)\mathrm{e}^{j\ell\theta_L}. \tag{9.33}$$

The second term of (9.30) is calculated as,

$$\begin{aligned}&\int_{B_G}\frac{\partial G_0(\mathbf{x},\mathbf{x}')}{\partial n'}\psi(\mathbf{x}')\mathrm{d}s' \\ &= -\frac{jk_0}{4}\sum_{m\ell\ell'}\varphi_m^G H_{\ell+\ell'}(2bk_0)J'_{\ell'}(k_0a)J_\ell(k_0a)\mathrm{e}^{j\ell\theta_L}\oint \mathrm{e}^{j(m-\ell')\theta'_G}d\theta'_G,\end{aligned} \tag{9.34}$$

which due to the orthogonality property of the trigonometric function can be simplified to,

$$\int_{B_G}\frac{\partial G_0(\mathbf{x},\mathbf{x}')}{\partial n'}\psi(\mathbf{x}')\mathrm{d}s' = -j\frac{\pi k_0}{2}\sum_{m\ell}\varphi_m^G H_{\ell+m}(2bk_0)J'_m(k_0a)J_\ell(k_0a)\mathrm{e}^{j\ell\theta_L}. \tag{9.35}$$

The Green's boundary integral for the lossy resonator is now,

$$\begin{aligned}&\int_{B_G}\left(G_0(\mathbf{x},\mathbf{x}')\frac{\partial\psi(\mathbf{x}')}{\partial n'} - \frac{\partial G_0(\mathbf{x},\mathbf{x}')}{\partial n'}\psi(\mathbf{x}')\right)\mathrm{d}s' \\ &= -j\frac{\pi}{2a}\sum_{m\ell}\varphi_m^G H_{\ell+m}(2bk_0)J_\ell(k_0a)\mathrm{e}^{j\ell\theta_L}\left[F_m^G J_m(k_0a) - k_0aJ'_m(k_0a)\right].\end{aligned} \tag{9.36}$$

Likewise, the Green's boundary integral on the gain resonator due to the presence

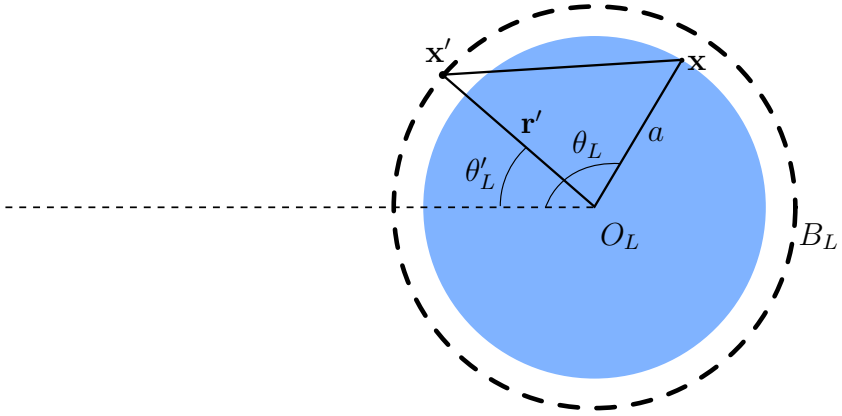

Figure 9.6 | Expansion of the self-contribution Green's function by the Graf's addition theorem.

of the lossy resonator,

$$\begin{aligned}&\int_{B_L}\left(G_0(\mathbf{x},\mathbf{x}')\frac{\partial\psi(\mathbf{x}')}{\partial n'}-\frac{\partial G_0(\mathbf{x},\mathbf{x}')}{\partial n'}\psi(\mathbf{x}')\right)\mathrm{d}s'\\&=-j\frac{\pi}{2a}\sum_{m\ell}\varphi_m^L H_{\ell+m}(2bk_0)J_\ell(k_0a)\mathrm{e}^{j\ell\theta_G}\left[F_m^L J_m(k_0a)-k_0aJ'_m(k_0a)\right]\end{aligned}\tag{9.37}$$

As such (9.36) describes the contribution of the gain resonator to the lossy resonator while (9.37) describes the contribution of the lossy resonator to the gain resonator.

Following the cross-contribution to the Green's integral, the self-contributions to the Green's integral can be calculated. First consider only the lossy resonator as depicted in Fig. 9.6. The self-contribution of the lossy resonator can be calculated as,

$$\int_{B_L}\left(G_0(\mathbf{x},\mathbf{x}')\frac{\partial\psi(\mathbf{x}')}{\partial n'}-\frac{\partial G_0(\mathbf{x},\mathbf{x}')}{\partial n'}\psi(\mathbf{x}')\right)\mathrm{d}s'.\tag{9.38}$$

As before, first expand the free-space Green's function with respect to the triangle $\mathbf{x}'$ O_L $\mathbf{x}$. By using the Graf's theorem, the Hankel function can be expanded as,

$$H_0(k_0|\mathbf{x}-\mathbf{x}'|)=\sum_\ell H_\ell(k_0\mathbf{r}')J_\ell(k_0a)\mathrm{e}^{j\ell(\theta_L-\theta'_L)}.\tag{9.39}$$

As such the Green's function and its derivative at the boundary are given by

$$G_0(\mathbf{x},\mathbf{x}') = -\frac{j}{4}\sum_{\ell} H_\ell(k_0\mathbf{r}')J_\ell(k_0a)\mathrm{e}^{j\ell(\theta_L-\theta'_L)}, \tag{9.40}$$

$$\frac{\partial G_0(\mathbf{x},\mathbf{x}')}{\partial n'} = -j\frac{k_0}{4}\sum_{\ell} H'_\ell(k_0a)J_\ell(k_0a).\mathrm{e}^{j\ell(\theta_L-\theta'_L)} \tag{9.41}$$

Integrating the first term in (9.38) gives,

$$\begin{aligned}
&\int_{B_L} G_0(\mathbf{x},\mathbf{x}')\frac{\partial\psi(\mathbf{x}')}{\partial n'}\mathrm{d}s' \\
&\quad= -\frac{j}{4a}\sum_{m\ell}\varphi_m^L F_m^L H_\ell(k_0a)J_\ell(k_0a)\mathrm{e}^{j\ell\theta_L}\oint \mathrm{e}^{j(m-\ell)\theta'_L}d\theta'_L \\
&\quad= -j\frac{\pi}{2a}\sum_{m}\varphi_m^L F_m^L H_m(k_0a)J_m(k_0a)\mathrm{e}^{jm\theta_L},
\end{aligned} \tag{9.42}$$

and integrating the second term results in,

$$\begin{aligned}
&\int_{B_L} \frac{\partial G_0(\mathbf{x},\mathbf{x}')}{\partial n'}\psi(\mathbf{x}')\mathrm{d}s' \\
&= -j\frac{k_0}{4}\sum_{m\ell}\varphi_m^L H'_\ell(k_0a)J_\ell(k_0a)\mathrm{e}^{j\ell\theta_L}\oint \mathrm{e}^{j(m-\ell)\theta'_L}d\theta'_L \\
&= -j\frac{\pi k_0}{2}\sum_{m}\varphi_m^L H'_m(k_0a)J_m(k_0a)\mathrm{e}^{jm\theta_L}.
\end{aligned} \tag{9.43}$$

Hence the Green's integral due to self-contribution of the lossy resonator is,

$$\begin{aligned}
&\int_{B_L}\left(G_0(\mathbf{x},\mathbf{x}')\frac{\partial\psi(\mathbf{x}')}{\partial n'} - \frac{\partial G_0(\mathbf{x},\mathbf{x}')}{\partial n'}\psi(\mathbf{x}')\right)\mathrm{d}s' \\
&= j\frac{\pi}{2a}\sum_{m}\varphi_m^L J_m(k_0a)\mathrm{e}^{jm\theta_L}\left[k_0aH'_m(k_0a) - F_m^L H_m(k_0a)\right].
\end{aligned} \tag{9.44}$$

Likewise, the self-contribution of the gain resonator can be obtained as,

$$\begin{aligned}
&\int_{B_G}\left(G_0(\mathbf{x},\mathbf{x}')\frac{\partial\psi(\mathbf{x}')}{\partial n'} - \frac{\partial G_0(\mathbf{x},\mathbf{x}')}{\partial n'}\psi(\mathbf{x}')\right)\mathrm{d}s' \\
&= j\frac{\pi}{2a}\sum_{m}\varphi_m^G J_m(k_0a)\mathrm{e}^{jm\theta_G}\left[k_0aH'_m(k_0a) - F_m^G H_m(k_0a)\right].
\end{aligned} \tag{9.45}$$

Summing the self-contribution and cross-contribution for each resonator and substituting in (9.25), it can be shown that the Green's boundary integral for the gain resonator becomes

$$\begin{aligned}&\sum_m J_m(k_0a)H_m(k_0a)\left[F_m^G - k_0a\frac{H_m'(k_0a)}{H_m(k_0a)}\right]\varphi_m^G\\ &+\sum_{m\ell} J_m(k_0a)H_{\ell+m}(2bk_0)J_\ell(k_0a)\left[F_m^L - k_0a\frac{J_m'(k_0a)}{J_m(k_0a)}\right]\varphi_m^L = 0,\end{aligned} \tag{9.46}$$

and for the lossy resonator,

$$\begin{aligned}&\sum_m J_m(k_0a)H_m(k_0a)\left[F_m^L - k_0a\frac{H_m'(k_0a)}{H_m(k_0a)}\right]\varphi_m^L\\ &+\sum_{m\ell} J_m(k_0a)H_{\ell+m}(2bk_0)J_\ell(k_0a)\left[F_m^G - k_0a\frac{J_m'(k_0a)}{J_m(k_0a)}\right]\varphi_m^G = 0.\end{aligned} \tag{9.47}$$

Equations (9.46) and (9.47) can also be expressed in matrix form as,

$$\begin{aligned}\boldsymbol{D}^G\varphi^G + \boldsymbol{C}^{GL}\varphi^L &= 0\\ \boldsymbol{C}^{LG}\varphi^G + \boldsymbol{D}^L\varphi^L &= 0,\end{aligned} \tag{9.48}$$

where,

$$\boldsymbol{\varphi}^G = \begin{pmatrix}\vdots\\ \varphi_m^G\\ \varphi_{m+1}^G\\ \vdots\end{pmatrix} \qquad \text{and} \qquad \boldsymbol{\varphi}^L = \begin{pmatrix}\vdots\\ \varphi_m^L\\ \varphi_{m+1}^L\\ \vdots\end{pmatrix} \tag{9.49}$$

are Fourier representations of the solution on the boundaries of the gain and lossy resonators respectively. The matrices D^G and D^L are diagonal with entries

$$D_{mm}^{G,L} = J_m(u)H_m(u)\left(F_m^{G,L} - \frac{uH_m'(u)}{H_m(u)}\right), \qquad \text{where } u = k_0a, \tag{9.50}$$

and provide the solutions for the isolated resonators. The matrices C^{GL} and C^{LG} de-

scribe coupling between the resonators. The matrix C^{GL} has entries of the form

$$C_{lm}^{GL} = J_l(u)H_{l+m}(w)J_m(u)\left(F_m^L - \frac{uJ'_m(u)}{J_m(u)}\right), \tag{9.51}$$

where $u = k_0 a$, $w = k_0 b$ and b is the centre-centre distance between the gain and lossy resonators as indicated in Fig. 9.1. The matrix C^{LG} is defined analogously by exchanging the labels G and L.

It is interesting to note that in the case of an non-interacting resonator, there is no coupling between the resonators, i.e. $C_{lm}^{GL} = C_{lm}^{LG} \equiv 0$; the self-contribution of the Green's integral $D_{mm}^{G,L}$ is then equivalent to (9.17) which describes the problem of the isolated single resonator.

9.3.4 $\mathcal{PT}$-Symmetry in the Exact Solution

The system (9.48) can be presented more symmetrically by using the scaled Fourier coefficients

$$\tilde{\varphi}_m^L = J_m(u)\left(F_m^L - \frac{uJ'_m(u)}{J_m(u)}\right)\varphi_m^L \tag{9.52}$$

(along with an analogous definition of $\tilde{\varphi}_m^G$). Then (9.48) can be rewritten

$$\begin{aligned} \tilde{\boldsymbol{D}}^G\tilde{\varphi}^G + \tilde{\boldsymbol{C}}\tilde{\varphi}^L &= 0 \\ \tilde{\boldsymbol{C}}\tilde{\varphi}^G + \tilde{\boldsymbol{D}}^L\tilde{\varphi}^L &= 0, \end{aligned} \tag{9.53}$$

where the diagonal matrices $\tilde{D}^{G,L}$ have entries

$$\tilde{D}_{mm}^{G,L} = -j\frac{H_m(u)F_m^{G,L} - uH'_m(u)}{J_m(u)F_m^{G,L} - uJ'_m(u)}, \qquad \text{where } u = k_0 a, \tag{9.54}$$

and the matrix $\tilde{C}$, with entries

$$\tilde{C}_{lm} = -jH_{l+m}(w), \tag{9.55}$$

couples solutions symmetrically in both directions.

An overall factor of $-j$ is included in these equations to emphasise an approximate $\mathcal{PT}$-symmetry that occurs when $n_G = n_L^*$. Then, in the limit of high-Q (low loss) whispering gallery resonances, the following approximations hold,

$$jH_m(u) \simeq Y_m(u) \qquad \text{and} \qquad jH_{l+m}(u) \simeq Y_{l+m}(u), \tag{9.56}$$

and the matrices in (9.53) satisfy the approximate conditions

$$\left(\tilde{D}^L\right)^* \simeq \tilde{D}^G \qquad \text{and} \qquad \tilde{C}^* \simeq \tilde{C}, \tag{9.57}$$

which are a manifestation of $\mathcal{PT}$-symmetry of the system as a whole: deviation from these conditions is a consequence of the radiation losses.

9.3.5 Perturbative Weak-Coupling Approximation

The system of (9.53) can be used as the basis of an efficient numerical method for determining the resonances of the coupled system with arbitrary accuracy. In practice, once the gap $g = b - 2a$ between the resonators is wavelength-sized or larger, a truncation of the full system to a relatively small number of modes suffices to describe the full solution.

In the limit of very weak coupling an effective perturbative approximation can be achieved by restricting our calculation to a single mode in each resonator. We

consider in particular the case of near left-right symmetry in which

$$n_G \approx n_L. \tag{9.58}$$

$\mathcal{PT}$-symmetry is achieved by further imposing $n_G = n_L^*$, but for now the effects of dispersion are allowed by assuming that this is not the case. The full solution is built around modes for which

$$\psi_\pm \approx \psi_G \pm \psi_L, \tag{9.59}$$

where ψ_G and ψ_L are the solutions of the isolated resonators described at the beginning of this section. A single value of m is used for both ψ_G and ψ_L and in particular the global mode is approximate using a chiral state in which the wave circulates in opposite senses in each resonator. That is, the coupling between m and $-m$ that occurs in the exact solution is neglected.

Then a simple perturbative approximation is achieved by truncating the full system of (9.53) to the 2×2 system

$$\mathbf{M} \begin{pmatrix} \tilde{\varphi}^G_{mm} \\ \tilde{\varphi}^L_{mm} \end{pmatrix} = 0, \qquad \text{where} \quad \mathbf{M} = \begin{pmatrix} \tilde{D}^G_{mm} & \tilde{C}_{mm} \\ \tilde{C}_{mm} & \tilde{D}^L_{mm} \end{pmatrix}. \tag{9.60}$$

Resonant frequencies of the coupled problem are then realised when

$$0 = \det \mathbf{M} = \tilde{D}^G_{mm}\tilde{D}^L_{mm} - \tilde{C}^2_{mm}. \tag{9.61}$$

In the general, dispersive and non-$\mathcal{PT}$-symmetric, case this reduces the calculation to a semi-analytic solution in which the (complex) roots of the known 2×2 determinant in (9.60) are sought, in which the matrix elements depend on frequency through both $k_0 = \omega/c$ and $n = n(\omega)$.

9.3.6 Further Analytic Development of the Perturbative Solution

To develop a perturbative expansion let,

$$D^0_{mm} = \frac{1}{2}\left(\tilde{D}^G_{mm} + \tilde{D}^L_{mm}\right) \qquad \text{and} \qquad D^I_{mm} = \frac{1}{2j}\left(\tilde{D}^G_{mm} - \tilde{D}^L_{mm}\right) \tag{9.62}$$

(and note that in the high-Q-factor $\mathcal{PT}$-symmetric case, $\tilde{D}^G \simeq (\tilde{D}^L)^*$, both D^0_{mm} and D^I_{mm} are approximately real). It is assumed that both D^I_{mm} and C_{mm} are small and comparable in magnitude. Expand the angular frequency

$$\omega_{1,2} = \omega_0 \pm \frac{\Delta\omega_0}{2} + \cdots \tag{9.63}$$

about a real resonant angular frequency of an averaged isolated resonator satisfying

$$D^0_{mm}(\omega_0) = 0. \tag{9.64}$$

Then to first order of accuracy the coupled resonance condition becomes

$$0 = \det \mathbf{M} = \Delta\omega_0^2 {D^0_{mm}}'(\omega_0)^2 + D^I_{mm}(\omega_0)^2 - \tilde{C}_{mm}(\omega_0)^2 + \cdots \tag{9.65}$$

from which the angular frequency shifts can be written as,

$$\frac{\Delta\omega_0}{2} = \frac{\sqrt{\tilde{C}_{mm}(\omega_0)^2 - D^I_{mm}(\omega_0)^2}}{{D^0_{mm}}'(\omega_0)}, \tag{9.66}$$

where ${D^0_{mm}}'(\omega)$ denotes a derivative of $D^0_{mm}(\omega)$ with respect to frequency.

The simple condition

$$\tilde{C}_{mm}(\omega_0)^2 = D^I_{mm}(\omega_0)^2 \tag{9.67}$$

is obtained for the threshold at which $\Delta\omega_0 = 0$ and the two resonant frequencies of the coupled system collide. In the $\mathcal{PT}$-symmetric case, where $\tilde{C}_{mm}$ and D^I_{mm} are approximately real (and whose small imaginary parts represent corrections due to radiation losses), we therefore have a prediction for a real threshold frequency.

9.4 Results and Discussions

In this section, the impact of dispersion on the resonant frequencies and threshold behaviour of the $\mathcal{PT}$-symmetric microresonators is analysed. Frequency mismatch between the resonant frequency of the microresonator and gain pump frequency is investigated for practical levels of dispersion and the practical implications of a slight unbalance between the gain and loss in the system are investigated. The section concludes with an investigation of how coupling between resonators manifests itself in the time development of solutions.

9.4.1 Effects of Dispersion on Threshold Behaviour in the Frequency Domain

For all cases, weakly coupled microresonators are considered, the coupled resonators each have a dielectric constant $\varepsilon_\infty = 3.5$ [9.22,9.26] radius $a = 0.54$ μm and are separated by distance $g = 0.24$ μm. Operation at two different whispering-gallery modes is analysed, namely a low Q-factor mode (7,2) and a high Q-factor mode (10,1). The corresponding isolated resonator resonant frequencies are respectively $f_0^{(7,2)} = 341.59$ THz and $f_0^{(10,1)} = 336.85$ THz, with Q-factors $Q^{(7,2)} = 2.73 \times 10^3$

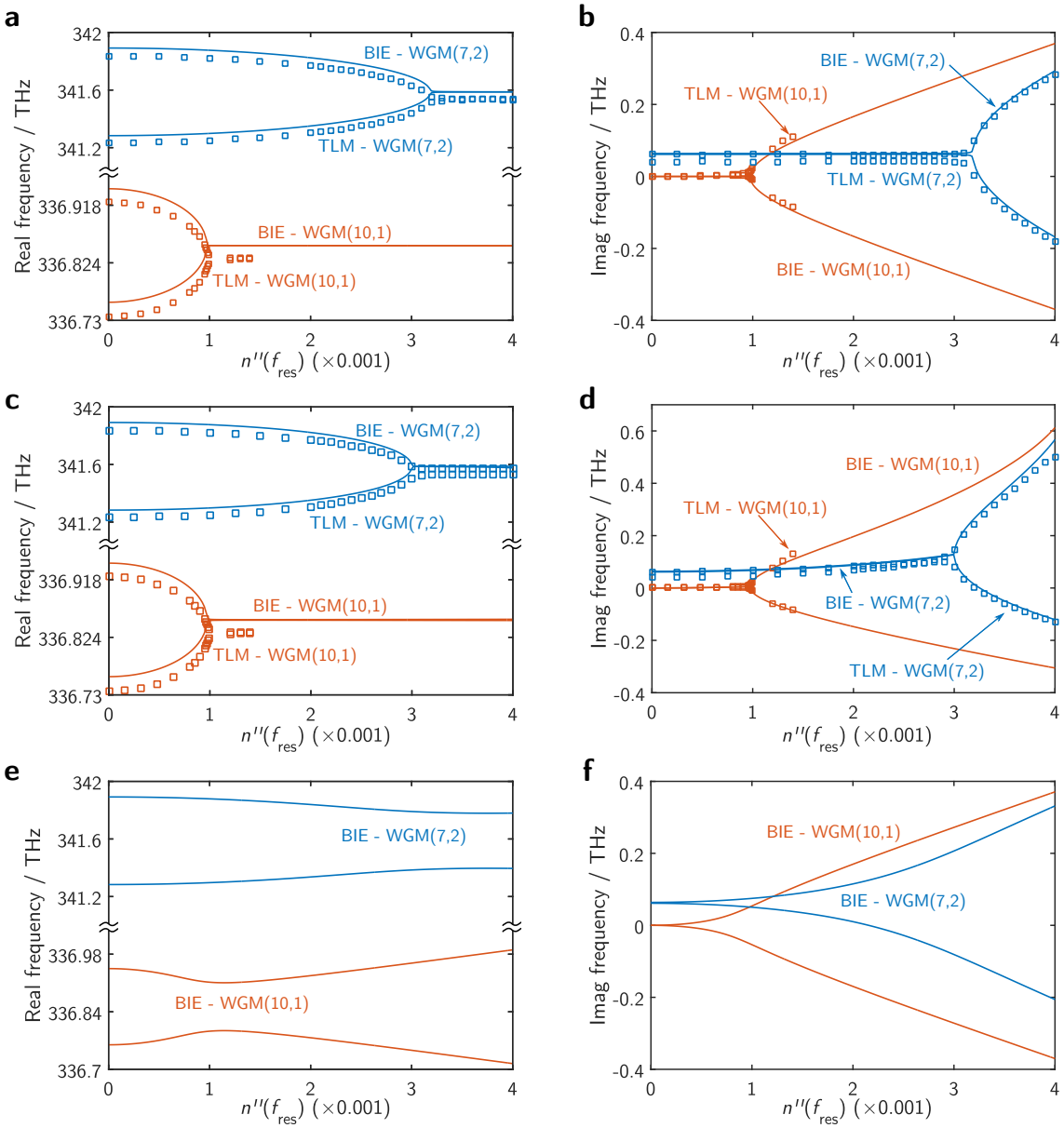

Figure 9.7 | Frequency bifurcation of $\mathcal{PT}$-coupled microresonator. Resonators have balanced gain/loss ($n''_G = -n''_L$). The plots shows the real and imaginary part of the resonant frequenices calculated by both the Boundary Integral Equation (BIE) and the numerical Transmission-Line Modelling (TLM) method. Results from the BIE are shown by solid lines and from the TLM by discrete points. These are displayed as a function of the gain/loss parameter calculated at the peak of pumping beam $n''(f_{\text{res}})$ for three different dispersion parameters, **(a,b)** $\omega_\sigma \tau = 0$, **(c,d)** $\omega_\sigma \tau = 212$ and **(e,f)** $\omega_\sigma \tau = 0.7$.

and $Q^{(10,1)} = 1.05 \times 10^7$ as they are displayed before in Fig. 9.2(a).

Figure 9.7 shows the real and imaginary parts of the eigenfrequencies f_1 and f_2 of

the $\mathcal{PT}$-symmetric coupled microresonators with balanced gain and loss, $n''_G = -n''_L$, and is depicted as a function of the imaginary part of the refractive index $n''(f_{\text{res}})$ for both the low and high Q-factor modes. The gain and loss are assumed to be tuned to the resonant frequency of an isolated microresonator, i.e. $\omega_\sigma = 2\pi f_{\text{res}}$. Three different levels of dispersion, controlled by the parameter τ, are considered. These are $\omega_\sigma\tau = 0$ corresponding to the case of no dispersion, $\omega_\sigma\tau = 212$ taken from [9.26] to exemplify the case of high dispersion and $\omega_\sigma\tau = 0.7$ to exemplify the case of low dispersion.

Figures 9.7(a and b) show the frequency splitting of the real and imaginary part of the complex eigenfrequencies for the case of no dispersion. In the passive case, where $n'' = 0$, the super-modes beat at a rate corresponding to the frequency differences $\text{Re}(f_1 - f_2) = 0.61$ THz and 0.185 THz for the (7,2) and (10,1) modes respectively. Figure 9.7(a) indicates that operation in a higher Q-factor mode results in weaker coupling between the microresonators compared to the case of operation in the lower Q-factor mode. Increasing the gain and loss in the system, decreases the beating rate and the super-modes coalesce at the threshold points of $n''(f_{\text{res}}) = 0.0032$ and 0.001 for the low and high Q-factor modes of operation respectively, confirming that the high-Q factor mode has a lower threshold point [9.3]. In the case of operation in the low Q-factor mode, the eigenfrequencies shown in Fig. 9.7(b) have a significant constant and positive imaginary part before the threshold point, which is a consequence of the higher intrinsic losses due to radiation in that case. The corresponding imaginary part is insignificant in the case of the high Q-factor mode, for which radiation losses are much smaller. Furthermore it is noted here that the coupled system first starts to lase, i.e. one of the eigenfrequencies satisfies $\text{Im}(f_{1,2}) < 0$, only when operated significantly beyond the threshold $n''(f_{\text{res}}) = 0.00326$ for the low Q-factor operation while this onset occurs immediately after the threshold point in the high Q-factor case.

Figures 9.7(c and d) show the real and imaginary parts of the eigenfrequencies for

the case of strong dispersion, corresponding to the parameter values $\omega_\sigma \tau = 212$ taken from [9.26]. These are again shown for both high and low Q-factor modes. It is noted that the threshold point for the low Q-factor mode is reduced from $n''(f_{\text{res}}) = 0.0032$ to $n''(f_{\text{res}}) = 0.0030$ in this case while for the high Q-factor mode it remains unchanged at 0.001 (compared to the case of no dispersion). Below the threshold point the imaginary parts of the eigenfrequencies are not constant, but are instead skewed towards a lossy state with positive and increasing imaginary part. Extension beyond the threshold point shows that the imaginary parts of the eigenfrequencies do not split evenly and are also skewed towards overall loss, implying that in the highly dispersive case the eigenfrequencies both are complex but no longer complex conjugates after the threshold point.

Furthermore, Figs. 9.7(a-d) compares the eigenfrequencies calculated by the Boundary Integral Equation (BIE), i.e. zeros of the linear problem (9.53), and the time-domain 2D-TLM method described in Chapter 8. The TLM method simulates the same problem as the BIE counterpart except that the TLM model introduces spatial discretisation for which in these calculations $\Delta\ell = 2.5 \times 10^{-3}$ μm is used[‡]. The TLM model uses electric dipole excitation with Gaussian profile modulated at the resonant frequency of the isolated resonator f_{res} with FWHM of 250 fs to provide a narrow bandwidth source for a total simulation time of 3 ps. The complex eigenfrequencies are extracted by using the harmonic inversion method [9.27–9.29]; for these calculations the freely available Harminv package [9.29] was used. Details of the harmonic inversion by filter diagonalisation method are not described in this thesis and reader is referred to [9.27–9.29]; the package used in this work is freely available to download[*].

By comparing the eigenfrequencies calculated by the BIE and the TLM methods (discrete bullet points), it can be seen from Figs. 9.7(a,c) that the real part of the

[‡]This discretisation parameter is equivalent with $\lambda_{\text{sim}}/100$, where λ_{sim} is the maximum simulation bandwidth in material, i.e. $\lambda_{\text{sim}} = 0.875$ μm/3.5.

[*]http://ab-initio.mit.edu/wiki/index.php/Harminv

eigenfrequencies calculated by the TLM method are shifted to the lower frequencies (red-shifting) which occurs due to numerical dispersion and stair-casing approximation. It is noted that a similar red-shifting error was also observed during the investigation of $\mathcal{PT}$-Bragg grating in Section 6.3 using the TLM method. This error can be minimised by reducing the mesh discretisation length with the cost of longer CPU simulation time. Nevertheless, Figs. 9.7(a,c) show that both the TLM and the BIE calculations predict and follow the same threshold behaviours. A more detail temporal analysis using the TLM model will be discussed in the next section.

The real and imaginary parts of the eigenfrequencies for the case of low levels of dispersion, for which we take $\omega_\sigma \tau = 0.7$, are shown in Fig. 9.7(e and f). Figure 9.7(e) shows that there is no clear threshold point in this case: the imaginary parts split for a very low value of the gain/loss parameter $n''(f_{\text{res}})$, with no sharp point of onset. The appearance of a threshold point typically associated with $\mathcal{PT}$-behaviour is lost and the eigenfrequencies are always complex valued.

The key conclusion to be made from Fig. 9.7 is therefore that $\mathcal{PT}$-like threshold behaviour is observed in the cases of no dispersion and of high dispersion, but not for the case of intermediate dispersion. While there is some skewness in the high-dispersion case, which amounts to a quantitative deviation from strict $\mathcal{PT}$-symmetry, there is an essential qualitative similarity to the dispersionless case in which there appears to be a sharp threshold. By contrast, in the case of intermediate dispersion there is no sharp transition point and the imaginary parts of the two resonant frequencies begin to diverge from the beginning.

To further investigate and explain this phenomenon, we examine the dependence of the real part of the complex refractive index on the dispersion parameter $2\omega_\sigma \tau$. This dependence is plotted in Fig. 9.8(a) for the cases of both gain and loss, and which $\sigma_0 = \pm 2\varepsilon_0 \omega_\sigma$ and $\omega_\sigma = \omega_0$ respectively. Figure 9.8(a) shows that the real parts of the refractive indices behave differently for the cases of loss and gain in the system,

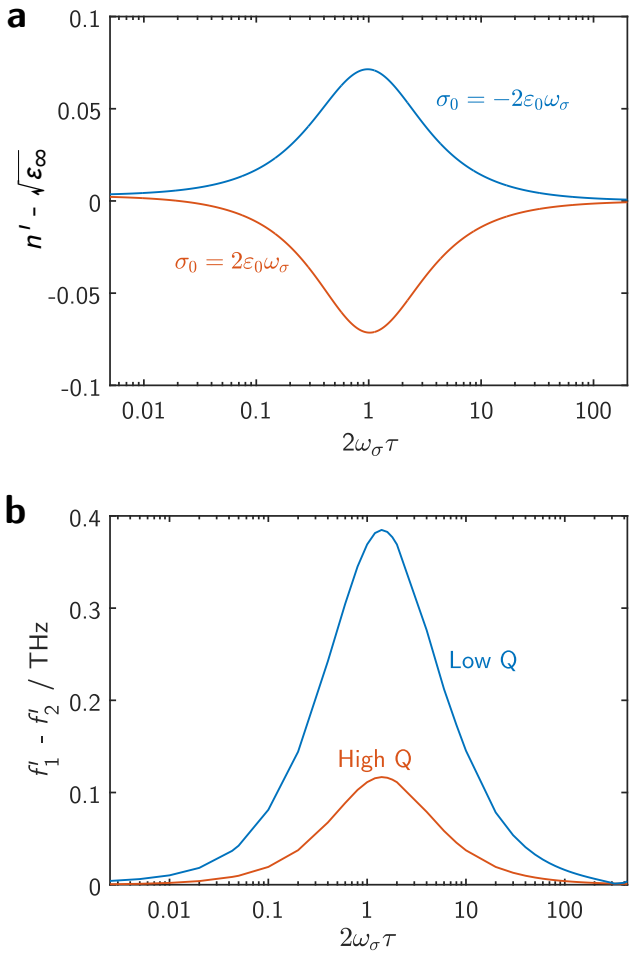

Figure 9.8 | Relation between gain/loss dispersion and eigenfrequencies after threshold. (**a**) Impact of dispersion to the real part of material at atomic transitional angular frequency ω_σ due to the presence of gain and loss for different dispersion parameters; (**b**) Contrast between the real part of eigenfrequencies of $\mathcal{PT}$-coupled microresonators for two different gain/loss parameter, i.e. $n''(f_{\text{res}}) = 0.0035$ for (7,2) and 0.0012 for the (10,1) mode as function of dispersion parameter τ.

with the maximum difference occurring when $\tau = 1/(2\omega_\sigma)$. However, in two limiting cases $\tau = 0$ (dispersion-less system) and $\tau \to \infty$ (strong dispersion), the real parts of the refractive index converge. This means that the $\mathcal{PT}$-condition $n_G = n_L^*$ can only be satisfied accurately for the cases of no dispersion and of high dispersion. For the case of intermediate dispersion there is necessarily some discrepancy between the real parts of the refractive indices of the resonators.

Figure 9.8(b) shows the minimum difference in the real parts of the two eigenfre-

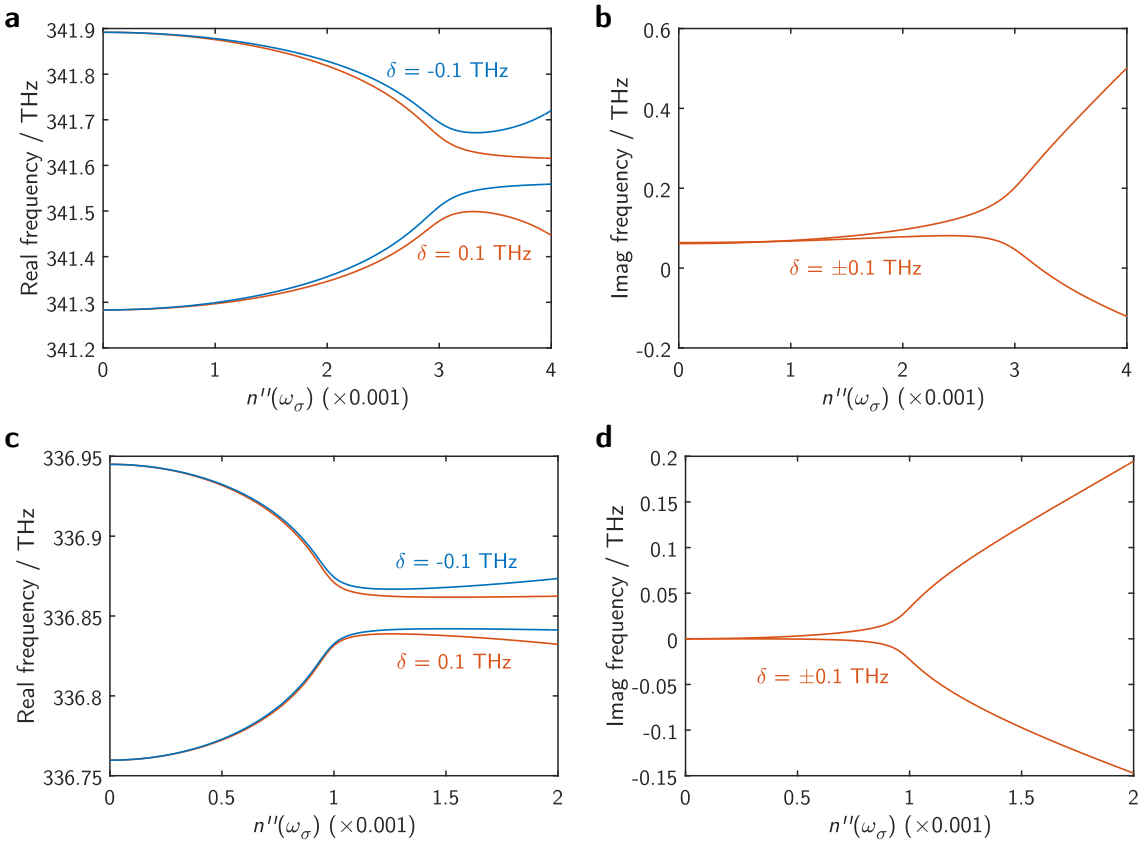

Figure 9.9 | Mismatching gain/loss material transitional frequency and the resonator resonant frequency. Frequency bifurcation of coupled microresonators with balanced gain and loss as function of gain/loss parameters $n''(\omega_\sigma)$, for two different atomic transitional frequencies $\omega_\sigma = 2\pi(f_{\text{res}} + \delta)$ with $\delta = -0.1$ and 0.1 THz.

quencies for different dispersion levels and operated at a fixed value of the gain/loss parameter, i.e. at $n''(f_{\text{res}}) = 0.0035$ for the low Q-factor and at 0.0012 for high Q-factor modes of operation. These values of the gain/loss parameter are chosen to lie above the expected threshold so that qualitatively $\mathcal{PT}$-like behaviour would imply eigenfrequencies with a common real part. Figures 9.8(a,b) confirm that the maximum difference between the real parts of the two refractive indices coincides with the maximum deviation from $\mathcal{PT}$-like threshold behaviour, where the difference between the real parts of the eigenfrequencies is greatest. This result further confirms the fact that realistic levels of dispersion preserve the essential features of $\mathcal{PT}$-behaviour.

Having confirmed that realistic levels of dispersion preserve $\mathcal{PT}$-behavior, Figure 9.9 considers a practical scenario in which there is high dispersion $\omega_\sigma\tau = 212$ and a frequency mismatch between the resonant frequency and the gain/loss atomic angular frequency. The material atomic frequency is defined to be $\omega_\sigma = 2\pi(f_{\text{res}} + \delta)$, where δ is the mismatch parameter. The structure is operated with balanced gain and loss, i.e. $n''_G = -n''_L$ and two values are assumed for the frequency mismatch, namely $\delta = -0.1$ and 0.1 THz. Figure 9.9(a,b) shows the results for the low Q-factor mode (7,2) and Fig. 9.9(c,d) for the high-Q factor mode (10,1). In both cases there is no sharp threshold point for the real parts of eigenfrequencies and the imaginary parts begin to diverge at low gain/loss values. Neither are the imaginary parts symmetrically placed about a branching value. This result confirms the fact that $\mathcal{PT}$-behaviour is preserved only when the angular transitional frequency of the dispersive gain/loss profile is aligned with the resonant frequency of the microresonators. If that is not the case, the frequency misalignment causes the coupled system to continue to beat after a threshold region.

Another practical scenario is considered in Fig. 9.10 where the gain and loss are not balanced, i.e. μR_L has a loss $|n''_L|$ while μR_G has a gain $|n''_G|$. Figure 9.10(a,b) shows the real and imaginary parts of the eigenfrequency for three different values of loss namely, $|n''_L| = 0.0026$, 0.0030 and 0.0034 which correspond to values below, at, and above the threshold point of a $\mathcal{PT}$-symmetric structure with balanced gain and loss respectively. The low Q-factor mode is considered with a practical dispersion parameter of $\omega_\sigma\tau = 212$ as taken from [9.26]. Interestingly, it can now be observed that the $\mathcal{PT}$-threshold point can also exist for structures with unbalanced gain/loss as shown by the plots for $|n''_L| = 0.0026$ and $|n''_L| = 0.0034$ in Fig. 9.10. In the former case, the $\mathcal{PT}$-threshold is increased and in the latter case the $\mathcal{PT}$-threshold is decreased when compared with the $\mathcal{PT}$-threshold of the balance structure. Of special interest is the observation that increasing loss results in the reduction of the $\mathcal{PT}$-threshold which consequently reduces the levels of gain at which lasing occurs.

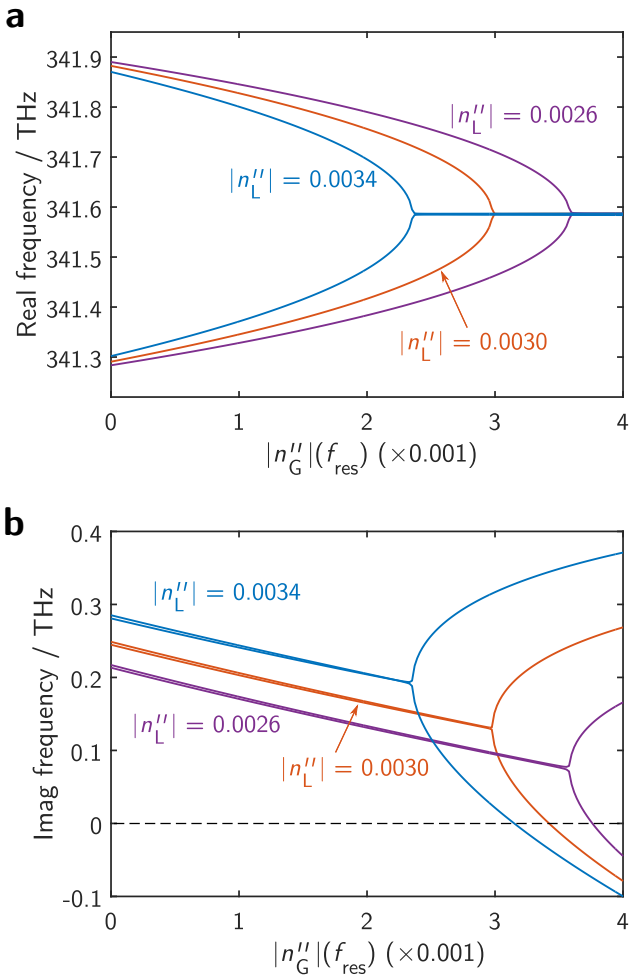

Figure 9.10 | Complex eigenfrequency in a $\mathcal{PT}$-coupled microresonator system with variable gain and fixed loss. Plotted as a function of gain parameter $|n_G''|$, dispersion parameter $\omega_\sigma \tau = 212$ [9.26] and shown for three different fixed loss value, i.e. $|n_L''| = 0.0026$, 0.0030, and 0.0034.

This counter-intuitive principle of switching lasing on by increasing loss has been experimentally demonstrated in [9.2] where a metal probe was used to enhance loss in the lossy microresonator.

9.4.2 Real Time Operation of $\mathcal{PT}$-Symmetric Coupled Microresonators

In this subsection the real-time operation of the $\mathcal{PT}$-symmetric coupled microresonators is demonstrated for different levels of dispersion. For this purpose, the two-dimensional (2D) time-domain Transmission Line Modeling (TLM) numerical method is used. A more detailed description of the TLM method and the implementation of dispersive gain/loss materials is presented in Chapter 8. In each of the simulations shown in this section, the low Q-factor (7,2) mode is excited by a very narrow-band Gaussian dipole located in $\mu \mathrm{R}_G$ whose frequency is matched to the resonant frequency of this mode as used in the calculation for Fig 9.7. Depending on the levels of gain and loss, and their relation to the threshold points, it is found in practice, however, that small unintentional initial excitations of the high Q-factor (10,1) mode may grow to become a significant feature and even dominate the evolved state. In all cases it is found that the TLM simulations are consistent with the frequency-domain calculations provided in the previous section and in fact have been used to independently validate the BIE analysis, comparison with which are presented in Figs. 9.7.

First consider the case of evolution from the low Q-factor mode using a model with no dispersion. Figure 9.11(a) shows the spatial electric field distribution of coupled microresonators with no gain and loss ($n''_G = n''_L = 0$) and operating at the resonant frequency of the low Q-factor (7,2) mode. The black line connecting the centre of the two resonators denotes a monitor line on which the electric field is observed during the TLM simulation. Figures 9.11(b and c) show the temporal evolution and the spectra of the electric field observed along the monitor line for the case of no gain and loss, respectively.

The case of no gain and loss, reported in Fig. 9.11(b), shows a typical oscillation of the electric field between the microresonators having a regular beating pattern

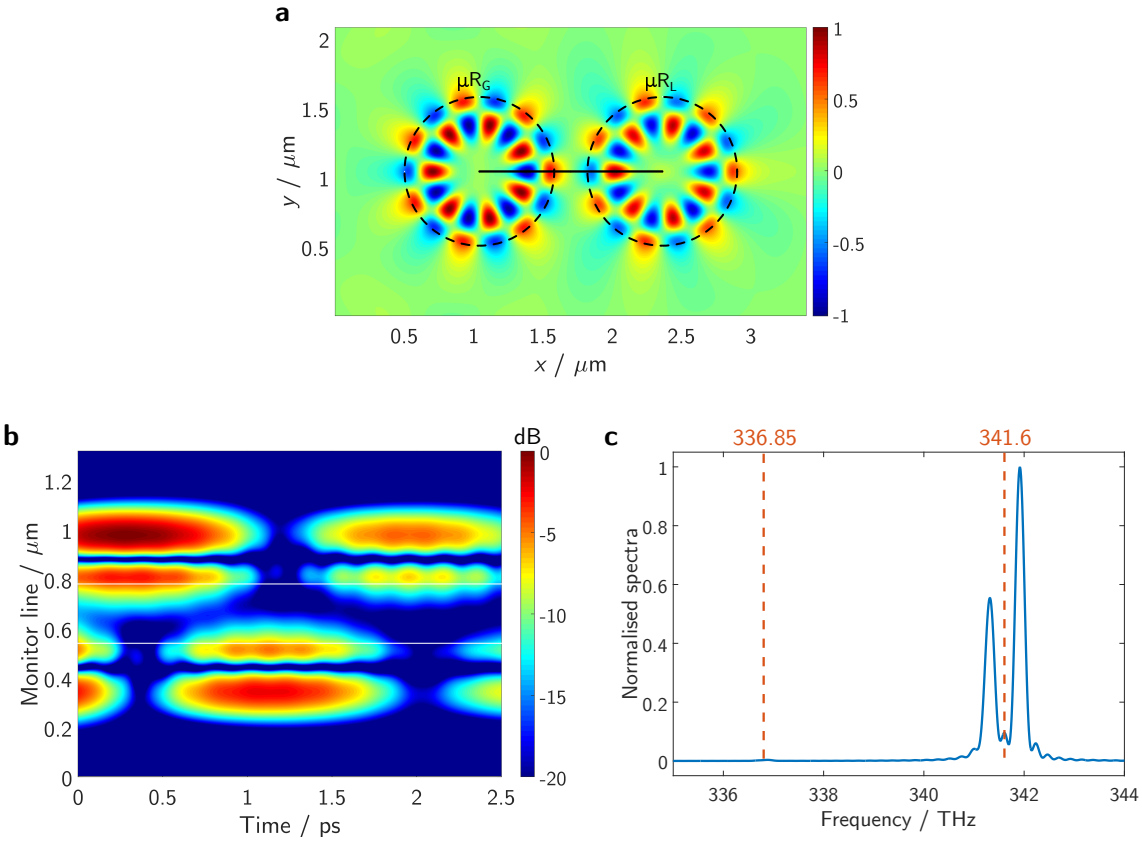

Figure 9.11 | Passive coupled resonator modelled by the 2D-TLM method. (**a**) Spatial electric field distribution of the coupled microresonators operated in the (7,2) mode. The black line connecting the centre of the two resonators denotes the monitor line. The temporal evolution (**b**) and spectra (**c**) of the field on the monitor line are shown for the passive case.

in which maximum intensity being observed in one microresonator corresponds to minimum intensity being observed in the other. It is noted that the slight modulation in the beating profile pattern is due to the unintentional excitation of the higher Q-factor mode (10,1). Figure 9.11(c) shows the frequency content of the modes, indicating the presence of two resonating frequencies centered around $f_{\text{res}}^{(7,2)}$, in agreement with Fig. 9.7(a).

The real-time performance of $\mathcal{PT}$-coupled microresonators with balanced gain and loss $n''_G = n''_L = n''$ and with no dispersion is depicted in Fig. 9.12. The temporal evolution and the spectra of the electric field are observed along the monitor line for two levels of gain and loss: the levels of gain and loss are $n''(f_{\text{res}}) = 0.002$, i.e.

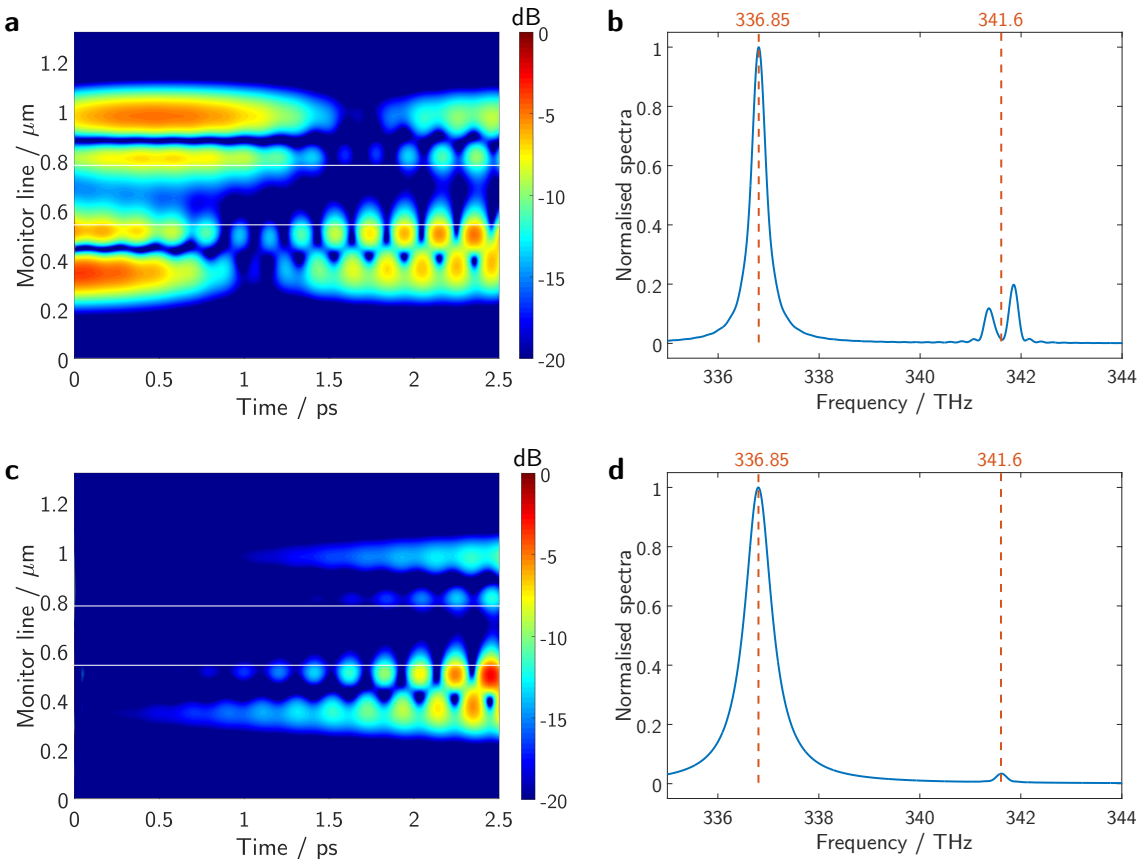

Figure 9.12 | Real time operation in the non-dispersive case. The temporal evolution and spectra of the field on the monitor line are shown for different gain/loss parameters, (**a,b**) for $n''(f_{\text{res}}) = 0.002$ and (**c,d**) for $n''(f_{\text{res}}) = 0.0034$ with a negligible dispersion parameter using the TLM method.

lower than the threshold point of the low Q-factor mode but beyond the threshold of the high Q-factor mode in Fig. 9.12(a and b), and $n''(f_{\text{res}}) = 0.0034$, i.e. lying above the threshold points of both modes in Fig. 9.12(c) and 9.12(d).

Figure 9.12(a) shows the energy beating between the microresonators with gain/loss $n''(f_{\text{res}}) = 0.002$, set below the threshold point of the low-Q-factor mode. Comparing the results shown with those presented for the passive coupled resonator in Fig. 9.11, it is noticeable that beating between microresonators is reduced, i.e. it takes longer time for the field to be coupled to the other resonator. Additionally, Fig. 9.12(a) indicates the presence of additional modes, observable at later times. Frequency analysis of the fields is given in Fig. 9.12(b) and shows an additional peak at 336.85

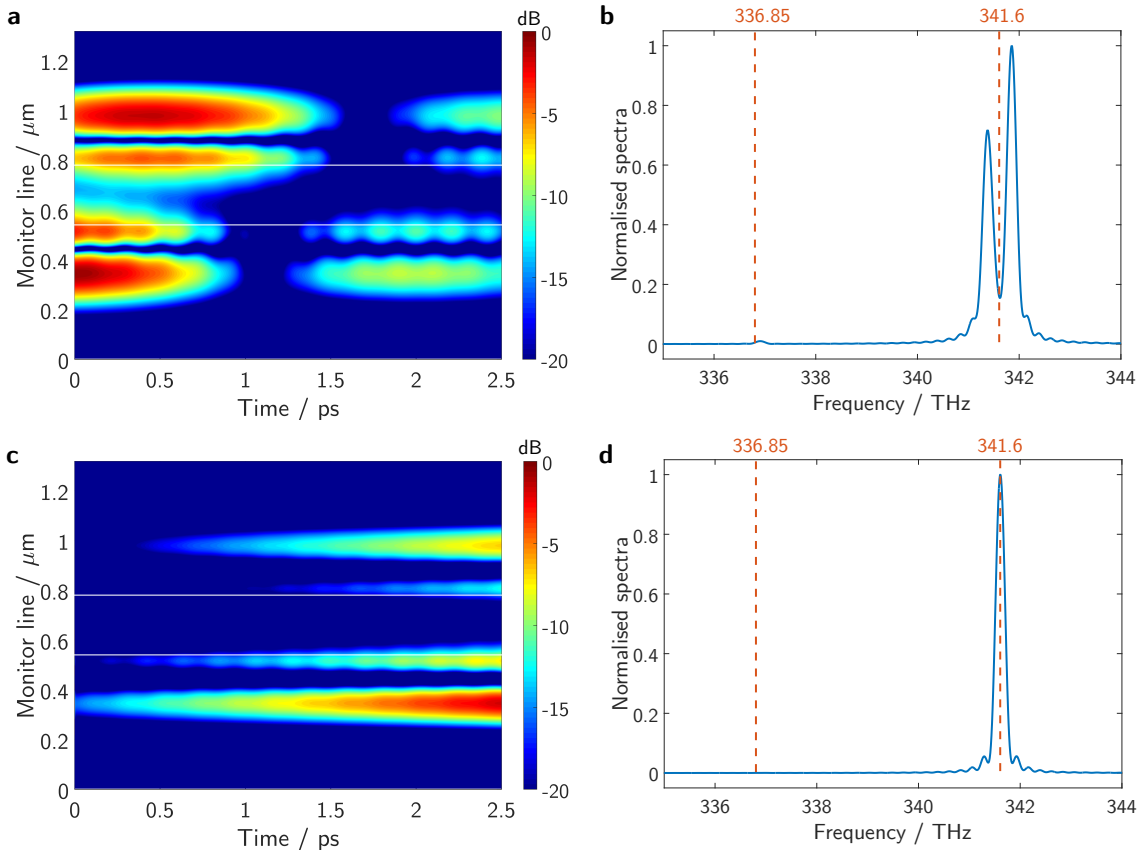

Figure 9.13 | Real time operation of $\mathcal{PT}$-coupled resonators with realistic gain/loss dispersion. Temporal and spectra of electric field along the monitor line with balanced gain and loss parameters operated for (7,2) mode with practical dispersion parameters $\omega_\sigma \tau = 212$ [9.26] and for two different gain/loss parameter, i.e. **(a,b)** $n''(f_{\text{res}}) = 0.002$, and **(c,d)** $n''(f_{\text{res}}) = 0.0034$,.

THz, which corresponds to the resonant frequency of the mode (10,1), explaining the high frequency beating in Fig. 9.12(a). Referring to Fig. 9.7(a) it can be seen that at $n''(f_{\text{res}}) = 0.002$, the (10,1) mode is operating above its threshold point and is thus experiencing amplification, whilst the (7,2) mode is still below its threshold point.

A further increase in gain/loss to $n''(f_{\text{res}}) = 0.0034$, in Fig. 9.12(c), shows an exponentially growing field in the gain microresonator with no beating between the resonators and a stronger presence of the high Q-factor mode as shown in Fig. 9.12(d). Referring to Fig. 9.7(a,b) it is confirmed that for $n''(f_{\text{res}}) = 0.0034$ both

low and high Q-factor modes are operating above their threshold.

Figure 9.13 shows corresponding results for the case of realistically high dispersion with $\omega_\sigma\tau = 212$. The gain/loss parameters $n''(f_{\text{res}}) = 0.002$ and 0.0034 are chosen. Figure 9.13(a) shows a decaying beating pattern. The corresponding spectral analysis in Fig. 9.13(b) shows that the beating may be attributed to low Q-factor modal frequencies, indicating that the highly dispersed gain/loss profile has stabilized the operation of $\mathcal{PT}$-coupled resonators system at a desired mode of operation. For operation with gain/loss parameter $n''(f_{\text{res}}) = 0.0034$, the temporal response in Fig. 9.13(c) indicates an exponentially growing field with no presence of other modes. The spectrum in Fig. 9.13(d) shows a single peak at the resonant frequency of the (7,2) mode, confirming that the resonators are operating above the $\mathcal{PT}$-threshold point. The strongly dispersive gain/loss profile limits operation of $\mathcal{PT}$-coupled microresonator system to the low Q-factor (7,2) mode only in this case. This again confirms the result that when the material atomic frequency is chosen to be at a desired resonant frequency, the $\mathcal{PT}$-symmetry is limited to that particular mode only [9.8,9.30], as in the case of the $\mathcal{PT}$-symmetric Bragg grating discussed in Chapters 6, Section 6.2.

Figure 9.14 demonstrates the real-time operation of the $\mathcal{PT}$-structure with unbalanced gain and loss shown in Fig. 9.10. Here, the same scenario as in [9.2] was applied, where the gain in the active microresonator is fixed at $|n''_G| = 0.0033$ and the loss is varied in the lossy microresonator. The low Q-factor mode with practical dispersion parameters of $\omega_\sigma\tau = 212$ is considerd [9.26]. Figure 9.14(a) shows the electric field observed along the monitor line for the case of loss $|n''_L| = 0.0026$, i.e. more gain than loss in the system. It can be seen that there is a non-periodic and long temporal beating pattern. The field is not growing, which indicates that the system is stable and is not lasing. The spectral decomposition shown in Fig. 9.14(b) is unable to distinguish the splitting of the resonant frequency due to the limited spectral resolution of the Fourier transformation of the time domain simulation re-

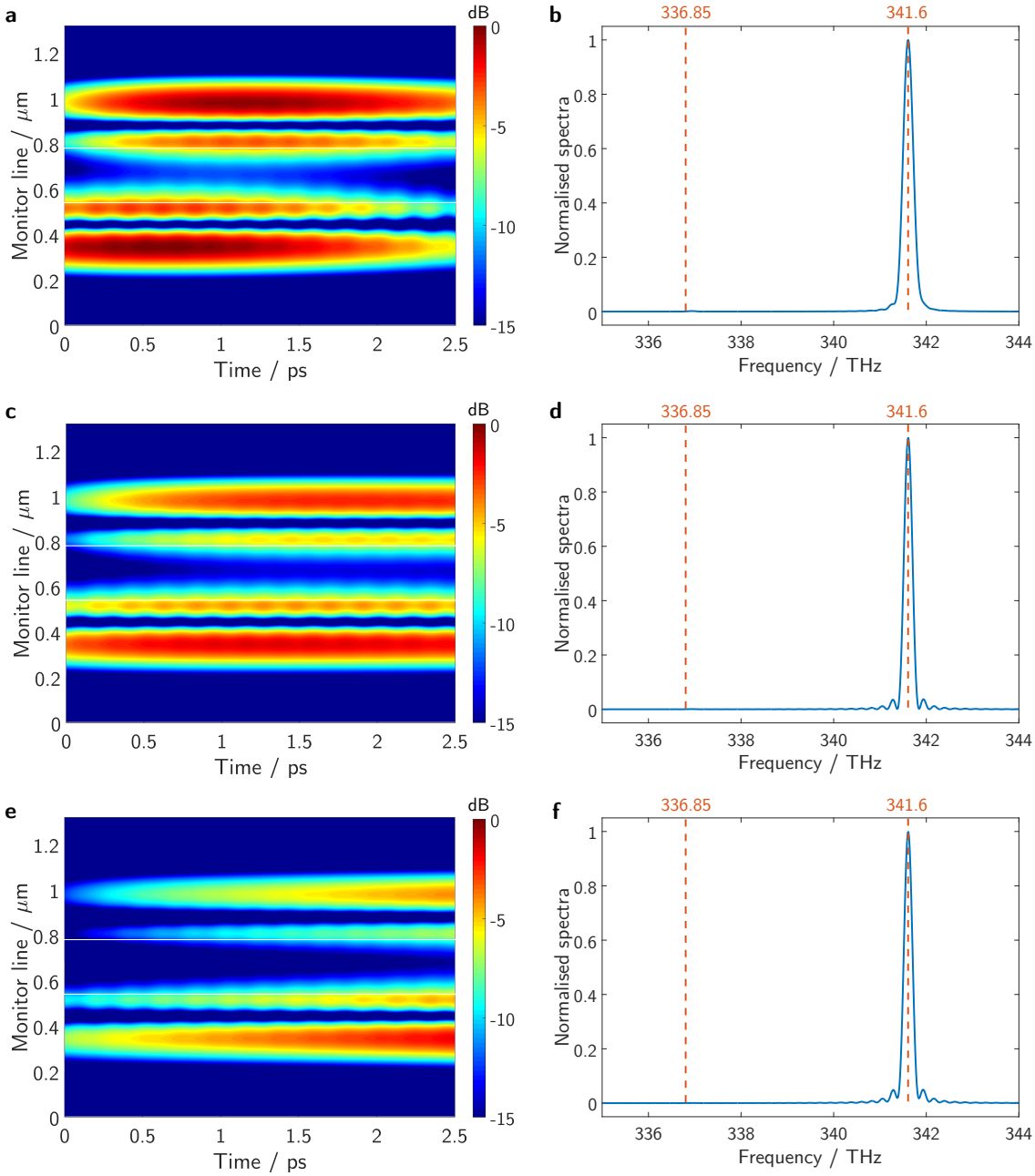

Figure 9.14 | Laser operation in an unbalanced gain/loss $\mathcal{PT}$-coupled resonators. Temporal and spectra of electric field along the monitor line for operation of low Q-factor (7,2) mode with realistic dispersion parameters $\omega_\sigma \tau = 212$ [9.26], i.e. **(a,b)** $|n_L''| = 0.0026$, **(c,d)** $|n_L''| = 0.0030$ and **(e,f)** $|n_L''| = 0.0034$ while the gain parameter is kept constant at $|n_G''| = 0.0033$.

sult.

Figure 9.14(c) shows the temporal evolution of the field for the case of $|n_L''| = 0.0030$.

It can be seen that there is no beating between the resonators and no growing field, suggesting that the structure is operating above the $\mathcal{PT}$-threshold point but before the lasing point which occurs at $|n''_G| = 0.0034$ (Fig.9.10(b)). The spectral analysis shows only a single peak centred at $f_{\text{res}}^{(7,2)}$.

Figure 9.14(e) shows the temporal evolution for $|n''_L| = 0.0034$ and $|n''_G| = 0.0033$, i.e. more loss than gain in the system. It can be observed that the field is growing with no beating between the microresonators, suggesting lasing action. This result is in agreement with observations in [9.2] where laser generation by reversing the effect of loss at threshold is demonstrated. The corresponding spectrum is depicted in Fig. 9.14(f) and has a sharp peak centred at $f_{\text{res}}^{(7,2)}$.

9.5 Summary

In this chapter, an eigenfrequency analysis of an isolated circular dielectric resonator as a boundary condition solution of Maxwell's equations was presented. An exact model of a coupled microresonator using the Boundary Integral Equation (BIE) method was developed. For the case of very high-Q factor resonator, a perturbation analysis was applied on the BIE model to approximately locate the threshold point of $\mathcal{PT}$-symmetric coupled resonators.

The chapter demonstrates the validity of the 2D-TLM method to model $\mathcal{PT}$-symmetric coupled microresonator, in which the complex eigenfrequencies are extracted by using the Harminv package. Although, the 2D-TLM model suffers from a numerical dispersion due to discretisation and staircasing approximations, it is capable of physically modelling the structure with considerable accuracy.

Furthermore, in this chapter the impact of material dispersion on the spectral propetries of $\mathcal{PT}$-symmetric coupled microresonators was studied in detail. It has

been shown that the practical case of high dispersion preserves the requirement for a $\mathcal{PT}$-structure. However the results show that this is only the case when the material atomic frequency is aligned with the resonant frequency of the microresonator. This comes as a direct consequence of the Kramers-Kronig relationship, which implies that changes in the imaginary part of the refractive index cause the real part of the refractive index to change too. Moreover the chapter also demonstrated the concept of lasing generation by reversing the effect of loss in threshold which is triggered by an early $\mathcal{PT}$-symmetry breaking. Real-time operation of $\mathcal{PT}$-coupled microresonators verifies that the dispersion due to the Kramers-Kronig relationship limits the operation of $\mathcal{PT}$-coupled microresonators to a single frequency and hence forbids multi-mode $\mathcal{PT}$-symmetry breaking.

References

[9.1] C. E. Rüter, K. G. Makris, R. El-Ganainy, D. N. Christodoulides, M. Segev, and D. Kip, "Observation of paritytime symmetry in optics," Nat. Phys. **6**, 192–195 (2010).

[9.2] B. Peng, . K. Ozdemir, S. Rotter, H. Yilmaz, M. Liertzer, F. Monifi, C. M. Bender, F. Nori, and L. Yang, "Loss-induced suppression and revival of lasing." Science **346**, 328–32 (2014).

[9.3] B. Peng, . K. Özdemir, F. Lei, F. Monifi, M. Gianfreda, G. L. Long, S. Fan, F. Nori, C. M. Bender, and L. Yang, "Paritytime-symmetric whispering-gallery microcavities," Nat. Phys. **10**, 394–398 (2014).

[9.4] L. Feng, Z. J. Wong, Y. Wang, X. Zhang, and R.-M. Ma, "Single-mode laser by parity-time symmetry breaking," Science **346**, 972–975 (2014).

[9.5] H. Hodaei, M.-A. Miri, M. Heinrich, D. N. Christodoulides, and M. Khajavikhan, "Parity-time-symmetric microring lasers," Science (80-.). **346**, 975–978 (2014).

[9.6] H. Hodaei, M.-a. Miri, M. Heinrich, D. N. Christodoulides, and M. Khajavikhan, "PT-symmetric microring lasers: Self-adapting broadband mode-selective resonators," arXiv Prepr. arXiv 1405.2103 p. 12 (2014).

[9.7] L. D. Landau, J. S. Bell, M. J. Kearsley, L. P. Pitaevskii, E. M. Lifshitz, and J. B. Sykes, *Electrodynamics of continuous media* (Elsevier, London, England, 1984), 2nd ed.

[9.8] A. A. Zyablovsky, A. P. Vinogradov, A. V. Dorofeenko, A. A. Pukhov, and A. A. Lisyansky, "Causality and phase transitions in PT-symmetric optical systems," Phys. Rev. A **89**, 033808 (2014).

[9.9] C. A. Balanis, *Advanced Engineering Electromagnetics: Traditions v. 2* (John Wiley, NJ, 2012), 2nd ed.

[9.10] D. M. Pozar, *Microwave Engineering* (John Wiley, New York, NY, 2011), 4th ed.

[9.11] S. Ramo, J. R. Whinnery, and T. V. Duzer, *Fields and Waves in Communication Electronics* (John Wiley, 1999), 3rd ed.

[9.12] E. Kreyszig, *Advanced Engineering Mathematics* (John Wiley, New York, NY, 2011), 10th ed.

[9.13] M. Abramowitz and I. A. Stegun, *Handbook of Mathematical Functions* (U.S. Department of Commerce, NIST, New York: Dover, 1972).

[9.14] E. I. Smotrova, T. M. Benson, P. Sewell, J. Ctyroky, and A. I. Nosich, "Lasing frequencies and thresholds of the dipole supermodes in an active microdisk concentrically coupled with a passive microring," J. Opt. Soc. Am. A **25**, 2884 (2008).

[9.15] E. Smotrova, A. Nosich, T. Benson, and P. Sewell, "Optical coupling of whispering-gallery modes of two identical microdisks and its effect on photonic molecule lasing," IEEE J. Sel. Top. Quantum Electron. **12**, 78–85 (2006).

[9.16] E. Smotrova, A. Nosich, T. Benson, and P. Sewell, "Ultralow Lasing Thresholds of pi-Type Supermodes in Cyclic Photonic Molecules Composed of Submicron Disks With Monopole and Dipole Modes," IEEE Photonics Technol. Lett. **18**, 1993–1995 (2006).

[9.17] E. I. Smotrova, A. I. Nosich, T. M. Benson, and P. Sewell, "Threshold reduction in a cyclic photonic molecule laser composed of identical microdisks with whispering-gallery modes," Opt. Lett. **31**, 921 (2006).

[9.18] E. I. Smotrova and A. I. Nosich, "Optical coupling of an active microdisk to a passive one: effect on the lasing thresholds of the whispering-gallery supermodes." Opt. Lett. **38**, 2059–61 (2013).

[9.19] S. V. Boriskina, "Spectrally-engineered photonic molecules as optical sensors with enhanced sensitivity: a proposal and numerical analysis," J. Opt. Soc. Am. B **15**, 14 (2006).

[9.20] S. V. Boriskina, "Coupling of whispering-gallery modes in size-mismatched microdisk photonic molecules," Opt. Lett. **32**, 1557–1559 (2007).

[9.21] S. V. Boriskina, "Spectral engineering of bends and branches in microdisk coupled-resonator optical waveguides." Opt. Express **15**, 17371–17379 (2007).

[9.22] S. Phang, A. Vukovic, S. C. Creagh, T. M. Benson, P. D. Sewell, and G. Gradoni, "Parity-time symmetric coupled microresonators with a dispersive gain/loss," Opt. Express **23**, 11493 (2015).

[9.23] J.-M. Liu, *Photonic Devices* (Cambridge University Press, Cambridge, 2005).

[9.24] J. W. S. Rayleigh, *Theory of Sound. vol. II* (Macmillan, London, 1878).

[9.25] S. C. Creagh and M. D. Finn, "Evanescent coupling between discs: A model for near-integrable tunnelling," J. Phys. A. Math. Gen. **34**, 3791–3801 (2001).

[9.26] S. C. Hagness, R. M. Joseph, and A. Taflove, "Subpicosecond electrodynamics of distributed Bragg reflector microlasers: Results from finite difference time domain simulations," Radio Sci. **31**, 931–941 (1996).

[9.27] F. Grossmann, V. A. Mandelshtam, H. S. Taylor, and J. S. Briggs, "Harmonic inversion of time signals and its applications," J. Chem. Phys. **107**, 6756–6869 (1997).

[9.28] V. A. Mandelshtam and H. S. Taylor, "Erratum: "Harmonic inversion of time signals and its applications" [J. Chem. Phys. 107, 6756 (1997)]," J. Chem. Phys. **109**, 4128 (1998).

[9.29] S. G. Johnson, "Harminv," http://ab-initio.mit.edu/wiki/index.php/Harminv (2015). Accessed: 2015-04-22.

[9.30] S. Phang, A. Vukovic, H. Susanto, T. M. Benson, and P. Sewell, "Impact of dispersive and saturable gain/loss on bistability of nonlinear parity-time Bragg gratings," Opt. Lett. **39**, 2603–6 (2014).

10

Localized Single Frequency Lasing States in a Finite Parity-Time Symmetric Resonator Chain

This chapter considers a finite Parity Time ($\mathcal{PT}$) chain made of resonant dielectric cylinders on which a more general case of $\mathcal{PT}$ symmetry is achieved by modulating both the real and imaginary part of the material refractive index along the resonator chain. The band-structure of the finite $\mathcal{PT}$ resonator chains is compared to infinite case in order to understand the complex interdependence of the Bloch phase and the amount of the gain/loss in the system that causes the $\mathcal{PT}$ symmetry to break. The results show that the type of the modulation along the unit cell can significantly affect the position of the threshold point of the $\mathcal{PT}$ system. In all cases the lowest threshold is achieved near the end of the Brillouin zone. For finite $\mathcal{PT}$-chains, and for a particular type of modulation, early $\mathcal{PT}$ symmetry breaking is observed and shown to cause the presence of termination states localised at the edges of the finite chain resulting in localised lasing and dissipative modes at each end of the chain.

* * *

10.1 Introduction

In the previous chapter, $\mathcal{PT}$-coupled resonator cavities comprised of two coupled resonators, one having gain while the other has loss, was considered. To study the spectral properties of such structures, an analytical representation of the coupling mechanism, based upon the Green's boundary integral equations (BIE) for a weakly coupled system was developed. In particular two different scenarios were considered, i.e. a balanced gain/loss condition and a fixed-loss-variable-gain scenario. Moreover an induced $\mathcal{PT}$-symmetry-breaking phenomenon was demonstrated by increasing loss in the system, which suggests a counter-intuitive concept of laser operation in a system dominated by loss rather than gain.

This chapter will further extend the capability of the BIE method to analyse a finite $\mathcal{PT}$ periodic chain structure comprised of two-dimensional resonant cavities each supporting whispering-gallery modes. The $\mathcal{PT}$-symmetry is introduced by either having a chain of resonators with constant refractive index and an alternating arrangement of gain/loss resonators, or in a more general case where both real and imaginary parts of the resonator refractive index are modulated.

10.2 Parity Time Symmetric Microresonator Chain

This section outlines the structure considered in this chapter, namely the $\mathcal{PT}$-symmetric microresonator chain. In order to satisfy the condition of $\mathcal{PT}$-symmetry [10.1,10.2], the refractive index profile should satisfy the condition $n(x) = n^*(-x)$, where $*$ denotes complex conjugate. This means that the real part of the refractive index is an even function and the imaginary part of the refractive index is an odd function in space. To capture this condition, a unit cell that is comprised of four resonant cavities, as shown schematically in Fig. 10.1 is considered. The unit cell is

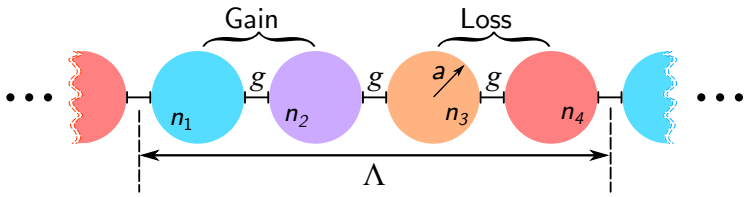

Figure 10.1 | Schematic illustration of the unit cell of the $\mathcal{PT}$ resonant chain.

of length Λ, all the resonant cavities have the same radius a and are separated by an equal gap g. The complex refractive index in each resonant cavity is given by,

$$\begin{cases} n_1 = n_{\text{avg}} + \Delta n' + jn'' \\ n_2 = n_{\text{avg}} - \Delta n' + jn'' \\ n_3 = n_{\text{avg}} - \Delta n' - jn'' \\ n_4 = n_{\text{avg}} + \Delta n' - jn'' \end{cases}, \tag{10.1}$$

where n_{avg} is the average real refractive index, $\Delta n'$ denotes the modulation of the real part and n'' is the imaginary part of the refractive index such that $n'' > 0$ represents gain and $n'' < 0$ represents loss. The E-type wave is considered where the electric field is directed along the longitudinal resonator axis and it is assumed that the system is weakly coupled, i.e. the coupling is considered to be only between nearest neighbours through the evanescent field.

Detailed calculations provided in this chapter are for the case of finite $\mathcal{PT}$ periodic resonator chains comprised of $N = 6$ unit cells, each containing four resonators having the same radius $a = 0.54$ μm, average real refractive index $n_{\text{avg}} = 3.5$ and separation gap $g = 0.3\mu m$. The background material is assumed to be air ($n_b = 1$). Corresponding isolated resonators are excited at $f_{\text{res}} = 336.85$ THz and support a high Q-factor whispering-gallery mode of azimuthal order $m = 10$, and radial order $n = 1$ with a Q-factor of 1.05×10^7.

10.3 Analytical Representation of the Coupling System

Here, the BIE technique, derived in Section 9.3, is extended to model a finite and infinitely long $\mathcal{PT}$-chain structure associated with Fig. 10.1.

Infinite $\mathcal{PT}$-Chain BIE Model - For the case of an infinite chain there exists a continuity of eigenstates $\tilde{\varphi}_i$ evolving between the left and right end of the unit cell with a phase delay given by the Bloch phase $\beta\Lambda$ [10.3]. Using the Bloch theorem, the BIE reduces to 4×4 linearly independent equations of the form,

$$\begin{pmatrix} \tilde{D}_1 & \tilde{C} & 0 & \mathrm{e}^{j\beta\Lambda}\tilde{C} \\ \tilde{C} & \tilde{D}_2 & \tilde{C} & 0 \\ 0 & \tilde{C} & \tilde{D}_3 & \tilde{C} \\ \mathrm{e}^{-j\beta\Lambda}\tilde{C} & 0 & \tilde{C} & \tilde{D}_4 \end{pmatrix} \begin{pmatrix} \tilde{\varphi}_1 \\ \tilde{\varphi}_2 \\ \tilde{\varphi}_3 \\ \tilde{\varphi}_4 \end{pmatrix} = 0 \tag{10.2}$$

where, elements $\tilde{D}_{i=1,2,3,4}$ describe the field of an individual isolated resonator derived in Section 9.3 and reproduced below as,

$$\tilde{D}_{i=1,2,3,4} = -j\frac{zH_m(u)J'_m(z_i) - uH'_m(u)J'_m(z_i)}{zJ_m(u)J'_m(z_i) - uJ'_m(u)J_m(z_i)} \tag{10.3}$$

where $z_i = n_i k_0 a$ and $u = k_0 a$, k_0 is the free space wavenumber, and m denotes an azimuthal order of the whispering gallery mode. The elements $\tilde{C}$ represent the field outside the resonator which couples the solution of the neighbouring resonator for a given mode m and are

$$\tilde{C} = -jH_{2m}(w) \tag{10.4}$$

where $w = k_0(2a + g)$. In (10.3) and (10.4), J_m and J'_m denote the Bessel function of order m and its derivative respectively, H_m and H'_m denote the Hankel function

of the second kind of order m and its derivative respectively. The eigenfrequencies are obtained as solutions of (10.2) which for the $\mathcal{PT}$ infinite chain comprised of four resonators results in four eigenfrequencies $f_{i=1,2,3,4}$ associated with the specified whispering-gallery mode m and at the desired Bloch phase $\beta\Lambda$.

Finite $\mathcal{PT}$-Chain BIE Model - In the case of the finite chain consisting of N unit cells, the coupling matrix given in (9.60) is modified to

$$\begin{pmatrix} \tilde{D}_1 & \tilde{C} & 0 & 0 & 0 & 0 \\ \tilde{C} & \tilde{D}_2 & \tilde{C} & 0 & 0 & 0 \\ 0 & \tilde{C} & \tilde{D}_3 & \tilde{C} & 0 & 0 \\ 0 & 0 & \tilde{C} & \tilde{D}_4 & \tilde{C} & 0 \\ 0 & 0 & 0 & \tilde{C} & \tilde{D}_1 & \ddots \\ 0 & 0 & 0 & 0 & \ddots & \ddots \end{pmatrix} \begin{pmatrix} \tilde{\varphi}_1 \\ \tilde{\varphi}_2 \\ \tilde{\varphi}_3 \\ \tilde{\varphi}_4 \\ \tilde{\varphi}_1 \\ \vdots \end{pmatrix} = 0 \tag{10.5}$$

The eigenfrequencies f_i for $i = 1, 2, \cdots, 4N$ are obtained by numerically solving (10.5) for the specified mode number m.

10.4 Results and Discussions

This section will start by describing the essential features and notation for the finite-chain models under investigation and summarises one of the key features, found in their solution: that when there is an appropriate modulation between resonators, then among the global modes of the system there are distinctive *termination states*. Unlike most global modes, which can be understood as simply discretely sampling the band-structure of the infinite-chain case, these termination states are localised near the ends of the finite chain and have resonant frequencies lying inside the band-gaps of the infinite case.

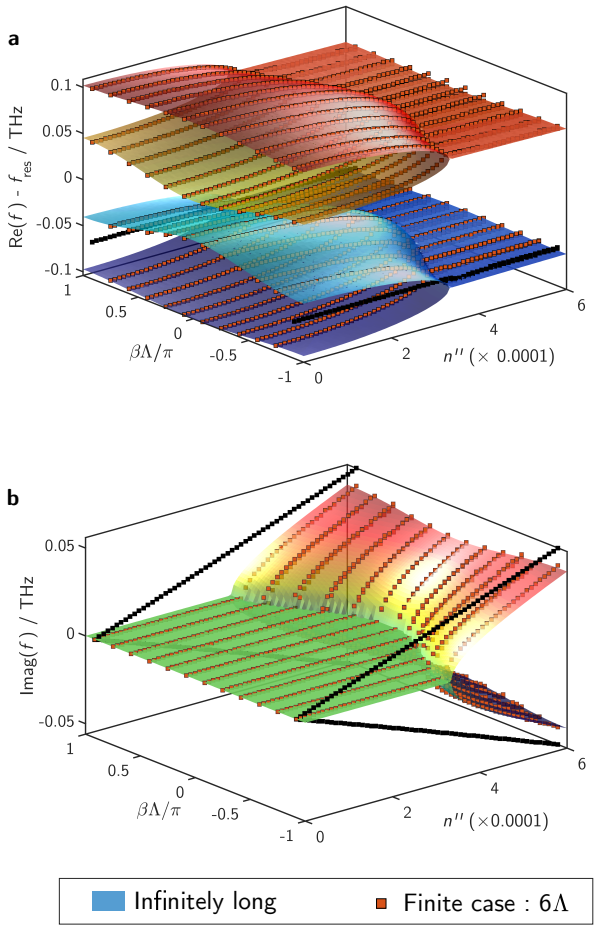

Figure 10.2 | Band structure diagram and termination states of finite $\mathcal{PT}$-chain. (**a**) Real and (**b**) imaginary part of the eigenfrequencies for the infinite chain (surface plot) and finite $\mathcal{PT}$-chain (discrete square bullets) as a function of Bloch phase $\beta\Lambda$ and gain/loss parameter n'' and for $\Delta n' = 0.0005$. The termination eigenfrequencies are depicted as the black bullets.

The qualitative features of the termination states and how they are related to the band structure of the infinite-chain limit will be first discussed. Figure 10.2 illustrates how the band-structure of a chain of resonators evolves as the gain/loss parameter n'' is increased: the case shown corresponds to the coupling of whispering-gallery modes for a sequence of refractive indices of the formats given in (10.1) with real modulation $\Delta n' = 0.0005$.

Real and imaginary parts of the resonant frequency are shown respectively in parts (a) and (b) of Fig. 10.2 as a function of n'' and of the Bloch phase $\beta\Lambda$, which is

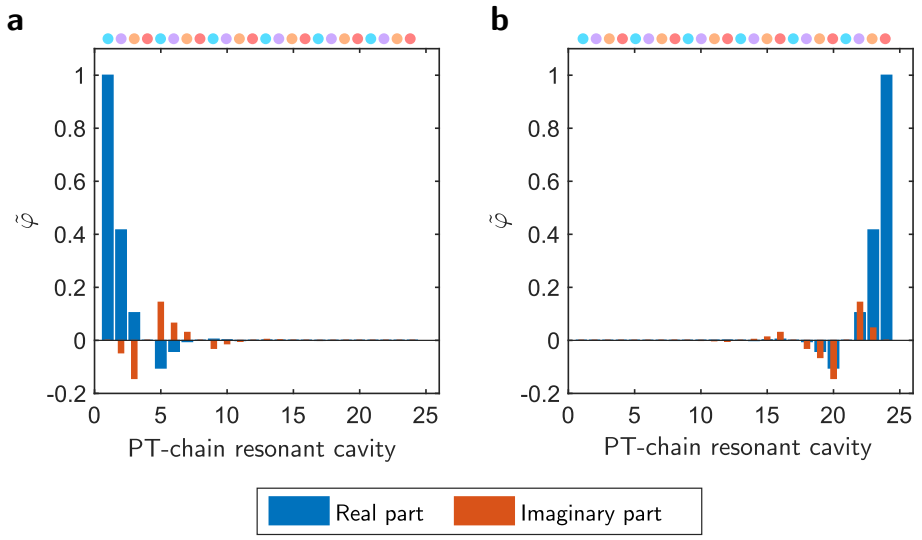

Figure 10.3 | Degree of excitation of the termination state within the finite $\mathcal{PT}$-chain. Eigenvector $\tilde{\varphi}$ of the termination states with operated at gain/loss parameter $n'' = 0.0004$. (**a**) Eigenvector for the lasing threshold states ($\mathrm{Im}(f) < 0$) and (**b**) for the dissipative threshold states ($\mathrm{Im}(f) > 0$). The $\mathcal{PT}$-chain structure is illustrated on the top of each plot.

defined so that the solution repeats with a phase delay $e^{j\beta\Lambda}$ from one unit cell to the next, and where Λ is the physical length of a unit cell as illustrated in Fig. 10.1. In Fig. 10.2, the band-structure of the limiting infinite-chain limit is shown as a surface. This surface shows threshold behaviour: for each value of $\beta\Lambda$, as the gain/loss parameter n'' is increased, the real parts of the resonant frequencies approach and coalesce at a critical value (which is dependant on $\beta\Lambda$), after which the imaginary parts split and become significantly complex. This is commonly referred to as the $\mathcal{PT}$-symmetric threshold, beyond which the structure is in the $\mathcal{PT}$ broken-symmetry phase [10.4,10.5]. For the case where the real part of the refractive index is modulated, as it is here, we find that there is a distinct threshold (at nonzero values of n'') for all values of $\beta\Lambda$. It will be seen in the more detailed discussion of the following sections that when the modulation is decreased, this threshold also decreases, so that when there is no modulation at all, the eigenvalues are thresholdless for some values of $\beta\Lambda$. It is important to note that there are multiple band-gaps formed between the band surfaces when the gain/loss parameter n'' is below the threshold, as seen in Fig. 10.2.

Most eigenvalues of the finite $\mathcal{PT}$-chain case can be understood by sampling this band surface at discrete values of the Bloch phase $\beta\Lambda$, as indicated by the bullets on Fig. 10.2. In addition, however, there are eigenvalues that are completely separate from the band structure of the infinite case. These correspond to the termination states and are denoted using the black bullets in Fig. 10.2. While typical eigenvectors behave in a pseudo-Bloch way, changing gradually from one unit cell to the next throughout the chain, the termination states are entirely different. Termination states are localized at one of the ends of the finite chain, as illustrated in Fig. 10.3. Figure 10.3 shows typical eigenvectors corresponding to termination states, in which each component describes the degree of excitation of the corresponding whispering gallery mode in an individual resonator. Note that these are related to each other by application of a $\mathcal{PT}$ transformation. In this example, the termination state localized on the left is lasing ($\mathrm{Im}(f) < 0$) while the termination state localized on the right is dissipating ($\mathrm{Im}(f) > 0$). Noting that the resonators terminating the chain on the left have gain whilst the resonators terminating the chain on the right are lossy. In this context, the localised termination states have the following meaning: modes at either end of the chain and have frequencies that are complex conjugate and are distinct from the band structure of the infinite chain.

In subsequent subsections, the spectral behaviour of the finite $\mathcal{PT}$-chain of resonators for two different cases of resonator medium refractive index modulation will be discussed in more detail. In the first case, $\mathcal{PT}$-symmetric behaviour is introduced by periodically modulating only the imaginary part of the refractive index whilst the real part stays constant ($\Delta n' = 0, n'' \neq 0$). This case is referred to as simple $\mathcal{PT}$-symmetry periodicity. In the second case, a more complex form of $\mathcal{PT}$-symmetric periodicity is also considered when the modulation of both the real part and imaginary part of the refractive index is present ($\Delta n' \neq 0, n'' \neq 0$). This will be referred to as the general case $\mathcal{PT}$-symmetric periodicity. In particular, it is shown that breaking $\mathcal{PT}$-symmetry forces the termination modes, which are initially de-

generate in the passive case, to form a complex conjugate pair. As the result, the termination mode with broken-$\mathcal{PT}$-symmetry is lasing at one end and dissipating at the other. These localised termination states are robust because they are protected by the breaking-$\mathcal{PT}$-symmetry.

10.4.1 Simple Finite $\mathcal{PT}$-Chain Case

The more detailed analysis is started by discussing the special case of a finite $\mathcal{PT}$-chain in the absence of a modulation in the real part of the refractive index, i.e. $\Delta n' = 0$ in (10.1). In this case, it was found that the spectra of the finite $\mathcal{PT}$-chains are obtained as a discrete sampling of the limiting infinite $\mathcal{PT}$-chain within the Brillouin zone. As such, the structure can be both in a $\mathcal{PT}$-symmetric phase and a symmetry-broken phase depending on the Bloch phase and the amount of gain/loss in the system. It is also important to comment that in the absence of a real refractive index modulation, the termination states that occur in the general $\mathcal{PT}$-chain case when both real and imaginary parts of the refractive index have modulation are not observed.

Figure 10.4(a-d) compares the real and the imaginary parts of the eigenfrequencies of the $\mathcal{PT}$-resonator chain for both an infinitely long chain (solid line) and a finite chain consisting of 6 unit cells (discrete points) as a function of the Bloch phase $\beta\Lambda$. Real and imaginary parts of eigenfrequencies are shown in the top and bottom panels respectively. Results are given for different values of gain/loss in the system i.e. $n'' = 0$, 0.0003, 0.0004472 and 0.0005 respectively. It is emphasized that in the case of no gain/loss, the system does not strictly represent a $\mathcal{PT}$-symmetric structure as it is an array of identical passive dielectric resonators but is included here for completeness. Figure 10.4(a) shows that in the case of the passive resonator chain, the real part of the eigenfrequency forms two clusters of modes centred at the operating frequency f_0 and the band-structure is symmetrical with respect to the

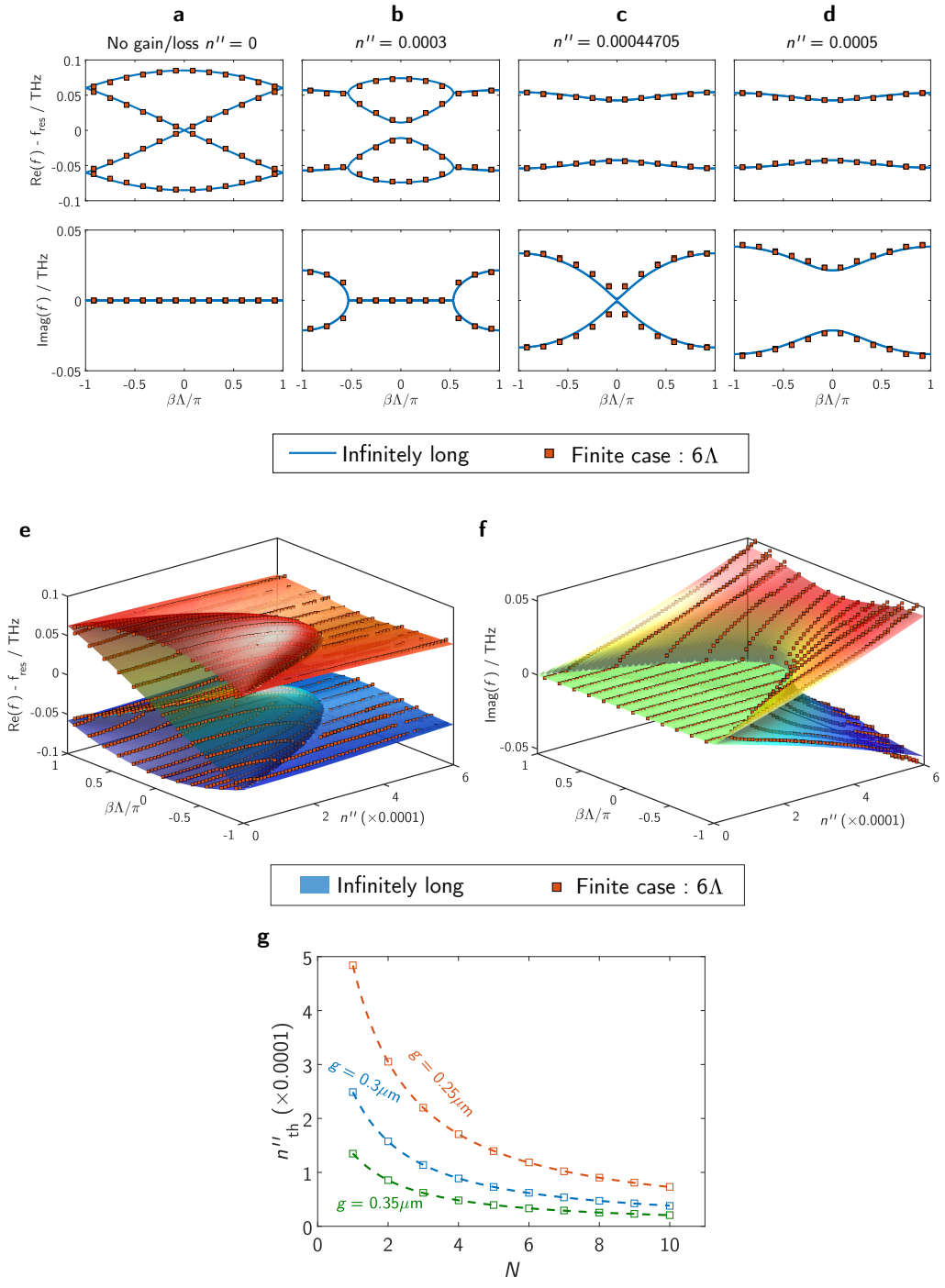

Figure 10.4 | Band structure diagram of the simple $\mathcal{PT}$-chain resonators. Subplots (**a-d**) show the real part (top panel) and the imaginary part (bottom panel) of the eigenfrequencies obtained for the case of $\Delta n' = 0$ for infinite $\mathcal{PT}$-chain (solid line) and finite $\mathcal{PT}$-chain (discrete square bullets) for: (**a**) passive chain $n'' = 0$; (**b**) $n'' = 0.0003$; (**c**) $n'' = 0.00044705$ and (**d**) $n'' = 0.0005$. Parts (**e**) and (**f**) show the surface plot of the real and imaginary part of the eigenfrequencies as a function of Bloch phase $\beta\Lambda$ and gain/loss parameter n''. Part (**g**) shows the minimum threshold of the simple finite $\mathcal{PT}$-chain.

$\beta\Lambda = 0$ axis. In the absence of gain/loss, where $n'' = 0$, the imaginary part of the eigenfrequency is very small due the coupling between the underlying high Q-factor resonator modes (Fig. 10.4(a) bottom panel), i.e. radiation loss is very small. The real part of the eigenfrequencies of the infinite passive resonator chain shows the presence of degenerate modes at the centre, $\beta\Lambda = 0$, and the end of Brillouin zone, $\beta\Lambda = \pm\pi$.

In the case of the finite chain with $N = 6$ unit cells, (Fig. 10.4(a)) the eigenfrequencies are discrete. They may be understood as sampling the continuous band-structure at discrete values of $\beta\Lambda = \pm\left(i - \frac{1}{2}\right)\frac{\pi}{N}$ around $\beta\Lambda = 0$, where $i = 1, 2, \cdots, N$. It is worth noting that although these discrete eigenfrequencies follow the general pattern of the eigenfrequencies of the infinite chain, they are not identical. Furthermore, the eigenfrequencies of the finite chain only approach Bloch phases at the points $\beta\Lambda = 0$ and $\pm\pi$, as N is increased.

When the amount of gain/loss in the system is increased to $n'' = 0.0003$ the band structure is modified in such a manner that the degenerate mode at $\beta\Lambda = 0$ splits and forms a bandgap around the frequency f_0, as shown in Fig. 10.4(b). At the same time at the end of Brillouin zone $\beta\Lambda = \pm\pi$, the real values of the eigenfrequencies coalesce but the imaginary parts split and form a complex conjugate pair. This shows that the threshold point is determined both by the amount of gain/loss in the system and the Bloch phase. The $\mathcal{PT}$-symmetric region corresponds to where the eigenfrequencies are approximately real. The $\mathcal{PT}$-broken-symmetric phase corresponds to where the eigenfrequencies become complex-conjugate pairs. This is in agreement with the case of $\mathcal{PT}$ periodic waveguide lattices, except that in the case of $\mathcal{PT}$-periodic resonator chains the eigenfrequencies have a lossy offset, see Fig. 9.7. This is due to the fact that a resonant structure is inherently radiative.

A further increase of gain/loss causes more modes to be in the $\mathcal{PT}$ broken-symmetry phase. The eigenfrequencies for a critical value of gain/loss $n'' = 0.0004472$ are pre-

sented in Fig. 10.4(c). In this specific case, the top panel shows that all the real parts of the eigenfrequencies have coalesced whilst the imaginary parts are split everywhere except at $\beta\Lambda = 0$. It is important to note that increase of gain/loss beyond $n'' > 0.0004472$ causes all eigenfrequencies to occur in complex conjugate pairs and hence the system is in a completely $\mathcal{PT}$-broken symmetry phase, as depicted in Fig. 10.4(d) for $n'' = 0.0005$.

As above, Figs. 10.4(e) and 10.4(f), show the band surface plots of the real and imaginary part of eigenfrequencies as a function of both gain/loss parameter n'' and the Bloch phase $\beta\Lambda$. The eigenfrequencies of the infinite $\mathcal{PT}$ chain are plotted as a surface plot while the eigenfrequencies of the finite $\mathcal{PT}$ chain are plotted as discrete bullet points. From Fig. 10.4(e), it can be seen that for the infinite-chain case, the degenerate mode at $\beta\Lambda = 0$ instantaneously splits to form a forbidden-gap around f_{res} whilst the high and low frequency eigenfrequency bands coalesce, starting from the edge of Brillouin zone $\beta\Lambda = \pm\pi$ towards the centre of the Brillouin zone $\beta\Lambda = 0$ as the gain/loss is increased. Equally Fig. 10.4(f) shows that the imaginary part starts splitting from $\beta\Lambda = \pm\pi$ towards $\beta\Lambda = 0$ as the gain loss increases, clearly showing that even a small amount of gain/loss can cause $\mathcal{PT}$ symmetry breaking in this case.

Moreover Fig. 10.4(e,f) show that the infinite $\mathcal{PT}$ chain is a thresholdless lasing structure when operated at the end of Brillouin zone ($\beta\Lambda = \pm\pi$). However, a practical finite $\mathcal{PT}$ chain will require a small amount of gain/loss to cause $\mathcal{PT}$-symmetry breaking at $\beta\Lambda = \pm\left(\frac{2N-1}{2N}\right)\pi$. This is referred to as *minimum threshold* gain/loss in the finite chain as n''_{th} and plot it in Fig. 10.4(g) that the minimum threshold n''_{th} decreases as the number of unit cells N increases. Figure 10.4(g) further shows that the minimum threshold can be further reduced by increasing the separation gap g. It is emphasised here that the minimum threshold n''_{th} of a practical finite simple $\mathcal{PT}$-chain behaves asymptotically as N increases, and as such a finite simple $\mathcal{PT}$-chain is not a thresholdless structure, in contrast to the finite

one.

The main conclusion of this subsection can be summarised as follows: an infinite chain of simple $\mathcal{PT}$-resonators exhibits no threshold, due to the presence of continuous band structure within the Brillouin zone $-\pi \leqslant \beta\Lambda \leqslant \pi$. In contrast, in the finite case, the eigenfrequencies are *discrete* and as such the presence of the mode close to the edge and centre of the Brilluoin zone can only be approached by increasing the number of unit cells. As a result there exists a threshold in order to break the $\mathcal{PT}$-symmetry.

10.4.2 Finite $\mathcal{PT}$-Chains with Real Modulation

This subsection focuses on the general finite $\mathcal{PT}$-chain when modulation of both real and imaginary part of the refractive index are present, i.e. ($\Delta n' \neq 0$ and $n'' \neq 0$) in (10.1). We find that, by introducing real refractive index modulation, field localization is achievable which leads to a formation of termination states. Furthermore, a judicious distribution of gain/loss causes the termination states to be in the $\mathcal{PT}$ broken-symmetry phase, which localizes the solution of the lasing and dissipative termination states at either end of the finite $\mathcal{PT}$-chain structure.

Consider a unit cell of the $\mathcal{PT}$ chain which is modulated in the manner of (10.1) with $\Delta n' = \pm 0.0005$, so that it satisfies the $\mathcal{PT}$condition, i.e. that the real part of the refractive index profile is an even function, while the imaginary part of the refractive index is an odd function in space. Figure 10.5 compares the corresponding band-structure of the infinite (solid line) and finite $\mathcal{PT}$-chains with $N = 6$ unit cells (discrete bullet points) for different values of the gain/loss parameter n''. It is emphasized here that the sign of the real index modulation will not affect the eigenfrequencies of the infinite chain as it results in identical set of coupled equation (10.2). However, for the finite $\mathcal{PT}$ chain case, the sign of modulation *will* affect the

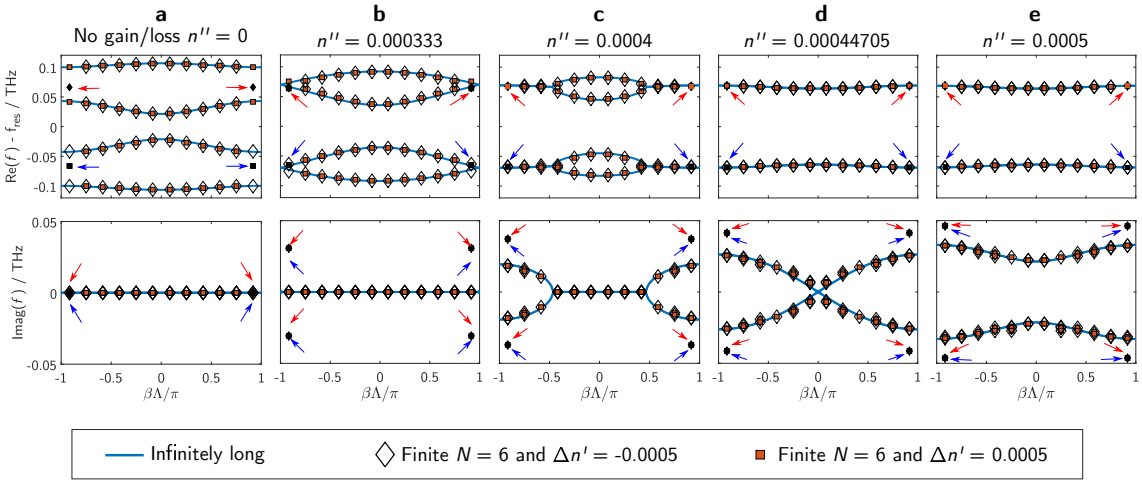

Figure 10.5 | Band structure diagram of finite $\mathcal{PT}$-chain with modulation at different gain/loss parameter. The real part (top panel) and the imaginary part (bottom panel) of the eigenfrequencies for the infinite (solid line) and finite (discrete points) $\mathcal{PT}$-chain as a function of Bloch phase $\beta\Lambda$ for different values of gain/loss n'': (**a**) passive chain $n'' = 0$; (**b**) $n'' = 0.000333$; (**c**) $n'' = 0.0004$, (**d**) $n'' = 0.00044705$ and (**e**) $n'' = 0.0005$. Real refractive index modulation $\Delta n' = -0.0005$ and 0.0005 are represented by diamond and square points respectively. The blue and red arrows points to the termination states of the negative and positive modulation respectively.

position of the eigenfrequencies which are denoted as diamonds for $\Delta n' = -0.0005$ and squares for $\Delta n' = +0.0005$.

Figure 10.5(a) shows the eigenfrequencies of the infinite and finite long passive resonator chain, i.e. $n'' = 0$. The band dispersion structure shows three band-gaps in the real eigenfrequenices whilst the imaginary parts of the eigenfrequencies are almost zero for all values of the Bloch phase. Comparing this result with Fig. 10.4(a), it can be seen that the introduction of the real index modulation has caused the splitting of degenerate eigenfrequencies at $\beta\Lambda = 0$ and $\pm\pi$ thus creating three forbidden band-gaps whereas there is only one in Fig. 10.4(a). In the case where the finite resonator chain is passive, the discrete eigenfrequencies mainly follow the path of the eigenfrequencies of the infinite resonator chain, with the exception of the degenerate modes at $\beta\Lambda = \pm 5.5\pi/6$, which are referred to here as the termination states (Fig. 10.5(a)). In the case of positive real refractive index modulation

($\Delta n' = 0.0005$) and for the real values of the eigenfrequencies, the termination states occur at the low frequency band cluster and are highlighted by blue arrows, whilst for the case of negative real refractive index modulation ($\Delta n' = -0.0005$) the termination states occur at the high frequency band-cluster and are highlighted by red arrows. Furthermore, for the finite passive resonator chain, the imaginary parts of the eigenfrequencies are almost zero for both cases of positive and negative real part modulation and are shown by overlapping discrete points in the bottom panel of Fig. 10.5(a). The imaginary part of the termination states is the same for both positive and the negative modulation of the real part of the refractive index as indicated by the red and blue arrows. It is emphasised that the presence of these degenerate modes at $\beta\Lambda = \pm 5.5\pi/6$ is a consequences of having a finite chain of resonator with real modulation.

The eigenvectors associated with the termination states of the finite passive chain of resonators are depicted in Fig. 10.6. As a passive chain, the termination states are a degenerate mode pair which led to the formation of even and odd spatial termination states. Note that the eigenvectors here are associated with the amplitude of the whispering-gallery mode distributed within the chain. The eigenvectors show that the termination states are highly localized; the field near the termination is the strongest in amplitude and the field amplitude decreases towards the middle of the chain. Figure 10.6(a) and 10.6(b) depict the eigenvectors for negative and positive real index modulation, respectively, and demonstrates the difference between the two modulations which cause the resonator to be excited with different phase but with equal strength. In practice, it is important to note that because the termination states of a passive chain are degenerate, both the even and odd termination states are simultaneously excited.

The band diagram for infinite and finite $\mathcal{PT}$-chain resonators with the gain/loss value $n'' = 0.000333$ is depicted in Fig. 10.5(b). The real part of the eigenfrequency is given by the top panel and demonstrates that the forbidden band-gaps at the

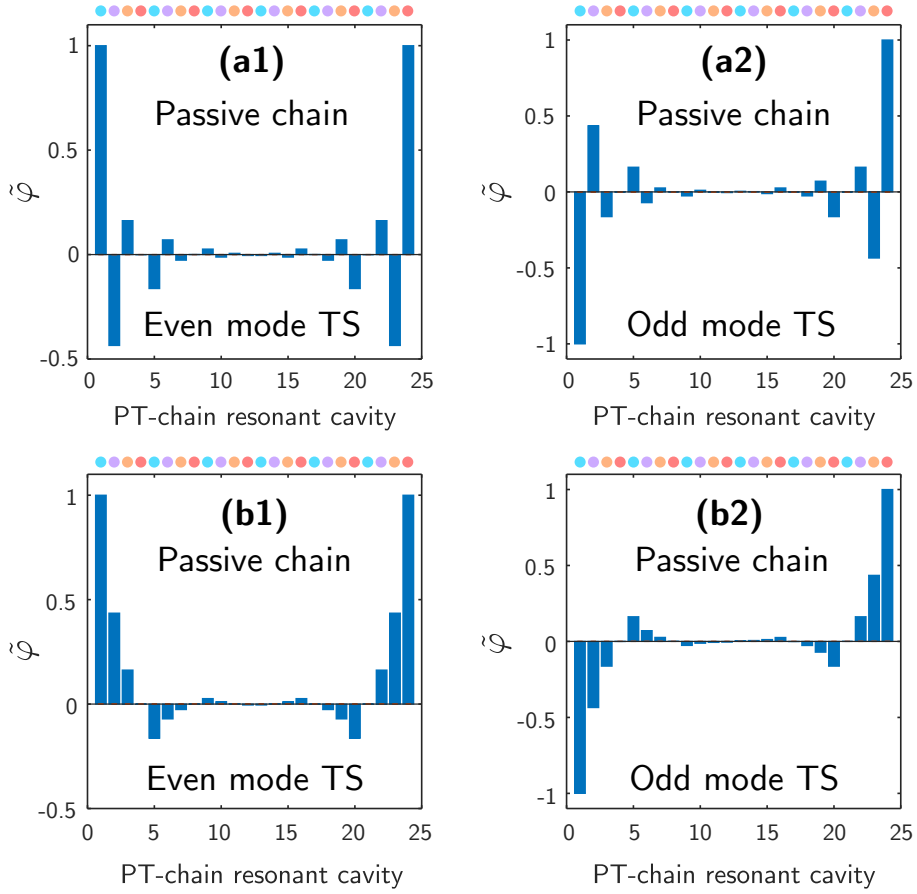

Figure 10.6 | Distribution of eigenvectors of termination states for the finite passive resonator chain. The top (**a**) and bottom (**b**) panel are for positive real index modulation respectively. The real refractive index modulation considered $\Delta n' = \pm 0.0005$. The eigenvector of index (1) associated with the even mode and index (2) associated for the odd termination states (TS).

high and low frequency clusters are reduced as the real part of eigenfrequencies coalesce at $\beta\Lambda = \pi$. Most of the eigenfrequencies of the finite $\mathcal{PT}$ chain mimic the behaviour of the eigenfrequencies of the infinite $\mathcal{PT}$ chain, with the exception of the eigenfrequencies of the termination states. The real parts of the eigenfrequencies of termination modes coalesce whilst the imaginary parts split into complex conjugate pairs as shown in the figure. It is important to note that although the values of real parts of the eigenfrequency of the termination states are approximately equal, they are not degenerate because the imaginary parts of the eigenfrequency are different.

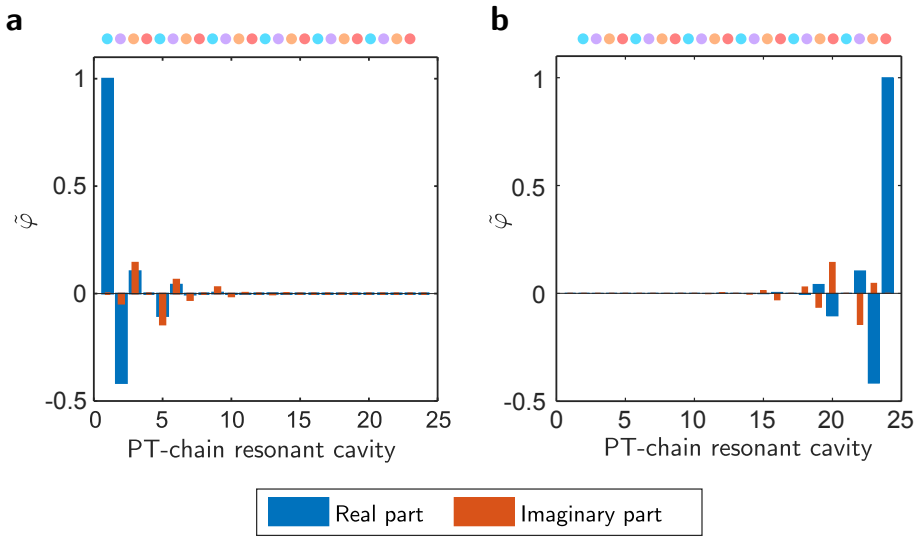

Figure 10.7 | Degree of excitation of the termination state within the finite $\mathcal{PT}$-chain. Eigenvector $\tilde{\varphi}$ of the termination states with operated at gain/loss parameter $n'' = 0.0004$. (**a**) Eigenvector for the lasing threshold states ($\mathrm{Im}(f) < 0$) and (**b**) for the dissipative threshold states ($\mathrm{Im}(f) > 0$). The $\mathcal{PT}$-chain structure is illustrated on the top of each plot. Negative sign real modulation $\Delta n' = -0.0005$.

With a further increase of gain/loss n'', in the case of both infinite and finite $\mathcal{PT}$ resonator chains, more states coalesce in both the high and low frequency band-clusters from $\beta\Lambda = \pm\pi$ towards $\beta\Lambda = 0$. Correspondingly, the imaginary part splits to form pairs of complex conjugates eigenfrequencies, as shown in Fig. 10.5(c,d). Operation with gain/loss $n'' > 0.00044705$ leads to an operation with completely complex conjugated eigenfrequencies, indicating that the system is completely in the $\mathcal{PT}$ broken-symmetry phase, as shown in Fig. 10.5(e). Finally, it can be observed from Fig. 10.5(b-e) that the imaginary parts of the termination states continue to increase in value as gain/loss increases in the system.

The eigenvectors of the termination states of the finite $\mathcal{PT}$-chain are depicted in Fig. 10.3 for the positive sign of real index modulation and Fig. 10.7 for the negative sign real index modulation with gain/loss value $n'' = 0.0004$. Comparing the eigenvectors of the termination states for the different signs of real index modulation, it is observed that the amplitudes of the eigenvectors are the same but have different phase. It confirms that for both cases the lasing termination states are localized

at the left end of the chain whilst the dissipative termination states are localized at the right end. It is important to note that the localisation of the eigenvectors is achieved by breaking the $\mathcal{PT}$-symmetry of the termination state. As a result the termination states have to be related by the $\mathcal{PT}$-transformation which causes one of the termination states to lase at one end and the other to be dissipative at the other end.

In practice, these termination states manifest themselves as localized lasing or dissipating modes at either termination end of the $\mathcal{PT}$chain. The imaginary part of the eigenvectors starts to increase as the gain/loss parameter n'' increases. It is worth commenting that these termination states are similar to the topological states induced in the $\mathcal{PT}$two-dimensional honeycomb photonic crystal lattices system [10.6] which are immune to the presence of a defect. Both termination and topological states exist on the edges of the periodic medium, but while topological states propagate around the edge of the structure, the termination modes in the present configuration are stationary and have either lasing or dissipating behaviour at different ends of the chain.

Figure 10.8 shows surface plots of the real and imaginary parts of the eigenfrequencies of the $\mathcal{PT}$ chain, with a real refractive index modulation of $\Delta n' = -0.0005$, as a function of both gain/loss parameter n'' and the Bloch phase $\beta\Lambda$. These results differ from the case illustrated in Fig. 10.2(a,b) by having a negative rather than a positive value of $\Delta n'$. Again, the eigenfrequencies of the infinite $\mathcal{PT}$ chains are plotted as a surface plot while the eigenfrequencies of the finite $\mathcal{PT}$ chain are plotted as discrete points. It is noticeable that the infinite $\mathcal{PT}$-chain with a general modulation has a significantly different band-structure compared to the band-structure for the case of simple $\mathcal{PT}$ modulation shown in Fig. 10.4(e,f). Prominent forbidden band-gaps appear in the $\mathcal{PT}$-chain with real index modulation; these band-gaps cause symmetry-breaking to occur at much higher values of gain/loss n''. However, the main difference is the presence of the termination states which are marked by black

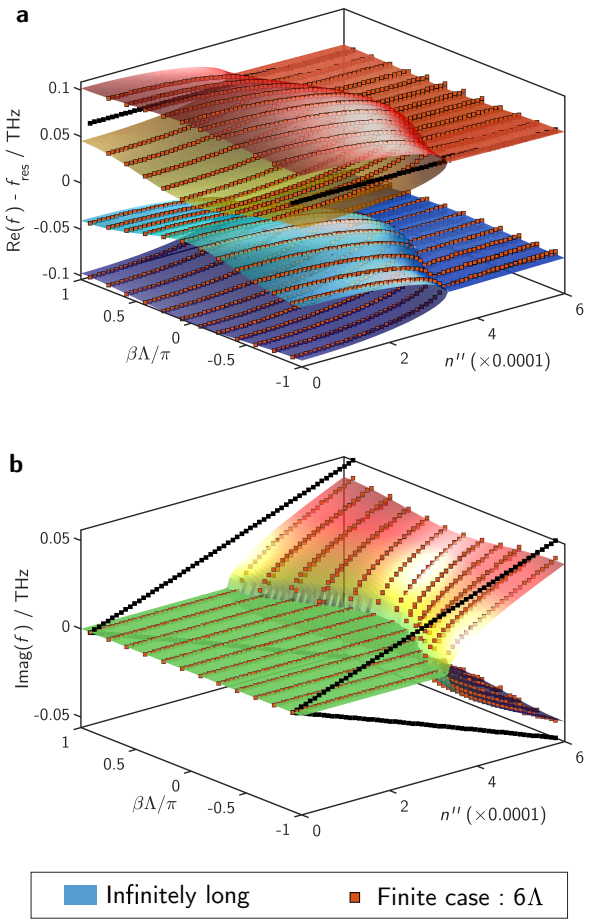

Figure 10.8 | Band structure diagram and termination states of finite $\mathcal{PT}$-chain with negative value real modulation. (**a**) Real and (**b**) imaginary part of the eigenfrequencies for the infinite (surface plot) and finite $\mathcal{PT}$-chain (discrete square bullets) as a function of Bloch phase $\beta\Lambda$ and gain/loss parameter n'' and for $\Delta n' = -0.0005$. The termination states are depicted as the black bullets.

bullets in all plots. It can be seen that for the case of negative modulation the termination states occur at the high frequency band-cluster, as shown in Fig. 10.8(a), while for the positive modulation the termination eigenfrequencies are located at the low frequency band-cluster as shown in Fig. 10.2(a). It can also be observed that for the Bloch phase $\beta\Lambda = \pm 5.5\pi/6$, the termination states undergo spontaneous $\mathcal{PT}$ symmetry-breaking. This is almost thresholdless as the imaginary part splits into pairs of complex conjugate eigenfrequencies immediately once gain/loss is present, see Fig. 10.2(b) and 10.8(b). This almost zero gain/loss threshold indicates that a

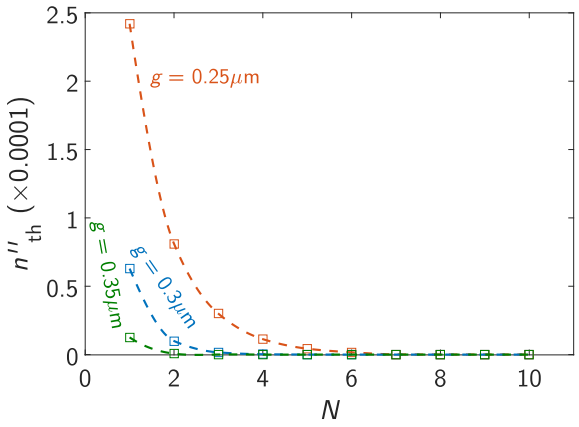

Figure 10.9 | Threshold point of the termination states of the finite $\mathcal{PT}$ chain. The impact of the number of unit cell N and separation gap g to the critical gain/loss parameter n''_{th}. For the general $\mathcal{PT}$-chain case with real modulation $\Delta n' = 0.0005$

finite $\mathcal{PT}$-chain can support lasing modes with very low amounts of added gain/loss in the system. The lasing mode is highly localized at one end of the chain. In order to reach the next gain/loss threshold much higher gain/loss is needed at which point the system reaches the $\mathcal{PT}$ symmetry-broken phase when more modes start to lase.

Closer investigation of the threshold points of the finite $\mathcal{PT}$-chains in Fig. 10.4 and Fig. 10.5 suggests that the minimum threshold for a finite $\mathcal{PT}$-chain with real modulation occurs at lower values of gain/loss than for the case of the $\mathcal{PT}$-chain with simple modulation. The minimum modulation termination states undergo a $\mathcal{PT}$ symmetry-breaking at lower values of gain/loss than for the case of the $\mathcal{PT}$-chain with simple modulation. The minimum threshold for the finite chain with simple modulation is given in Fig. 10.4(g). For comparison, the minimum thresholds n''_{th} needed to break the $\mathcal{PT}$-symmetry of the termination states of the $\mathcal{PT}$-chain with real modulation is plotted in Fig. 10.9 as the function of number of unit cells and the separation gap g. By comparing Figs. 10.4(g) and 10.9, it can be observed that the gain/loss needed to cause $\mathcal{PT}$ symmetry-breaking is lower in the case of $\mathcal{PT}$-chain with real modulation. Furthermore, it can also be seen that the rate at which minimum threshold decreases is faster for the $\mathcal{PT}$-chain with

real modulation. The minimum threshold can be further reduced by increasing the separation gap g between the resonators, which decreases the coupling strength between the resonators. It is emphasised here, that in contrast to the simple finite $\mathcal{PT}$-chain case, if N is "large enough", the threshold does not strongly depend on the number of periods. "Large enough" is only $N = 2$ for $g = 0.35$ μm and is $N = 3$ for $g = 0.3$ μm, confirming that there is no strong dependence of the threshold above this number of periods.

10.5 Summary

In this chapter the spectral properties of finite $\mathcal{PT}$-symmetric chains of dielectric resonators have been analysed. The $\mathcal{PT}$-symmetry was introduced either as a simple modulation of resonators refractive index along the chain i.e., as a chain of alternating gain and loss resonators or, by additionally introducing a modulation of the real part of the resonator refractive index so that $\mathcal{PT}$ symmetry condition is satisfied. In order to consider the more general $\mathcal{PT}$ symmetry condition a unit cell of four dielectric resonators is considered. The results show that in the case of simple $\mathcal{PT}$ modulation, the infinite $\mathcal{PT}$ resonator chain has a zero $\mathcal{PT}$ threshold whilst the finite $\mathcal{PT}$ resonator chain needs a certain critical gain/loss to achieve $\mathcal{PT}$-symmetry breaking. Furthermore the band-structure of the finite $\mathcal{PT}$-chain is a discretely sampled limit of the infinite $\mathcal{PT}$-chain case.

In the case of general $\mathcal{PT}$ symmetry the band-structure shows clear band-gaps for both infinite and finite $\mathcal{PT}$-chains. Furthermore the finite $\mathcal{PT}$-chain shows the existence of termination states, which have their highest field intensity localized near the termination ends of the resonator chain. Although general $\mathcal{PT}$ symmetry-breaking occurs at much higher values of gain/loss compared to $\mathcal{PT}$-chains with simple modulation, the presence of the termination states in the practical finite-

chain causes an almost thresholdless $\mathcal{PT}$ symmetry-breaking. This $\mathcal{PT}$-breaking is now localized to the edge resonators, with one end of the chain lasing and the other dissipating. Significantly higher gain/loss is needed to achieve complete $\mathcal{PT}$-symmetry breaking in the case of $\mathcal{PT}$ resonator chains with general $\mathcal{PT}$ symmetry, indicating that the region in between localized $\mathcal{PT}$-symmetry can be utilized for lasing applications.

In both cases the amount of the threshold gain can be further reduced by reducing the coupling in the system, for example by increasing the resonator separation or by increasing the number of unit cells in the finite $\mathcal{PT}$ chains.

References

[10.1] S. Longhi, "Optical realization of relativistic non-hermitian quantum mechanics," Phys. Rev. Lett. **105**, 013903 (2010).

[10.2] S. Longhi, "Invisibility in PT-symmetric complex crystals," J. Phys. A Math. Theor. **44**, 485302 (2011).

[10.3] R. E. Collin, *Field Theory of Guided Waves* (IEEE Press, New York, NY, 1991), 2nd ed.

[10.4] Y. D. Chong, L. Ge, and a. D. Stone, "PT-symmetry breaking and laser-absorber modes in optical scattering systems," Phys. Rev. Lett. **106**, 093902 (2011).

[10.5] L. Ge, Y. D. Chong, and a. D. Stone, "Conservation relations and anisotropic transmission resonances in one-dimensional PT-symmetric photonic heterostructures," Phys. Rev. A - At. Mol. Opt. Phys. **85**, 1–10 (2012).

[10.6] G. Harari, Y. Plotnik, M. A. Bandres, Y. Lumer, M. C. Rechtsman, and M. Segev, "Topological insulators in PT-Symmetric lattices," in "CLEO 2015," (2015), p. FTh3D.3.

11

Summary and Conclusion

11.1 Summary of the Work Presented in this Thesis

Loss has, without a doubt, been one of the key issues in optical telecommunication and quantum technologies [11.1,11.2]. On the other hand, the applications of gain materials have been primarily in laser technologies. As a result, it has been a scientific quest to find a way to compensate loss by using a gain material, but in a controllable manner, and to investigate a range of potential applications that emerge as a result. The work presented in this thesis studied a relatively new Parity-Time ($\mathcal{PT}$) symmetry photonics concept, as a direct translation from $\mathcal{PT}$-symmetric systems in Quantum Mechanics, which offers the avenue to compensate loss by having a judicious design of gain and loss media within a stable system. Numerous theoretical designs and configurations of $\mathcal{PT}$-symmetric photonic systems have been recently proposed and are found to exhibit unique properties which have never been observed before. An asymmetric response, depending on the direction of the wave incidence, *broadband* unidirectional invisibility, simultaneous laser-absorber operation and lasing in a loss-dominated system are some of the unique properties that can be exploited from a $\mathcal{PT}$-symmetric photonic structure.

It is noted, however, that oversimplification in the early theoretical studies of $\mathcal{PT}$-symmetric phontonics structures has raised questions regarding the practical aspects of the realisation of $\mathcal{PT}$-symmetric photonic technology. As a result the aims of this work were: (1) to model $\mathcal{PT}$-symmetric structures in a realistic scenario, including gain/loss material dispersion, saturation and material non-linearity; (2) to analyse the fundamental limitations of $\mathcal{PT}$-symmetric optical devices under these realistic scenario; (3) to explore a range of different applications that can be exploited by using the $\mathcal{PT}$-symmetric concept in photonics.

The concept of $\mathcal{PT}$-symmetry in Quantum Mechanics was first introduced in Chapter 3, which was then extended to photonics by showing the isomorphism of the Hamiltonian in Quantum Mechanics and in photonics scattering systems. From this isomorphism, it was shown that a $\mathcal{PT}$-symmetric photonic system can be achieved by having a judicious design of the complex refractive index profile in space. It was further shown that, for a $\mathcal{PT}$-symmetric scattering system, the more general conservation relationship, which accommodates the asymmetric left-right response, should be used instead of the conventional conservation relation. Different operational regimes of $\mathcal{PT}$-symmetric structures, such as $\mathcal{PT}$-symmetric phase, broken $\mathcal{PT}$-symmetry phase, and $\mathcal{PT}$-breaking point were also defined in this chapter.

In Chapter 4 the concept of $\mathcal{PT}$-symmetry breaking was analysed in detail by studying the spectral properties of an *idealised* $\mathcal{PT}$-symmetric Bragg grating (PTBG) structure. The idealised $\mathcal{PT}$-symmetric Bragg grating structure referred to here was a PTBG structure with a constant complex refractive index, i.e. non-dispersive, which has also been widely studied in the published literature. It was shown that in the *idealised* case the $\mathcal{PT}$-symmetric condition is satisfied at all frequencies, and as such the unique $\mathcal{PT}$-behaviour can be observed regardless of the operational frequency; this led to the claim by several authors that unidirectional invisibility in a $\mathcal{PT}$-symmetric Bragg grating is a broadband phenomenon.

To model a more realistic PTBG, including materials with dispersive gain/loss material, a simple yet realistic gain (or loss) material model was presented in Chapter 5. The simple realistic gain/loss material model described was based on the three-energy level model which is typically used to illustrate an erbium-doped gain material. The dispersive gain/loss model was further implemented into the Transmission-Line Modelling (TLM) method. The TLM is the time-domain numerical method of choice used in this thesis and was overviewed in Chapter 5.

By using both the analytical Transfer matrix (T-matrix) method and the time-domain numerical TLM method, the impact of realistic dispersive gain/loss material on the performance of a $\mathcal{PT}$-symmetric Bragg grating structure was studied in Chapter 6. The key finding of the study was that the $\mathcal{PT}$-symmetric condition can only be satisfied at a single frequency; this frequency is associated with the atomic transitional frequency which is an inherent property of the gain/loss material. As a result, it was shown that the unique behaviours of a PTBG, such as unidirectional invisibility and coherent perfect absorber and lasing (CPAL) operations, can only be achieved at this single frequency; this limits the practical application of a PTBG to operation only at a single frequency. This is considered to be one of the main findings of this thesis. Nevertheless, it was demonstrated that practical application such as all-optical switching can be still achieved, exploiting the unidirectional invisibility operation at this particular frequency, by temporally turning "on" and "off" the gain in the structure.

Chapter 7 investigated the properties of a $\mathcal{PT}$-Bragg grating structure with material non-linearity. For this purpose the Duffing model for non-linear material was implemented in the time-domain TLM method. Two different non-linear $\mathcal{PT}$-Bragg grating structures were studied, namely the non-linear $\mathcal{PT}$-Bragg grating (NPTBG) and the Kerr-induced $\mathcal{PT}$-Bragg grating (K-NPTBG). For both cases, it was demonstrated that gain/loss saturation intensity plays a crucial role in securing stable operation of non-linear $\mathcal{PT}$-based devices. It was noted, however, that in

order to allow the interplay of $\mathcal{PT}$-symmetric behaviour and the Kerr non-linear behaviour at high input intensity, a material with a high saturation intensity is required. Nevertheless, two applications were demonstrated in this chapter, namely a memory and all-optical logic gate device.

Following the detailed studies of $\mathcal{PT}$-symmetric Bragg gratings in a one-dimensional spatial domain, the focus moved to two-dimensional (2D) problems to investigate the spectral properties of $\mathcal{PT}$coupled microresonators. Chapter 8 extended the realistic dispersive gain/loss model to the 2D TLM method.

A coupled microresonator structure, where one resonator has gain whilst the other has loss, was the focus of the study of 2D $\mathcal{PT}$-symmetric structures in Chapter 9. In this chapter, a semi-analytical method was developed based on the Boundary Integral Equation (BIE) method to study the intercoupling problem of $\mathcal{PT}$-symmetric coupled microresonators. The BIE method was used to model the coupled $\mathcal{PT}$-symmetric microresonator with a realistic dispersive gain/loss model. The results obtained with the BIE method were compared with the results obtained from the TLM method; it was found that although the results from the TLM suffered from a red-shifting error due to numerical dispersion, this can be minimised by using a finer mesh. The TLM method was capable of resolving the $\mathcal{PT}$-symmetric behaviour such as $\mathcal{PT}$-symmetry breaking.

Furthermore, Chapter 9 analysed the impact of dispersion of gain/loss material on the spectral properties of $\mathcal{PT}$-coupled microresonators. It was found that the $\mathcal{PT}$-symmetric behaviour can only be observed at a single frequency; this observation was in agreement with the conclusion in Chapter 6 for the case of a $\mathcal{PT}$-symmetric Bragg grating structure. Furthermore, a lasing application has been demonstrated exploiting the early $\mathcal{PT}$-symmetry breaking by increasing the loss of the lossy resonator.

The final chapter investigated the $\mathcal{PT}$- symmetric chain of coupled microresonators.

The chapter studied the band-structure of an infinite and finite $\mathcal{PT}$-chain structure with two different kinds of $\mathcal{PT}$-symmetric refractive index modulations, i.e. a simple $\mathcal{PT}$-chain and a $\mathcal{PT}$-chain with real index modulation. The simple $\mathcal{PT}$-chain considered a chain of microresonators with gain and loss. The $\mathcal{PT}$-chain with real index modulation considered a chain of microresonators with an even function modulation of the real part of refractive index and an odd function modulation of the imaginary part of the refractive index. It was shown that in the case of a simple $\mathcal{PT}$-chain, an infinite $\mathcal{PT}$-resonator chain has a zero $\mathcal{PT}$-threshold whilst the finite $\mathcal{PT}$-chain needs a certain critical gain/loss to break the $\mathcal{PT}$-symmetry. In the case of a $\mathcal{PT}$-chain with real index modulation, the band-structure shows clear band-gaps for both infinite and finite case chains. The existence of localised termination modes was noted; i.e a modes exists at either end of the chain which have frequencies that are complex conjugates of each other and which are distinct from the band structure of the infinite $\mathcal{PT}$-chain. As such the localised termination modes are characterised by lasing at one end and dissipation at the other end.

11.2 Areas for Future Work

$\mathcal{PT}$-symmetry in photonics is a relatively young research theme but has already gained popularity in the community with more than one new publication published daily from 2014. Nevertheless, I personally believe that there is still plenty of room for exploration in $\mathcal{PT}$-symmetric photonics which may lead to more exciting physics discoveries. This section presents my attempts to outline some research themes which can be associated with $\mathcal{PT}$-symmetric photonics.

Complex $\mathcal{PT}$-symmetric photonic structure - There is an infinite amount of possible $\mathcal{PT}$-symmetric photonic structure configurations. Studies of simple $\mathcal{PT}$-symmetric structures, such as waveguides, gratings, coupled resonators and many

others, have been extensively reported. The TLM model, which is developed in this thesis, can be directly extended to model a more complex $\mathcal{PT}$-symmetry structure, for example by combination with non-linear, magnetic, plasmonic, thermal-dependent, time-dependent material properties. In particular introducing the $\mathcal{PT}$-symmetric concept within a plasmonic structure may offer a solution for the fundamental limitation in the application of plasmonic technology of high ohmic losses in metal [11.1]. Moreover, the studies of microresonator structures presented in Chapter 9 and Chapter 10 can easily be extended to study Fano resonance in coupled resonator systems. It is noted that, the BIE method developed in Chapter 9 can easily be extended for study of disordered resonator chain structures in order to study localised modes in a disordered system. It is also important to note that a $\mathcal{PT}$-symmetric structure is in fact a member of a larger class of non-Hermitian systems [11.3,11.4]. One can construct a different non-Hermitian class problem from a $\mathcal{PT}$-symmetric problem by deviating from the strict definition of $\mathcal{PT}$-symmetry condition which requires balanced gain/loss. For example, the coupled microresonator structure with dispersive gain/loss studied in Chapter 9, strictly speaking, is not a $\mathcal{PT}$-symmetric structure due to the fact that the structure has imbalanced gain-loss.

Topologically protected modes in a $\mathcal{PT}$-symmetry structure - The recent discovery of topologically protected modes in photonics [11.5] has led to the realisation of one way travelling modes in photonic crystals and topological insulators (or super conductors) [11.6–11.8]. In a topological photonic structure only a forward propagating mode is allowed while the time-reversed backward travelling wave is forbidden; realisation of this phenomena requires a spontaneous time-reversal symmetry breaking. A one-way travelling mode is crucial in the development of an optical insulator, which is important in optical telecommunication devices to suppress spurious interferences, interactions between different devices and undesired light routing [11.9]. Typical optical-insulators employ opto-magnetic active elements in

order to break the time-reversal symmetry, such as a Faraday rotator, but opto-magnetic effects become negligible at high frequency and an optical insulator based on the Faraday effect is highly sensitive to temperature changes [11.10]. On the other hand, a $\mathcal{PT}$-symmetric structure allows spontaneous $\mathcal{PT}$-symmetry breaking by means of increasing gain/loss or reducing coupling mechanically (for example decreasing the coupling strength between gain and loss elements by increasing the gap size) [11.11]; as such $\mathcal{PT}$-symmetric photonics may offer a pathway for the realisation of high-frequency optical insulators.

11.3 Overall Conclusion

In this thesis, $\mathcal{PT}$-symmetric structures have been studied within a realistic material scenario, i.e. including dispersion, saturation and Kerr non-linear behaviour. It was established that gain/loss dispersion is an important material property which should not be ignored; as such it was shown that gain/loss dispersion limits the operation of $\mathcal{PT}$-symmetric structures to a single frequency. Moreover, it was shown that for a practical application of a $\mathcal{PT}$-symmetric structure with strong signal excitation a high gain/loss saturation intensity is essential if an interplay between $\mathcal{PT}$-behaviour and the Kerr non-linear behaviour is to be allowed and exploited. It was also shown that if the saturation effect is neglected, the unbounded gain in the material may cause instability.

Different practical applications of $\mathcal{PT}$-symmetric structures are identified, such as all-optical switching, memory, logical-gate, laser and localised modes. It was demonstrated that $\mathcal{PT}$-symmetric devices offer more degrees of freedom in their operation; for example by modulating the gain/loss, the intensity of the input signal compared to a passive structure which can be manipulated solely by using the input signal intensity.

Furthermore, the thesis studied the spectral properties of the $\mathcal{PT}$-coupled microresonators. A BIE method was developed which accurately modelled the coupling between resonators. The impact of dispersion and unbalancing gain and loss were investigated. The dispersion of a realistic gain/loss material causes $\mathcal{PT}$-symmetry to be satisfied at a single frequency. Furthermore, it was observed that by increasing loss in the lossy resonator causes the $\mathcal{PT}$-symmetry to break earlier than in the case of balanced gain/loss.

The work described in the thesis also demonstrated a topologically protected mode in a $\mathcal{PT}$-chain structure with a real index modulation. This causes localised termination modes, which means that modes exist only at either end of the structure with one mode lasing at one end and the other dissipating at the other end.

References

[11.1] M. S. Tame, K. R. McEnery, . K. Özdemir, J. Lee, S. A. Maier, and M. S. Kim, "Quantum plasmonics," Nat. Phys. **9**, 329–340 (2013).

[11.2] J. Pritchard and S. Till, "UK Quantum Technology Landscape 2014," Tech. rep., Defence Science and Technoloogy Laboratory, UK (2014).

[11.3] C. M. Bender, D. C. Brody, and H. F. Jones, "Complex extension of quantum mechanics," Phys. Rev. Lett. **89**, 270401 (2002).

[11.4] Q.-H. Wang, S.-Z. Chia, and J.-H. Zhang, "PT symmetry as a generalization of Hermiticity," J. Phys. A Math. Theor. **43** (2010).

[11.5] L. Lu, J. D. Joannopoulos, and M. Soljačić, "Topological photonics," Nature Photonics **8**, 821–829 (2014).

[11.6] Y. Ando, "Topological insulator materials," J. Phys. Soc. Japan **82**, 102001 (2013).

[11.7] M. Z. Hasan and C. L. Kane, "Colloquium: Topological insulators," Rev. Mod. Phys. **82**, 3045–3067 (2010).

[11.8] J. E. Moore, "The birth of topological insulators." Nature **464**, 194–8 (2010).

[11.9] D. Jalas, A. Petrov, M. Eich, W. Freude, S. Fan, Z. Yu, R. Baets, M. Popović, A. Melloni, J. D. Joannopoulos, M. Vanwolleghem, C. R. Doerr, and H. Renner, "What is and what is not an optical isolator," Nat. Photonics **7**, 579–582 (2013).

[11.10] K. Shiraishi and S. Kawakami, "Cascaded optical isolator configuration having high-isolation characteristics over a wide temperature and wavelength range," Optics Letters **12**, 462 (1987).

[11.11] S. Phang, A. Vukovic, S. C. Creagh, P. D. Sewell, G. Gradoni, and T. M. Benson, "Localized single frequency lasing states in a finite parity-time symmetric resonator chain," Scientific reports **6**, (20499) 1–11 (2016).

A

Kramers-Kronig Relations

An introductory concept of time-causality is given in Section 2.3, in this supplementary material, the Kramers-Kronig relations (2.45) are derived in detail.

First consider the fact that a causal material properties has zero response before being excited with an external field, as such the material properties in time-domain can be expressed as

$$\chi_e(t) = \chi_e(t)H(t) \tag{A.1}$$

where, $H(t)$ is a Heaviside function and is defined as

$$H(t) = \begin{cases} 0, & \text{for} \quad t < 0 \\ 1, & \text{for} \quad t > 0 \end{cases} \tag{A.2}$$

Performing a convolution operation on (A.1) yield,

$$\mathcal{F}\{\chi_e(t)\} = \mathcal{F}\{\chi_e(t)H(t)\} = \mathcal{F}\{\chi_e(t)\} * \mathcal{F}\{H(t)\} \tag{A.3}$$

The Fourier transform of a Heaviside function $\mathcal{F}\{H(t)\}$ is given by [A.1],

$$\mathcal{F}\{H(t)\} = \int_{-\infty}^{\infty} H(t)\mathrm{e}^{-j\omega t}dt = \frac{1}{2}\delta(\omega) + \text{p.v. } \frac{j}{2\pi\omega}$$

and the Fourier transform of the material parameter $\mathcal{F}\{\chi_e(t)\}$ is,

$$\mathcal{F}\{\chi_e(t)\} = \int_{-\infty}^{\infty} \chi_e(t)\mathrm{e}^{-j\omega t}dt.$$

Noting that the property of the convolution operator:

$$p * q = \int_{-\infty}^{\infty} p(\Omega)q(\omega - \Omega)d\Omega$$

Upon applying the convolution property on (A.3), it can be shown

$$\begin{aligned}
\mathcal{F}\{\chi_e(t)\} &= \mathcal{F}\{\chi_e(t)\} * \mathcal{F}\{H(t)\} \\
&= \int_{-\infty}^{\infty} \left\{ \int_{-\infty}^{\infty} \chi_e(t)\mathrm{e}^{-j\Omega t}dt \right\} \left\{ \frac{1}{2}\delta(\omega - \Omega) + \text{p.v. } \frac{j}{2\pi(\omega - \Omega)} \right\} d\Omega \\
&= \frac{1}{2}\int_{-\infty}^{\infty}\int_{-\infty}^{\infty} \chi_e(t)\delta(\omega - \Omega)\mathrm{e}^{-j\Omega t}dtd\Omega + \int_{-\infty}^{\infty}\int_{-\infty}^{\infty} \chi_e(t)\text{p.v. } \frac{j}{2\pi(\omega - \Omega)}\mathrm{e}^{-j\Omega t}dtd\Omega \\
&= \frac{1}{2}\underbrace{\int_{-\infty}^{\infty} \chi_e(t)\mathrm{e}^{-j\omega t}dt}_{} + \frac{j}{2\pi}\int_{-\infty}^{\infty} \text{p.v. } \frac{1}{(\omega - \Omega)}\underbrace{\int_{-\infty}^{\infty} \chi_e(t)\mathrm{e}^{-j\Omega t}dt}_{}\, d\Omega \\
\chi_e(\omega) &= \frac{1}{2}\chi_e(\omega) + \frac{j}{2\pi}\text{p.v. } \int_{-\infty}^{\infty} \frac{\chi_e(\Omega)}{(\omega - \Omega)}d\Omega
\end{aligned}$$

As such that it can be found that,

$$\chi_e(\omega) = \frac{j}{\pi}\text{p.v. } \int_{-\infty}^{\infty} \frac{\chi_e(\Omega)}{(\omega - \Omega)}d\Omega$$

Considering the complex material constant in frequency domain that is defined as,

$\chi_e(\omega) = \chi'_e(\omega) + j\chi''_e(\omega)$, it follows that

$$\begin{aligned}
\chi_e(\omega) &= \frac{j}{\pi}\text{p.v.} \int_{-\infty}^{\infty} \frac{\chi_e(\Omega)}{(\omega - \Omega)} d\Omega \\
\chi'_e(\omega) + j\chi''_e(\omega) &= \frac{j}{\pi}\text{p.v.} \int_{-\infty}^{\infty} \frac{\chi'_e(\Omega) + j\chi''_e(\Omega)}{(\omega - \Omega)} d\Omega \\
&= \frac{j}{\pi}\text{p.v.} \int_{-\infty}^{\infty} \frac{\chi'_e(\Omega)}{(\omega - \Omega)} d\Omega + \frac{j}{\pi}\text{p.v.} \int_{-\infty}^{\infty} \frac{j\chi''_e(\Omega)}{(\omega - \Omega)} d\Omega
\end{aligned}$$

We have the Kramers-Kronig relations as,

$$\begin{aligned}
\chi'_e(\omega) &= -\frac{1}{\pi}\ \text{p.v.} \int_{-\infty}^{\infty} \frac{\chi''_e(\Omega)}{\omega - \Omega} d\Omega \\
\chi''_e(\omega) &= \frac{1}{\pi}\ \text{p.v.} \int_{-\infty}^{\infty} \frac{\chi'_e(\Omega)}{\omega - \Omega} d\Omega
\end{aligned}$$

or

$$\begin{aligned}
\chi'_e(\omega) &= \frac{1}{\pi}\ \text{p.v.} \int_{-\infty}^{\infty} \frac{\chi''_e(\Omega)}{\Omega - \omega} d\Omega \\
\chi''_e(\omega) &= -\frac{1}{\pi}\ \text{p.v.} \int_{-\infty}^{\infty} \frac{\chi'_e(\Omega)}{\Omega - \omega} d\Omega
\end{aligned}$$

These Kramers-Kronig relations has the significant to relate the real and imaginary part of the material parameter χ_e. As such the Kramers-Kronig relations state that a realistic material with non-zero imaginary part has to be dispersive. Moreover, it is important to note that during the derivation of the Kramers-Kronig relation a Fourier transform is performed; this implies that the inverse of the Fourier transform should exist which requires that the material parameter in the frequency domain has to be analytical in the lower half-plane of the complex plane.

B

The Transfer Matrix Method

This section presents the frequency-domain Transfer matrix (T-matrix) method used in the modelling 1-dimensional multi-layers problem. The method is well-suited to describe the relation between input-output ports in a multiple layered dielectric problem associated with Fig. B.1. The transfer matrix $\mathbf{M}$ for the given structure is defined as,

$$\begin{bmatrix} \psi_{\text{left}} \\ \varphi_{\text{left}} \end{bmatrix} = \mathbf{M} \begin{bmatrix} \psi_{\text{right}} \\ \varphi_{\text{right}} \end{bmatrix} \tag{B.1}$$

where, $\psi_{(\text{left,right})}$ denotes the amplitude of the forward propagating, whilst $\varphi_{(\text{left,right})}$ is the backward propagating electric field amplitudes at the left and right side of the structure as illustrated in Fig. B.1. By associating the transfer matrix $\mathbf{M}$ with the effective transmission and reflection coefficient of the structure, the following result

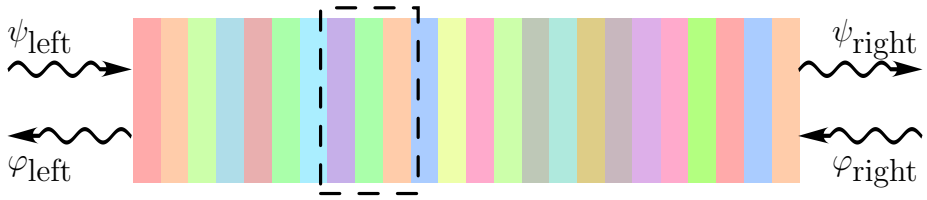

Figure B.1 | Schematic illustration of a multi layers structures.

for $\mathbf{M}$ holds,

$$\mathbf{M} = \begin{bmatrix} \frac{1}{t_L} & -\frac{r_R}{t_L} \\ \frac{r_L}{t_L} & t_R - \frac{r_L r_R}{t_L} \end{bmatrix} \tag{B.2}$$

where the entries of matrix $\mathbf{M}$ are defined as,

$$\begin{aligned} t_L &: \text{effective transmission coefficient for left incident} \\ t_R &: \text{effective transmission coefficient for right incident} \\ r_L &: \text{effective reflection coefficient for left incident} \\ r_R &: \text{effective reflection coefficient for right incident} \end{aligned} \tag{B.3}$$

Is important to note that if the structure studied is reciprocal[‡], the transmittance is equal for both sides, i.e. $t_R = t_L \equiv t$. This has a direct consequence that,

$$\det(\mathbf{M}) = 1 \tag{B.4}$$

Note that the quantities given in (B.3), are in general complex numbers. The real quantities which relate the transmitted and reflected powers are,

$$\begin{aligned} T_{L \text{ or } R} &\equiv |t|^2_{L \text{ or } R} \\ R_{L \text{ or } R} &\equiv |r|^2_{L \text{ or } R} \end{aligned}$$

Here, the T and R is commonly referred as the transmittance and reflectance coefficient, respectively.

In detail, the procedure to calculate the transfer matrix $\mathbf{M}$ are described as follows. Consider a multi-layer dielectric structure schematically illustrated in Fig. B.1, which is comprised of N dielectric layers with piece-wise refractive index profile. To accommodate, discontinuities at the interface between two layers and the change of

[‡]See Lorentz reciprocity theorem in Section 2.2.2

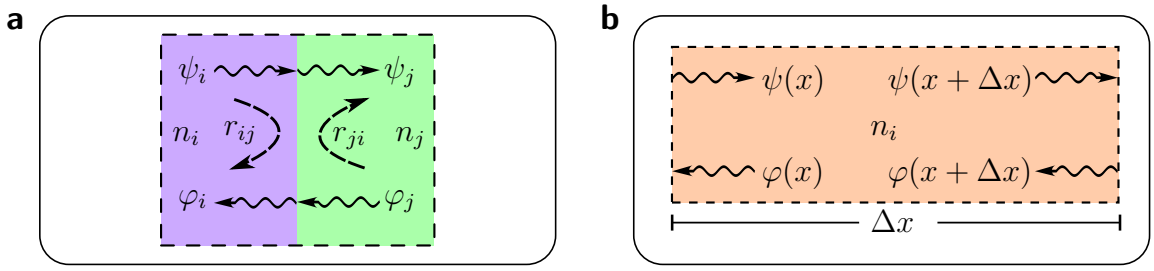

Figure B.2 | Transfer matrix method illustration.

propagation constant γ within layers, the transfer matrix $\mathbf{M}$ is comprised of all the junction $\mathbf{J}$ and phase matrices $\mathbf{P}$.

The junction matrix $\mathbf{J}$ describes the change of amplitude and phase due to the boundary condition at the interface. For illustration, Fig. B.2(a) depicts an interface between two layers of uniform refractive index n_i and n_j, with the ingoing wave ψ_i and φ_j from left and right of the interface respectively; and the scattered electric field amplitude φ_i and ψ_j. By imposing the boundary condition at the interface, the junction matrix is formulated as,

$$\begin{bmatrix} \psi_i \\ \varphi_i \end{bmatrix} = \mathbf{J}_{ij} \begin{bmatrix} \psi_j \\ \varphi_j \end{bmatrix}, \quad \text{where} \quad \mathbf{J}_{ij} = \begin{bmatrix} \frac{1}{t_{ij}} & -\frac{r_{ji}}{t_{ij}} \\ \frac{r_{ij}}{t_{ij}} & t_{ji} - \frac{r_{ij}r_{ji}}{t_{ij}} \end{bmatrix} \tag{B.5}$$

Here, t_{ij} and r_{ij} are the transmission and the reflection coefficient between the interface for normal incident and are given as,

$$t_{ij} = \frac{2n_i}{n_i + n_j} \quad \text{and} \quad r_{ij} = \frac{n_i - n_j}{n_i + n_j} \tag{B.6}$$

Substituting (B.6) to (B.5), the junction matrix has an alternative form as,

$$\mathbf{J}_{ij} = \begin{bmatrix} \frac{n_i+n_j}{2n_i} & \frac{n_i-n_j}{2n_i} \\ \frac{n_i-n_j}{2n_i} & \frac{n_i+n_j}{2n_i} \end{bmatrix} \tag{B.7}$$

Moreover, propagation within the layer also contributes to the phase change of the electric field. To illustrate this, Fig. B.2(b) displays the propagation of electric field

in the medium with refractive index n_i and hence the phase change for displacement by Δx in matrix form can be shown as,

$$\begin{bmatrix} \psi(x) \\ \varphi(x) \end{bmatrix} = \mathbf{P}_i \begin{bmatrix} \psi(x+\Delta x) \\ \varphi(x+\Delta x) \end{bmatrix}, \quad \text{where} \quad \mathbf{P}_i = \begin{bmatrix} e^{jk_0 n_i \Delta x} & 0 \\ 0 & e^{-jk_0 n_i \Delta x} \end{bmatrix} \tag{B.8}$$

Consequently, the transfer matrix of the multiple thin layer of dielectrics with piece wise refractive index distribution can be formulated as the products of all the junctions and phase matrices,

$$\begin{bmatrix} \psi_{\text{left}} \\ \varphi_{\text{left}} \end{bmatrix} = \mathbf{M} \begin{bmatrix} \psi_{\text{right}} \\ \varphi_{\text{right}} \end{bmatrix}, \quad \text{with} \quad \mathbf{M} = \mathbf{J}_{b1} \left(\prod_{i=1}^{N-1} \mathbf{P}_i \mathbf{J}_{i(i+1)} \right) \mathbf{P}_N \mathbf{J}_{Nb} \tag{B.9}$$

where, $\mathbf{J}_{b1}$ and $\mathbf{J}_{Nb}$ denote the junction matrices at the left and right sides of the structure respectively.

Furthermore, by comparing (B.9) and (2.30), the scattering matrix $\mathbf{S}$ can be expressed as,

$$\begin{bmatrix} \varphi_{\text{left}} \\ \psi_{\text{right}} \end{bmatrix} = \mathbf{S} \begin{bmatrix} \psi_{\text{left}} \\ \varphi_{\text{right}} \end{bmatrix}, \quad \text{where} \quad \mathbf{S} = \begin{bmatrix} \frac{M_{21}}{M_{11}} & M_{22} - \frac{M_{12}M_{21}}{M_{11}} \\ \frac{1}{M_{11}} & -\frac{M_{12}}{M_{11}} \end{bmatrix} \tag{B.10}$$

C

Free-Space 2D Green's Function in Cylindrical Coordinates

Green's function is the solution of the Helmholtz equation for a unit point source. For detail the reader referred to [A.2, see §7.2], while a summary is provided in this supplementary appendix. We assume that a point source is located at $\mathbf{x}'$ and the response is being observed at point $\mathbf{x}$ [A.2, see (7.2.5)], the inhomogeneous Helmholtz equation is given by,

$$\nabla^2 G(\mathbf{x}, \mathbf{x}') + k^2 G(\mathbf{x}, \mathbf{x}') = -\delta(\mathbf{x}, \mathbf{x}') \tag{C.1}$$

We will consider the solution of (C.1) in a cylindrical coordinate (r, θ, z) system, for a two-dimensional problem which is invariant in z-direction. Assuming that the source is located at the origin, such that the vector $\mathbf{x} - \mathbf{x}'$ can be simplified as $r = |\mathbf{x} - \mathbf{x}'|$ as such,

$$\nabla^2 G(r) + k^2 G(r) = -\delta(r) \tag{C.2}$$

where δ is the kronecker delta function in two-dimension. Equation (C.2) can also expressed as,

$$\frac{1}{r}\frac{d}{dr}\left(r\frac{G(r)}{dr}\right) + k^2 G(r) = -\delta(r) \tag{C.3}$$

since,

$$\delta(r) = \begin{cases} 1, & r = 0 \\ 0, & \text{else} \end{cases} \tag{C.4}$$

Equation (C.3) can expressed as,

$$\frac{1}{r}\frac{d}{dr}\left(r\frac{G(r)}{dr}\right) + k^2 G(r) = 0. \tag{C.5}$$

Equation (C.5) is known as the Bessel differential equation [A.1,A.3,A.4], and has a solution of Bessel functions $J_0(kr)$ and $Y_0(kr)$ and its combination as Hankel functions the first kind $H_0^{(1)}(kr) = J_0(kr) + jY_0(kr)$ and the second kind $H_0^{(2)}(kr) = J_0(kr) - jY_0(kr)$. Since the Bessel function J and Y are real functions for real arguments, they each represent a standing-wave, in-comparison to the complex Hankel functions which represent a travelling-waves. Furthermore, considering that the wave is travelling outwards from the source, the appropriate solution is the Hankel function of the second kind as it contains the factor e^{-jkr}. The Hankel function of the first kind contains the factor e^{jkr} and hence represents an incoming wave, [A.4, see (9.2.3)&(9.2.4)]. It follows that the appropiate solution for (C.5) is,

$$G(r) = CH_0^{(2)}(kr), \tag{C.6}$$

where C is a constant. The constant C can be obtained by substituting (C.6) to (C.3) and integrate within a small circle S around the source δ. Assuming that the radius a of the small circle is infinitesimally small, the approximation of the Hankel

function for small argument can be applied [A.4, see (9.1.7)&(9.1.8)],

$$H_0^{(2)}(kr) \approx 1 - j\frac{2}{\pi}\ln(kr), \quad \text{for } r \to 0 \tag{C.7}$$

By integrating (C.3) around the small area S, [A.4, see discussion on §7.2] , it can be shown that,

$$C \iint_S \left(\nabla\cdot\nabla + k^2\right)\left(1 - j\frac{2}{\pi}\ln(kr)\right) d\boldsymbol{S} = \iint_S (-\delta) dr \equiv -1 \tag{C.8}$$

By Gauss divergence theorem it can be shown

$$\begin{aligned} C \iint_S \left(\nabla\cdot\nabla + k^2\right)\left(1 - j\frac{2}{\pi}\ln(kr)\right) d\boldsymbol{S} = C \oint_{\partial S} \nabla\left(1 - j\frac{2}{\pi}\ln(kr)\right) d\boldsymbol{\ell} \\ + Ck^2 \iint_S \left(1 - j\frac{2}{\pi}\ln(kr)\right) d\boldsymbol{S} \end{aligned} \tag{C.9}$$

where $\oint_{\partial S} \cdots d\boldsymbol{\ell}$ is the contour integral around the boundary of the small area ∂S. The contour integral is calculated as,

$$\oint_{\partial S} \nabla\left(1 - j\frac{2}{\pi}\ln(kr)\right) d\boldsymbol{\ell} = -j\frac{2}{\pi}\int_0^{2\pi} \frac{1}{r} r d\theta = -4j. \tag{C.10}$$

The surface integration yields,

$$k^2 \lim_{a\to 0} \int_0^a \left(1 - j\frac{2}{\pi}\ln(kr)\right) 2\pi r dr = 4jk^2 \lim_{a\to 0} \frac{r^2}{4}\left(2\ln(kr) - 1\right)\Big|_0^a = 0, \tag{C.11}$$

so that, from (C.8), it can be shown that

$$C = -\frac{j}{4}. \tag{C.12}$$

The free-space Green function of 2D cylindrical coordinates is then given by,

$$G(r) = -\frac{j}{4} H_0^{(2)}(kr). \tag{C.13}$$

For the case when the source is not located at the origin, the generalised Green's function are given by,

$$G(\boldsymbol{r}, \boldsymbol{r'}) = -\frac{j}{4} H_0^{(2)}(k|\boldsymbol{r} - \boldsymbol{r'}|), \tag{C.14}$$

where $\boldsymbol{r'}$ is the location of the unit source point and $\boldsymbol{r}$ is the observation point.

References for Appendixes

[A.1] G. B. Arfken, H. J. Weber, and F. E. Harris, *Mathematical Methods for Physicists, Seventh Edition: A Comprehensive Guide* (Academic Press, Amsterdam, 2012), 7th ed.

[A.2] P. M. Morse and H. Feshbach, *Methods of Theoretical Physics, Part I* (McGraw-Hill, New York, NY, 1953).

[A.3] E. Kreyszig, *Advanced Engineering Mathematics* (John Wiley, New York, NY, 2011), 10th ed.

[A.4] M. Abramowitz and I. A. Stegun, *Handbook of Mathematical Functions* (U.S. Department of Commerce, NIST, New York: Dover, 1972).